

# **Synergistic Design of a Combined Floating Wind Turbine - Wave Energy Converter**

by

**Jocelyn Maxine Kluger**

B.S., Cornell University (2012)

S.M., Massachusetts Institute of Technology (2014)

Submitted to the Department of Mechanical Engineering  
in partial fulfillment of the requirements for the degree of

Doctor of Philosophy

at the

**MASSACHUSETTS INSTITUTE OF TECHNOLOGY**

June 2017

© Massachusetts Institute of Technology 2017. All rights reserved.

Author .....  
Department of Mechanical Engineering  
May 19, 2017

Certified by .....  
Alexander H. Slocum  
Pappalardo Professor of Mechanical Engineering  
Thesis Supervisor

Certified by .....  
Themistoklis P. Sapsis  
Associate Professor of Mechanical and Ocean Engineering  
Thesis Supervisor

Accepted by .....  
Rohan Abeyaratne  
Chairman, Department Committee on Graduate Theses



# **Synergistic Design of a Combined Floating Wind Turbine - Wave Energy Converter**

by

Jocelyn Maxine Kluger

Submitted to the Department of Mechanical Engineering  
on May 19, 2017, in partial fulfillment of the  
requirements for the degree of  
Doctor of Philosophy

## **Abstract**

Offshore energy machines have great potential: higher capacity factors, more available space, and lower visual impacts than onshore machines. This thesis investigates how combining a wave energy converter (WEC) with a floating wind turbine (FWT) may produce offshore renewable energy cost savings. Attaching the WEC to the FWT greatly reduces the WEC's steel frame, mooring lines, electric transmission lines, and siting/permitting costs, which may comprise 56% of a standalone WEC's cost. A 5 MW FWT currently requires up to 1700 tons of platform steel and 5700 tons of ballast concrete for stabilization in the ocean. This required material may be reduced if the WEC stabilizes the FWT.

This thesis addresses several challenges to designing a combined FWT-WEC.

First, parameter sweeps for optimizing ocean machine performance are limited by high dimensionalities and nonlinearities, including power takeoff control and wave viscous forcing, which normally require computationally expensive time-domain simulations. This thesis develops a statistical linearization approach to rapidly compute machine dynamics statistics while accounting for nonlinearities in the frequency domain. It is verified that the statistical linearization method may capture significant dynamics effects that are neglected by the traditional Taylor series linearization approach, while computing the results approximately 100 times faster than time domain simulations. Using Morison's equation for wave viscosity and quasi-steady blade-element/momentum theory for rotor aerodynamics, we find that viscous effects and nonlinear aerodynamics may increase the FWT motion and tower stress by up to 15% in some wind-sea states compared the the Taylor series linearized system.

Second, the WEC must stabilize rather than destabilize the FWT. This thesis investigates the dynamics statistics of different FWT-WEC configurations using a long wavelength, structurally coupled model. It is shown that simultaneous targeted energy transfer from both the FWT and waves to the WEC when the WEC and FWT are linked by a tuned spring is unlikely. That being said, this thesis considers heave-mode oscillating water column WEC's that are linked to the FWT platform by 4-bar linkages, so that the FWT and WEC's are uncoupled for small heave motions and rigidly coupled in all other degrees of freedom. It is shown that this configuration allows the WEC to move with a large ampli-

tude in its energy harvesting degree of freedom, and therefore harvest a significant amount of power without significantly increasing the FWT motion in the same direction. In the rigidly-connected modes, the WEC inertial resistance to motion must be greater than the wave forcing, as these properties are transmitted to the FWT.

Third, the WEC requires power robustness in different sea states. Typical WEC's require control schemes to maintain good power performance when the ocean wave dominant frequency differs from the WEC resonant frequency. This thesis introduces a nonlinearity into the WEC design that passively increases power adaptability in different sea states. While the optimized nonlinear WEC requires 57% more steel than the optimized linear WEC, the nonlinear WEC produces 72% more power on average, resulting in a 3% lower levelized cost of energy. Further optimization of the nonlinear WEC may find improved performance.

This thesis determines that attaching a single linear hinged floating spar oscillating water column to the FWT reduces the levelized cost of energy from \$0.31/kWh for the standalone system to \$0.27/kWh (13%) without changing stress on the FWT tower. Attaching a single nonlinear hinged floating spar oscillating water column to the FWT reduces the levelized cost of energy to \$0.26/kWh (16%) and reduces the lifetime equivalent fatigue stress on the FWT tower from 32.4 MPa to 31 MPa (5%). A 6-unit array of the nonlinear WEC's encircling the FWT platform may generate an average of 400 kW while reducing the FWT tower stress by over 50%.

In wave tank experiments, the response statistics of four different combined FWT-WEC configurations are measured, verifying the FWT-WEC dynamics model.

Thesis Supervisor: Alexander H. Slocum  
Title: Pappalardo Professor of Mechanical Engineering

Thesis Supervisor: Themistoklis P. Sapsis  
Title: Associate Professor of Mechanical and Ocean Engineering



## **Doctoral Committee**

Alexander Slocum, Ph.D.

Thesis Supervisor and Committee Chair

Pappalardo Professor of Mechanical Engineering

Massachusetts Institute of Technology

Themistoklis Sapsis, Ph.D.

Thesis Supervisor

Associate Professor of Mechanical and Ocean Engineering

Massachusetts Institute of Technology

Paul Sclavounos, Ph.D.

Professor of Mechanical Engineering and Naval Architecture

Massachusetts Institute of Technology



## Acknowledgments

First and foremost, I would like to thank my advisors Dr. Alex Slocum and Dr. Themis Sapsis for all their guidance and support that allowed my Ph.D. to become a reality. Alex's positive attitude, never-settling determination, and seamless work-life balance are inspirational. Themis's willingness to help work through research challenges, his vast knowledge on all things nonlinear and stochastic, and his calm approach are equally appreciated and inspirational. I feel very fortunate to have learned from them for 5 years. I'd like to thank my third committee member Dr. Paul Sclavounos for his valuable feedback and constructive advice.

It takes a village to get a Ph.D. Many members of the community helped me achieve my goals. My PERG labmates provided many design reviews and experiment advice- especially Maha Haji, Kevin Simon, David Taylor, Douglas Jonart, Nathan Mills, Nevan Hanumara, and Folkers Rojas. Amanda Hamlet, Dalia Leibowitz, Hilary Johnson, and Stephan Van Der Kemp all volunteered to be my safety buddy in the wave tank. Stephan walked through a blizzard so he could be there. My SAND labmates Han Kyul Joo and Mustafa Mohamed provided encouragement and helped me overcome several simulation challenges. The MIT Tow tank lab members Dixia Fan and Jacob Izraelevitz trained me to use the wave tank and allowed me to use the wave tank amid a very in-demand tank schedule. The undergraduate researcher Wesley Cox was very helpful fabricating and testing the nonlinear load cells for my Ph.D. side-project. The undergraduate researcher Justin Carrus made significant contributions designing the model-scale floating wind turbine, fabricating it, and configuring the accelerometers used in the experiment. Ken Stone, Hayami Arakawa, and Mark Belanger in the machine shops provided countless assistance and creative solutions for how to fabricate the prototypes. Irina Gazyeva, Barbara Smith, Deborah Alibrandi, and Leslie Regan provided critical administrative support.

I'm very thankful for the financial support I received from the National Science Foundation Graduate Research Fellowship, the MIT Energy Initiative grant *Energy harvesting from broad-band vibrational sources by mimicking turbulent energy transfer mechanisms*, the Naval Engineering Education Research Center grant No. 3002883706, the MIT Energy

Initiative *S.D. Bechtel, Jr. Foundation* grant, and the generous support from the Pappalardo and Martin Family fellowships.

I'm also very thankful for having great advisors at Cornell who mentored me as I learned how to do research and applied to grad school; Dr. Francis Moon, Dr. Timothy Bond, and Dr. Richard Rand.

My MIT friends Deepak Subramani, William Li, and Raghav Aggarwal turned many Friday nights into great stress relievers and fun times. I've really enjoyed our adventures in Boston.

I feel extremely fortunate to have been given the opportunity to study at MIT. I made it here by standing on the shoulders of everyone who worked hard before me, especially my parents who raised me. My Mom and Dad provided countless emotional support, encouragement, the occasional care package, and a lot of good times as we tackled the nuances of wedding planning. Some of my happiest work breaks have been phone calls with my Grandma Phyllis. All of my other relatives have also been very supportive.

Hannah and Dan provided much serious support and comic relief throughout this experience, especially during our occasional Sibling Night. Katie Aston is like a sister to me, helping me in so many ways. I look forward to continuing to experience countless fun and important events together.

Sam, the love of my life, has kept me going during this 5-year marathon; providing logistic support (e.g. being my safety buddy in the wave tank for days on end), advice, emotional support, and bringing me happiness every day. This thesis is dedicated to my family.

# Contents

<b>1</b>	<b>Introduction</b>	<b>23</b>
1.1	Survey of Wind and Wave Resources and Grid Integration Design Challenges	24
1.2	Survey of Floating Wind Turbines . . . . .	27
1.2.1	Design Challenges of Floating Wind Turbines . . . . .	28
1.3	Survey of Wave Energy Converters . . . . .	31
1.3.1	Design Challenges for Wave Energy Converters . . . . .	34
1.4	Survey of Combined Floating Wind Turbine- Wave Energy Converters and Their Design Challenges . . . . .	35
1.5	Summary of this thesis . . . . .	35
1.5.1	Fundamental Contributions . . . . .	36
<b>2</b>	<b>Linear Dynamics Model for Coupled FWT-WECs</b>	<b>39</b>
2.1	Introduction . . . . .	39
2.2	Wave Elevation and Wind Modeling . . . . .	45
2.3	Linear Floating Wind Turbine Model . . . . .	47
2.3.1	Reduced order modeling of the tower bending dynamics . . . . .	49
2.4	Linear Wave Energy Converters . . . . .	57
2.4.1	Internal Tuned Mass Damper . . . . .	61
2.4.2	Parameters for a Spherical WEC Geometry . . . . .	63
2.4.3	Parameters for a Spar-like WEC Geometry . . . . .	65
2.4.4	Power Harvested . . . . .	71
2.4.5	Matrix Components . . . . .	72
2.5	Wells Turbine Effective Damping Coefficient Modeling . . . . .	73

2.6	Structural Coupling Between Floating Wind Turbines And Wave Energy Converters . . . . .	78
2.6.1	Linkage Rotational Modes . . . . .	81
2.6.2	Linkage Translation Modes . . . . .	83
2.6.3	Rotational Coupling of 2 Linkage System . . . . .	85
2.6.4	Loading on the Links and Junctions . . . . .	86
2.6.5	Connections to the Nacelle . . . . .	87
2.6.6	Power Harvested . . . . .	88
2.6.7	Simplifications for a WEC and FWT aligned along the x-axis . . . . .	89
2.7	Platform modifications . . . . .	90
2.7.1	Parameters for a submerged cylindrical ballast . . . . .	93
2.7.2	Ideal Wells Turbine in the Spar . . . . .	98
2.8	Final equations of motion matrices . . . . .	100
2.9	Response Statistics in Stochastic Forcing . . . . .	102
2.9.1	Stress statistics . . . . .	103
<b>3</b>	<b>Statistical Linearization of Nonlinear FWT and WEC Dynamics</b>	<b>107</b>
3.1	Introduction . . . . .	107
3.2	Derivation of the Statistical Linearization Method . . . . .	110
3.3	Nonlinear Floating Wind Turbine Dynamics . . . . .	114
3.3.1	Viscous wave forcing . . . . .	114
3.3.2	Rotor Aerodynamics and Control . . . . .	118
3.3.3	Mooring Lines . . . . .	126
3.3.4	Taylor Series Linearization . . . . .	128
3.4	Results for the OC3-Hywind and OC4 semi-submersible Floating Wind Turbines . . . . .	130
3.4.1	Response Amplitude Operators . . . . .	131
3.4.2	Computed Statistics . . . . .	134
<b>4</b>	<b>Dynamics of a Wave Energy Converter with Cubic Nonlinear Hydrostatic Stiffness</b>	<b>141</b>

4.1	Introduction . . . . .	141
4.2	Cubic Stiffness Design . . . . .	143
4.3	Dynamics Model . . . . .	148
4.4	Statistical Linearization of the Cubic Nonlinear Hydrostatic Stiffness . . . . .	149
<b>5</b>	<b>Cost Model</b>	<b>151</b>
5.1	Introduction . . . . .	151
5.2	Capital Cost . . . . .	152
5.2.1	Structure Costs . . . . .	153
5.2.2	Power Takeoff Costs . . . . .	155
5.3	Fixed Charge Rate . . . . .	156
5.4	Annual Energy Production . . . . .	156
5.5	Annual Operating Expenses . . . . .	156
5.6	Final Cost Equation and Uncertainty . . . . .	157
<b>6</b>	<b>System Optimization Under Stochastic Conditions</b>	<b>159</b>
6.1	Introduction . . . . .	159
6.1.1	Common constraints for all computations . . . . .	161
6.2	Ideal Hydrokinetic and Mass Inertia Elements Rigidly Attached to FWT . . . . .	162
6.3	Linear Spherical WEC's With Tuned Spring Coupling to the FWT . . . . .	164
6.3.1	Modal Analysis . . . . .	165
6.3.2	Results . . . . .	169
6.4	Heave-Mode Floating Oscillating Water Columns With Varied Coupling to the FWT . . . . .	174
6.4.1	Rigidly Attached Oscillating Water Column . . . . .	175
6.4.2	Linear Oscillating Water Column Attached by Hinges . . . . .	179
6.4.3	Nonlinear Oscillating Water Columns Attached by Hinges . . . . .	182
6.4.4	Oscillating Water Column Comparison . . . . .	186
6.4.5	Array of Nonlinear Heave-Mode Floating Oscillating Water Columns	194

<b>7</b>	<b>Wave Tank Experiments</b>	<b>199</b>
7.1	Introduction . . . . .	199
7.2	Model Scaling . . . . .	199
7.2.1	Froude scaling . . . . .	199
7.2.2	Orifice model for a Wells Turbine . . . . .	200
7.3	Systems Tested . . . . .	201
7.4	Results and Discussion . . . . .	212
<b>8</b>	<b>Conclusions and Future Work</b>	<b>223</b>
<b>A</b>	<b>Floating Wind Turbine Parameters</b>	<b>233</b>
A.1	OC3-Hywind spar . . . . .	234
A.2	OC4-DeepCwind Semisubmersible . . . . .	237



# List of Figures

1-1	Annual average wind power in the United States, from the National Renewable Energy Laboratory Geographic Information System [105]. . . . .	25
1-2	Annual mean wave power around the world, from Cornett, 2008 [28]. . . . .	26
1-3	Annual mean currents around the world, from Lumpkin and Johnson, 2013 [93]. . . . .	26
1-4	Floating wind turbine platform concepts for varied water depth, image from Barin-Gould, 2013 [9]. . . . .	28
1-5	Strengths and weaknesses of different FWT platform designs, table from James and Ros, 2015 [63]. . . . .	30
1-6	Various wave energy converters, from Lopez et al., 2013 [92]. . . . .	31
2-1	Thesis model overview: (blue) components considered, (red) modeling challenges addressed, (green) modeling simplifications made. . . . .	40
2-2	Floating wind turbines considered in this thesis: (Left) NREL OC3-Hywind spar, image from [66]; (Right) NREL OC4-DeepCwind semisubmersible, images from [118, 144]. . . . .	46
2-3	Catenary moored spar floating wind turbine with head-on wind and incident waves. The wind turbine platform has 3 translational and 3 rotational degrees of freedom. The model allows the tower to bend in its 2 lowest fore-aft modes and two lowest side-side modes. . . . .	50
2-4	Eigenshapes and von-Mises stress trends for the tower's two lowest fore-aft bending modes found by ANSYS <sup>®</sup> finite element modal analysis. (a) Mode 1, $u_1(z)$ , 0.42 Hz. (b) Mode 2, $u_2(z)$ , 2.57 Hz. . . . .	53

2-5	Illustration of an internal tuned mass damper in the FWT nacelle. . . . .	61
2-6	Illustration of a (Left) submerged sphere and (Right) floating sphere; used as approximations in the WEC model. . . . .	63
2-7	Illustration of spar-like WEC with air Wells turbine: (Left) side view; (Center) Top view with the Wells turbine; (Right) Top view with the air turbine and turbine duct hidden. . . . .	66
2-8	Experimental data for a Wells turbine with unswept and 30-degree backward swept NACA 0015 and unswept HSIM bladed rotor turbines, without guide vanes. (a) efficiency, (b) pressure drop, (c) torque versus flow rate coefficient. From Brito-Melo, Ocean Engineering 2002 [13]. . . . .	76
2-9	Air Wells turbine coefficients for varied radius and angular velocity. . . . .	77
2-10	Water Wells turbine effective damping coefficients for varied radius and angular velocity. We assume a ratio of $A_{Inlet}/A_{Turbine} = 9$ . . . . .	77
2-11	Illustrations of FWT-WEC links: (a) surge-mode spherical form-factor WEC placed next to FWT with horizontal links, (b) heave-mode spherical form-factor WEC, (c) surge-mode spherical form-factor WEC placed in front of FWT with a vertical link (d) spar with 1 hinge, (e) spar with 2 hinges. . . . .	78
2-12	External cylindrical ballast rigidly attached to the FWT. . . . .	94
2-13	Illustration of the linked FWT and a horizontal tube-like WEC. . . . .	99
2-14	Calculation procedure for response statistics in the frequency domain. . . . .	102
3-1	Calculation procedure for response statistics in the frequency domain with statistical linearization of the nonlinear terms. . . . .	110
3-2	The effective platform diameter using for computing the viscous loads of the (Blue) OC3-Hywind spar and (Red) OC4-DeepCwind semisubmersible. . . . .	116
3-3	Torque versus speed response of the variable-speed rotor controller. Image from Jonkman, 2009 [68]. . . . .	119
3-4	Equilibrium values of generator speed, generator torque, generator power, and blade pitch, among other variables. Image from Jonkman, 2009 [68]. . . . .	120
3-5	NREL-Hywind power coefficient. . . . .	122

3-6	NREL-Hywind thrust coefficient. . . . .	122
3-7	NREL-Hywind torque coefficient. . . . .	123
3-8	NREL-Hywind power coefficient. . . . .	127
3-9	Response amplitude operators computed using Taylor series linearization and statistical linearization in the frequency domain for white noise wave excitation, with significant wave height $H_s = 0.01$ m and wind speed $U = 0$ m/s. Thick lines: statistically linearized. Thin lines: Taylor series linearized. Markers: time domain. . . . .	133
3-10	Response amplitude operators computed using Taylor series linearization and statistical linearization in the frequency domain for white noise wave excitation, with significant wave height $H_s = 1$ m and wind speed $U = 8$ m/s. Thick lines: statistically linearized. Thin lines: Taylor series linearized. Markers: time domain. . . . .	134
3-11	Response statistics for the OC3 spar and OC4 semisubmersible computed using Taylor series linearization in the frequency domain, statistical linearization in the frequency domain, and the nonlinear time domain, in a Bretschneider sea state with $H_s = 8$ m, $T_p = 12.5$ s, $U = 0$ m/s. . . . .	136
3-12	Response statistics for the OC3 spar and OC4 semisubmersible computed using Taylor series linearization in the frequency domain, statistical linearization in the frequency domain, and the nonlinear time domain, in a Bretschneider sea state with $H_s = 8$ m, $T_p = 12.5$ s, $U = 8$ m/s. . . . .	137
3-13	Response statistics computed for the OC3 spar and OC4 semisubmersible using Taylor series linearization and statistical linearization in the frequency domain over a 22 wind-sea state lifetime off the coast of Eureka, CA. . . . .	138
4-1	Steady state amplitude responses of a single degree of freedom oscillator with the governing equation, $\ddot{z} + b\dot{z} + \alpha((1 - c)z + cz^3) = F\cos(\omega t)$ . The red curve is the linear system response, the blue curve is the essentially nonlinear system response, and the green curve is a weakly nonlinear system response. Image and analysis from Quinn et al., 2011 [111]. . . . .	144

4-2	Diagram of a spar oscillating water column with a cubic nonlinear hydrostatic stiffness: (a) side view, (b) top view with air Wells turbine, (c) top view with hidden Wells turbine and air chamber top. . . . .	145
5-1	Installed Capital Cost Model based on Sandia National Laboratory flap and point absorber WEC references. . . . .	153
6-1	Response statistics for a neutrally buoyant external cylindrical ballast rigidly attached to the FWT at varied depth. . . . .	163
6-2	Response statistics for a massless damping element between the FWT and incident waves at varied depth. The dashed line represents the unmodified FWT. . . . .	164
6-3	Sketches of combined FWT-WEC array concepts for the OC3-Hywind floating wind turbine: (a) surge-mode internal surge tuned mass damper, (b) heave-mode internal tuned mass damper, and (c) heave-mode external WEC. . . . .	166
6-4	Idealized free body diagram for analyzing the mode shapes of the combined floating wind turbine-wave energy converter. . . . .	168
6-5	Annual response statistics for various FWT-WEC's attached by a spring $K_J$ for 1 : -1 modal tuning. . . . .	172
6-6	Cost uncertainty for various FWT-WEC's attached by a spring $K_J$ for 1 : -1 modal tuning. . . . .	173
6-7	CAD illustration of the rigidly-attach oscillating water column . . . . .	176
6-8	Representative free body diagrams of the rigidly attached oscillating water column FWT-WEC system in a) surge and b) heave . . . . .	176
6-9	Response statistics of an oscillating water column rigidly attached to the FWT, for varied submerged tube length and Wells turbine coefficient, for the 3 wind-sea states representing a year in Eureka, CA . . . . .	177
6-10	Cost uncertainty of an oscillating water column rigidly attached to the FWT, for varied submerged tube length and Wells turbine coefficient, for the 3 wind-sea states representing a year in Eureka, CA . . . . .	178

6-11 CAD illustration of the linear oscillating water column attached by a hinge to the FWT . . . . .	180
6-12 Representative free body diagrams of the hinged linear oscillating water column FWT-WEC system in a) surge and b) heave . . . . .	180
6-13 Response statistics of a linear oscillating water column attached by hinges to the FWT, for varied still waterline area and Wells turbine coefficient, for the 3 wind-sea states representing a year in Eureka, CA . . . . .	181
6-14 FWT-WEC cost uncertainty for a floating oscillating water column with varied still waterline area and Wells turbine coefficient. . . . .	182
6-15 CAD illustration of the nonlinear oscillating water column attached by a hinge to the FWT. . . . .	184
6-16 CAD illustration of increasing hydrostatic stiffness nonlinearity. . . . .	184
6-17 Representative free body diagrams of the hinged nonlinear oscillating water column FWT-WEC system in a) surge and b) heave. . . . .	184
6-18 Response statistics of a nonlinear oscillating water column attached by hinges to the FWT, for varied nonlinear spring coefficient and Wells turbine coefficient, for the 3 wind-sea states representing a year in Eureka, CA. . . . .	185
6-19 FWT-WEC cost uncertainty for varied nonlinear spring coefficient and Wells turbine coefficient. . . . .	186
6-20 Performance comparison for linear and nonlinear floating oscillating water columns, attached to the FWT in different ways. . . . .	190
6-21 Cost comparison for linear and nonlinear floating oscillating water columns, attached to the FWT in different ways. . . . .	191
6-22 Comparison of the response amplitude operators for linear and nonlinear floating oscillating water columns, attached to the FWT in different ways. These RAO's are independent of the sea state. . . . .	192

6-23	Comparison of the heave and pressure response amplitude operators for linear and nonlinear floating oscillating water columns, attached to the FWT in different ways. The rigid and LinFOWC RAO's remain the same in different sea states. The NonFOWC response changes for the different sea states. The 3 sea states considered are listed in Table 6.1. . . . .	193
6-24	CAD illustration of a nonlinear WEC array with 6 WEC's . . . . .	195
6-25	Response statistics for an array of nonlinear oscillating water columns attached by hinges to the FWT, for an increased number of WEC's in the array. The WEC uses the optimal nonlinear spring coefficient and Wells turbine coefficient for the 3 wind-sea states representing a year in Eureka, CA. . . . .	196
6-26	FWT-WEC cost uncertainty for an array of nonlinear oscillating water columns attached by hinges to the FWT, for an increased number of WEC's in the array. The WEC uses the optimal nonlinear spring coefficient and Wells turbine coefficient for the 3 wind-sea states representing a year in Eureka, CA. . . . .	197
6-27	Comparison of the platform response amplitude operators for an increasing number of nonlinear WEC's in an array encircling the FWT. The WEC uses the optimal nonlinear spring coefficient and Wells turbine coefficient for the 3 wind-sea states representing a year in Eureka, CA . . . . .	198
7-1	Experiment set-up in the MIT Tow Tank. . . . .	203
7-2	Freely floating experiment set-up. . . . .	204
7-3	Fixed load cell experiment set-up. . . . .	205
7-4	Experiment set-up for rigidly attached 3-OWC array. . . . .	206
7-5	Experiment set-up for rigidly attached, large OWC chamber. . . . .	207
7-6	Flexibly attached linear floating OWC's: (a) experiment set-up, (b) CAD rendering with more details. . . . .	208
7-7	Flexibly attached nonlinear floating OWC's: (a) experiment set-up, (b) CAD rendering with more details. . . . .	209

7-8	Comparison of experimental motion results for the FWT alone and two rigidly connected WEC arrays. . . . .	216
7-9	Comparison of heave motion and chamber pressure experimental results for the FWT alone and two rigidly connected WEC arrays. . . . .	217
7-10	Comparison of experimental forcing results for the FWT alone and two rigidly connected WEC arrays. . . . .	218
7-11	Comparison of experimental motion results for the FWT alone and two flexibly connected WEC arrays. . . . .	219
7-12	Comparison of heave motion and chamber pressure experimental results for the FWT alone and two flexibly connected WEC arrays. . . . .	220
7-13	Comparison of experimental forcing results for the FWT alone and two flexibly connected WEC arrays. . . . .	221
8-1	Thesis design flow chart. . . . .	226
A-1	OC3-Hywind frequency-dependent hydrodynamic added mass and damping from [66]. . . . .	235
A-2	OC3-Hywind frequency-dependent wave force normalized by wave amplitude from [66]. . . . .	236
A-3	OC4-DeepCwind semisubmersible frequency-dependent hydrodynamic added mass and damping from [118]. . . . .	238
A-4	OC4-DeepCwind semisubmersible frequency-dependent wave force normalized by wave amplitude from [118]. . . . .	239





# List of Tables

2.1	Floating wind turbine properties . . . . .	51
2.2	Coefficients for neutral axis line-of-best-fit for the tower bending modes, $u_1(z)$ and $u_2(z)$ . . . . .	54
2.3	Bending mode coefficients and natural frequencies derived by Galerkin projection. . . . .	55
2.4	WEC parameters . . . . .	60
3.1	Sea and wind states used in the statistical linearization study that has re- sponse statistics plotted in Fig. 3-13. These wind-sea states are based on data from a NOAA buoy 10 NM off the coast of Eureka, CA from 2005- 2014. $H_S$ is the significant wave height, $T_p$ is the dominant wave period, $U$ is the mean wind speed, and $p$ is the state occurrence probability. We model the sea conditions by the Bretschneider spectrum. . . . .	139
5.1	WEC cost model parameters . . . . .	158
6.1	Basic sea and wind state distribution loosely based on Eureka, CA NOAA buoy data. $H_S$ is the significant wave height, $T_p$ is the dominant wave period, $U$ is the mean wind speed, and $p$ is the state occurrence probability. We model the sea conditions by the Bretschneider spectrum. . . . .	161
6.2	Linear spherical WEC's attached to FWT considered in this section . . . . .	165
6.3	Relation of vibration analysis parameters to FWT-WEC parameters . . . . .	167
6.4	Floating wind turbine - wave energy converter properties . . . . .	169
6.5	Final Parameters of Heave-Mode Oscillating Water Columns . . . . .	189

7.1	Froude scaling . . . . .	200
7.2	Parameters of the experimental rigidly-connected WEC systems . . . . .	210
7.3	Parameters of the experimental flexibly-connected WEC systems . . . . .	211
8.1	Summary of performance for FWT-WEC's considered in this thesis. . . . .	227

# Chapter 1

## Introduction

Economic and climate change pressures have driven the development of renewable energy technology. In 2015, renewable energy accounted for 64% of all new U.S. electricity capacity installations [85]. Offshore energy machines benefit from higher capacity factors and lower visual impacts compared to onshore machines [91].

Wave power is a more predictable, constant, and energy-dense renewable resource compared to wind power, which is highly erratic [12], [30], [49]. Predictability and low variation are beneficial to electric grid operation, which requires supply-demand matching. The high energy density of wave power indicates that a smaller (cheaper) device may capture the same power as a wind device. The energy resource in waves may be as high as 50-60 kW/m average annually [30]. Despite these promising qualities, electricity from ocean wave energy converters is currently much more costly than from other sources, with levelized costs of energy ranging from \$0.28-\$1.00/kWh [15]-[90]. In comparison, on-land wind power costs an average of \$0.07/kWh. Natural gas and coal are as low as \$0.05/kWh [136].

Offshore wind is typically stronger and more constant than onshore wind, giving it the potential for cheaper, more manageable electricity than onshore wind. Less visibility from onshore is also a regulatory advantage of offshore wind. Despite these promising qualities, offshore wind power has levelized costs of energy ranging from \$0.19-0.23/kWh (predicted for floating) [66, 100].

This thesis investigates a combining a floating wind turbine with a wave energy con-

verter with the overall goal of reducing the cost of energy for both machines.

## **1.1 Survey of Wind and Wave Resources and Grid Integration Design Challenges**

The U.S. Department of Energy estimates that the United States has currently installed 84 GW capacity of onshore wind farms, and it has the onshore resource potential to reach 11,000 GW. The United States has the resource potential for 4200 GW fixed-bottom offshore wind power and an additional 6,600 GW of floating wind power in 50 to 1,000 m water depths [128].

The maximum theoretical annual power production from wave power is 100-140 GW in the United States. The maximum theoretical annual power production from ocean currents is much lower at 5-20 GW [33, 102].

Different locations around the United States and the world are more suitable for different forms of ocean resource harvesting. Fig.s 1-1 to 1-3 show the wind, ocean wave, and current resources around the world.

The western United States coast experiences an annual average of 50 kW/m power flux from ocean waves while the Northeast United States coast experiences an annual average of 15 kW/m power flux from ocean waves [30]. While Florida's eastern coast sees an average power of nearly 3 kW/m from the Gulf Stream ocean current, the rest of the United States sees less than 4 kW/m current power [29]. While small waves may make the East coast unsuitable for a wave power device, the combination of small waves and strong winds make it very suitable for an offshore wind turbine. The West coast has both strong winds and strong waves. This makes the West coast a suitable location for a combined wave-wind machine. Both the WEC and FWT would be exposed to a lot of environmental power, and the WEC could reduce wave loads on a FWT.

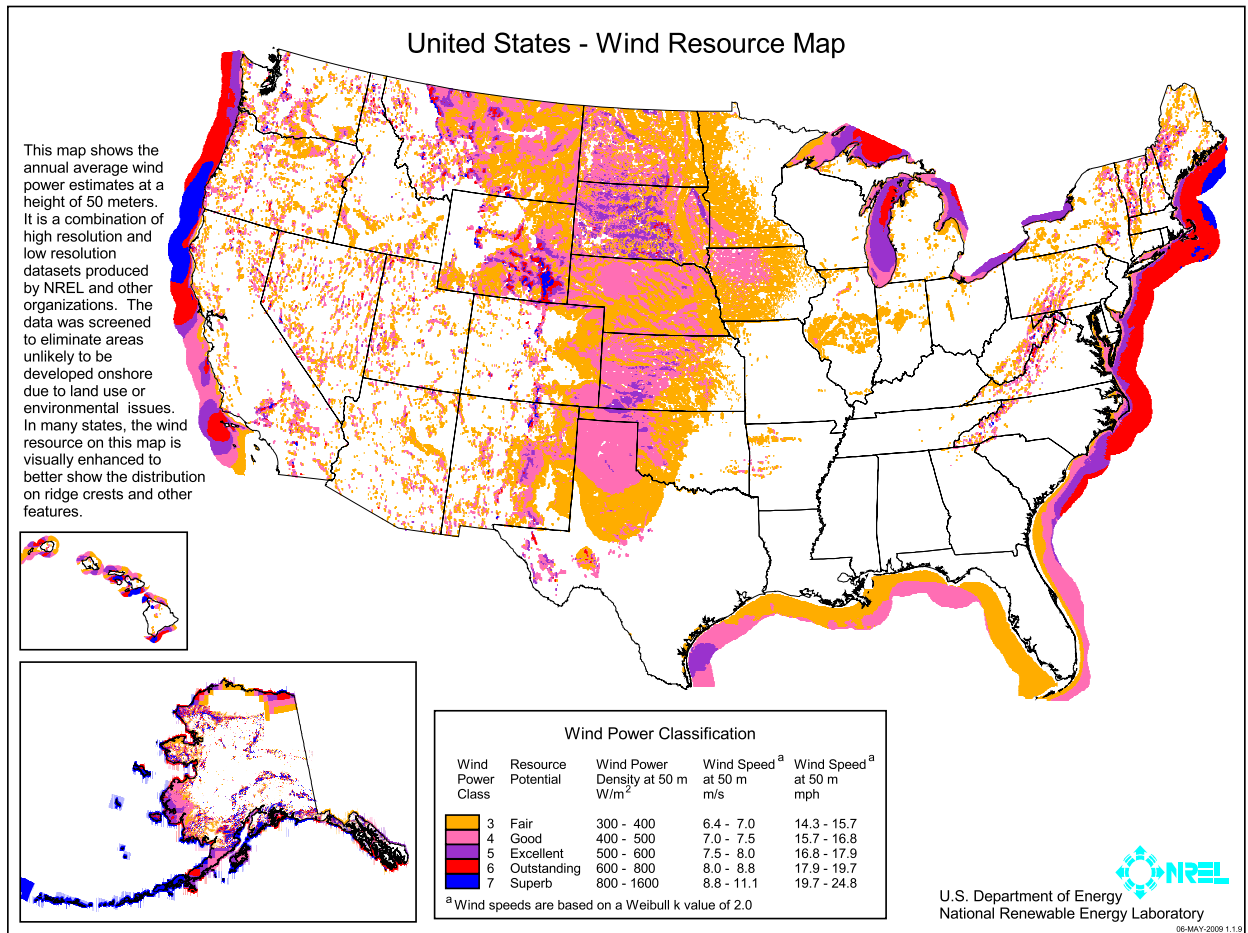


Figure 1-1: Annual average wind power in the United States, from the National Renewable Energy Laboratory Geographic Information System [105].

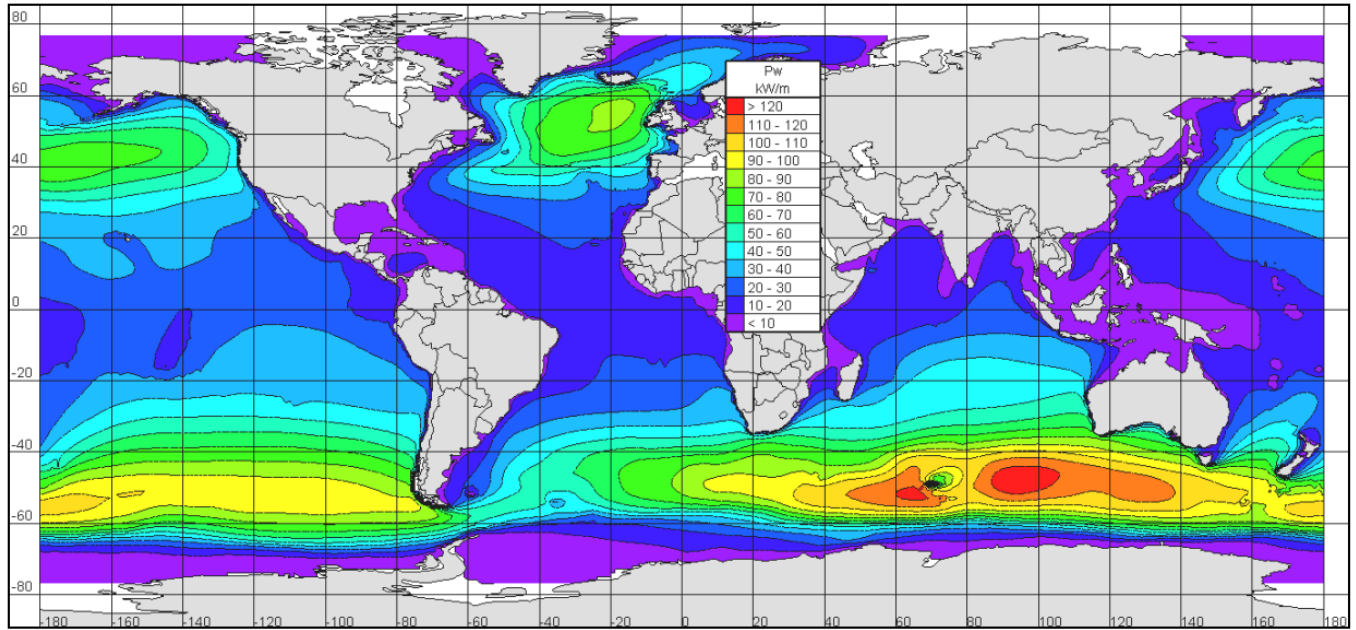


Figure 1-2: Annual mean wave power around the world, from Cornett, 2008 [28].

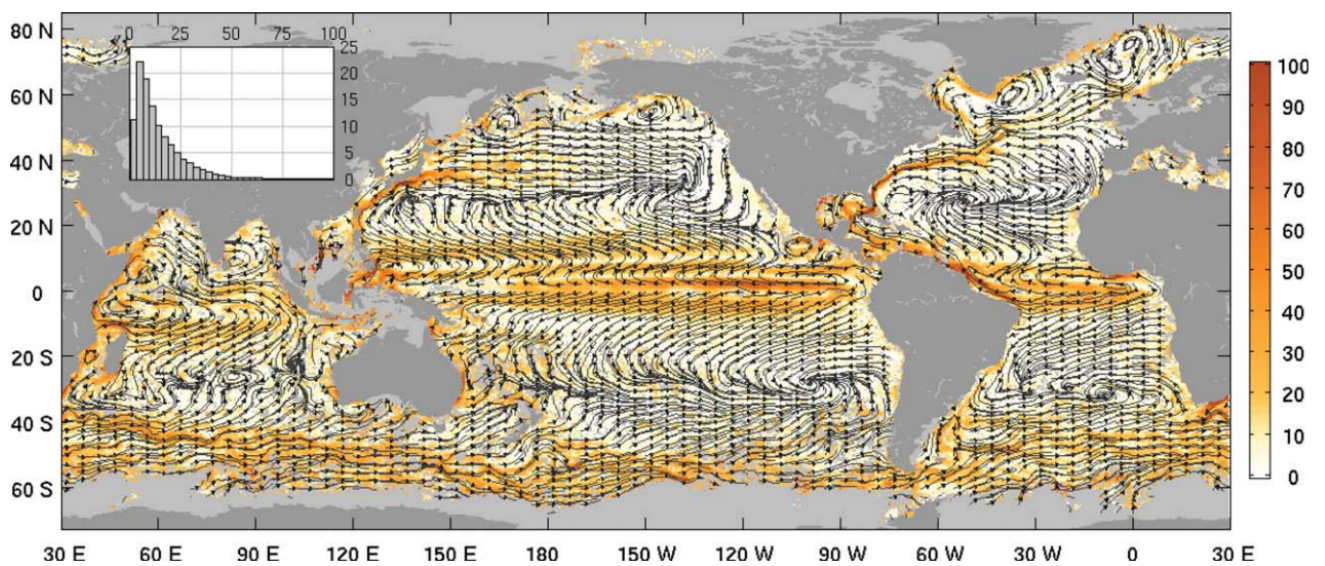


Figure 1-3: Annual mean currents around the world, from Lumpkin and Johnson, 2013 [93].

## 1.2 Survey of Floating Wind Turbines

Fig. 1-4 shows the state of the art in offshore wind turbine platforms [9]. At ocean sites with depths greater than 50 m, floating wind turbines are more economical than monopile wind turbines (Myhr et al., 2014; Jonkman, 2010). The platforms are currently designed to support turbines rated at 5-7 MW [66]. Floating platform design strategy is predominantly governed by static stability. The strategies to achieve static stability include [16],

1. ballast stabilization by a deep-submerged center of mass (e.g. the OC3-Hywind spar),
2. taut mooring line stabilization (e.g. the MIT/NREL tension leg platform),
3. buoyancy stabilization by a weighted water plane area (e.g. the ITI Energy Barge).

This thesis focuses on the the NREL/Statoil OC3-Hywind ballast stabilized spar because of its simplicity and readily-available documentation. This floating platform mass is 7,500 metric tons, with a tapered diameter ranging from 6.5-9.4 m [66].

Europe now has an installed offshore wind capacity of 12,631 MW from 3,589 wind turbines in 10 countries. In 2016, 88% of the installed offshore wind turbines in Europe had monopile foundations and 12% had jacket foundations. The average water depth for these installations was 29 m, and the average distance from shore was 44 km, both slight increases from 2015 and following the trend of the past decade [109].

The United States installed its first offshore wind farm near Block Island, Rhode Island in the summer of 2016; 5 6-MW jacket-based wind turbines. There are currently plans for 21 new offshore projects totaling 15,650 MW, in varying stages of progress [5].

A number of demonstration floating wind turbines with scaled-down capacities of 2 MW are currently in operation around the world [63]: the OC3-Hywind spar in Norway, the WindFloat semisubmersible in Portugal, and the Kabashima hybrid concrete-steel spar in Japan. Farms with capacities of 12-50 MW are planned for Japan, the United Kingdom, and France. A 30 MW WindFloat farm with 6-MW turbines is planned for the United States Pacific coast.

Fixed-bottom wind farms installed in Europe in 2012 had an average capital cost of \$5385/kW. This cost has been increasing since the year 2000, as farms are placed in deeper water further offshore [36].

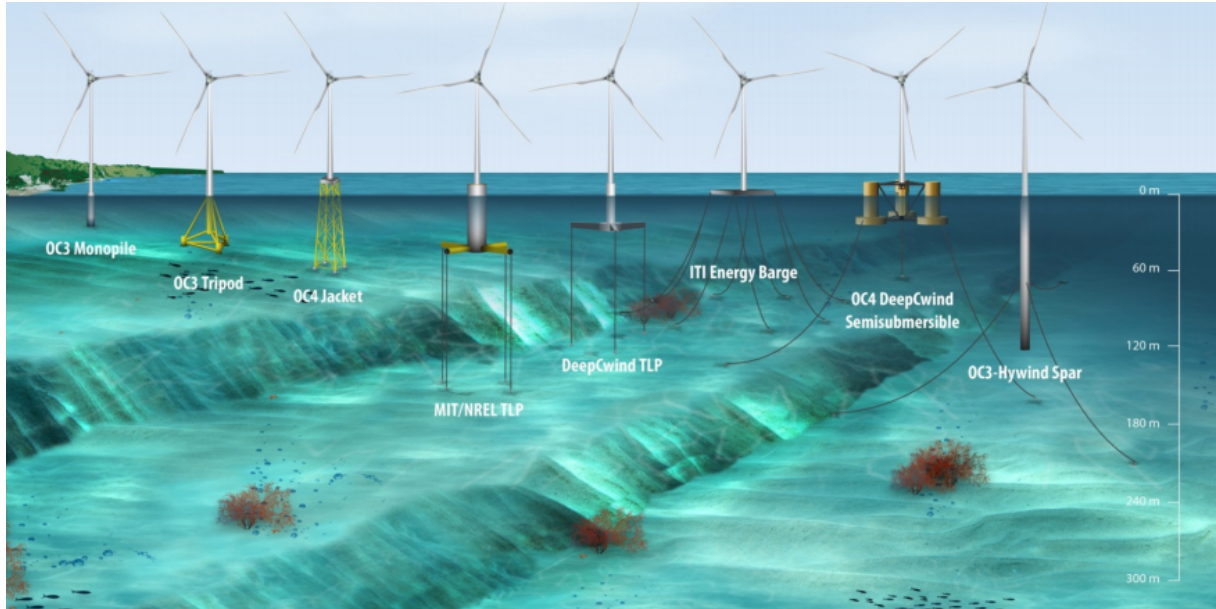


Figure 1-4: Floating wind turbine platform concepts for varied water depth, image from Barin-Gould, 2013 [9].

### 1.2.1 Design Challenges of Floating Wind Turbines

Typical floating wind turbines have estimated levelized costs of energy (LCOE) ranging from \$0.12-0.27/kWh (Myhr et al., 2014; Jonkman, 2010), which is significantly higher than the typical \$0.07/kWh for onshore wind power (Tegen et al., 2013). Fig. 1-5, from The Carbon Trust [63], lists the strengths and weaknesses of the different platforms.

Much of the FWT cost is due to the challenge of platform stabilization in the ocean. FWT platform motion is undesirable because it complicates the rotor aerodynamics and control. Pitch and yaw motions cause skewed flow and wind shear. Rapid velocity changes and rotor-wake interactions cause transitional and turbulent states (Sebastian and Lackner, 2013; Tran and Kim, 2015) [124, 138]. The floating platform must restrain pitch, roll, and heave motions within acceptable limits for the turbine (Butterfield et al., 2005) [16]. Furthermore, platform motion increases stresses on the blades, rotor shaft, yaw bearing,



and tower base (Matha, 2009) [96]. It is possible that some FWT platform motion may be desirable: when properly controlled, increased rotor motion may allow the rotor act as a wave-motion damper with increased power output, but this idea has yet to be implemented and tested (Christiansen et al., 2013) [20].

For stabilization, a semi-submersible requires a large steel mass, and sometimes an active water ballast, both associated with high costs. A tension leg platform has expensive taut moorings. A spar-buoy is constrained to deep locations and has a complex assembly. The National Renewable Energy Laboratory (NREL) OC3-Hywind spar 5 MW concept requires 1700 tons of platform steel and 5700 tons of ballast concrete to support the 285 ton tower and rotor. This large amount of steel contributes to an installed capital cost of \$22.8 million (Myhr et al., 2014; Jonkman, 2010).

Another challenge related to platform stability is floating wind turbine rotor control. The gains of a standard wind turbine torque-rotational speed controller induce negative damping on the platform pitch motion. An improved controller needs to stabilize the coupled system while maximizing power collection [121]. One strategy is predictive control to decrease fatigue loads [121, 122]. Nonlinear model predictive control can reduce tower, shaft, and blade fatigue; and reduce variation in the power and rotor speed standard deviation up to 90% [121]. Model predictive control may be implemented using a LIDAR preview of wind speeds for the feedforward control.

Many patents have been published regarding floating wind turbine platform stability. Patents related to passive platform stabilization include,

1. horizontal water entrapment plates for pitch stabilization (US 2011/0037264 Roddier),
2. fin stabilizers (US 2014/0345510 Li),
3. a deep-submerged ballast consisting of rocks exposed to the water to promote drag (US 2013/0277984 Rozinitsky).

Patents related to realizing platform stabilization via active control include,

1. controlling rotor speed to damp the wave-induced surge, pitch, and yaw motions (US 2012/0098265, Skaare; US 2015/0354532, Nielsen),

Typology	Strengths	Weaknesses
<b>Semi-submersible</b>	<ul style="list-style-type: none"> <li>✓ Flexible application due to the ability to operate in shallow water depths</li> <li>✓ Low vessel requirement – only basic tug boats required</li> <li>✓ Onshore turbine assembly</li> <li>✓ Amenable to port-side major repairs</li> </ul>	<ul style="list-style-type: none"> <li>✗ High structural mass to provide sufficient buoyancy and stability</li> <li>✗ Complex steel structures with many welded joints can be difficult to fabricate</li> <li>✗ Potentially costly active ballast systems</li> </ul>
<b>Spar-buoy</b>	<ul style="list-style-type: none"> <li>✓ Simple design is amenable to serial fabrication processes</li> <li>✓ Few moving parts (no active ballast required)</li> <li>✓ Excellent stability</li> </ul>	<ul style="list-style-type: none"> <li>✗ Constrained to deep water locations</li> <li>✗ Offshore turbine assembly requires dynamic positioning vessels and heavy-lift cranes</li> <li>✗ Large draft limits ability to tow the structure back to port for major repairs</li> </ul>
<b>Tension leg platform</b>	<ul style="list-style-type: none"> <li>✓ Low structural mass</li> <li>✓ Onshore turbine assembly</li> <li>✓ Few moving parts (no active ballast required)</li> <li>✓ Excellent stability</li> </ul>	<ul style="list-style-type: none"> <li>✗ High loads on the mooring and anchoring system</li> <li>✗ Challenging installation process</li> <li>✗ Bespoke installation barge often required</li> </ul>
<b>Multi-turbine platform</b>	<ul style="list-style-type: none"> <li>✓ Net reduction in structural mass per turbine</li> <li>✓ Platform can be used to site auxiliary equipment and facilities</li> </ul>	<ul style="list-style-type: none"> <li>✗ Wake effects can reduce yield</li> <li>✗ Large platform could be susceptible to higher bending loads</li> <li>✗ Large platform can cause fabrication and installation challenges</li> </ul>
<b>Hybrid wind/wave</b>	<ul style="list-style-type: none"> <li>✓ Merging wind and wave technologies can reduce intermittency of supply and increase total power output</li> </ul>	<ul style="list-style-type: none"> <li>✗ Challenge to integrate two energy generation systems</li> <li>✗ Increased floater motion can increase turbine loads</li> <li>✗ High structural mass</li> <li>✗ Complex O&amp;M</li> </ul>

Figure 1-5: Strengths and weaknesses of different FWT platform designs, table from James and Ros, 2015 [63].

2. an active water ballast for redistributing mass to minimize pitch (US 2011/0037264 Roddier),
3. adjustment of tension leg platform buoyancy using ballasts (US 2015/0204045 Palomas, US 2015/0044045 Alvarez),
4. underwater propeller thrusters (US 2013/0236309 Rossetti),
5. blade and rotor control to reduce tower vibration during installation (US 2008/0260514 Nielsen).

### 1.3 Survey of Wave Energy Converters

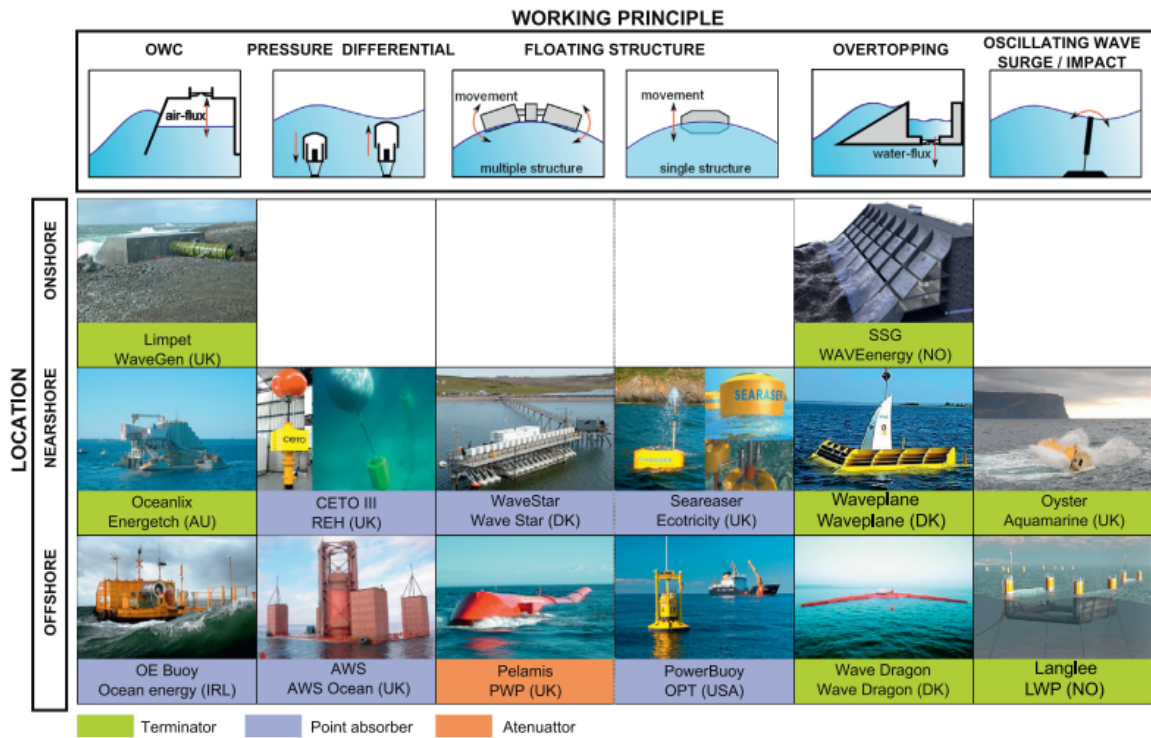


Figure 1-6: Various wave energy converters, from Lopez et al., 2013 [92].

Unlike the onshore wind industry, the wave energy industry has not converged on any one general wave energy converter (WEC) design. This is due to the wave industry being in an

earlier developmental stage than the wind industry, and also because different water depths and locations (onshore, near-shore, and offshore) are better suited for different designs [39]. General WEC designs can be categorized as overtopping devices, oscillating bodies, and oscillating water columns [12], [32], [39]. The most common types of WEC's are shown in Fig.1-6.

WEC designs are typically designed with smaller capacities than FWT's. The NREL reference surge converter is rated for 360 kW and operates at a 0.3 capacity factor. Containing 800 tons of steel and fiberglass, it has an installed capital cost of \$4.9 million (Yu et al., 2015). These properties result in a LCOE of \$0.67/kWh. 300 of the WEC's 800 tons of steel are for the support frame. While wave power is currently much more expensive than wind power, waves have higher predictability and less variation than wind, which is important for electric grid operation (Georgilakis, 2008) [49].

Overtopping devices allow waves to flow into a reservoir and then release the water back to the sea through turbines. An example is the Wave Dragon. At 260 m wide, with a reservoir capacity of 5,000 m<sup>3</sup>, and at a weight of 22,000 metric tons (including ballast), the device can produce an estimated annual average power of 1.3 MW [84].

Oscillating bodies may generate power in heave, pitch, or surge, and may be floating or submerged. The commercial-stage Pelamis WEC generates electricity by the relative motion of four 35-m-long cylindrical segments that are connected by hydraulic cylinders [30]. Rated at 750 kW with a capacity factor of about 20%, and weighing 700 tons, each device has an initial capital cost of about \$2.4 million and can produce power at a levelized cost of \$0.11-\$0.16/kWh, depending on the location's subsidies and the wave farm size [31].

Oscillating water column (OWC) devices extract power from the fluid flow in a heaving or surging column of water and air in a tube or chamber. A self-rectifying Wells turbine placed in the tube rotates in the same direction regardless of the fluid flow direction. OWC's may be fixed near shore or as part of floating buoys [39]. OWC's are an attractive technology because of their simplicity, few moving parts, easy maintenance, and efficient use of sea space [62].

Queen's University Belfast and Voith Hydro Wavegen installed the LIMPET (Land In-

stalled Marine Power Energy Transmitter) in a shoreline rock wall in Islay, Scotland in 2000. The device consists of three 6x6 m tubes inclined at 40° that feed into a 2.6 m diameter counter-rotating Wells turbine with an installed capacity of 500 kW. While the device collects an annual average pneumatic power of 100 kW, generator inefficiencies reduce the power sent to the grid to 12 kW [23]. The equipment proved itself to be robust and reliable after logging over 60,000 grid-connected operating hours in 10 years continuous operation [62].

In 1996, a pilot OWC plant was built on the shore of the island of Pico, Azores, Portugal. The column has a 12x12 m<sup>2</sup> cross-section and the turbine is rated at 560 kW. The project supplies about 108 kW average power to the island's electrical grid [22].

Several projects have worked on offshore floating OWC's. In 1998, the Japan Marine Science and technology Center installed the Mighty Whale in Gokasho Bay, Japan. The device measures 50x30x12 m (8 m draft), comprises 1,290 tons steel and weighs 4,380 tons with ballast water. It is located in water with a depth of 40 m, and its six mooring lines are designed to withstand typhoon-strength wind and wave forces. Three turbines rated at 30-60 kW each supply electricity to instruments on the device. The Mighty Whale creates a calm sea space behind it [17], [107].

In 1987, Masuda [95] studied the backward bent duct buoy (BBDB). The BBDB uses an L-shaped water column that faces away from the incident wave direction. This allows the device to be deployed in shallower waters and decreases drag. An 18-meter wide, 300 ton prototype is estimated to produce an annual average power of 53 kW.

In 2010, Oceanlinx installed a 500 kW floating oscillating water column, the Mk3PC, 100 meters off a breakwater in Port Kembla Harbour, Australia. Designed for short-term testing, adverse weather destroyed the prototype two months after installation. While commissioned, the \$4.7 million Mk3PC contributed 500 kW power to the electrical grid while simultaneously desalinating 2,000 L drinking water per day [2], [135].

### 1.3.1 Design Challenges for Wave Energy Converters

The main challenge to making wave energy converters (WEC's) cost effective is increasing their power efficiency. At a given ocean site, the various sea states throughout the year have dominant frequencies ranging from about 0.06 Hz for a severe storm to 0.16 Hz for calm water [1], [15]. The optimal performance of a wave energy converter occurs when its natural frequency matches the dominant frequency of the ocean wave spectrum [40], [71]. Therefore, one of the main challenges of wave power devices is power robustness to changes in the sea state.

One strategy for increasing the system power in various sea states is latching, where the oscillating WEC is held at its maximum position until the wave has fallen away, and then the device is held at its minimum position until the wave has risen. Latching is a nonlinear method for maximizing device power by ensuring that the wave force and WEC velocity remain in phase [12], [42], [43]. Another strategy for increasing the power robustness is to vary the system mass because a heavier WEC resonates at a lower frequency and a lighter WEC resonates at a higher frequency. [45] describes a Bipartite point absorber for which the oscillating mass can have two values, depending on whether or not a rigid connection with a fully submerged body is engaged. This strategy is implemented in the Wavebob prototype [39].

Other optimization strategies control the power takeoff damping [14], [40]. For the oscillating water column, this can be done by adjusting the Wells turbine rotational speed [8], [19], [40], electrical impedance, or blade pitch [47]. Another OWC active control approach is to use an air chamber relief valve, which prevents chamber overpressure and underpressure, an important variable for turbine efficiency (too high a pressure causes a severe drop in output power due to turbine stall) [22], [41], [108].

Introducing geometric nonlinearity or multiple degrees of freedom are other robustness strategies for stochastic excitations [48], [132]. A nonlinear strategy may be used in conjunction with control methods for optimal robustness. An additional benefit of nonlinear geometry may be that a conical shaped hull minimizes the risk of slamming [45].

## **1.4 Survey of Combined Floating Wind Turbine- Wave Energy Converters and Their Design Challenges**

Several previous studies have considered combined FWT-WEC concepts (Slocum, 2014). The WindFloat FWT has a three-column semi-submersible platform. Two columns could both be converted into 10 m diameter oscillating water columns and produce a total of 240 kW, based on tow tank experiments (Aubault et al., 2011) [7]. Muliawan et al. (2013) [7] consider a theoretical 418 ton, 20 m diameter toroid heave-mode WEC that could encircle a FWT and produce 350 kW. Kelly (2013) [77] considered a 250-m long V-shaped array of 32 oscillating water columns that could support a FWT and possibly produce up to 700 kW, based on wave tank experimental measurements. Aubault and Kelly both concluded that an attached WEC would increase the FWT pitch motion.

The hypothesis of this thesis is that combining FWT's and WEC's into one system can significantly decrease the cost of energy for both systems. 56% of the NREL reference surge converter capital cost is for the steel frame, mooring lines, electric transmission lines, and siting/permitting costs, which can be greatly reduced when combined with a FWT. Simultaneously, it is important to understand the WEC's effects on the FWT platform motion because motion reduction is beneficial while motion increase is harmful [16, 96, 124, 138].

## **1.5 Summary of this thesis**

The goal of this dissertation is to create methods and analysis techniques to help reduce the cost of wave energy converters (WEC's) and floating wind turbines (FWT's). Three principal strategies for reducing cost are investigated along with challenges to designing a combined FWT-WEC.

First, parameter sweeps for optimizing ocean machine performance are limited by high dimensionalities and nonlinearities, including power takeoff control and wave viscous forcing, which normally require computationally expensive time-domain simulations. We develop a statistical linearization approach to rapidly compute machine dynamics statistics while accounting for nonlinearities in the frequency domain. We verify that the statisti-

cal linearization method may capture significant dynamics effects that are neglected by the traditional Taylor series linearization approach, while computing the results approximately 100 times faster than time domain simulations.

Second, the WEC must stabilize rather than destabilize the FWT. We investigate the dynamics statistics of different FWT-WEC configurations using a long wavelength, structurally coupled model. We make several conclusions about WEC design constraints regarding its form factor and coupling modes with the FWT. We show that simultaneous targeted energy transfer from both the FWT and direct wave forcing to the WEC is unlikely.

Third, the WEC requires power robustness in different sea states. Typical WEC's require control schemes to maintain good power performance when the ocean wave dominant frequency differs from the WEC resonant frequency. We introduce a nonlinearity into the WEC design that passively increases power robustness in different sea states. This nonlinearity could reduce the financial and power costs of a controller.

In wave tank experiments, we measure the response statistics of four different combined FWT-WEC configurations; verifying the FWT-WEC dynamics model.

In Chapter 2, we model the linear dynamics of coupled FWT-WEC's. In Chapter 3, we develop a statistical linearization method for rapidly and more accurately computing the response statistics when the system has significant nonlinearities due to viscous wave forcing, aerodynamics, and rotor control. In Chapter 4, we design and apply the statistical linearization method to a wave energy converter with a nonlinear hydrostatic stiffness physically implemented by a varied cross-sectional area. In Chapter 5, we develop a cost model for the WEC's. In Chapter 6, we obtain the results of parameter optimization for various combined FWT-WEC's. In Chapter 7, we experimentally verify the dynamics model and results. In Chapter 8, we make conclusions.

## **1.5.1 Fundamental Contributions**

Fundamental contributions of this dissertation are,

1. Development of a statistical linearization method for FWT's and WEC's. The traditional frequency domain approach for parameter optimization at early stages of



design uses Taylor series linearization and neglects system nonlinearities. The traditional time series approach for performance evaluation at later stages of design accounts for nonlinearities but requires approximately 100 times longer to compute the response statistics than the frequency domain. The statistical linearization method used in this thesis accounts for nonlinear aerodynamics, rotor control, and viscous wave forcing in the frequency domain. This method allows potentially more accurate parameter optimization than the Taylor series linearization approach, at approximately 100 times higher computational efficiency than the time domain. This thesis shows that for some types of FWT's, the Taylor series linearization approach may underestimate fatigue stress by up to 15% in extreme wind-sea states and by up to 7% over the FWT's lifetime. Ongoing work will finalize a comparison of the statistical linearization, Taylor series linearization, and time domain results to verify accuracy.

2. Optimization of WEC's attached to FWT's. We show that static synergy is possible, whereby the wave energy converter has reduced cost and the FWT platform has reduced motion. For the sea states and high capacity-factor WEC's considered, the WEC levelized cost of energy may be reduced from \$0.31/kWh to \$0.27/kWh (13%) while the equivalent fatigue stress at the FWT tower root remains unchanged (32.4 MPa). The WEC harvests power in the heave-mode while adding both wave forcing and inertia to the FWT surge mode. Simultaneous targeted energy transfer from both the ocean waves and FWT to the WEC (the tuned mass damper effect), which would result in increased synergy, is unlikely.
3. Design of a hydrostatic nonlinearity for a heave-mode WEC. A WEC with a cross-sectional area that increases quadratically with its height acts like a cubic nonlinear spring. We show that adding this modification to a floating oscillating water column with a fixed 4-meter column radius both increases the WEC mass and improves the WEC power performance. The net result is a levelized cost of energy reduction of 4% compared to the linear floating oscillating water column.
4. Experimental verification of the FWT platform stabilization effects for various combined FWT-WEC's.



# Chapter 2

## Linear Dynamics Model for Coupled FWT-WECs

### 2.1 Introduction

Modeling the dynamics and responses of floating wind turbines and wave energy converters is important for optimizing the machine power output and cost [27, 35]. Floating wind turbine (FWT) dynamics consists of many coupled subsystem dynamics: turbulent aerodynamics; rotor control; tower, blade, and mooring line elastic deformations; and stochastic linear and nonlinear platform hydrodynamics; as sketched in Fig. 2-1 [57, 68, 70, 66, 75, 99, 101, 103, 118]. Attaching a wave energy converter (WEC) to a FWT adds additional hydrodynamic interactions, nonlinearities, control, and spring/damper coupling effects to the system [106, 7, 13, 87]. There are multiple ways to model each of these subsystems. Choosing a model normally involves a trade-off between detail and computation cost.

The most accurate subsystem models often involve nonlinearities. A FWT-WEC system with nonlinearities is typically solved in time-domain simulations. These simulations determine the system response by time-step integration using Euler or Runge-Kutta methods [3, 67]. With time steps of 0.1 seconds, computing the steady-state response of a floating wind turbine requires a simulated time of about 8,000 seconds, which translates into a computation time of approximately 13 minutes [67, 113, 79]. For a floating wind

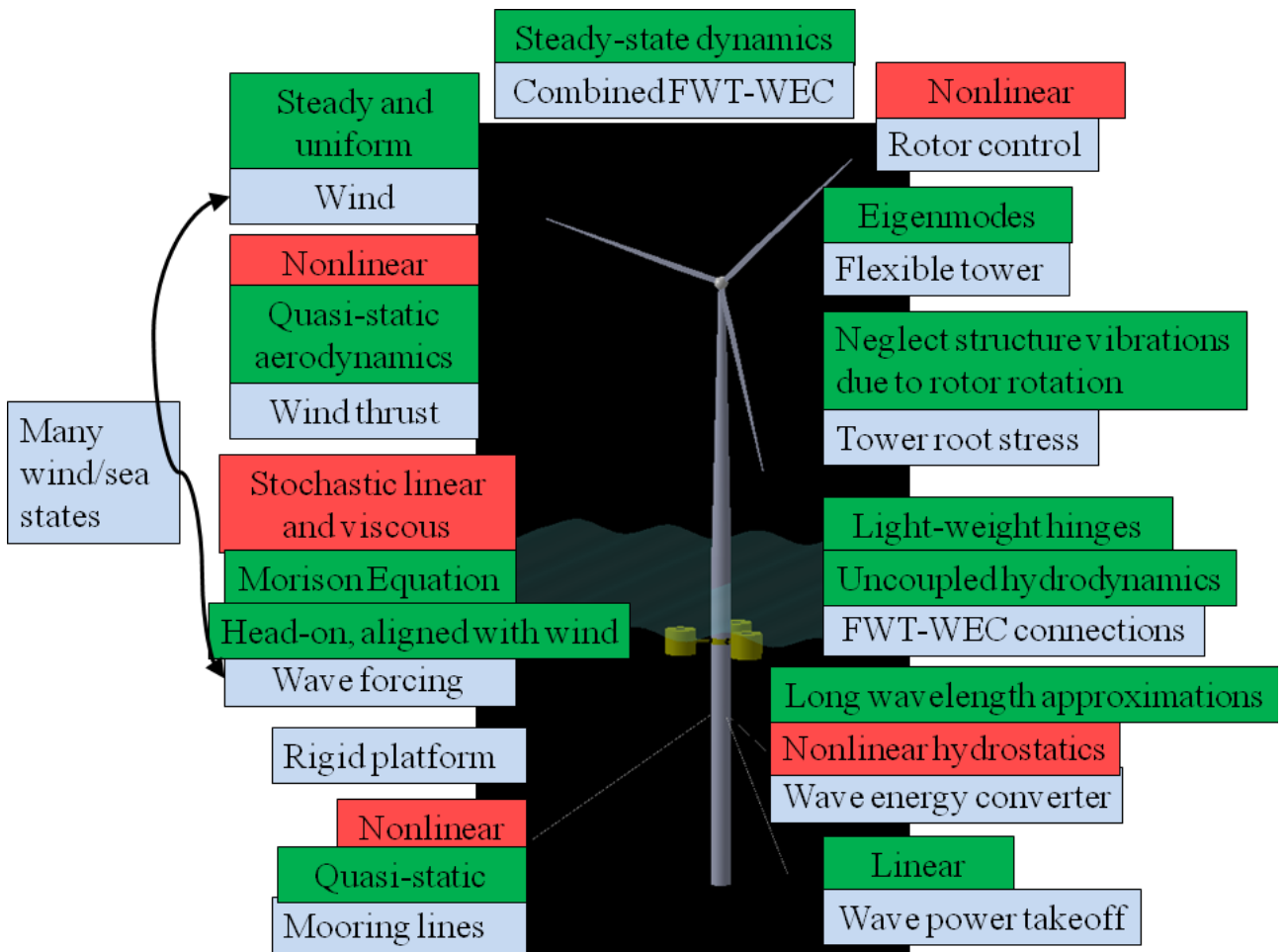


Figure 2-1: Thesis model overview: (blue) components considered, (red) modeling challenges addressed, (green) modeling simplifications made.

turbine, these codes often consider over 100 degrees of freedom, including the discretized motion and stress along the tower and each blade, and motion and stress in the rotor teeter, rotor shaft, yaw bearing, nacelle, and platform. The motion of each component has 3 translational and 3 rotational degrees of freedom. The National Renewable Energy Laboratory code FAST computes these system responses using a FORTRAN code [67]. FAST can be linked to other subsystem programs such as MoorDyn for simulating the mooring line dynamics [57]. WEC-Sim by the National Renewable Energy Laboratory simulates wave energy converters [106]. HAWC2 by The Technical University of Denmark is another freely downloadable FWT simulation program [86]. Common commercial nonlinear simulators include the general multi-body system dynamics solvers MSC ADAMS, SIMPACK, and MathWorks Simscape Multibody [3, 27].

Dynamics models typically consider hydrodynamic forces due to incident, diffracted, and radiated linear Airy waves in nonviscous potential flow. It is normally assumed that the body responses are small, so that the hydrodynamic forces are linear. The incident wave force, hydrodynamic damping, and added mass are often numerically computed using a panel method program such as WAMIT [88, 104]. In addition to panel methods, the diffracted wave velocity potentials may be theoretically computed using modal-type representations satisfying boundary conditions; for example, on a submerged cylinder (McCamy Fuchs theory) [123] or a submerged oscillating water column chamber [37, 50]. Diffraction effects are negligible if,

$$\frac{D}{\lambda} < 0.2, \quad (2.1)$$

where  $D$  is the submerged body's characteristic dimension and  $\lambda$  is the wave length. Jonkman [66] shows that  $\frac{D}{\lambda} < 0.2$  in all but very calm sea states, when loads are small anyways, for the OC3-Hywind floating wind turbine, which has characteristic dimensions in the range  $D = [6.5, 9.4]$  m. This may not be the case for typical wave energy converters, which typically have larger characteristic dimensions up to  $D = 30$  m, or other FWT platforms [143]. When diffraction effects are negligible, one may use long-wave length approximations rather than a panel method to compute the wave forcing, hydrodynamic damping and added mass [123, 103].

In addition to linear wave excitation forces, viscous effects are important when the Keulegan-Carpenter number,

$$K_C = \frac{U_{wave}T}{D} > 2, \quad (2.2)$$

where  $U_{wave}$  is the wave velocity amplitude and  $T$  is the wave period.  $K_C > 2$  indicates that flow separation occurs. Jonkman [66] shows that  $K_C < 2$  in all but the most extreme sea states, and then viscous effects are only significant near the top of the OC3 spar platform. The nonlinear viscous effects are often accounted for with Morison elements based on the incident potential flow [75]. Viscous effects may be more significant in wave energy converters than floating wind turbines, because one typically wants to minimize the FWT velocity but maximize the WEC velocity.

We model the stochastic ocean wave elevations by the Bretschneider spectrum. Since the Bretschneider spectrum model takes the significant wave height and dominant wave period as inputs, the model is not limited by a long-fetch assumption like the Pierson-Moskowitz spectrum, and can be applied to sea states ranging from developing to decaying [133]. In time domain numeric models, each discretized wave amplitude is associated with a random phase [101]. In our frequency-domain computations, the linear system response is the summation of its response to each wave component at each discretized frequency.

To model the tower and rotor blade continuous elastic bending, FAST employs modal analysis, where the continuous vibration problem is approximated by several independent single degree-of-freedom oscillators corresponding to the bending modes. With resonant frequencies well above ocean wave frequencies, FAST considers the tower's two lowest bending modes in the fore-aft and side-side directions [67]. HAWC2 uses a finite element formulation where the structure is divided into approximately 10 Timoshenko beams connected to each other by constraints [67, 75, 86].

There are three typical methods for modeling the mooring line dynamics, another continuous subsystem. The most basic approach is to linearize the mooring line forces and treat the mooring lines as massless springs. A more advanced model is to treat the mooring lines as nonlinear springs. While catenary mooring lines have a negligible effect on the platform dynamics in calm sea states, the mooring lines significantly stiffen for large

platform displacements [68]. Taut mooring lines significantly affect the dynamics of tension leg platforms [16]. The most detailed approach is to discretize the mooring lines into approximately a dozen lumped-masses with their own degrees of freedom, hydrodynamic loading, and friction on the sea floor. This model is required for predicting mooring line fatigue. In most sea states, the choice of mooring model has a small impact on the platform dynamics [58].

Wind turbine aerodynamics include stochastic turbulence, wake interaction and skewed flow due to platform pitching [138]. The highest-accuracy modeling method is solving the Reynolds averaged Navier Stokes (RANS) equation in a computational fluid dynamics approach to determine the air flow, rotor power, and rotor thrust [139]. This approach is normally too computationally expensive for floating wind turbine simulations. FAST and other time domain FWT simulation codes use the simpler quasi-static blade element momentum theory with standard Prandtl tip-losses [64, 67, 75]. A lifting-line theory and free vortex wake method is more closely related to the physical flow effects and may be more accurate than the blade element method while more computationally efficient than RANS [34, 60].

Wind turbines normally have generator-torque and blade-pitch control based on a rotor speed input. The generator control is implemented in below-rated wind conditions to adjust rotor speed for maximum aerodynamic efficiency. The blade-pitch control is implemented in above-rated wind conditions to hold the power constant at the wind turbine's power capacity. While the control laws typically use standard linear proportional and integral gains (PI), the aerodynamic responses make wind turbine control a nonlinear system. This thesis uses the PI control strategy for the NREL reference 5-MW wind turbine, described in [68]. Nonlinear model predictive control can reduce tower, shaft, and blade fatigue; and reduce variation in the power and rotor speed by up to 90% [121].

The nonlinearities of wave energy converters are typically more significant than the nonlinearities of floating wind turbines. One reason is that WEC motions are typically larger than FWT motions, which makes viscous effects more significant. Another reason is that the power takeoff may have nonlinear properties, such as hydraulics or Wells turbine stalling [13, 38]. Additional power takeoff and structural nonlinearities are important for

counteracting the linear system frequency mistuning problem (increasing power robustness in different sea states). These power robustness strategies include latching control, where an actuator holds the WEC fixed until the wave velocity exceeds a certain threshold; and varied cross-section geometry, where cubic-spring hydrostatic stiffness increases robustness (Joo and Sapsis, 2014; Kluger et al., 2014) [73, 80].

If nonlinearities are not significant or required in a preliminary analysis, then a more computationally efficient approach than the time domain for computing system responses is the linear frequency-domain (Newman, 1977; Ramachandran et al., 2013; Jonkman, 2010). In contrast to a typical 13-minute runtime using the time-domain, the frequency domain can solve for the steady-state responses in 7.5 seconds [79]. For offshore machines, the frequency domain considers linear wave forcing due to potential flow (Newman and Sclavounos, 1988). It ignores nonlinear effects related to wave viscous wave forcing or power takeoff control.

Linear frequency-domain models capture the important characteristics of many FWT platforms; however, they cannot compute transient effects and may inaccurately compute extreme loads during storms (Jonkman, 2010, Wayman et al., 2006). Furthermore, linearized systems may neglect significant resonances due to platform-flexible tower coupling (Matha, 2009). On the other hand, even as advances are being made to accelerate the time-domain simulations by substructuring and parallel processing, the intrinsic challenge of time-domain simulations is high computation cost (Schafhirt et al., 2015). The purpose of this thesis is to analyze significant changes to the FWT-WEC dynamics. Therefore, in most cases, the linear frequency domain is sufficient. In Chapters 3 and 4, we implement the method of statistical linearization to account for nonlinearities in the frequency domain model, and consider when the nonlinearities are important. In Chapter 6, we use our model to optimize the performance of a combined FWT-WEC.

In this Chapter, we describe the baseline linear model for a floating wind turbine in the frequency domain, accounting for potential flow forcing, hydrodynamic damping and added mass, and tower bending. We model and statistically linearize viscous wave forcing, nonlinear rotor control, and nonlinear mooring lines in Chapter 3. We consider only tower bending stress rather than stress at other vulnerable locations to simplify our model and



because blade-root bending moment, low-speed-shaft bending moment, and yaw-bearing bending moment all follow similar dependencies on platform surge and pitch [117]. We first model linear WEC's with form factors similar and then expand the model to include floating oscillating water column spars. In Section 5, we describe the power takeoff model and limitations of a Wells turbine. In Section connectionsSection, we model the coupling between the FWT and WEC's due to hinged links. In Section 7, we model the dynamics effects of a modified FWT platform. In Section 8, we summarize how all these aforementioned systems combine into a matrix equation of motion. Finally, in Section 9, we describe how the matrix equation of motion is combined with the Weinder-Khinchine theorem to determine the system response statistics.

## 2.2 Wave Elevation and Wind Modeling

We model the stochastic ocean wave elevation by the Bretschneider spectrum. Since the Bretschneider spectrum model takes the significant wave height and dominant wave period as inputs, the model is not limited by a long-fetch assumption like the Pierson-Moskowitz spectrum, and can be applied to sea states ranging from developing to decaying [133]. We use the Bretschneider model for the system optimization of Chapter 6. In time domain numeric models, each discretized wave amplitude is associated with a random phase [101]. In our frequency-domain computations, the linear system response is the summation of its response to each wave component at each discretized frequency. We approximate the ocean waves by 100 discrete frequencies evenly distributed between 0.01 Hz to 0.45 Hz for the parameter optimization study in Chapter 6, and by 400 discrete frequencies over the same range for the statistical linearization study in Chapter 3.

We use the single-sided Bretschneider spectrum with the standard form,

$$S_U^+ = \frac{1.25}{4} \frac{\omega_p^4}{\omega^5} H_S^2 e^{-\frac{5}{4}(\frac{\omega_p}{\omega})^4}, \quad (2.3)$$

where  $H_S$  is the significant wave height and  $\omega_p$  is the dominant wave period.

As mentioned in the Introduction of this chapter, we model steady, uniform wind at the

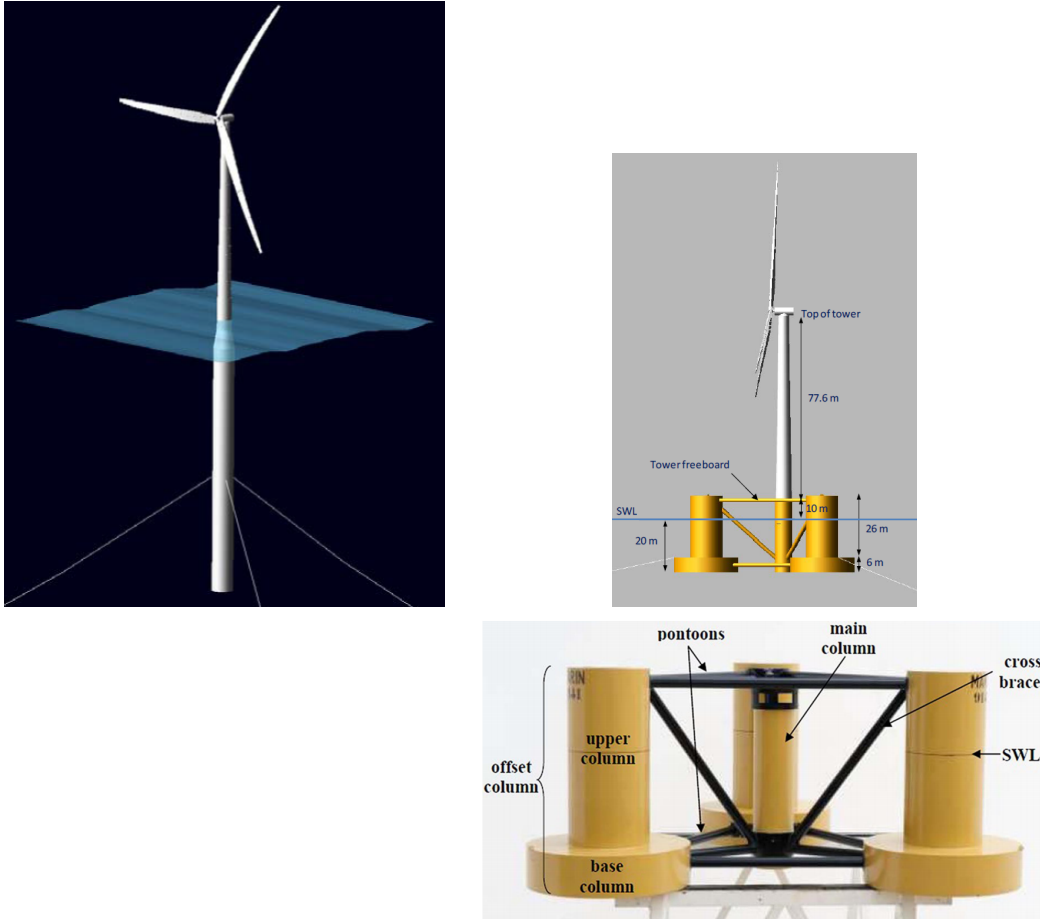


Figure 2-2: Floating wind turbines considered in this thesis: (Left) NREL OC3-Hywind spar, image from [66]; (Right) NREL OC4-DeepCwind semisubmersible, images from [118, 144].

nacelle with the value,

$$U \text{ m/s.} \tag{2.4}$$

In this thesis, we assume that the wind and waves are aligned and approach the wind turbine head-on. Future studies may easily consider the effect of non-head-on and misaligned wind and waves using the model described in this chapter.

## 2.3 Linear Floating Wind Turbine Model

The combined floating wind turbine-wave energy converter (FWT-WEC) optimization of this thesis considers the OC3-Hywind spar floating wind turbine described by Jonkman in the National Renewable Energy Laboratory (NREL) reports, [64], [66], [68]. The statistical linearization portion of this thesis considers both the OC3-Hywind spar and the OC4-DeepCwind Semisubmersible, also described in detail by NREL [118]. These FWTs are shown in Fig. 2-2.

We model floating wind turbine (FWT) dynamics using coupled linear equations of motion in matrix form. As Jonkman describes in [67], the entire floating wind turbine may be modeled with over 100 degrees of freedom.

We are interested in large effects on the system's steady-state response to ocean waves. Many of the FWT degrees of freedom responses increase proportionally with the platform motion, so explicitly modeling them increases computation cost without adding a lot of benefit for our purposes.

For simplicity in our analysis, we consider the coupled degrees of freedom that affect nacelle motion and tower bending,

$$\vec{x} = \begin{bmatrix} \vec{x}_{Platform} \\ \dots \\ \vec{x}_{Tower\ Bending} \\ \dots \\ \vec{x}_{Rotor} \end{bmatrix} = \begin{bmatrix} x_1 \\ x_2 \\ x_3 \\ x_4 \\ x_5 \\ x_6 \\ u_{1FA} \\ u_{2FA} \\ u_{1SS} \\ u_{2SS} \\ \Omega \\ \theta \end{bmatrix}. \quad (2.5)$$

$\vec{x}_{Platform} = x_1 - x_6$  are the rigid platform surge, sway, heave, roll, pitch, and yaw motions about the mean water level, respectively, as labeled in Fig. 2-3.  $\vec{x}_{Tower}^{Bending} = u_{1FA} - u_{2SS}$  are the nacelle deflection due to the flexible tower's bending modes. That is,  $u_{1FA}$  is the nacelle deflection due to bending in the first fore-aft mode,  $u_{2FA}$  is the nacelle deflection due to bending in the second fore-aft mode,  $u_{1SS}$  and  $u_{2SS}$  are the first and second tower bending modes, respectively, in the side-side direction.  $\vec{x}_{Rotor} = [\Omega \ \theta]'$  are the rotor angular velocity and blade pitch. Due to the large amount of nonlinearities in the rotor dynamics, the equations of motion for the rotor are described in Section 3.3.2 of the statistical linearization chapter.

We model the linear dynamics of the floating wind turbine by the linear equation of motion,

$$\mathbf{I}_{FWT}(\omega)\ddot{\vec{x}} + \mathbf{B}_{FWT}(\omega)\dot{\vec{x}} + \mathbf{K}_{FWT}\vec{x} = \vec{f}_{FWT}(\omega). \quad (2.6)$$

$\mathbf{I}_{FWT}(\omega)$ ,  $\mathbf{B}_{FWT}(\omega)$ , and  $\mathbf{K}_{FWT}$  are inertia, damping, and stiffness matrices respectively. Throughout this thesis, we refer to a coordinate system with an origin at the still water level, so the matrices contain nondiagonal terms as per the parallel axis theorem and a platform center of mass (CM) at a submergence of 90 m (for the OC3 spar).

We define the inertia matrix as

$$\mathbf{I}_{FWT}(\omega) = \mathbf{M}_{Platform} + \mathbf{M}_{Tower} + \mathbf{A}_{Hydro}(\omega), \quad (2.7)$$

where  $\mathbf{M}_{Platform}$  and  $\mathbf{M}_{Tower}$  are the mass matrices of the rigid platform and flexible tower, respectively.  $\mathbf{M}_{Tower}$  contains elements coupling the tower's bending modes and tower's rigid heave motion with the platform, described in more detail below.  $\mathbf{A}_{Hydro}(\omega)$  is the floating platform's added mass obtained from the panel radiation/diffraction program WAMIT [88]. The values of  $\mathbf{M}_{Platform}$  and  $\mathbf{A}_{Hydro}(\omega)$  for the OC3-Hywind and OC4-DeepCwind semisubmersible are given in Appendix A.

The damping matrix is

$$\mathbf{B}_{FWT}(\omega) = \mathbf{B}_{Hydro}(\omega), \quad (2.8)$$

where  $\mathbf{B}_{Hydro}(\omega)$  is the frequency-dependent platform hydrodynamic damping. The values

of  $\mathbf{B}_{\text{Hydro}}(\omega)$  for the OC3-Hywind and OC4-DeepCwind semisubmersible are also given in Appendix A.

The spring stiffness matrix is

$$\mathbf{K}_{FWT} = \mathbf{C}_{\text{Hydro}} + \mathbf{K}_{\text{Mooring}} + \mathbf{K}_{\text{Tower}}, \quad (2.9)$$

where  $\mathbf{C}_{\text{Hydro}}$  contains the platform hydrostatic restoring coefficients,  $\mathbf{K}_{\text{Mooring}}$  is the spring stiffness matrix for the linearized the mooring lines, and  $\mathbf{K}_{\text{Tower}}$  contains the tower stiffness coefficients. The values of  $\mathbf{C}_{\text{Hydro}}$  and  $\mathbf{K}_{\text{Mooring}}$  for the OC3-Hywind and OC4-DeepCwind semisubmersible are given in Appendix A.  $\mathbf{K}_{\text{Tower}}$  is described below.

The forcing vector from the incident and diffracted wave potential is,

$$\vec{f}_{FWT} = \vec{f}_{\text{Hydro}} = \Re \left\{ \vec{F} e^{i\omega t} \right\} = \Re \left\{ \begin{pmatrix} F_1 \\ 0 \\ F_3 \\ 0 \\ F_5 \\ 0 \\ 0 \\ 0 \\ 0 \\ 0 \\ 0 \end{pmatrix} e^{i\omega t} \right\}. \quad (2.10)$$

$\vec{f}_{\text{Hydro}}$  is the linear hydrodynamic forcing found by WAMIT and is listed in Appendix A for the OC3-Hywind and OC4-DeepCwind semisubmersible.

### 2.3.1 Reduced order modeling of the tower bending dynamics

The differential equation for the transverse tower deflection relative to the floating platform,  $u(z_T, t)$ , is

$$EI(z_T) \frac{\partial^4 u}{\partial z_T^4} + \rho A(z_T) \left( \frac{\partial^2 u}{\partial t^2} + \frac{\partial^2 y(z_T, t)}{\partial t^2} \right) = 0. \quad (2.11)$$

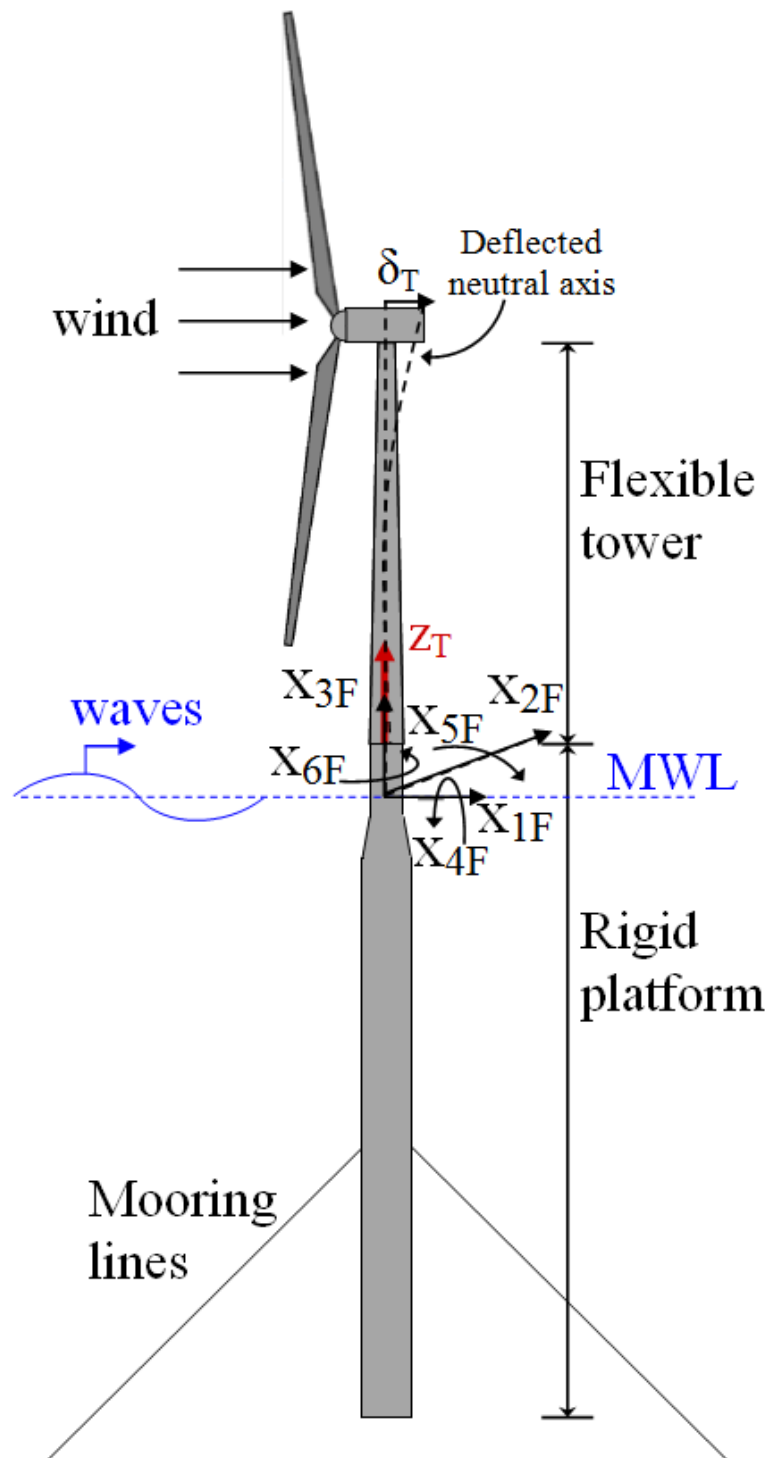


Figure 2-3: Catenary moored spar floating wind turbine with head-on wind and incident waves. The wind turbine platform has 3 translational and 3 rotational degrees of freedom. The model allows the tower to bend in its 2 lowest fore-aft modes and two lowest side-side modes.

Table 2.1: Floating wind turbine properties

Parameter	Value
Tower length, $L_{Tower}$	77.6 m
Distance from the SWL to the tower base, $L_{SWL,Base}$	10 m
Distance from the SWL to the tower top, $L_{SWL,Top}$	87.6 m
Tower base diameter	6.5 m
Tower base thickness	2.7 cm
Tower top diameter	3.87 m
Tower top thickness	1.9 cm
Tower top point mass, $m_{Top}$	$3.50 \times 10^5$ Kg
Tower elastic modulus, $E$	210 GPa
Tower density, $\rho_{Steel}$	8500 Kg/m <sup>3</sup>
Tower ultimate strength, $S_{Ult}$	2260 MPa
Tower Wohler parameter, $m$	5
Rotor moment of inertia about SWL	$4.32 \times 10^8$ Kgm <sup>2</sup>
Rotor diameter	126 m
Rotor swept area, $S$	$1.25 \times 10^4$ m

For the NREL offshore 5-MW baseline wind turbine, the tower is a hollow tapered cylinder with a radius and thickness dependent on the tower coordinate,  $z_T$ , as described in Jonkman et al. [66, 68],

$$r_T = 3.25 - 0.0169z_T \text{ m}, \quad (2.12)$$

$$t_T = 0.0135 - 5.15 \times 10^{-5}z_T \text{ m}. \quad (2.13)$$

The corresponding tower second moment of area,  $I(z_T)$ , and cross sectional area,  $A(z_T)$  are,

$$I_T = \pi \frac{r_T^3 t_T}{4}. \quad (2.14)$$

$$A_T = 2\pi r_T t_T. \quad (2.15)$$

We model the hub, nacelle, and rotor masses as a single point mass on the tower top with a mass of  $3.50 \times 10^5$  Kg, as listed in Table 2.1.

For head-on waves, lateral tower acceleration caused by the platform acceleration,  $\partial^2 y(z_T, t) / \partial t^2$ , depends on the tower coordinate  $z_T$ , because of the contribution of platform pitch,

$$\frac{\partial^2 y(z_T, t)}{\partial t^2} = \frac{d^2 x_1}{dt^2} + (L_{SWL,Base} + z_T) \frac{d^2 x_5}{dt^2}, \quad (2.16)$$

where  $L_{SWL,Base} = 10$  m is the distance from the still water level to the tower base for the OC3-Hywind system.

We use the Galerkin method to convert the continuous differential equation describing the tower fore-aft bending dynamics, Eq. 2.11, to several discrete differential equations based on the tower's natural frequencies and corresponding eigenshapes. That is, we approximate a solution to the tower bending with the form,

$$u(t, z_T) \approx \alpha_1(t)u_1(z_T) + \alpha_2(t)u_2(z_T) + \dots \quad (2.17)$$

Here, we consider the tower bending shapes,  $u_1(z_T)$  and  $u_2(z_T)$ , corresponding to its two lowest natural frequencies. The higher bending modes, with frequencies exceeding 10 Hz, have negligible impact on the structure dynamics when the structure is excited by sea waves, which have frequencies less than 5 Hz.

We use the tower eigenmode deformations and frequencies predicted by the NREL code BModes [10]. BModes discretizes the tower into 50 interconnected uniform beam elements along the tower axis, each with 5 nodes that account for torsional, axial, fore-aft, and side-side deformations. BModes fits the fore-aft mode nodal deformations to the curve,

$$u_i(z_T) = a_2z_T^2 + a_3z_T^3 + a_4z_T^4 + a_5z_T^5 + a_6z_T^6. \quad (2.18)$$

Eq. 2.18 represents the eigenshape's neutral axis deformation. This eigenshape satisfies the tower's kinematic boundary conditions at the base of zero deformation ( $u(0) = 0$ ) and slope ( $\partial u(0)/\partial z_T = 0$ ). Table 2.2 lists the coefficients for the tower's two lowest frequency bending modes. The coefficients in Eq. 2.18 and Table 2.2 are normalized so that  $u_i(z_T = l_{Tower}) = 1$ .

The normal stress along an Euler beam is,

$$s(z_T)_{Euler-Bernoulli} = \frac{Mr_T}{I} = -Er_T \frac{\partial^2 u_i}{\partial z_T^2}. \quad (2.19)$$

Since the tower exhibits both shell-like and beam-like behavior, we add a concentration



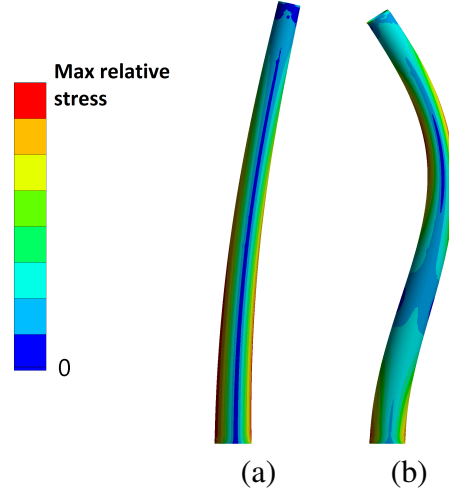


Figure 2-4: Eigenshapes and von-Mises stress trends for the tower's two lowest fore-aft bending modes found by ANSYS<sup>®</sup> finite element modal analysis. (a) Mode 1,  $u_1(z)$ , 0.42 Hz. (b) Mode 2,  $u_2(z)$ , 2.57 Hz.

factor to the stress along the tower,

$$s(z_T)_{Euler-Bernoulli} = K_{ci} \frac{Mr_T}{I}. \quad (2.20)$$

Applying Eq. 2.19 to stress at the tower root,

$$s(z_T = 0)_{Euler-Bernoulli} = -2EK_{ci}r_{T,z=0}a_2. \quad (2.21)$$

We use ANSYS<sup>®</sup> finite element software modal analysis to determine the stress concentration factor,  $K_{ci}$ . Relative von-Mises stress along the tower for the two lowest bending modes is shown in Fig. 2-4. We find that  $K_{c1} = 1.7$  and  $K_{c2} = 1.6$ , resulting in the expression for stress at the tower root due to the two lowest fore-aft bending modes,

$$s_{Root,F-A} = 330\alpha_1 + 15050\alpha_2 \text{ MPa}. \quad (2.22)$$

Having determined the tower bending shapes,  $u_1(z_T)$  and  $u_2(z_T)$ , we substitute the as-

Table 2.2: Coefficients for neutral axis line-of-best-fit for the tower bending modes,  $u_1(z)$  and  $u_2(z)$ .

Coefficient	Mode 1, $u_1(z)$ , 0.42 Hz	Mode 2, $u_2(z)$ , 2.57 Hz
$a_2$	$1.44 \times 10^{-4}$	$7.10 \times 10^{-3}$
$a_3$	$4.72 \times 10^{-7}$	$-3.99 \times 10^{-5}$
$a_4$	$-2.50 \times 10^{-9}$	$-5.61 \times 10^{-7}$
$a_5$	$4.15 \times 10^{-11}$	$-8.27 \times 10^{-9}$
$a_6$	$-5.28 \times 10^{-13}$	$9.47 \times 10^{-11}$
$K_c$	1.7	1.6

summed solution, Eq.s 2.17 and 2.18, into the governing equation, Eq. 2.11,

$$EI(\alpha_1 u_1^{iv} + \alpha_2 u_2^{iv}) + \rho A (\ddot{\alpha}_1 u_1 + \ddot{\alpha}_2 u_2 + \ddot{y}) = 0, \quad (2.23)$$

where the roman numerals indicate derivatives with respect to space and dots with respect to time. To find the governing equation of the first bending mode, we multiply Eq. 2.23 by  $u_1$  and integrate along  $z_T$ ,

$$\int_0^l EI(\alpha_1 u_1^{iv} u_1 + \alpha_2 u_2^{iv} u_1) dz_T + \int_0^l \rho A (\ddot{\alpha}_1 u_1 u_1 + \ddot{\alpha}_2 u_2 u_1 + \ddot{y} u_1) dz_T = 0. \quad (2.24)$$

Using the self-adjoint and orthogonality properties of the eigenshapes, and substituting in Eq. 2.16 for  $\ddot{y}$ , Eq. 2.24 reduces to,

$$\alpha_1 \left( \int_0^l EI (u_1^{ii})^2 dz_T \right) + \ddot{\alpha}_1 \left( \int_0^l \rho A u_1^2 dz_T \right) + \ddot{\alpha}_2 \left( \int_0^l \rho A (l_{S_{WL,Base}} + z_T) u_1 dz_T \right) = 0. \quad (2.25)$$

We define new coefficients to express Eq. 2.25 as,

$$k_1 \alpha_1 + m_1 \ddot{\alpha}_1 + m_{1,p1} \ddot{\alpha}_2 + m_{1,p5} \ddot{\alpha}_5 = 0. \quad (2.26)$$

Repeating the procedure from Eq. 2.23 for  $u_2$  produces the second tower bending mode governing equation,

$$k_2 \alpha_2 + m_2 \ddot{\alpha}_2 + m_{2,p1} \ddot{\alpha}_2 + m_{2,p5} \ddot{\alpha}_5 = 0. \quad (2.27)$$

Table 2.3 lists the calculated coefficients. It is important to note that  $m_i$ ,  $m_{i,p1}$ , and  $m_{i,p5}$  account for the tower end mass.

Table 2.3: Bending mode coefficients and natural frequencies derived by Galerkin projection.

Coefficient	Mode 1, $f_1 = 0.42$ Hz	Mode 2, $f_2 = 2.57$ Hz
$m_i$	$3.479 \times 10^5$	$1.430 \times 10^7$
$k_i$	$2.44 \times 10^6$	$3.731 \times 10^9$
$m_{i,p1}$	$3.625 \times 10^5$	$1.323 \times 10^6$
$m_{i,p5}$	$3.091 \times 10^7$	$8.185 \times 10^7$

Next, we determine the tower's influence on the platform dynamics by using the Euler-Lagrange approach for the tower-platform four coupled degrees of freedom; platform surge  $x_1$ , platform pitch  $x_5$ , and two tower bending modes contained in  $u$  (Eq. 2.17). The system potential energy is due to the tower bending,

$$V = \frac{E}{2} \int_0^l I(u'')^2 dz_T. \quad (2.28)$$

The kinetic energy is

$$T = \frac{1}{2} m_{FWT1} \dot{x}_1^2 + \frac{1}{2} m_{FWT5} \dot{x}_5^2 + m_{FWT15} \dot{x}_1 \dot{x}_5 + \frac{1}{2} \int_0^l \rho A (\dot{x}_1 + (L_{SWL,Base} + z) \dot{x}_5 + \dot{u})^2 dz_T + \frac{1}{2} m_{Top} (\dot{x}_1 + (L_{SWL,Base} + L_{Tower} \dot{x}_5 + \dot{u}_{z_T=L_{Tower}}))^2 + \frac{1}{2} I_{Top} (\dot{u}'_{z_T=L_{Tower}} \dot{x}_5)^2, \quad (2.29)$$

where  $m_{FWT1}$ ,  $m_{FWT5}$ , and  $m_{FWT15}$  are the platform surge mass, pitch inertia, and product of inertia, respectively,  $m_{Top}$  is the combined hub, rotor, nacelle mass at the tower top, and  $I_{Top}$  is the rotor inertia about the SWL. Defining the Lagrangian as

$$\mathcal{L} = T - V, \quad (2.30)$$

and substituting Eq.s 2.28-2.30 into the equation,

$$\frac{d}{dt} \left( \frac{\partial \mathcal{L}}{\partial \dot{q}} \right) - \frac{\partial \mathcal{L}}{\partial q} = 0, \quad (2.31)$$

for  $q = x_1$  and  $q = x_5$  results in the rigid and flexible coupling terms between the platform and tower. The final tower mass and stiffness matrices, coupled to the platform degrees of freedom, are,

$$\mathbf{M}_{Tower} = \begin{bmatrix} 6.02 \times 10^5 & 0 & 0 & 0 & 4.16 \times 10^7 & 0 & 3.62 \times 10^5 & 1.32 \times 10^6 & 0 & 0 \\ 0 & 6.02 \times 10^5 & 0 & -4.16 \times 10^7 & 0 & 0 & 0 & 0 & 3.62 \times 10^5 & 1.32 \times 10^6 \\ 0 & 0 & 6.02 \times 10^5 & 0 & 0 & 0 & 0 & 0 & 0 & 0 \\ 0 & -4.16 \times 10^7 & 0 & 3.30 \times 10^9 & 0 & 0 & 0 & 0 & -3.09 \times 10^7 & -8.18 \times 10^7 \\ 4.16 \times 10^7 & 0 & 0 & 0 & 3.30 \times 10^9 & 0 & 3.09 \times 10^7 & 8.18 \times 10^7 & 0 & 0 \\ 0 & 0 & 0 & 0 & 0 & 0 & 0 & 0 & 0 & 0 \\ \hline 3.62 \times 10^5 & 0 & 0 & 0 & 3.09 \times 10^7 & 0 & 3.48 \times 10^5 & 6.66 \times 10^5 & 0 & 0 \\ 1.32 \times 10^6 & 0 & 0 & 0 & 8.18 \times 10^7 & 0 & 6.66 \times 10^5 & 1.43 \times 10^7 & 0 & 0 \\ 0 & 3.62 \times 10^5 & 0 & -3.09 \times 10^7 & 0 & 0 & 0 & 0 & 3.48 \times 10^5 & 6.66 \times 10^5 \\ 0 & 1.32 \times 10^6 & 0 & -8.18 \times 10^7 & 0 & 0 & 0 & 0 & 6.66 \times 10^5 & 1.43 \times 10^7 \end{bmatrix}, \quad (2.32)$$

where the units are standard SI  $Kg$ ,  $Kgm$ , and  $Kgm^2$ .

$$\mathbf{K}_{Tower} = \begin{bmatrix}
0 & 0 & 0 & 0 & 0 & 0 & 0 & 0 & 0 & 0 \\
0 & 0 & 0 & 0 & 0 & 0 & 0 & 0 & 0 & 0 \\
0 & 0 & 0 & 0 & 0 & 0 & 0 & 0 & 0 & 0 \\
0 & 0 & 0 & 0 & 0 & 0 & 0 & 0 & 0 & 0 \\
0 & 0 & 0 & 0 & 0 & 0 & 0 & 0 & 0 & 0 \\
0 & 0 & 0 & 0 & 0 & 0 & 0 & 0 & 0 & 0 \\
0 & 0 & 0 & 0 & 0 & 0 & 2.44 \times 10^6 & -4.92 \times 10^6 & 0 & 0 \\
0 & 0 & 0 & 0 & 0 & 0 & -4.92 \times 10^6 & 3.73 \times 10^9 & 0 & 0 \\
0 & 0 & 0 & 0 & 0 & 0 & 0 & 0 & 2.44 \times 10^6 & -4.92 \times 10^6 \\
0 & 0 & 0 & 0 & 0 & 0 & 0 & 0 & -4.92 \times 10^6 & 3.73 \times 10^9
\end{bmatrix}, \quad (2.33)$$

where the units are standard SI  $N/m$ ,  $N/rad$ , and  $Nm/rad$ . Coupling between the bending modes shows numeric errors in the eigenmodes.

$\mathbf{K}_{Tower}$  is a sparse matrix because it represents just the dynamics of the tower bending degrees of freedom (rows 7 - 10). This matrix is added to the 10x10 FWT platform stiffness matrix, Eq. A.3, which defines stiffness terms for the platform in rows 1-6, as shown in Eq. 2.9. Coupling between the lightly damped tower bending and platform is expressed by nondiagonal terms in the tower mass matrix in Eq. 2.32.

## 2.4 Linear Wave Energy Converters

Here, we model wave energy converters using long wavelength approximations. Section 2.6 describes how the WEC's and FWT are coupled together. In Chapter 6, we apply parameter constraints on the coupled FWT-WEC 's and compute the system lifetime response statistics.

We consider tuned mass dampers inside the FWT, spherically-shaped WEC's, and spar-like WEC's with a vertical through-hole in which an air or water Wells turbine is placed. These 3 WEC's are illustrated in Figs 2-5 to 2-7. For simplicity in this analysis, we assume that the WEC may translate in surge, sway, and heave directions relative to the FWT,

but it is rigidly coupled with the FWT in the rotational roll, pitch, and yaw. This is the case for a 2-bar linkage between the FWT and WEC. Linkages that pivot about torsional springs and dampers on the FWT connect the WEC and FWT, as described in Section 2.6. These links provide off-diagonal coupling between the FWT and WEC's. Depending on the equilibrium orientation of the links, the WEC and FWT may be rigidly coupled in a translation mode. Nonzero values of these torsional springs and dampers cause moments and forces on the FWT and forces on the WEC that are proportional to the FWT-WEC relative translations. Incident wave pitch forcing on the WEC is rigidly transmitted to the FWT. The WEC's rotational (roll, pitch, and yaw) properties for inertia, hydrodynamic added mass and damping, and hydrostatic stiffness are rigidly transmitted to the FWT. We further assume that the WEC motions are small and can be linearized.

The WEC may harvest wave power using a horizontal axis hydrokinetic Wells turbine, vertical axis hydrokinetic or air Wells turbine, or a resistance torque acting on a link between the WEC and FWT (discussed in more detail in Section 2.6). These are some of the most common types of wave energy converter power takeoff mechanisms [40, 143].

We consider 5 degrees of freedom for the WEC,

$$\vec{x}_{WEC} = \begin{bmatrix} x_{WEC} \\ y_{WEC} \\ z_{WEC} \\ z_{Col} \\ p_C \end{bmatrix} = \begin{bmatrix} \text{WEC surge} \\ \text{WEC sway} \\ \text{WEC heave} \\ \text{Vertical water column heave relative to WEC} \\ \text{Vertical water column chamber pressure} \end{bmatrix}. \quad (2.34)$$

The coupled equations of motion for the general WEC are,

$$\begin{bmatrix} (m_W + A_{11,W}) \ddot{x}_W + B_{11,W} \dot{x}_W + d_{WellsX} (\dot{x}_W - u_{Wave})^2 & = & F_{1,WEC} \\ (m_W + A_{22,W}) \ddot{y}_{WEC} + B_{22,W} \dot{y}_{WEC} & = & 0 \\ (m_W + A_{33,W}) \ddot{x}_{3,W} + B_{33,W} \dot{x}_{3,W} + C_{33n} x_{3,W}^3 & = & F_{3,WEC} + P_C A_{ColZ} \\ P_C + \frac{I_{ZCol}}{A_{ColZ}} (\ddot{z}_{WEC} + \ddot{z}_{Col}) + \frac{B_{33,Col}}{A_{ColZ}} (\dot{z}_{WEC} + \dot{z}_{Col}) + \rho g (z_{WEC} + z_{Col}) & = & \frac{F_{3,Wave,Col}}{A_{ColZ}} \\ P_C + \frac{k_{Wells} V_{Air}}{\gamma P_{Atm}} \dot{p}_C - k_{Wells} A_{Col} \dot{z}_{Col} & = & 0 \end{bmatrix}. \quad (2.35)$$

Parameter definitions are listed in Table 2.4. We calculate the parameter values in Eq. 2.35 from the WEC geometry based on long-wavelength approximations. The mathematical expressions differ significantly depending on if the WEC has the form factor of a sphere or vertical cylinder. Therefore, we derive the expressions separately.

Table 2.4: WEC parameters

$m_W$	WEC mass
$A_{11W}$	WEC surge added mass
$B_{11,W}$	WEC surge hydrodynamic damping
$F_{1,WEC}$	WEC surge linear wave force
$A_{33W}$	WEC heave added mass
$B_{33,W}$	heave hydrodynamic damping
$C_{33}$	WEC linear hydrostatic heave nonlinear stiffness coefficient
$C_{33n}$	WEC hydrostatic heave nonlinear stiffness coefficient
$F_{3,WEC}$	WEC heave linear wave force
$P_C$	air chamber pressure
$I_{Col}$	sum of the water column mass and heave added mass
$B_{33,Col}$	water column heave added mass
$F_{3,Wave,Col}$	linear heave wave forcing on the bottom of the water column
$V_{Air}$	volume of the air chamber
$\gamma = 1.4$	specific heat ratio of air
$P_{Atm}$	atmospheric pressure
$A_{Tube}$	WEC tube cross-sectional area
$A_{Float}$	WEC float cross-sectional area
$L_{Float}$	float length
$A_{ColZ}$	water column and chamber cross-sectional area
$r_{Tube}$	tube radius
$r_{Float}$	float radius
$(L_{XW}, L_{YW})$	spar center $x$ and $y$ axes
$L_{ZW}$	float center depth
$L_{TubeSub}$	tube keel depth
$t_{Steel}$	steel sheet thickness
$\rho_{St}$	steel mass density
$a$	wave amplitude
$V_{Air}$	air chamber volume
$d_{WellsX}$	horizontal hydrokinetic Wells turbine damping coefficient
$u_{Wave}$	horizontal wave velocity at the horizontal Wells turbine depth



## 2.4.1 Internal Tuned Mass Damper

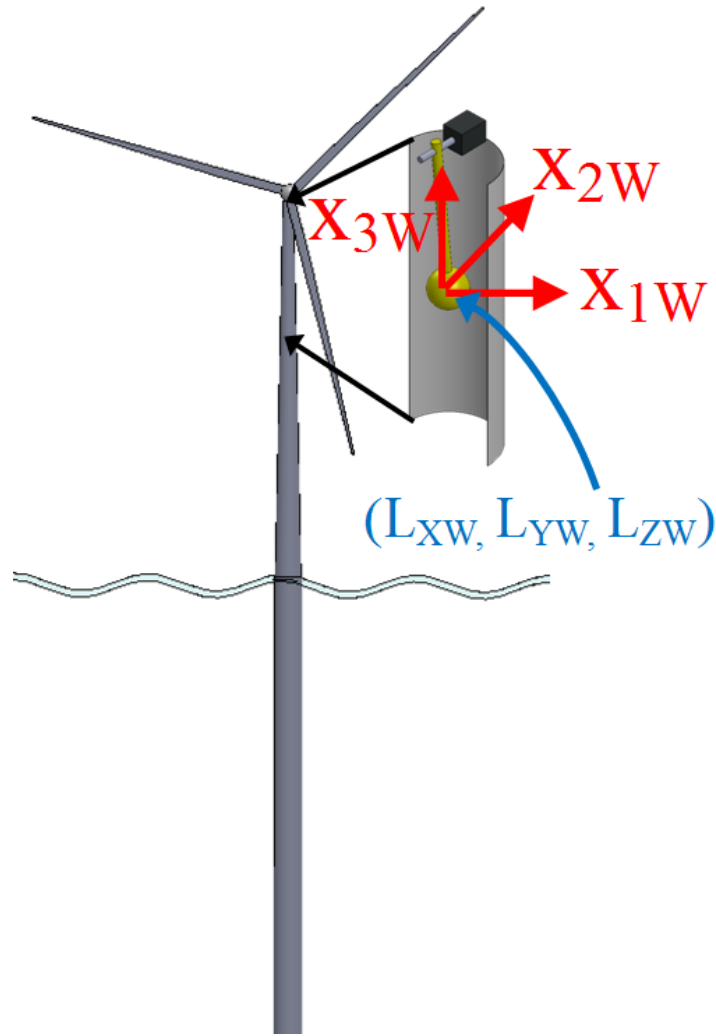


Figure 2-5: Illustration of an internal tuned mass damper in the FWT nacelle.

If the WEC is inside the FWT platform or nacelle, then many of the parameters in Eq. 2.35 are set to 0,

$$\begin{aligned}
 A_{11,W} &= A_{22,W} = A_{33,W} = B_{11,W} = B_{22,W} = B_{33,W} = C_{33,W} = 0, \\
 F_{1,W} &= F_{3,W} = F_{3,Wave,Col} = k_{WellsX} = k_{Wells} = A_{ColX} = A_{ColZ} = I_{ZCol} = B_{33,Col} = P_C = 0.
 \end{aligned}
 \tag{2.36}$$

The only nonzero parameter that remains in Eq. 2.35 is  $m_W$ . The other nonzero pa-

rameters that affect the system dynamics are the linkage, torsional springs, and torsional dampers connecting the mass  $m_W$  to the FWT. Those parameters are described in Section 2.6, and relate to the center of mass (CM) of the WEC,

$$(L_{XW}, L_{YW}, L_{ZW}). \quad (2.37)$$

As described in Section 2.6, the WEC may rotate rigidly with the FWT. In those equations,

$$A_{44,W} = A_{55,W} = A_{66,W} = B_{44,W} = B_{55,W} = B_{66,W} = C_{44,W} = C_{55,W} = F_{5,W} = 0. \quad (2.38)$$

The WEC mass moment of inertia about its CM is

$$I_{44} = I_{55} = I_{66} = \frac{2m_W r_W^2}{3}, \quad (2.39)$$

For a steel sphere,

$$r_W = \left( \frac{3m_W}{4\pi\rho_{St}} \right)^{1/3}, \quad (2.40)$$

where  $\rho_{St}$  is the steel density.

For neutral buoyancy, we subtract  $m_W$  from the concrete ballast in the FWT. The unmodified OC3-Hywind has 5950 Tons concrete ballast centered at a submergence of -98 m [100]. Therefore, to maintain neutral buoyancy, we add a negative mass to the FWT platform,

$$-m_W \text{ centered at } (0, 0, -98) \text{ m.} \quad (2.41)$$

We use the procedure described in Section 2.7 to modify the FWT platform properties with the ballast reduction.

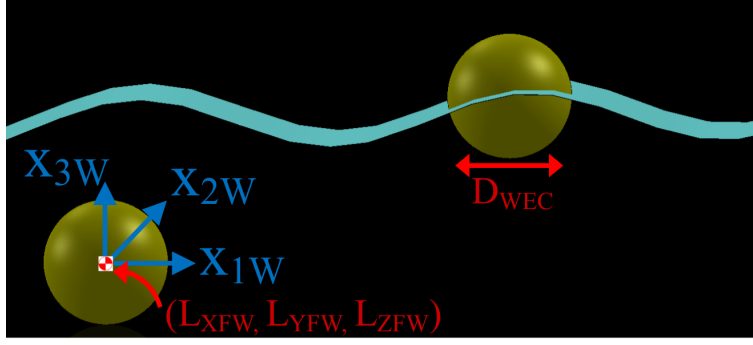


Figure 2-6: Illustration of a (Left) submerged sphere and (Right) floating sphere; used as approximations in the WEC model.

## 2.4.2 Parameters for a Spherical WEC Geometry

For our most basic external WEC model, we assume that the WEC has a spherical form-factor, as shown in Fig. 2-6. The sphere is centered at,

$$(L_{XW}, L_{YW}, L_{ZW}). \quad (2.42)$$

The sphere has a radius,

$$r_{\text{WEC}}. \quad (2.43)$$

The corresponding submerged WEC volume is,

$$V_{\text{WEC, Sub}} = \begin{cases} \frac{4}{3}\pi r_{\text{WEC}}^3, & \text{if external submerged WEC,} \\ \frac{2}{3}\pi r_{\text{WEC}}^3, & \text{if external floating WEC.} \end{cases} \quad (2.44)$$

We assume that the sphere is neutrally-buoyant,

$$m_{\text{WEC}} = \rho V_{\text{WEC, Sub}}. \quad (2.45)$$

We model the WEC hydrostatic stiffness as,

$$C_{3W} = \begin{cases} 0, & \text{if internal or fully submerged WEC,} \\ \omega_{\text{Design}}^2 (m + A_{33W}), & \text{if floating external WEC,} \end{cases} \quad (2.46)$$

where we choose a design frequency based on the environmental site's historically most common ocean spectrum peak frequency,

$$\omega_{\text{Design}} = 2\pi/T_{\text{Design}}. \quad (2.47)$$

Due to its symmetry, the sphere rotational hydrostatic stiffnesses are,

$$C_{44W} = C_{55W} = 0. \quad (2.48)$$

Using long-wave approximations, the spherical WEC added mass is [103],

$$A_{11W} = A_{22W} = A_{33W} = \frac{\rho V_{\text{WEC, Sub}}}{2}, \quad (2.49)$$

where  $\rho = 1025 \text{ Kg/m}^3$  is the water density.

Due to its symmetry, the sphere rotational added masses are,

$$A_{44W} = A_{55W} = A_{66W} = 0. \quad (2.50)$$

The wave forcing from the G.I. Taylor approximation [103] is,

$$\begin{bmatrix} f_{1,W} \\ f_{3,W} \end{bmatrix} = \begin{bmatrix} -(\rho V_{\text{Sub}} + A_{11W}) \frac{igk \cosh(k(L_{ZW}+H))}{\cosh(kH)} e^{ikL_{XW}+i\phi-i\omega t} \\ -(\rho V_{\text{Sub}} + A_{33W}) \frac{-gk \sinh(k(L_{ZW}+H))}{\cosh(kH)} e^{ikL_{XW}+i\phi-i\omega t} \end{bmatrix}. \quad (2.51)$$

Using the Haskind relation, the hydrodynamic damping is,

$$\begin{bmatrix} B_{11,W} = B_{22,W} \\ B_{33,W} \end{bmatrix} = \begin{bmatrix} \frac{k}{8\rho g V_g} |f_{1,W}/a|^2, \\ \frac{k}{4\rho g V_g} |f_{3,W}/a|^2, \end{bmatrix}, \quad (2.52)$$

where  $\omega$  is the wave excitation frequency and  $k$  is the wave number.

For the sphere approximation, we assume,

$$f_{5,W} = B_{44,W} = B_{55,W} = 0. \quad (2.53)$$

For WEC's with a hydrokinetic Wells turbine in the WEC body, the turbine force and power depends on the relative velocity between the WEC and the ocean waves. We approximate the ocean wave velocity from the incident wave potential,

$$\begin{bmatrix} u_{wave} \\ v_{wave} \end{bmatrix} = \begin{bmatrix} \frac{-agk \cosh(k(L_{ZW}+H))}{\omega \cosh(kH)} e^{ikL_{XW}+i\phi-i\omega t} \\ \frac{aigk \sinh(k(L_{ZW}+H))}{\omega \cosh(kH)} e^{ikL_{XW}+i\phi-i\omega t} \end{bmatrix}, \quad (2.54)$$

where  $u_{wave}$  is the horizontal velocity in the  $x$  direction,  $v_{wave}$  is the vertical velocity,  $a$  is wave amplitude,  $H$  is the ocean depth and  $k$  is the wave number.

For a simple spherical WEC without a Wells turbine, then many of the parameters in Eq.s 2.35 are set to 0,

$$F_{3,Wave,Col} = d_{WellsX} = k_{Wells} = A_{ColX} = A_{ColZ} = I_{ZCol} = B_{33,Col} = P_C = 0. \quad (2.55)$$

### 2.4.3 Parameters for a Spar-like WEC Geometry

Next, we consider a spar WEC with the geometry shown in Fig. 2-7. It has a submerged float that 1. satisfies buoyancy, 2. provides a horizontal area subject to vertical wave forcing beyond the tube alone, and 3. allows the WEC surface-piercing cross-sectional area to remain small, which is necessary for a low natural frequency. The float is filled with concrete ballast to satisfy neutral buoyancy. A hollow toroid with radius  $r_{OutSWL}$  encircles the tube from  $z = \pm L_{OutSWL}$ . The purpose of this toroid is to adjust the still waterline area, which in turn adjusts the WEC hydrostatic stiffness and natural frequency.

The spar has a long water column tube exposed to heave wave forcing. The top of the water column pushes air through a Wells turbine that generates electricity. The water in the tube moves relative to the WEC spar, and the air may compress, which creates two degrees of freedom relative to the WEC structure motion.

The spar is centered at,

$$(L_{XW}, L_{YW}). \quad (2.56)$$

The float is centered at a depth,

$$L_{ZW}. \quad (2.57)$$

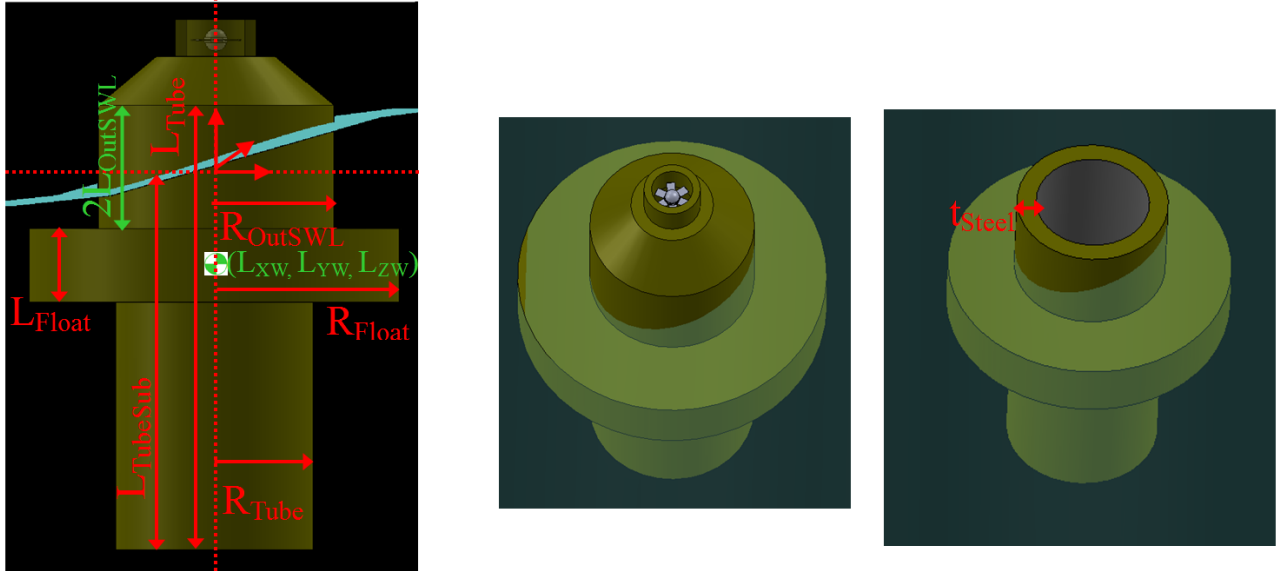


Figure 2-7: Illustration of spar-like WEC with air Wells turbine: (Left) side view; (Center) Top view with the Wells turbine; (Right) Top view with the air turbine and turbine duct hidden.

The tube keel is at a depth,

$$L_{TubeSub} \quad (2.58)$$

The total WEC submerged volume is,

$$V_{SubW} = V_{SubSWL} + V_{TubeSub} + V_{Float}, \quad (2.59)$$

where the submerged volume of the still waterline (SWL) modification is,

$$V_{SubSWL} = L_{OutSWL} A_{OutSWL}, \quad (2.60)$$

the submerged volume of the tube is,

$$V_{TubeSub} = L_{TubeSub} A_{Tube}, \quad (2.61)$$

and the submerged volume of the float is,

$$V_{Float} = L_{Float}A_{Float}. \quad (2.62)$$

The cross-sectional areas of the SWL modification, tube, and float, respectively, are,

$$A_{OutSWL} = \pi \left( r_{OutSWL}^2 - r_{Tube}^2 \right), \quad (2.63)$$

$$A_{Tube} = 2\pi r_{Tube} t_{Steel}, \quad (2.64)$$

$$A_{Float} = \pi \left( r_{Float}^2 - r_{Tube}^2 \right), \quad (2.65)$$

where  $r_{OutSWL}$  is the radius of the SWL toroid,  $r_{Float}$  is the float radius, and  $r_{Tube}$  is the tube radius.

The equilibrium submerged volume of the WEC,  $V_{SubW}$ , must satisfy neutral buoyancy,

$$\rho V_{SubW} = m_W, \quad (2.66)$$

where  $m_W$  is the structural mass,

$$m_W = m_{SWL} + m_{Tube} + m_{Float} + m_{Ballast}. \quad (2.67)$$

The mass of the SWL modification is,

$$m_{SWL} = \rho_{Steel} t_{Steel} S A_{SWL}, \quad (2.68)$$

where surface area of the SWL modification is

$$S A_{SWL} = 4\pi r_{Tube} L_{OutSWL} + 2\pi r_{OutSWL}^2 - \pi r_{Tube}^2, \quad (2.69)$$

which accounts for the SWL modification's outer sides, top, and bottom. The mass of the tube is,

$$m_{Tube} = 2\rho_{Steel} t_{Steel} \pi r_{Tube} L_{Tube}. \quad (2.70)$$

The steel mass of the float is,

$$m_{Float} = \rho_{Steel} t_{Steel} S A_{Float}, \quad (2.71)$$

where the surface area of the float is,

$$S A_{Float} = 2\pi r_{Float} L_{Float} + 2\pi r_{Float}^2 - \pi r_{Tube}^2 - \pi r_{OutSWL}^2, \quad (2.72)$$

which accounts for the outer sides, top, and bottom.

A mass of concrete ballast is added inside the float to satisfy neutral buoyancy, at an approximated height of  $L_{ZW}$ .

The WEC center of mass is located at a height of,

$$\bar{z} = \frac{m_{Tube} (L_{Tube}/2 - L_{TubeSub}) + (m_{Float} + m_{Ballast}) L_{ZW}}{m_W}. \quad (2.73)$$

The center of buoyancy is located at a height of,

$$\bar{z}_{Sub} = \frac{-V_{SubSWL} L_{OutSWL}/2 - V_{TubeSub} L_{TubeSub}/2 + V_{Float} L_{ZW}}{V_{SubW}}. \quad (2.74)$$

The surge added mass is found using strip theory,

$$A_{11W} = \int_{-L_{TubeSub}}^0 \pi r_W^2 dz, \quad (2.75)$$

which accounts for the WEC outer radius due to the SWL modification, tube, and float,

$$r_W = \begin{cases} r_{OutSWL}, & \text{if } L_{ZW} - L_{Float}/2 < z < 0, \\ r_{Float}, & \text{if } L_{ZW} - L_{Float}/2 < z < L_{ZW} + L_{Float}/2, \\ r_{Tube}, & \text{if } -L_{TubeSub} < z < L_{ZW} - L_{Float}/2, \end{cases} \quad (2.76)$$

By symmetry, the sway added mass equals the surge added mass,

$$A_{22W} = A_{11W}. \quad (2.77)$$



The yaw added mass is,

$$A_{66W} = 0. \quad (2.78)$$

From strip theory, the roll and pitch added masses are,

$$A_{44W} = A_{55W} = \int_{-L_{TubeSub}}^0 z^2 \pi r_W^2 dz. \quad (2.79)$$

We approximate the heave added mass as,

$$A_{33W} = 0.5 \frac{4}{3} \rho \pi (r_{Float}^3 - r_{Tube}^3). \quad (2.80)$$

which is the added mass of a half-submerged sphere with the same frontal area as the float, (Newman) [103]. Using the G.I. Taylor long wavelength approximation, the heave excitation force is [103],

$$f_3 = -(\rho V_{SubW} + A_{33W}) \left. \frac{\partial P}{\partial z} \right|_{L_{ZKW}}. \quad (2.81)$$

According to linear plan progressive wave theory, the pressure gradient is [103],

$$P = \rho \frac{\partial \phi_i}{\partial t} = a \Re e \left\{ \rho g \frac{\cosh k(z+H)}{\cosh kh} e^{ikx-i\omega t} \right\}, \quad (2.82)$$

where the incident wave velocity potential is

$$\phi_i = a \Re e \left\{ \frac{ig \cosh k(z+H)}{\omega \cosh kh} e^{-ikx+i\omega t} \right\}. \quad (2.83)$$

The incremental surge force acting along the WEC is,

$$df_1 = \left( 2\rho \pi r_W^2 \frac{\partial P}{\partial x} \right) dz. \quad (2.84)$$

The total surge force acting on the spar is,

$$f_1 = \int_{L_{TubeSub}}^0 df_1. \quad (2.85)$$

Similarly, the pitch moment acting along the spar is,

$$f_5 = \int_{L_{TubeSub}}^0 z df_1. \quad (2.86)$$

Using the Haskind relation, the WEC heave hydrodynamic damping is,

$$B_{33} = \frac{k}{4\rho g V_g} \left| \frac{f_3}{a} \right|^2. \quad (2.87)$$

The WEC surge hydrodynamic damping is calculated by the 2D Haskind relation,

$$B_{11} = \int_{L_{TubeSub}}^0 \frac{|df_1|^2}{2a^2 \rho V_g} dz, \quad (2.88)$$

where the incremental surge force along the spar is given in Eq. 2.84.

The WEC pitch and roll hydrodynamic damping is,

$$B_{44} = B_{55} = \int_{L_{zKW}}^0 \frac{z^2 |df_1|^2}{2a^2 \rho V_g} dz. \quad (2.89)$$

The WEC hydrostatic stiffness is,

$$C_{33,W} = \rho g A_{SWL}, \quad (2.90)$$

where the area at the still water line is

$$A_{SWL} = A_{Tube} = 2\pi r_{Tube} t_{Steel}. \quad (2.91)$$

The WEC hydrostatic stiffness in roll and pitch about the WEC centroid  $z$  axis is,

$$C_{44,W} = C_{55,W} = \rho g V_{SubW} \bar{z}_{Sub} - mg \bar{z}. \quad (2.92)$$

For the water column and air pressure degrees of freedom,  $V_{Air}$  is the volume of the air chamber,

$$V_{Air} = A_{ColZ} L_{Above}, \quad (2.93)$$

where  $L_{Above}$  is the length of column above the still waterline.

From G.I. Taylor,

$$F_{3,Wave,Col} = -(\rho V_{Col} + A_{33,Col}) \left. \frac{\partial P}{\partial z} \right|_{L_{ZK,Col}}. \quad (2.94)$$

The water column volume is,

$$V_{Col} = A_{Col} L_{TubeSub}. \quad (2.95)$$

Using the Haskind relation and a correction factor based on our experiments, the water column heave hydrodynamic damping is,

$$B_{33,Col} = 25 \frac{k}{4\rho g V_g} \left| \frac{f_{3,Wave,Col}}{a} \right|^2. \quad (2.96)$$

#### 2.4.4 Power Harvested

The instantaneous power harvested by the air Wells turbine is,

$$P = \eta \frac{P_C^2}{k_{Wells}}, \quad (2.97)$$

where  $\eta = 0.6$  is the Wells turbine efficiency. The instantaneous power harvested by a surge-mode hydrokinetic turbine is,

$$P = \eta k_{Wells} A_{Col}^2 (\dot{x}_{WEC} - u_{Wells})^2. \quad (2.98)$$

## 2.4.5 Matrix Components

Now, we put the components of Eq. 2.35 into matrix form. In Section 2.6, we couple the WEC and FWT matrices. We consider a WEC with the following degrees of freedom,

$$\vec{x}_{WEC} = \begin{bmatrix} x_{WEC} \\ y_{WEC} \\ z_{WEC} \\ z_{Col} \\ p_C \end{bmatrix}. \quad (2.99)$$

The WEC inertia, damping, and stiffness matrices, and forcing vector are,

$$\mathbf{I}_{WEC} = \begin{bmatrix} m_W + A_{W11} & 0 & 0 & 0 & 0 \\ 0 & m_W + A_{W11} & 0 & 0 & 0 \\ 0 & 0 & m_W + A_{W33} & 0 & 0 \\ 0 & 0 & \frac{I_{ColZ}}{A_{ColZ}} & \frac{I_{ColZ}}{A_{ColZ}} & 0 \\ 0 & 0 & 0 & 0 & 0 \end{bmatrix}, \quad (2.100)$$

$$\mathbf{B}_{WEC} = \begin{bmatrix} B_{W11} + k_{WellsX}A_{ColX}^2 & 0 & 0 & 0 & 0 \\ 0 & B_{W11} & 0 & 0 & 0 \\ 0 & 0 & B_{W33} & 0 & 0 \\ 0 & 0 & B_{33,Col}/A_{ColZ} & B_{33,Col}/A_{ColZ} & 0 \\ 0 & 0 & 0 & -k_{Wells}A_{ColZ} & \frac{k_{Wells}V_{Air}}{\gamma P_{Am}} \end{bmatrix}, \quad (2.101)$$

$$\mathbf{K}_{WEC} = \begin{bmatrix} 0 & 0 & 0 & 0 & 0 \\ 0 & 0 & 0 & 0 & 0 \\ 0 & 0 & C_{33,WEC} & 0 & -A_{ColZ} \\ 0 & 0 & \rho g & \rho g & 1 \\ 0 & 0 & 0 & 0 & 1 \end{bmatrix}, \quad (2.102)$$

$$\mathbf{F}_{WEC} = \begin{bmatrix} F_{1,WEC} + k_{Wells} X A_{Col}^2 u_{Wells} \\ 0 \\ F_{3,WEC} \\ F_{3,Col} / A_{Col} \\ 0 \end{bmatrix}. \quad (2.103)$$

## 2.5 Wells Turbine Effective Damping Coefficient Modeling

As part of our first-order FWT-WEC performance model, we compare WEC's with Wells turbine power takeoff (PTO) mechanisms and electromagnetic junction PTO's. We model both PTO's by linear damping coefficients.

Mechanical drivetrains can use gear boxes and hydraulic drivetrains can use varied cross-sectional areas to increase the reaction force (effective damping coefficient) acting on the WEC [129]. The Wells turbine is different in that its maximum reaction force is related to the air or water that directly flows through it. Here, we relate the effective damping coefficient to the Wells turbine parameters and describe limitations to the model.

A Wells turbine in a WEC harvests power proportional to the relative velocity between the WEC and fluid flow. Here, we relate the Wells turbine parameters to the effective linear damping coefficient and fluid flow rate at which stall begins, so that we may approximate limitations in the WEC designs.

In an air Wells turbine, air is pushed or pulled through the turbine by the water column, which is excited by heave wave forcing. For a horizontal-axis water Wells turbine, relative motion between the turbine and incident wave velocity push water through the turbine. Our model bases the effective damping coefficient and damping limitations on Wells turbine experimental data. We dimensionalize experimental nondimensional parameters that describe the Wells turbine performance.

Typical experimental performance curves for the Wells turbine are shown in Fig. 2-8. This data was collected by Brito-Melo et. al [13]. The nondimensional parameters are,

- efficiency

$$\eta = \frac{L\Omega}{qp} = \frac{L\Omega}{V(1-S)\pi R^2 p}, \quad (2.104)$$

where  $L$  is the turbine torque,  $\Omega$  is the turbine angular velocity,  $q$  is the incident fluid volume flow rate,  $V$  is the fluid velocity at the turbine,  $S$  is the turbine solidity (ratio of total rotor planform area to total swept area),  $R$  is the turbine radius, and  $p$  is the pressure drop over the turbine. The experimental data has  $S = 0.64$ .

- pressure drop

$$p^* = \frac{p}{\rho\Omega^2 R^2}, \quad (2.105)$$

where  $\rho$  is the fluid density.

- flow coefficient

$$U^* = \frac{v_{Turbine}}{\Omega R}, \quad (2.106)$$

where  $v_{Turbine}$  is the fluid velocity seen by the turbine.

- torque

$$L^* = \frac{L}{\rho\Omega^2 R^5}. \quad (2.107)$$

Fig. 2-8b shows that the Wells turbine may have a linear nondimensional pressure/velocity slope of,

$$\bar{k} = \frac{P^*}{U^*} = 3.33. \quad (2.108)$$

We define the Wells turbine coefficient for the air turbine as,

$$k_{Wells} = \frac{p}{q} = \frac{\rho\Omega^2 R^2 p^*}{A v_{Turbine}} = \frac{\rho\Omega^2 R^2}{A_{Turbine} \Omega R U^*} \frac{p^*}{U^*} = \frac{3.33 \rho \Omega}{\pi R}. \quad (2.109)$$

We define a Wells turbine effective damping coefficient for the water turbine as,

$$F = pA = b_{Wells} v_{WEC} \longrightarrow b_{Wells} = \frac{pA}{v_{WEC}}. \quad (2.110)$$

We account for how duct taper may increase relative velocity at the turbine compared

to relative velocity at the duct inlet. By flow continuity, we relate the two velocities by,

$$A_{Inlet}v_{Inlet} = A_{Turbine}v_{Turbine} \longrightarrow v_{Turbine} = \frac{A_{Inlet}}{A_{Turbine}}v_{Inlet}. \quad (2.111)$$

We relate the the effective damping coefficient to the experimental data and parameters,

$$b_{Wells} = \frac{pA}{v_{WEC}} = \frac{\rho\Omega^2 R^2 p^* \pi R^2}{\frac{A_{Turbine}}{A_{Inlet}} v_{Turbine}} = \rho\pi\Omega R^3 \frac{A_{Inlet}}{A_{Turbine}} \frac{p^*}{U^*} = 3.33\rho\pi\Omega R^3 \frac{A_{Inlet}}{A_{Turbine}}. \quad (2.112)$$

The experimental data in Fig. 2-8 shows that avoiding turbine start-up and stall requires flow coefficients,

$$U^* > U_{Start\ Up}^* = 0.06 \longrightarrow v_{Turbine} > 0.06\Omega R. \quad (2.113)$$

$$U^* < U_{Stall}^* = 0.4 \longrightarrow v_{Turbine} < 0.4\Omega R. \quad (2.114)$$

The main constraint to maximizing the Wells turbine coefficient is  $U_{Stall}^*$ . If the Wells turbine spins to quickly, then the fluid flow will not generate a torque on it, and the Wells turbine will slow down, which decreases the effective damping coefficient.

From Eq. 2.113, the upper limit on the turbine angular velocity is,

$$U^* > 0.06 \longrightarrow \Omega < \frac{v_{Turbine}}{0.06R} = \frac{A_{Inlet}v_{Inlet}}{0.06RA_{Turbine}}. \quad (2.115)$$

To avoid choking the flow of a hydrokinetic Wells turbine, we limit the ratio of  $A_{Inlet}$  :  $A_{Turbine}$  to 9. We limit the flow of the air Wells turbine to 30.

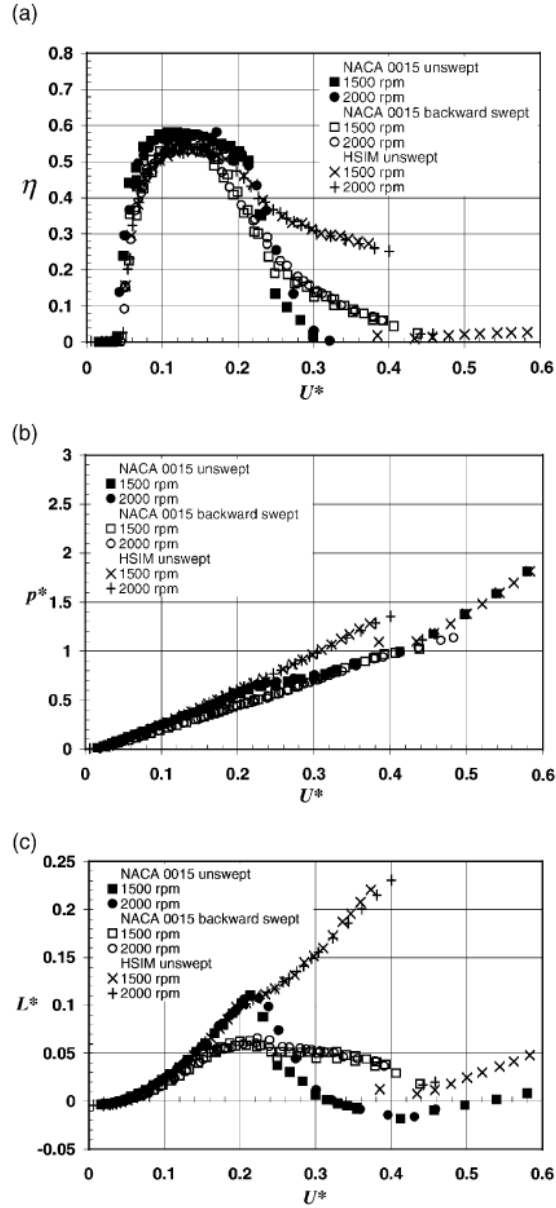


Figure 2-8: Experimental data for a Wells turbine with unswept and 30-degree backward swept NACA 0015 and unswept HSIM bladed rotor turbines, without guide vanes. (a) efficiency, (b) pressure drop, (c) torque versus flow rate coefficient. From Brito-Melo, Ocean Engineering 2002 [13].

Fig.s 2-9 and 2-10 show the dimensionalized Air turbine pressure and water turbine damping coefficients as functions of radius and RPM, accounting for the  $\Omega$  limit to avoid choking the flow. We note that based on feasible size and blade stress constraints, the largest achievable damping coefficient is on the order of  $1.5 \times 10^7$  Ns/m for the water turbine and



800 Pa/(m<sup>3</sup>/s) for the air turbine. Real Wells turbine effective damping coefficients will be further limited by wave diffraction (hydrokinetic turbine), stress, machine capital cost, and electromagnetic generator torque:size limitations. There is an optimal Wells turbine coefficient that maximizes power transfer from the WEC to electricity. Future work on this study includes further refinements of the power takeoff model and design.

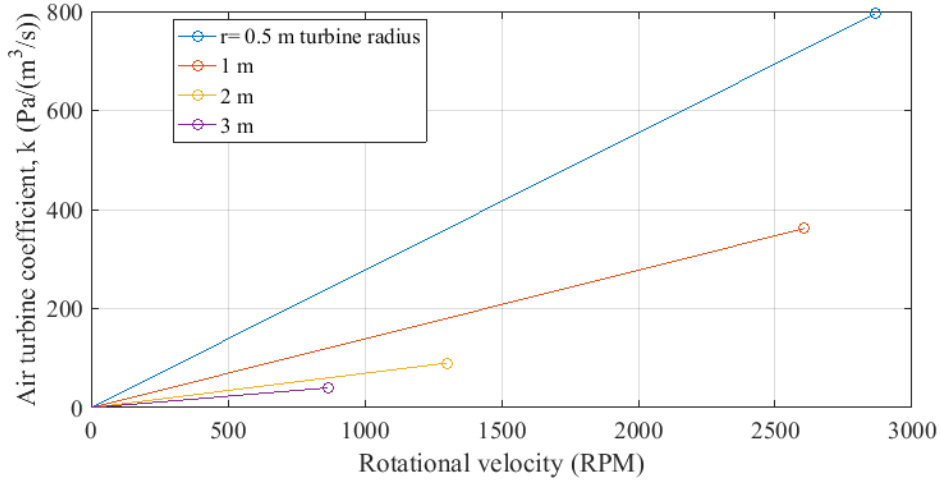


Figure 2-9: Air Wells turbine coefficients for varied radius and angular velocity.

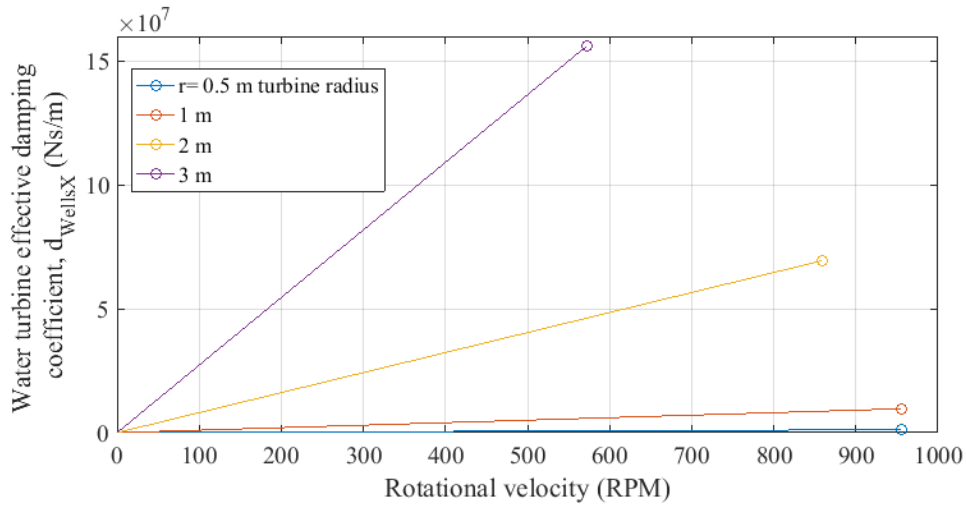


Figure 2-10: Water Wells turbine effective damping coefficients for varied radius and angular velocity. We assume a ratio of  $A_{Inlet}/A_{Turbine} = 9$ .

The experimental data in Fig. 2-8 shows that the Wells turbine has a peak efficiency of

$\eta = 0.6$ . In a real system, careful control is required to keep the turbine operating in the optimal flow regime. Such control strategies include a bypass valve [41].

## 2.6 Structural Coupling Between Floating Wind Turbines And Wave Energy Converters

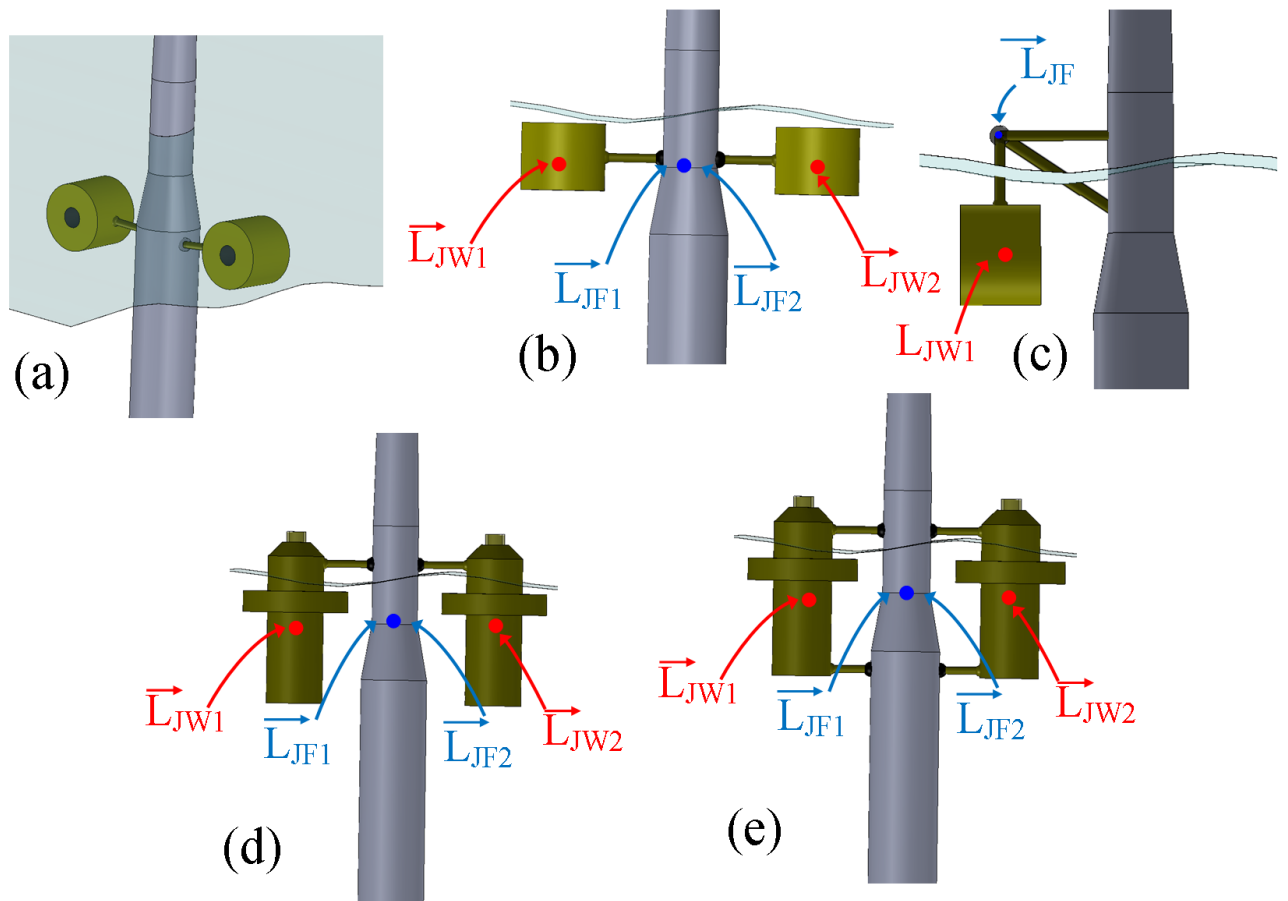


Figure 2-11: Illustrations of FWT-WEC links: (a) surge-mode spherical form-factor WEC placed next to FWT with horizontal links, (b) heave-mode spherical form-factor WEC, (c) surge-mode spherical form-factor WEC placed in front of FWT with a vertical link (d) spar with 1 hinge, (e) spar with 2 hinges.

One of the main goals of this thesis is to determine what kind of FWT-WEC coupling may reduce the FWT motion while still allowing the WEC to harvest wave power. To

investigate this goal, we model hinged links connecting the FWT and WEC [126]. These links allow relative motion between the two structures in some directions, since normally one wants to maximize WEC motion and minimize FWT motion. We consider hinges rather than translation interfaces because the larger surfaces of a translation mechanism are much more vulnerable to biofouling than the more compact and easily sealed surfaces of a rotational mechanism [137].

In this section, we describe the reaction forces on the FWT and WEC caused by the link connections, and put these effects and the WEC properties into matrix form. Fig. 2-11 sketches several of the FWT-WEC link configurations considered:

1. idealized horizontal link for a surge-mode WEC,
2. idealized vertical link for a heave-mode WEC,
3. single horizontal link for a heave-mode spar,
4. two-bar horizontal linkage for a heave mode spar.

If the spar is stable in pitch and roll, then only a single link may be required to prevent collision between the FWT and WEC. Two links rigidly couple the FWT and WEC rotation, which may stabilize the FWT pitch. The two links may also be required to prevent a FWT-WEC collision in storms.

We allow the junction point on the FWT to apply spring and damper torsional resistance between the FWT and link. The spring loads may be tuned for resonances while the damper loads may be used to harvest wave power. The load may be generated by a controlled mechanical structure, hydraulic system, or electric generator [129]. We assume that the junction point on the WEC does not have any torsional resistance between the link and WEC. A machine design with electronic or hydraulic components located on the FWT rather than on the WEC may simplify electric/hydraulic connections, and minimize wear on components, since the WEC is designed for maximized motion while the FWT is designed for minimized motion.

As this section shows, torsional springs located on the FWT with a moment arm effectively act like translation springs on the WEC. We keep the locations and torques gener-

alized for unconstrained spring and damping torques and WEC locations. We model just a single effective link connection to simplify the analysis. We assume small, linearizeable motions. We further assume that the linkage has negligible inertia compared to the WEC and FWT. We express degrees of freedom as column vectors and location coordinates as row vectors.

The derivation here applies to links that have equilibrium horizontal or equilibrium vertical orientations, but neglects some dynamics effects of angled links.

Section 2.6.1 derives FWT-WEC coupling from the link's rotation. Section 2.6.2 derives FWT-WEC coupling along the link's rigid length. Section 2.6.5 expands the linkage model to a tuned mass damper in the nacelle. Section 2.6.6 mathematically expresses the power harvested by the junction damping element. Section 2.6.7 simplifies the model for a FWT-WEC aligned with incident waves.

The effective junction point where the link contacts the FWT has equilibrium coordinates with respect to the still water line,

$$\vec{L}_{JF} = [L_{XJF}, L_{YJF}, L_{ZJF}]. \quad (2.116)$$

The effective junction point where the link contacts the WEC has equilibrium coordinates with respect to the still waterline,

$$\vec{L}_{JW} = [L_{XJW}, L_{YJW}, L_{ZJW}]. \quad (2.117)$$

$\vec{L}_{Link}$  is the link equilibrium vector pointing from the FWT junction point to the WEC junction point,

$$\vec{L}_{Link} = \vec{L}_{JW} - \vec{L}_{JF} = \begin{bmatrix} L_{xLink} & L_{yLink} & L_{zLink} \end{bmatrix} \quad (2.118)$$



Link rotation counterclockwise about each axis due to  $\vec{x}_{Rel}$  is,

$$\vec{\theta}_{Link} = \mathbf{J}_{xRelT\theta} \vec{x}_{Rel} = \begin{bmatrix} 0 & \frac{-1}{L_{Z,Link}} & \frac{1}{L_{Y,Link}} \\ \frac{1}{L_{Z,Link}} & 0 & \frac{-1}{L_{X,Link}} \\ \frac{-1}{L_{Y,Link}} & \frac{1}{L_{X,Link}} & 0 \end{bmatrix} \vec{x}_{Rel}. \quad (2.123)$$

To avoid a mathematical singularity, infinite values in the  $\mathbf{J}_{xRelT\theta}$  matrix are set to 0. Relative rotation between the link and FWT is,

$$\vec{\theta}_{Link,Rel} = \vec{\theta}_{Link} - \vec{\theta}_{FWT}, \quad (2.124)$$

where

$$\vec{\theta}_{FWT} = \begin{bmatrix} x_4 \\ x_5 \\ x_6 \end{bmatrix} = \mathbf{A}_{Rot} \vec{x} = \begin{bmatrix} 0 & 0 & 0 & 1 & 0 & 0 & | & 0 & 0 & 0 \\ 0 & 0 & 0 & 0 & 1 & 0 & | & 0 & 0 & 0 \\ 0 & 0 & 0 & 0 & 0 & 1 & | & 0 & 0 & 0 \end{bmatrix} \vec{x}. \quad (2.125)$$

The torque acting on the FWT due to the torsional springs and dampers is,

$$\vec{\tau} = -\vec{K}_\theta \vec{\theta}_{Link,Rel}^T - \vec{d}_\theta \dot{\vec{\theta}}_{Link,Rel}^T. \quad (2.126)$$

The force acting on the WEC due to the torsional springs is [6],

$$\vec{F}_{WEC,Rot} = -\mathbf{J}_{xRelT\theta} \vec{\tau}. \quad (2.127)$$

In summary, the rotational springs affect the equation of motion matrices by adding a spring matrix with a form,

$$\mathbf{K}_{Rot} = \begin{bmatrix} -\mathbf{F}_{FWT,Rot,K} \ddot{\mathbf{x}}^{-1} \\ \text{---} \\ -\tau_{FWT,Rot,K} \dot{\mathbf{x}}^{-1} \\ \text{---} \\ -\mathbf{F}_{WEC,Rot,K} \ddot{\mathbf{x}}^{-1} \end{bmatrix} = \begin{bmatrix} \mathbf{J}_{xRelTo\theta} \mathbf{K}_\theta (\mathbf{J}_{xRelTo\theta} \mathbf{A}_{Rel} - \mathbf{A}_{Rot}) \\ \text{---} \\ -\mathbf{K}_\theta (\mathbf{J}_{xRelTo\theta} \mathbf{A}_{Rel} - \mathbf{A}_{Rot}) \\ \text{---} \\ -\mathbf{J}_{xRelTo\theta} \mathbf{K}_\theta (\mathbf{J}_{xRelTo\theta} \mathbf{A}_{Rel} - \mathbf{A}_{Rot}) \end{bmatrix}. \quad (2.128)$$

By an analogous derivation, the rotational dampers lead to the damping matrix,

$$\mathbf{D}_{Rot} = \begin{bmatrix} -\mathbf{F}_{FWT,Rot,D} \dot{\mathbf{x}}^{-1} \\ \text{---} \\ -\tau_{FWT,Rot,D} \dot{\mathbf{x}}^{-1} \\ \text{---} \\ -\mathbf{F}_{WEC,Rot,D} \dot{\mathbf{x}}^{-1} \end{bmatrix} = \begin{bmatrix} -\mathbf{J}_{xRelTo\theta} \mathbf{D}_\theta (\mathbf{J}_{xRelTo\theta} \mathbf{A}_{Rel} - \mathbf{A}_{Rot}) \\ \text{---} \\ -\mathbf{D}_\theta (\mathbf{J}_{xRelTo\theta} \mathbf{A}_{Rel} - \mathbf{A}_{Rot}) \\ \text{---} \\ \mathbf{J}_{xRelTo\theta} \mathbf{D}_\theta (\mathbf{J}_{xRelTo\theta} \mathbf{A}_{Rel} - \mathbf{A}_{Rot}) \end{bmatrix}. \quad (2.129)$$

## 2.6.2 Linkage Translation Modes

We consider the forces transmitted along the direction of the link. If the link is a bar, then it has a rigidity,

$$K_{Link} = EA \approx \infty, \quad (2.130)$$

where  $E$  is the bar's elastic modulus and  $A$  is its cross-sectional area. Some of our simulations use a tuned  $K_{Link}$  and analogous power takeoff damping  $d_{Link}$  for relative motion between the FWT-WEC as a simplified model.

The spring stiffness,  $K_{Link}$  acts in the direction of the link axis. The components of the

spring stiffness in each of the translation directions are,

$$\vec{K}_{Link} = K_{Link} \frac{\vec{L}_{Link}}{\|\vec{L}_{Link}\|} = \begin{bmatrix} K_1 & K_2 & K_3 \end{bmatrix}, \quad (2.131)$$

where  $\vec{L}_{Link}$  is the link distance vector from the FWT to the WEC and is defined in Eq. 2.118. In matrix form, the link spring stiffness is,

$$\mathbf{K}_{Link} = \begin{bmatrix} 1 & 0 & 0 \\ 0 & 1 & 0 \\ 0 & 0 & 1 \end{bmatrix} \vec{K}_{Link}^T = \begin{bmatrix} K_1 & 0 & 0 \\ 0 & K_2 & 0 \\ 0 & 0 & K_3 \end{bmatrix}. \quad (2.132)$$

FWT displacement at the FWT-link junction point is,

$$\vec{x}_{FWT,J} = \vec{x}_{Translate} + \mathbf{J}_{SWL,J} \vec{\theta}_{FWT} = \vec{x}_{Translate} + \begin{bmatrix} 0 & L_{ZJF} & -L_{YJF} \\ -L_{ZJF} & 0 & L_{XJF} \\ L_{YJF} & -L_{XJF} & 0 \end{bmatrix} \vec{\theta}_{FWT}, \quad (2.133)$$

where the FWT rotational motion is defined in Eq. 2.125 and the FWT translation motion at the still waterline is,

$$\vec{x}_{Translate} = \mathbf{A}_{Translate} \vec{x} = \begin{bmatrix} x_1 \\ x_2 \\ x_3 \end{bmatrix} = \begin{bmatrix} 1 & 0 & 0 & 0 & 0 & 0 & 0 & 0 & 0 \\ 0 & 1 & 0 & 0 & 0 & 0 & 0 & 0 & 0 \\ 0 & 0 & 1 & 0 & 0 & 0 & 0 & 0 & 0 \end{bmatrix} \vec{x}. \quad (2.134)$$

WEC displacement at the FWT-link junction point is,

$$\vec{x}_{WEC} = \mathbf{A}_{WEC} \vec{x} = \begin{bmatrix} x_W \\ y_W \\ z_W \end{bmatrix} = \begin{bmatrix} 0 & 0 & 0 & 0 & 0 & 0 & 1 & 0 & 0 \\ 0 & 0 & 0 & 0 & 0 & 0 & 0 & 1 & 0 \\ 0 & 0 & 0 & 0 & 0 & 0 & 0 & 0 & 1 \end{bmatrix} \vec{x}. \quad (2.135)$$

The spring force acting on the FWT is

$$\vec{F}_{Link} = \mathbf{K}_{Link} (\vec{x}_{WEC} - \vec{x}_{FWT,J}), \quad (2.136)$$



The spring force acting on the FWT at the junction also causes a moment about the still water line [6],

$$\vec{\tau}_{FWT} = -\mathbf{J}_{SWL,J}\vec{F}_{Link}. \quad (2.137)$$

The spring force acting on the WEC is equal and opposite the force acting on the FWT.

In summary, the rigid link contribution to the equation of motion spring stiffness matrix has the form

$$\mathbf{K}_{Rigid} = \begin{bmatrix} -\mathbf{F}_{Link}\vec{x}^{-1} \\ \text{---} \\ -\tau_{Link}\vec{x}^{-1} \\ \text{---} \\ \mathbf{F}_{Link}\vec{x}^{-1} \end{bmatrix} = \begin{bmatrix} -\mathbf{K}_{Link}(\mathbf{A}_{WEC} - \mathbf{A}_{Translate} - \mathbf{J}_{SWL,J}\mathbf{A}_{Rotate}) \\ \text{---} \\ \mathbf{J}_{SWL,J}\mathbf{K}_{Link}(\mathbf{A}_{WEC} - \mathbf{A}_{Translate} - \mathbf{J}_{SWL,J}\mathbf{A}_{Rotate}) \\ \text{---} \\ \mathbf{K}_{Link}(\mathbf{A}_{WEC} - \mathbf{A}_{Translate} - \mathbf{J}_{SWL,J}\mathbf{A}_{Rotate}) \end{bmatrix}. \quad (2.138)$$

### 2.6.3 Rotational Coupling of 2 Linkage System

For the FWT-WEC system shown in Fig. 2-11e, the 2-bar linkage prevents the WEC from rotating relative to the FWT. In this case, the WEC pitch forcing and rotational parameters are transmitted to the FWT. This is in contrast to the system in 2-11d with 1 hinge, where the WEC may move in pitch without affecting the FWT. For rotationally coupled systems, we add the pitch force  $F_{5W}$ , rotational inertia  $[I_{44}, I_{55}, I_{66}]$  rotational added mas,  $[A_{44}, A_{55}, A_{66}]$ , rotational hydrodynamic damping  $[B_{44}, B_{55}, B_{66}]$ , and rotational hydrostatic stiffness  $[C_{44}, C_{55}]$ , to the FWT matrix. Nondiagonal cross-coupling terms (e.g.  $A_{15}$ ) are already accounted for in the link translation-mode matrix.

## 2.6.4 Loading on the Links and Junctions

The force and moment loadings on the links and junctions are important for sizing and stress design. Both the junction point on the FWT and the linkage bar have the following 3 sources of loading acting on them:

1. The rotational dampers and rotational springs cause a moment loading on both the junction point and link,  $\vec{\tau}$  from Eq. 2.126,
2. The rotational springs cause a force loading on the junction point,  $-\vec{F}_{WEC,Rot}$  from Eq. 2.127. This force vector creates bending moments on the the link. To derive this bending moment, we first define the component of the force that acts along the link,

$$\vec{F}_{WEC,Rot||} = \vec{F}_{WEC,Rot} \cdot \frac{\vec{l}_{Link}}{|\vec{l}_{Link}|}. \quad (2.139)$$

Then, the components of the force that act perpendicular to the link are,

$$\vec{F}_{WEC,Rot\perp} = \vec{F}_{WEC,Rot} - \vec{F}_{WEC,Rot||}. \quad (2.140)$$

The bending moment acting on the link is,

$$\vec{M}_{Link} = \vec{F}_{WEC,Rot\perp} |\vec{l}_{Link}|, \quad (2.141)$$

where  $|\vec{l}_{Link}|$  is the magnitude distance along the link away from the FWT junction point.

3. A force loading acts along the link axis,  $\vec{F}_{Link}$  from Eq. 2.136.

The normal stress loading along the link is,

$$\sigma_{Link} = \frac{|\vec{F}_{Link}|}{A_{Link}} + \frac{|\vec{M}_{Link} + \vec{\tau}|r}{I}, \quad (2.142)$$

where  $A_{Link}$  is the cross-sectional area of the link. Assuming an axisymmetric link,  $r$  is the maximum cross-section radial distance.  $I$  is the link area moment of inertia.

## 2.6.5 Connections to the Nacelle

In Chapter 6, we consider an internal tuned mass damper attached to the nacelle on top of the flexible tower. A WEC connection to the flexible tower adds a small complexity beyond a WEC connection to the rigid platform because of tower bending. We use a simplified link model that considers just translational tower-WEC coupling.

We consider the degrees of freedom,

$$\vec{x} = \begin{bmatrix} \vec{x}_{FWT} \\ \vec{u} \\ \vec{x}_{WEC} \end{bmatrix} = \begin{bmatrix} x_1 \\ x_2 \\ x_3 \\ x_4 \\ x_5 \\ x_6 \\ u_{1x} \\ u_{2x} \\ u_{1y} \\ u_{2y} \\ x_{1W} \\ y_{1W} \\ z_{1W} \end{bmatrix}. \quad (2.143)$$

For springs  $[K_{1J}, K_{2J}, K_{3J}]$  connecting the WEC and nacelle in the surge, sway, and heave directions respectively, the spring junction matrix is,

$$\mathbf{K}_{Link,Nac} = \begin{bmatrix}
K_{1J} & 0 & 0 & 0 & L_{Nac}K_{1J} & 0 & K_{1J} & 0 & K_{1J} & 0 & -K_{1J} & 0 & 0 \\
0 & K_{2J} & 0 & -L_{Nac}K_{2J} & 0 & 0 & 0 & K_{2J} & 0 & K_{2J} & 0 & -K_{2J} & 0 \\
0 & 0 & K_{3J} & 0 & 0 & 0 & 0 & 0 & 0 & 0 & 0 & 0 & 0 \\
0 & -L_{Nac}K_{2J} & 0 & L_{Nac}^2K_{2J} & 0 & 0 & 0 & -L_{Nac}K_{2J} & 0 & -L_{Nac}K_{2J} & 0 & L_{Nac}K_{2J} & 0 \\
K_{1J}L_{Nac} & 0 & 0 & 0 & L_{Nac}^2K_{1J} & 0 & L_{Nac}K_{1J} & 0 & L_{Nac}K_{1J} & 0 & -L_{Nac}K_{1J} & 0 & 0 \\
0 & 0 & 0 & 0 & 0 & 0 & 0 & 0 & 0 & 0 & 0 & 0 & 0 \\
\hline
K_{1J} & 0 & 0 & 0 & L_{Nac}K_{1J} & 0 & K_{1J} & 0 & K_{1J} & 0 & -K_{1J} & 0 & 0 \\
0 & K_{2J} & 0 & -L_{Nac}K_{2J} & 0 & 0 & 0 & K_{2J} & 0 & K_{2J} & 0 & -K_{2J} & 0 \\
K_{1J} & 0 & 0 & 0 & L_{Nac}K_{1J} & 0 & K_{1J} & 0 & K_{1J} & 0 & -K_{1J} & 0 & 0 \\
0 & K_{2J} & 0 & -L_{Nac}K_{2J} & 0 & 0 & 0 & K_{2J} & 0 & K_{2J} & 0 & -K_{2J} & 0 \\
\hline
-K_{1J} & 0 & 0 & 0 & -L_{Nac}K_{1J} & 0 & -K_{1J} & 0 & -K_{1J} & 0 & K_{1J} & 0 & 0 \\
0 & -K_{2J} & 0 & L_{Nac}K_{2J} & 0 & 0 & 0 & -K_{2J} & 0 & -K_{2J} & 0 & K_{2J} & 0 \\
0 & 0 & 0 & 0 & 0 & 0 & 0 & 0 & 0 & 0 & 0 & 0 & 0
\end{bmatrix}. \quad (2.144)$$

The damping junction matrix has the same form but uses the damping coefficients,  $[d_{1J}, d_{2J}, d_{3J}]$  in place of the spring coefficients  $K_J$ .

## 2.6.6 Power Harvested

For the rotational dampers at the FWT-link junction, the instantaneous power harvested is,

$$P = \eta \mathbf{d}_\theta \dot{\vec{\theta}}_{Link,Rel} \mathbf{d}_\theta^T, \quad (2.145)$$

where  $\mathbf{d}_\theta$  is the matrix of the junction rotational damper, given in Eq. 2.121.  $\vec{\theta}_{Link,Rel}$  is the relative rotation between the link and the FWT, given in Eq. 2.124, and  $\eta$  is the power takeoff efficiency.

If the WEC is an internal tuned mass damper in the nacelle, then the instantaneous power harvested depends on the relative translation motion between the nacelle and WEC,

$$\begin{aligned}
P = \eta d_{1J} (\dot{x}_1 + L_{Nac}\dot{x}_5 + \dot{u}_{1x} + \dot{u}_{2x} - \dot{x}_{1W})^2 \\
+ \eta d_{2J} (\dot{x}_2 - L_{Nac}\dot{x}_4 + \dot{u}_{1y} + \dot{u}_{2y} - \dot{y}_{1W})^2. \quad (2.146)
\end{aligned}$$

We model the junction power takeoffs as having efficiency  $\eta = 0.82$  [143].

## 2.6.7 Simplifications for a WEC and FWT aligned along the x-axis

For some of the optimization results, we consider a WEC and FWT aligned along the x-axis (wave travel direction). In this case, we can reduce the terms in the model and explicitly check the results. The torsional spring coefficients reduce to,

$$\vec{K}_\theta = [0, K_5, 0]. \quad (2.147)$$

We also assume that the junction point on the FWT aligns with the FWT vertical axis,

$$\vec{L}_{JF} = [0, 0, L_{ZJF}]. \quad (2.148)$$

Then, the coupling matrices reduce to,

$$\mathbf{K}_{Rot} = \begin{bmatrix} \frac{K_5}{L_z^2} & 0 & \frac{-K_5}{L_x L_z} & 0 & \frac{K_5 L_{ZJF}}{L_z^2} + \frac{K_5}{L_z} & 0 & \frac{-K_5}{L_z^2} & 0 & \frac{K_5}{L_x L_z} \\ 0 & 0 & 0 & 0 & 0 & 0 & 0 & 0 & 0 \\ \frac{-K_5}{L_x L_z} & 0 & \frac{K_5}{L_x^2} & 0 & \frac{-K_5 L_{ZJF}}{L_x L_z} + \frac{K_5}{L_x} & 0 & \frac{K_5}{L_x L_z} & 0 & \frac{-K_5}{L_x^2} \\ 0 & 0 & 0 & 0 & 0 & 0 & 0 & 0 & 0 \\ \frac{K_5}{L_z} & 0 & \frac{-K_5}{L_x} & 0 & \frac{K_5 L_{ZJF}}{L_z} + K_5 & 0 & \frac{-K_5}{L_z} & 0 & \frac{+K_5}{L_x} \\ 0 & 0 & 0 & 0 & 0 & 0 & 0 & 0 & 0 \\ \frac{-K_5}{L_z^2} & 0 & \frac{K_5}{L_x L_z} & 0 & \frac{-K_5 L_{ZJF}}{L_z^2} + \frac{-K_5}{L_z} & 0 & \frac{K_5}{L_z^2} & 0 & \frac{-K_5}{L_x L_z} \\ 0 & 0 & 0 & 0 & 0 & 0 & 0 & 0 & 0 \\ \frac{-K_5}{L_x L_z} & 0 & \frac{-K_5}{L_x^2} & 0 & \frac{K_5 L_{ZJF}}{L_x L_z} + \frac{-K_5}{L_x} & 0 & \frac{-K_5}{L_x L_z} & 0 & \frac{K_5}{L_x^2} \end{bmatrix}. \quad (2.149)$$

$$\mathbf{K}_{Rigid} = \begin{bmatrix} K_1 & 0 & 0 & 0 & K_1 L_{ZJF} & 0 & -K_1 & 0 & 0 \\ 0 & 0 & 0 & 0 & 0 & 0 & 0 & 0 & 0 \\ 0 & 0 & K_3 & 0 & 0 & 0 & 0 & 0 & -K_3 \\ 0 & 0 & 0 & 0 & 0 & 0 & 0 & 0 & 0 \\ K_1 L_{ZJF} & 0 & 0 & 0 & K_1 L_{ZJF}^2 & 0 & -K_1 L_{ZJF} & 0 & 0 \\ 0 & 0 & 0 & 0 & 0 & 0 & 0 & 0 & 0 \\ \hline -K_1 & 0 & 0 & -K_1 L_{ZJF} & 0 & 0 & K_1 & 0 & 0 \\ 0 & 0 & 0 & 0 & 0 & 0 & 0 & 0 & 0 \\ 0 & 0 & -K_3 & 0 & 0 & 0 & 0 & 0 & K_3 \end{bmatrix}. \quad (2.150)$$

In addition to Eq.s 2.149 and 2.150, if the FWT-WEC has 2 links preventing rotation between the FWT and WEC, we add the pitch force,  $F_{5W}$ , rotational inertia,  $I_{55}$  rotational added mass,  $A_{55}$ , rotational hydrodynamic damping  $B_{55}$ , and rotational hydrostatic stiffness  $C_{55}$  to the FWT matrix. Nondiagonal cross-coupling terms (e.g.  $A_{15}$ ) are already accounted for in the link translation-mode matrix.

## 2.7 Platform modifications

Combining a wave energy converter with a floating wind turbine requires rigidly attaching some components to the platform, such as the linkage frame or an external ballast. The WEC frame mass may not be negligible compared to the WEC. This was the case for the experimentally tested 3-OWC system. In this same experiment, we also attached an external cylinder to the platform to simultaneously resist platform horizontal motion and provide buoyancy. Adding a neutrally buoyant external ballast to the platform can counteract destabilization caused by an attached WEC. We also consider an idealized damping element attached to the platform, which can be used to determine some performance limits of a WEC attached to the FWT.

Here, we describe how a rigidly attached object affects the FWT inertia  $\mathbf{M}$ , added mass  $\mathbf{A}$ , hydrodynamic damping  $\mathbf{B}$ , and hydrostatic stiffness  $\mathbf{K}$  matrices. For the specific case of

a submerged cylindrical ballast encircling the platform, we relate the cylinder geometry to the FWT matrix equation of motion parameters.

The matrices here correspond to the floating wind turbine degrees of freedom,

$$\vec{x}_{Platform} = \begin{bmatrix} x_1 \\ x_2 \\ x_3 \\ x_4 \\ x_5 \\ x_6 \end{bmatrix}. \quad (2.151)$$

We assume that the structure has a known inertia matrix about its center of mass (CM). This CM may not match the FWT CM. We further assume that the structure is symmetrical about its CM so that its products of inertia are 0.

The structure's mass matrix about its CM is,

$$\mathbf{M}_{S,CM} = \begin{bmatrix} m_{1S} & 0 & 0 & 0 & 0 & 0 \\ 0 & m_{2S} & 0 & 0 & 0 & 0 \\ 0 & 0 & m_{3S} & 0 & 0 & 0 \\ 0 & 0 & 0 & I_{44S} & 0 & 0 \\ 0 & 0 & 0 & 0 & I_{55S} & 0 \\ 0 & 0 & 0 & 0 & 0 & I_{66S} \end{bmatrix}. \quad (2.152)$$

The structure's center of mass (CM) in the SWL coordinates is located at,

$$\vec{L}_S = [L_{XS}, L_{YS}, L_{ZS}]. \quad (2.153)$$

Standard strip theory and the parallel axis theorem transform the inertia matrix coordinates from the structure's CM to the floating wind turbine coordinate system origin at the still waterline [44, 76]

$$\mathbf{M}_S = \begin{bmatrix} m_{1S} & 0 & 0 & 0 & L_{ZS}m_{1S} & -L_{YS}m_{1S} \\ 0 & m_{2S} & 0 & -L_{ZS}m_{2S} & 0 & L_{XS}m_{2S} \\ 0 & 0 & m_{3S} & L_{YS}m_{3S} & -L_{XS}m_{3S} & 0 \\ 0 & -L_{ZS}m_{2S} & L_{YS}m_{3S} & I_{44S} + L_{ZS}^2m_{2S} + L_{YS}^2m_{3S} & L_{XS}L_{YS}m_{3S} & -L_{XS}L_{ZS}m_{2S} \\ L_{ZS}m_{1S} & 0 & -L_{XS}m_{3S} & L_{XS}L_{YS}m_{3S} & I_{55S} + L_{XS}^2m_{3S} + L_{ZS}^2m_{1S} & -L_{YS}L_{ZS}m_{1S} \\ -L_{YS}m_{1S} & L_{XS}m_{2S} & 0 & -L_{XS}L_{ZS}m_{2S} & -L_{YS}L_{ZS}m_{1S} & I_{66S} + L_{YS}^2m_{1S} + L_{XS}^2m_{2S} \end{bmatrix}, \quad (2.154)$$

The derivation of this matrix is very similar to the derivation for FWT-WEC coupling by a link described in Section 2.6. A similar matrix transforms the structure's hydrodynamic added mass and damping, when  $m$  is replaced by  $A$  or  $B$ , respectively. While inertial mass in all 3 translational directions for an object is always equal,  $m_{1S} = m_{2S} = m_{3S}$ , this may not be the case for the hydrodynamic coefficients.

The hydrostatic parameters follows a similar coordinate system transformation [64],

$$C_{ij}^{Hydrostatic} = \begin{bmatrix} 0 & 0 & 0 & 0 & 0 & 0 \\ 0 & 0 & 0 & 0 & 0 & 0 \\ 0 & 0 & \rho g A_{SWL} & -\rho g \int \int_{A_{SWL}} y dA & -\rho g \int \int_{A_{SWL}} x dA & 0 \\ 0 & 0 & -\rho g \int \int_{A_{SWL}} y dA & (\rho g \int \int_{A_{SWL}} y^2 dA + \rho g \nabla \bar{z}_{sub} - mg \bar{z}) & 0 & 0 \\ 0 & 0 & -\rho g \int \int_{A_{SWL}} x dA & 0 & (\rho g \int \int_{A_{SWL}} x^2 dA + \rho g \nabla \bar{z}_{sub} - mg \bar{z}) & 0 \\ 0 & 0 & 0 & 0 & 0 & 0 \end{bmatrix}, \quad (2.155)$$

where  $A_{SWL}$  is the structure's area at the still waterline.  $\bar{z}$  refers to the inertial center of the component.  $\bar{z}_{sub}$  refers to the center of the submerged section of the component.  $z$  is measured positive upwards from the still water line. Eq. 2.155 shows that the frame changes the floating platform's center of mass, which affects the pitch hydrostatic restoring coefficient.

Similarly, we consider the wave forces acting on the structure due to unidirectional



waves traveling in the  $x$  direction,

$$\vec{f}_{S,CM} = \begin{bmatrix} f_1 \\ 0 \\ f_3 \\ 0 \\ f_5 \\ 0 \end{bmatrix}. \quad (2.156)$$

The forces transmitted to the FWT due to the rigidly attached structure are,

$$\vec{f}_S = \begin{bmatrix} f_1 \\ 0 \\ f_3 \\ L_{YS} f_3 \\ f_5 + L_{ZS} f_1 \\ L_{XS} f_1 \end{bmatrix}. \quad (2.157)$$

### 2.7.1 Parameters for a submerged cylindrical ballast

For the submerged cylinder, we model the parameters similarly to those for a cylindrical spar WEC geometry, as described in Section 2.4.3, using long wavelength approximations [103].

The submerged cylinder has the shape and location shown in Fig. 2-12. We assume that it encircles the FWT platform, with a centroid location,

$$[L_{XCyl}, L_{YCyl}, L_{ZCyl}] = [0, 0, L_{ZCyl}]. \quad (2.158)$$

The cylinder length is  $h_{Cyl}$ , so it extends over the  $z$  coordinates,

$$z_{Cyl} = [L_{ZCyl,Keel}, L_{ZCyl,Top}], \quad (2.159)$$

The cylinder outer diameter is  $D_{Cyl}$ , and its mass is  $m_{Cyl}$ .

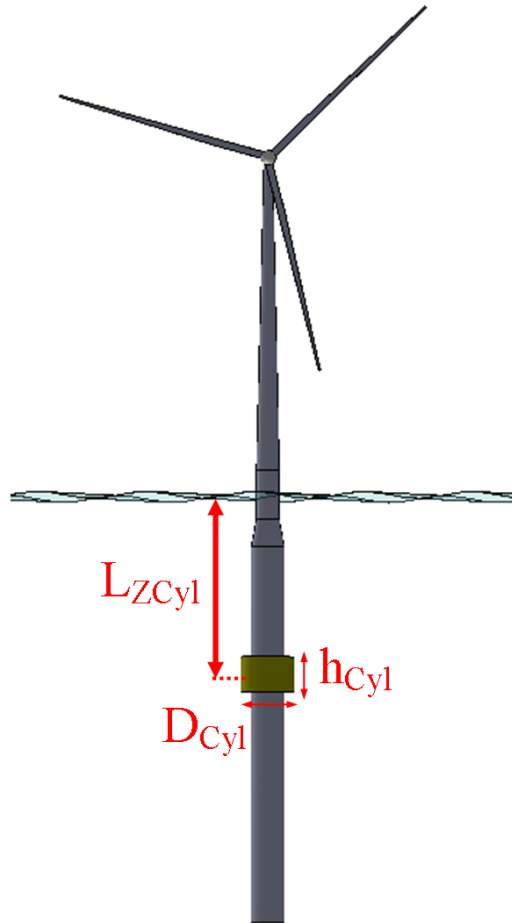


Figure 2-12: External cylindrical ballast rigidly attached to the FWT.

For the toroid shape encircling the FWT, the cylinder cross-sectional area is,

$$A_{Cyl} = \frac{\pi}{4}(D_{Cyl}^2 - D_{FWT}^2), \quad (2.160)$$

where we subtract the FWT cross-section from the cylinder outer cross-section.

The total submerged cylinder volume is,

$$V_{SubCyl} = A_{Cyl}h_{Cyl}, \quad (2.161)$$

Assuming the cylinder has an evenly distributed mass, its mass moment of inertia about the FWT still waterline coordinate system is,

$$I_{44Cyl} = I_{55Cyl} = \frac{m_{Cyl}h_{Cyl}^2}{12} + m_{Cyl}L_{ZCyl}^2. \quad (2.162)$$

For neutral buoyancy, we set,

$$m_{Cyl} = \rho V_{SubCyl}. \quad (2.163)$$

The effective surge added mass is found using strip theory,

$$A_{11Cyl} = \rho \int_{L_{ZCyl,Keel}}^{L_{ZCyl,Top}} \pi \frac{D^2 - D_{FWT}^2}{4} dz = \rho \pi h_{Cyl} \frac{D^2 - D_{FWT}^2}{4}. \quad (2.164)$$

Similarly, the pitch added mass is,

$$A_{55Cyl} = \rho \int_{L_{ZCyl,Keel}}^{L_{ZCyl,Top}} \pi \frac{D^2 - D_{FWT}^2}{4} z^2 dz = \rho \pi h_{Cyl} \frac{D^2 - D_{FWT}^2}{12} (L_{ZCyl,Top}^3 - L_{ZCyl,Keel}^3). \quad (2.165)$$

The surge-pitch added mass coupling is,

$$A_{15Cyl} = \rho \int_{L_{ZCyl,Keel}}^{L_{ZCyl,Top}} \pi \frac{D^2 - D_{FWT}^2}{4} z dz = \rho \pi \frac{D^2 - D_{FWT}^2}{8} (L_{ZCyl,Top}^2 - L_{ZCyl,Keel}^2). \quad (2.166)$$

We approximate the heave added mass as,

$$A_{33Cyl} = \frac{1}{6}\rho\pi(D_{cyl}^3 - D_{FWT}^3), \quad (2.167)$$

which is the added mass of a submerged sphere with the same frontal area as the cylinder, (Newman) [103].

Using the G.I. Taylor long wavelength approximation, the heave excitation force is [103],

$$f_{3Cyl} = -(\rho V_{Cyl} + A_{33Cyl}) \frac{\partial P}{\partial z} \Big|_{L_{ZCyl}}. \quad (2.168)$$

According to linear plan progressive wave theory, the pressure gradient is [103],

$$P = \rho \frac{\partial \phi_i}{\partial t} = a \Re e \left\{ \rho g \frac{\cosh k(z+H)}{\cosh kh} e^{ikx-i\omega t} \right\}, \quad (2.169)$$

where the incident wave velocity potential is

$$\phi_i = a \Re e \left\{ \frac{ig}{\omega} \frac{\cosh k(z+H)}{\cosh kh} e^{ikx-i\omega t} \right\}. \quad (2.170)$$

The effective incremental surge force along the cylinder is due to the frontal area it adds to the FWT platform,

$$df_1 = \left( 2\rho\pi \frac{D^2 - D_{FWT}^2}{4} \frac{\partial P}{\partial x} \right) dz. \quad (2.171)$$

The surge force acting on the spar is the summation of the incremental surge force,

$$f_1 = \int_{L_{ZCyl,Keel}}^{L_{ZCyl,Top}} df_1. \quad (2.172)$$

The pitch moment is,

$$f_5 = \int_{L_{ZCyl,Keel}}^{L_{ZCyl,Top}} z df_1. \quad (2.173)$$

Using the Haskind relation, the cylinder heave hydrodynamic damping is,

$$B_{33Cyl} = \frac{k}{4\rho g V_g} \left| \frac{f_3}{a} \right|^2. \quad (2.174)$$

Similarly, the surge and pitch hydrodynamic damping are calculated by the 2D Haskind relation,

$$B_{11} = \int_{L_{ZCyl,Keel}}^{L_{ZCyl,Top}} \frac{|df_1|^2}{2a^2\rho V_g} dz, \quad (2.175)$$

$$B_{15} = \int_{L_{ZCyl,Keel}}^{L_{ZCyl,Top}} z \frac{|df_1|^2}{2a^2\rho V_g} dz, \quad (2.176)$$

$$B_{55} = \int_{L_{ZCyl,Keel}}^{L_{ZCyl,Top}} z^2 \frac{|df_1|^2}{2a^2\rho V_g} dz, \quad (2.177)$$

where the incremental surge force along the cylinder is given by Eq. 2.171.

The submerged cylinder does not have a hydrostatic stiffness since it is submerged.

The parameters relate to the FWT system equation of motion matrices by

$$\mathbf{M}_{Cyl} = \begin{bmatrix} m_{Cyl} & 0 & 0 & 0 & L_{ZCyl}m_{Cyl} & 0 \\ 0 & m_{Cyl} & 0 & -L_{ZCyl}m_{Cyl} & 0 & 0 \\ 0 & 0 & m_{Cyl} & 0 & 0 & 0 \\ 0 & -L_{ZCyl}m_{Cyl} & 0 & I_{44Cyl} + L_{ZCyl}^2 m_{Cyl} & 0 & 0 \\ L_{ZCyl}m_{Cyl} & 0 & 0 & 0 & I_{55Cyl} + L_{ZCyl}^2 m_{Cyl} & 0 \\ 0 & 0 & 0 & 0 & 0 & 0 \end{bmatrix}, \quad (2.178)$$

$$\mathbf{A}_{Cyl} = \begin{bmatrix} A_{11Cyl} & 0 & 0 & 0 & A_{15Cyl} & 0 \\ 0 & A_{11Cyl} & 0 & -A_{15Cyl} & 0 & 0 \\ 0 & 0 & A_{33Cyl} & 0 & 0 & 0 \\ 0 & -A_{15Cyl} & 0 & A_{55Cyl} & 0 & 0 \\ A_{15Cyl} & 0 & 0 & 0 & A_{55Cyl} & 0 \\ 0 & 0 & 0 & 0 & 0 & 0 \end{bmatrix}, \quad (2.179)$$

$$\mathbf{B}_{Cyl} = \begin{bmatrix} B_{11Cyl} & 0 & 0 & 0 & B_{15Cyl} & 0 \\ 0 & B_{11Cyl} & 0 & -B_{15Cyl} & 0 & 0 \\ 0 & 0 & B_{33Cyl} & 0 & 0 & 0 \\ 0 & -B_{15Cyl} & 0 & B_{55Cyl} & 0 & 0 \\ B_{15Cyl} & 0 & 0 & 0 & B_{55Cyl} & 0 \\ 0 & 0 & 0 & 0 & 0 & 0 \end{bmatrix}, \quad (2.180)$$

The forcing vector on the cylinder is,

$$\vec{f}_{Cyl} = \begin{bmatrix} f_{1Cyl} \\ 0 \\ f_{3Cyl} \\ 0 \\ f_5 \\ 0 \end{bmatrix}. \quad (2.181)$$

## 2.7.2 Ideal Wells Turbine in the Spar

Next, we consider the effects of an ideal horizontal damping element on the FWT. Studying the effects of a damping element along the spar is useful for understanding how the WEC affects the FWT dynamics. This damping element could be implemented by the hydrokinetic Wells turbines shown in Fig. 2-13, which harvest wave power proportional to the relative velocity between the Wells turbine and incident waves.

We consider a Wells turbine with a damping coefficient,  $d_{WellsX}$ , at a submergence depth of,  $L_{3W}$ . Then, similarly to Section 2.7.1, the Wells turbine adds damping to the FWT platform 6 degrees of freedom damping matrix according to,

$$\mathbf{B}_{Wells} = \begin{bmatrix} d_{WellsX} & 0 & 0 & 0 & L_{3W}d_{WellsX} & 0 \\ 0 & 0 & 0 & 0 & 0 & 0 \\ 0 & 0 & 0 & 0 & 0 & 0 \\ 0 & 0 & 0 & 0 & 0 & 0 \\ L_{3W}d_{WellsX} & 0 & 0 & 0 & L_{3W}^2d_{WellsX} & 0 \\ 0 & 0 & 0 & 0 & 0 & 0 \end{bmatrix}, \quad (2.182)$$

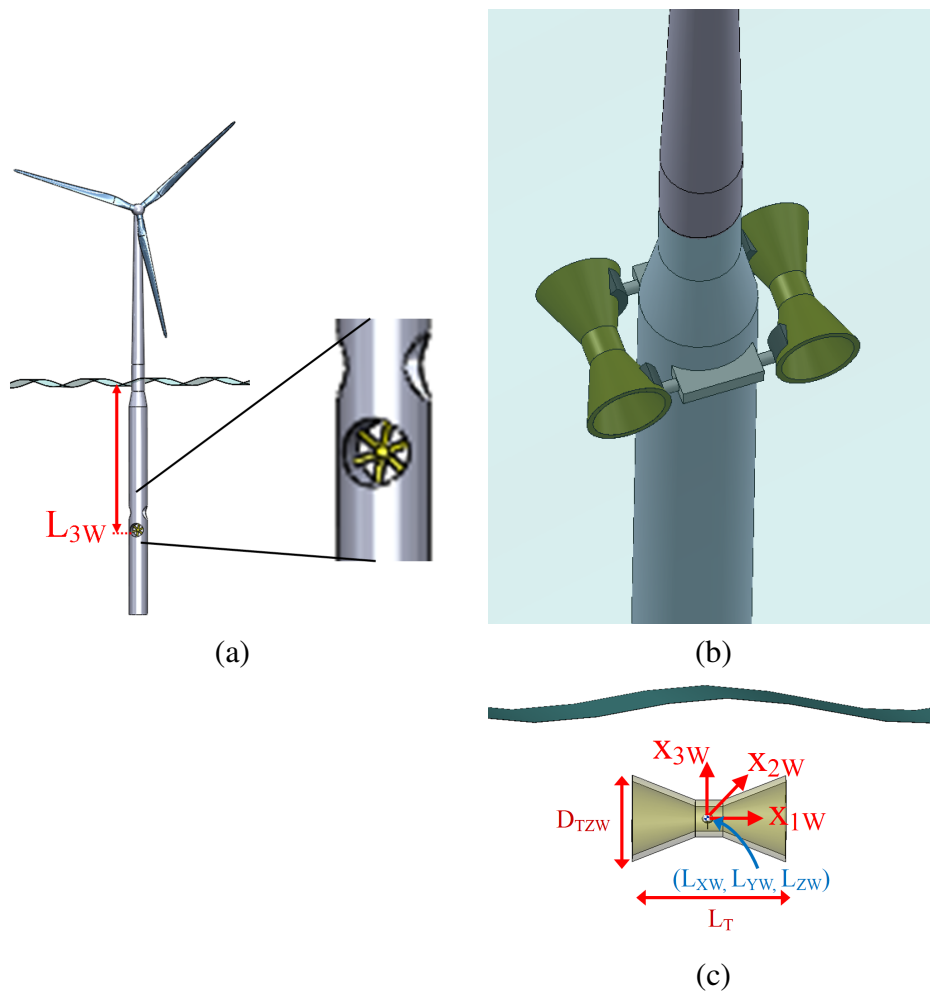


Figure 2-13: Illustration of the linked FWT and a horizontal tube-like WEC.

The ideal damping element adds forcing to the FWT platform,

$$\vec{f}_{Wells} = \begin{bmatrix} d_{WellsX} u_{WellsX} \\ 0 \\ 0 \\ 0 \\ d_{WellsX} L_{3W} u_{WellsX} \\ 0 \end{bmatrix}, \quad (2.183)$$

where  $u_{WellsX}$  is the incident horizontal wave velocity at the depth of the damping element,

$$u_{WellsX} = \frac{-agk \cosh(k(L_{3W} + H))}{\omega \cosh(kH)} e^{ikL_{3W} + i\phi - i\omega t}. \quad (2.184)$$

The instantaneous power harvested is,

$$P = \eta d_{WellsX} (\dot{x}_1 + L_{3W} \dot{x}_5 - u_{WellsX})^2. \quad (2.185)$$

A real attached WEC affects the FWT dynamics similarly to a combined idealized damping element and inertia element.

## 2.8 Final equations of motion matrices

The equation of motion for the entire coupled FWT-WEC system has the form,

$$\mathbf{I}(\omega) \ddot{\vec{x}} + \mathbf{B}(\omega) \dot{\vec{x}} + \mathbf{K} \vec{x} + \int_0^t \mathbf{L} \vec{x} dt = \vec{f}(\omega). \quad (2.186)$$

Here, we introduce the matrix,  $\mathbf{L}$ , which contains coefficients used in integral control for the wind turbine rotor. Section 3.3.2 describes details of  $\mathbf{L}$ , and the rotor angular velocity  $\Omega$ , and collective blade pitch,  $\theta$ .



The degrees of freedom are

$$\vec{x} = \begin{bmatrix} \vec{x}_{FWT} \\ \vec{u} \\ \Omega \\ \theta \\ \hline \vec{x}_{WEC1} \\ \hline \vec{x}_{WEC2} \\ \hline \vdots \end{bmatrix} = \begin{bmatrix} x_1 \\ x_2 \\ x_3 \\ x_4 \\ x_5 \\ x_6 \\ u_{1x} \\ u_{2x} \\ u_{1y} \\ u_{2y} \\ \Omega \\ \theta \\ \hline x_{1W} \\ y_{1W} \\ z_{1W} \\ \hline x_{2W} \\ y_{2W} \\ z_{2W} \\ \hline \vdots \end{bmatrix}. \quad (2.187)$$

The structural mass and frequency-dependent added mass are accounted for in the inertia matrix,

$$\mathbf{I} = \begin{bmatrix} \mathbf{I}_{FWT} + \mathbf{I}_{Structure} & \mathbf{0} & \mathbf{0} & \dots \\ \mathbf{0} & \mathbf{I}_{WEC1} & \mathbf{0} & \dots \\ \mathbf{0} & \mathbf{0} & \mathbf{I}_{WEC2} & \dots \\ \vdots & \vdots & \vdots & \vdots \end{bmatrix}, \quad (2.188)$$

The damping matrix is,

$$\mathbf{B} = \begin{bmatrix} \mathbf{B}_{FWT} + \mathbf{B}_{Structure} + \mathbf{B}_{Rot,WEC1}(1:6, 1:9) + \mathbf{B}_{Rot,WEC2}(1:6, 1:9) & \mathbf{0} & \mathbf{0} & \dots \\ \mathbf{0} & \mathbf{B}_{WEC1} + \mathbf{B}_{Rot,WEC1}(7:9, 1:9) & \mathbf{0} & \dots \\ \mathbf{0} & \mathbf{0} & \mathbf{B}_{WEC2} + \mathbf{B}_{Rot,WEC2}(7:9, 1:9) & \dots \\ \vdots & \vdots & \vdots & \ddots \end{bmatrix} \quad (2.189)$$

The stiffness matrix includes the summation of,

$$\mathbf{K} = \mathbf{K}_{FWT} + \mathbf{C}_{Structure} + \mathbf{K}_{Rot,WEC1} + \mathbf{K}_{Rigid,WEC1} + \mathbf{K}_{\theta Rel,WF,WEC1} + \mathbf{K}_{WEC1} + \mathbf{K}_{WEC2} + \dots, \quad (2.190)$$

where  $\mathbf{0}$  submatrices are added to each matrix term according to which degrees of freedom the term affects, following the pattern shown in Eq. 2.189.

The forcing vector is,

$$\vec{f} = \begin{bmatrix} \vec{f}_{FWT} + \vec{f}_{Structure} \\ \vec{f}_{WEC1} \\ \vec{f}_{WEC2} \\ \vdots \end{bmatrix}. \quad (2.191)$$

## 2.9 Response Statistics in Stochastic Forcing

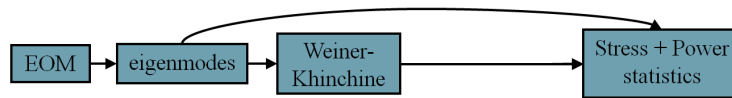


Figure 2-14: Calculation procedure for response statistics in the frequency domain.

Fig. 2-14 outlines the calculation procedure for computing the system response statistics when excited by the stochastic wave forcing. Eq. 2.186 is the combined FWT-WEC equation of motion. Section 2.2 describes the continuous ocean wave elevation power spectrum. Section 2.3.1 reduces the continuous bending problem of the tower to 4 degrees of freedom corresponding to the tower's lowest-frequency bending modes and relates those bending modes to stress at the tower root. In this Section, we use the Weiner Khinchine

theorem to relate the equation of motion and ocean wave elevation power spectrum to the system response statistics.

The complex frequency response function of the system with the equation of motion defined in Eq. 2.186 for waves with amplitude  $a$  and frequency  $\omega$  is,

$$\alpha(\omega) = \frac{\vec{X}}{a} = (-\omega^2 \mathbf{I} + j\omega \mathbf{B} + \mathbf{K})^{-1} \frac{\vec{F}}{a}. \quad (2.192)$$

Using the Wiener-Khinchine theorem for a joint stationary process, the power spectrum matrix of the system response is [116],

$$S_{x_i x_j}^+(\omega) = \alpha S_u^+ \alpha^{T*}, \quad (2.193)$$

where  $\alpha^{T*}$  is the conjugate transpose of  $\alpha$ .  $S_{x_i x_j}^+(\omega)$  are the cross-spectral density functions between two degrees of freedom.  $S_u^+$  is the single-sided wave forcing matrix,

$$S_u^+ = \left( \mathcal{I} \frac{\vec{f}}{a} \right) S_u^+ \left( \mathcal{I} \frac{\vec{f}}{a} \right)^{T*}, \quad (2.194)$$

where  $\mathcal{I}$  is the identity matrix, transforming the forcing vector into a forcing matrix.

The standard deviation in the response of a degree of freedom,  $x_i$ , is [116],

$$\sigma_{x_i} = \sqrt{\int_0^\infty S_{x_i x_i}^+(\omega) d\omega}. \quad (2.195)$$

### 2.9.1 Stress statistics

Traditional time-domain simulations rainflow-count the alternating stress cycles over a structure's lifetime to determine the equivalent fatigue stress (EFS) [96, 117]. The National Renewable Energy Laboratory provides several programs to rainflow count the loads based on loading time series [61]. We use the approach described in [101] to compute the equivalent fatigue stress based on dynamics response statistics found using the frequency-domain approach.

As the tower vibrates in its two lowest frequency bending modes, the maximum stress

at the tower base, as given in Eq. 2.22 based on ANSYS analysis, is,

$$s_{\text{Base,Max}} = 330\alpha_1(t) + 15050\alpha_2(t) \text{ MPa}, \quad (2.196)$$

where  $\alpha_1$  is the nacelle deflection due to the first fore-aft bending frequency and  $\alpha_2$  is the nacelle deflection due to the second fore-aft bending frequency. Using results from ANSYS static analysis, the thrust force on the rotor due to steady wind causes an additional mean stress on the tower base,

$$s_{\text{Base,Thrust}} = \bar{s} = 9.03 \times 10^{-2} F_{\text{Thrust}} (V_{\text{Hub}}) \text{ MPa}, \quad (2.197)$$

where the rotor thrust force,  $F_{\text{Thrust}}$ , in units of kN, is a function of the hub-height wind speed as given in [68].

For a given sea and wind state, the tower bending is considered a stationary, narrow-banded Gaussian process, allowing us to approximate the fluctuating stress peaks,  $s_p$ , from Eq. 2.196, with a Rayleigh probability density,

$$f_{s_p}(s_p) = \frac{s_p}{\sigma_{s_p}^2} e^{-\frac{s_p^2}{2\sigma_{s_p}^2}}, \quad s_p > 0, \quad (2.198)$$

where  $\sigma_{s_p}$  is the standard deviation of the stress. We approximate the stress cycle period as,

$$T_z = 2\pi \frac{\sigma_{s_p}}{\dot{\sigma}_{s_p}}, \quad (2.199)$$

where

$$\dot{\sigma}_{s_p} = \sqrt{\int_0^\infty \omega^2 S_{s_p}^+(\omega) d\omega}. \quad (2.200)$$

The wave-induced stress power spectral density is,

$$S_{s_p}^+(\omega) = |330H_{\alpha_1}(\omega) + 15050H_{\alpha_2}(\omega)|^2 S_u^+, \quad (2.201)$$

where  $H_{\alpha_1}(\omega)$  and  $H_{\alpha_2}(\omega)$  are the transfer functions of the tower bending coefficients and

$S_u^+$  is the ocean power spectral density. We approximate the number of cycles of a certain stress amplitude and mean  $(s_p, \bar{s})$  during each wind/sea state as,

$$n_{\text{State}, s_p, \bar{s}} \approx f_{S_p}(s_p) \Delta S_p \frac{T_{\text{State}}}{T_z}, \quad (2.202)$$

where  $\Delta S_p$  is the stress peak step-width used in our numerical summation, and the time spent in a given sea state over the device lifetime is,

$$T_{\text{State}} = p_{\text{State}} T_{\text{Life}}. \quad (2.203)$$

$p_{\text{State}}$  is the fraction of the device's lifetime,  $T_{\text{Life}}$ , when the structure is in a certain wind-sea state based on historical site data.

From Basquin's equation, the number of cycles to fatigue failure for a stress mean/peak pair is (Dowling, 2007),

$$N_F = \frac{1}{2} \left( \frac{s_{Ut} - |\bar{s}|}{s_p} \right)^m, \quad (2.204)$$

where for the steel material properties, we use ultimate stress,  $s_{Ut} = 2260$  MPa, and Wohler parameter  $m = 5$ , which are limits used by Matha (2009). Using the Palmgren-Miner Rule, the damage incurred over the device lifetime is,

$$D_{\text{Life}} = \sum_{\text{States}} \sum_{s_p, \bar{s} \text{ pairs}} \frac{n_{\text{State}, s_p, \bar{s}}}{N_F}, \quad (2.205)$$

where  $D \geq 1$  indicates likely device failure.

The equivalent fatigue stress (EFS) is the constant peak-peak stress amplitude applied over the entire turbine lifetime that causes the same accumulated damage as caused by the stochastic loads. Rearranging Eq.s 2.202-2.205 shows

$$EFS = 2 \left( \frac{D_{\text{Life}}}{2n_{\text{Life}}} \right)^{1/m} (\sigma_{Ut} - |\bar{s}_{\text{Life}}|), \quad (2.206)$$

where  $n_{\text{Life}}$  is the total stress cycles over the device's lifetime,

$$n_{\text{Life}} = \sum_{\text{States}} \frac{T_{\text{State}}}{T_z}, \quad (2.207)$$

and  $\bar{s}_{\text{Life}}$  is the weighted mean stress over the device's lifetime,

$$\bar{s}_{\text{Life}} = \sum_{\text{States}} p_{\text{State}} \bar{s}_{\text{State}}. \quad (2.208)$$

# Chapter 3

## Statistical Linearization of Nonlinear FWT and WEC Dynamics

### 3.1 Introduction

Many concepts have been considered for improving offshore wind turbine performance: different platform designs, tower and rotor types, controls, and hybrid systems with wave energy converters [96], [127]. Dynamics studies aid in assessing these different wind turbine concepts. Wind turbines are complex systems, comprising of coupled aerodynamic, hydrodynamic, elastic, and control subsystems, which themselves contain stochasticities and nonlinearities. There are two traditional approaches to modeling wind turbine dynamics.

The first, simpler approach is a linear frequency-domain analysis [103]. This approach considers linear wave forcing while ignoring nonlinear effects related to viscosity or wind thrust. The main advantage of this approach is its very fast runtime for computing steady-state responses. The limitation is that it does not capture nonlinear dynamic characteristics.

The second approach is a nonlinear time-domain simulation using a software such as FAST [70]. This approach can consider nonlinear wave viscous forcing and wind turbine thrust in addition to linear wave forcing. The main advantages of time domain simulations over linearized frequency domain models are the ability to compute transient effects and responses when nonlinear effects are significant, such as during storms [70]. The intrinsic

challenge of time-domain simulations is high computation cost. The number of Monte Carlo simulation runs required for the results to converge to the theoretical statistic values may be on the order of 10-100 [113, 116].

The two methods are appropriate for different stages of design and machines with different degrees of nonlinearity. The linear approach will always be the fastest for basic design analysis, while only time domain simulations are rigorous enough to verify if a wind turbine meets design standards. Some machines, such as the OC3-Hywind FWT behave predominantly linearly, even in rough seas. On the other had, floating wind turbines with large near-surface volumes or wave energy converters with large frontal areas can have more significant nonlinear viscous effects [118, 143].

In between the Taylor series linearized frequency domain and nonlinear time domain are an array of other methods for computing nonlinear dynamics effects with better efficiency than simulation time-stepping. These approaches are summarized in [72]:

1. Statistical linearization replaces nonlinear terms with equivalent linear terms in the equation of motion. The values of the linear terms are chosen so that they minimize the statistical difference between the true solution and approximation. Restrictions on this approach are that one must make assumptions about the response probability distribution: normally one assumes it is Gaussian. This is the case for offshore structures that are weakly nonlinear [4]. The approach can easily be generalized to multiple degrees of freedom, non-white excitations, and non-stationary excitations and responses [116].
2. Perturbation methods can solve the nonlinear equation when the nonlinearities are of a sufficiently smaller order than the linearities. Then the system response can be expanded into a series where the dominant term is linear and the nonlinear terms depend on that dominant term.
3. The stochastic averaging method reduces the stochastic dynamics to fluctuating amplitude envelopes and phases. An added advantage of stochastic averaging is that it often reduces the dimensionality of the problem. The method is limited to broadband excitations, light damping, and small nonlinearities [72, 115].



4. Moment closure schemes make assumptions about the response probabilistic moments to solve the nonlinear stochastic differential equations. That is, they ignore higher moments or assume the response is Gaussian distributed. While this approach is more complex than statistical linearization, it can compute the responses of systems with non-Gaussian statistics, such as bimodality and heavy tails [72].
5. The Fokker-Planck-Kolmogorov equation models the diffusion of probability in state space, analogously to the heat equation. It usually requires a finite element approach to solve for multiple degree-of-freedom systems.

Based on the above list, statistical linearization is the most computationally efficient and simplest approach for machines in the ocean environment, where the wave forcing is largely Gaussian, the system has many degrees of freedom, and the system is weakly nonlinear.

Statistical linearization was first developed independently by Booton for control engineering [11] and Caughey [18] for structural nonlinearities. Applications that have used statistical linearization in the past include the sliding motions of a structure on a randomly moving surface [25], nonlinear soil-structure interaction during building vibration (Chu, 1985) [21], large amplitude responses of clamped plates and skin structures (Mei and Paul, 1986) [98], the motion of a vehicle traversing rough ground (Harrison and Hammond, 1986) [59], and the sloshing of liquids in tanks subject to earthquake excitation (Sakata, 1984) [119].

In the field of offshore engineering, Gumestad and Connor (1983) [55] apply statistical linearization to solve the problem of viscous wave force on a long piled steel platform, which resonates with the harmonics of the dominant wave frequency. Gumestad and Connor compute more accurate responses when using a cubic probability distribution instead of a Gaussian distribution. Spanos and Agarwal [130] apply the method to the response of a tension leg platform in rough seas. Leira [89] considers viscous drag forces on multiple degree-of-freedom systems. Grigoriu and Alibe [54] show that Taylor series linearization of the viscous drag force underestimate an offshore platform's motion while statistical linearization is sufficient. Shao et al. [125] compare the statistical linearization method to

experimental results of platform heave, and find good agreement in moderate sea states.

In this chapter, we apply the method of statistical linearization to a floating wind turbine to account for nonlinearities in the frequency domain. First, we briefly derive the statistical linearization method. Then, we describe three nonlinear effects on the floating wind turbine: viscous wave forcing, nonlinear aerodynamics acting on a nonlinearly controlled rotor, and nonlinear mooring lines. In Section 3.3.4, we describe the traditional Taylor series linearization that may be used for some nonlinear forces, so that we may compare these traditional linear results with the statistically linearized results. In Section 3.4, we compare the response amplitude operators and response statistics found using Taylor series linearization, statistical linearization, and time domain simulations. We show that statistical linearization accounts for nonlinear effects neglected by Taylor series linearization and computes the responses with over 100 times higher computational efficiency than the time domain simulations.

In Chapter 4, we model and statistically linearize a wave energy converter (WEC) with a hydrostatic cubic nonlinear nonlinearity. In Chapter 6, we optimize this WEC for maximum power robustness and compare it to linear WEC's.

## 3.2 Derivation of the Statistical Linearization Method

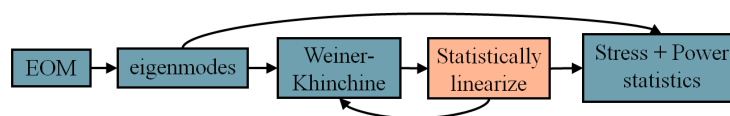


Figure 3-1: Calculation procedure for response statistics in the frequency domain with statistical linearization of the nonlinear terms.

The statistical linearization procedure is sketched in Fig. 3-1. To illustrate the method, we first consider a single degree-of-freedom oscillator with a nonlinear forcing function,  $f$ ,

$$\ddot{x} + \beta\dot{x} + \alpha x = f(t, x, \dot{x}), \quad (3.1)$$

where  $\beta$  and  $\alpha$  are constants, and  $f(t, x, \dot{x})$  is a nonlinear function.

Statistical linearization replaces the nonlinear system of Eq. 3.1 with the equivalent linear system,

$$\ddot{x}_0 + (\beta + \beta_{eq})\dot{x}_0 + (\alpha + \alpha_{eq})x_0 + \alpha m_x = f_0(t) + m_f. \quad (3.2)$$

The first step to deriving Eq. 3.2 is to decompose the general problem into a mean component which is readily solvable, and a zero-mean fluctuating component which can undergo statistical linearization. To simplify the derivation, we assume that the forcing  $f$ , and response  $x$ , are stationary processes. We define,

$$x(t) = m_x + x_0. \quad (3.3)$$

$$f(t) = m_f + f_0. \quad (3.4)$$

$m_x$  and  $m_f$  are the mean components and  $x_0$  and  $f_0$  are the 0-mean components. Taking the expectation of both sides of Eq. 3.1 shows,

$$\alpha E\{x\} = \alpha m_x = E\{f(t, x, \dot{x})\} = m_f. \quad (3.5)$$

We substitute Eq.s 3.3 and 3.4 into Eq. 3.1 and subtract Eq. 3.5,

$$\ddot{x}_0 + \beta\dot{x}_0 + \alpha x_0 = f(t, x, \dot{x}) - m_f. \quad (3.6)$$

The final solution will have the form,

$$x(t) = x_0 + m_x, \quad (3.7)$$

where

$$m_x = \frac{E\{f(t, x, \dot{x})\}}{\alpha}. \quad (3.8)$$

This decomposition is relevant for the nonzero-mean wind thrust on the floating wind turbine, which causes a mean response of the rotor angular velocity and blade pitch, and platform surge and pitch displacement.

Now, we consider the 0-mean nonlinear process,

$$\ddot{x}_0 + \beta \dot{x}_0 + \alpha x_0 - f_0(x_0, \dot{x}_0, t) = 0, \quad (3.9)$$

which we will linearize to,

$$\ddot{x}_0 + (\beta + \beta_{eq})\dot{x}_0 + (\alpha + \alpha_{eq})x_0 = 0. \quad (3.10)$$

Nonlinear forcing is incorporated into the equation of motion as negative equivalent stiffness or damping.

The error between the equivalent linear system and nonlinear system is Eq. 3.9 - Eq. 3.10,

$$\varepsilon = -f_0(x_0, \dot{x}_0, t) - \beta_{eq}\dot{x}_0 - \alpha_{eq}x_0. \quad (3.11)$$

Traditionally, one chooses values of  $\beta_{eq}$  and  $\alpha_{eq}$  that minimize the expectation of the squared error,

$$\frac{\partial E\{\varepsilon^2\}}{\partial \beta_{eq}} = 0. \quad (3.12)$$

$$\frac{\partial E\{\varepsilon^2\}}{\partial \alpha_{eq}} = 0. \quad (3.13)$$

Substituting Eq. 3.11 into Eq.s 3.12 and 3.13,

$$\frac{\partial E\{\varepsilon^2\}}{\partial \beta_{eq}} = E\{-2\dot{x}_0(-f_0(x_0, \dot{x}_0, t) - \beta_{eq}\dot{x}_0 - \alpha_{eq}x_0)\} = 0. \quad (3.14)$$

$$\frac{\partial E\{\varepsilon^2\}}{\partial \alpha_{eq}} = E\{-2x_0(-f_0(x_0, \dot{x}_0, t) - \beta_{eq}\dot{x}_0 - \alpha_{eq}x_0)\} = 0. \quad (3.15)$$

A stationary process with zero mean has the property,

$$E\{x\dot{x}\} = 0. \quad (3.16)$$

The variances of the process are defined as,

$$E\{\dot{x}^2\} = \sigma_{\dot{x}}^2, \quad (3.17)$$

$$E\{x^2\} = \sigma_x^2. \quad (3.18)$$

Substituting Eq.s 3.16-3.18 into Eq.s 3.14 and 3.15 results in,

$$\beta_{Eq} = \frac{E\{-\dot{x}_0 f_0(x_0, \dot{x}_0, t)\}}{\sigma_{\dot{x}}^2} \quad (3.19)$$

$$\alpha_{Eq} = \frac{E\{-x_0 f_0(x_0, \dot{x}_0, t)\}}{\sigma_x^2}. \quad (3.20)$$

A Gaussian process has the property,

$$E\{f(\vec{x})\vec{x}\} = E\{\vec{x}\vec{x}^T\}E\{\nabla f(\vec{x})\}. \quad (3.21)$$

Applying Eq. 3.21 to Eq.s 3.19 and 3.20 results in the final forms,

$$\beta_{Eq} = E\left\{\frac{-\partial f_0(x, \dot{x}, t)}{\partial \dot{x}_0}\right\}, \quad (3.22)$$

$$\alpha_{Eq} = E\left\{\frac{-\partial f_0(x, \dot{x}, t)}{\partial x_0}\right\}. \quad (3.23)$$

As shown in [116], the formulas in Eq. 3.22 and 3.23 are readily generalizable to multiple degrees of freedom.

Finding the expectations of the nonlinear functions requires the joint probability density functions (p.d.f.'s) of the different degrees of freedom. We assume that the responses are Gaussian, so that the joint p.d.f.'s have the form [116],

$$f(\vec{x}) = \frac{1}{(2\pi)^{n/2}|\mathbf{V}|} \exp\left(\frac{-1}{2}(\vec{x} - \vec{m}_x)^T \mathbf{V}^{-1}(\vec{x} - \vec{m}_x)\right), \quad (3.24)$$

where the covariance matrix, which includes the variances and covariances of the FWT-WEC responses is found using the Weiner-Khinchine theorem, Eq. 2.193,

$$V = S_{x_i, x_j}^+ \quad (3.25)$$

To summarize the derived results, computing the statistically linearized responses re-

quires,

1. Solve the linear system while neglecting nonlinearities, according to Eq. 2.193.
2. Use the covariance values of the linear system response to estimate the probability density functions according to the Gaussian process assumption, Eq. 3.24.
3. Use these p.d.f.'s to estimate the linear terms, Eq. 3.22, 3.23, in the statistically equivalent linear equation of motion, Eq. 3.10.
4. Repeat the Weiner-Khinchine process, Eq. 2.193 for the equivalent linear system.
5. Repeat steps 2-4 until the solution converges within an acceptable limit.

This procedure is illustrated in Fig. 3-1.

### 3.3 Nonlinear Floating Wind Turbine Dynamics

We consider 3 nonlinearities of the floating wind turbine: viscous wave forcing, nonlinear wind thrust on the nonlinearly controlled rotor, and nonlinear mooring lines.

#### 3.3.1 Viscous wave forcing

Viscous forces play a significant role in rough sea states for some FWT's [66, 118]. We consider the effects of viscous forcing on the OC3-Hywind spar and OC4-DeepCwind semisubmersible platforms shown in Fig. 2-2.

We consider the degrees of freedom,

$$\vec{x}_{Platform} = \begin{bmatrix} x_1 \\ x_2 \\ x_3 \\ x_4 \\ x_5 \\ x_6 \end{bmatrix}. \quad (3.26)$$

Using Morison's equation, the instantaneous viscous surge force and pitch moment acting on the FWT are,

$$\vec{F}_{Visc} = \begin{bmatrix} F_{V1} \\ 0 \\ 0 \\ 0 \\ F_{V5} \\ 0 \end{bmatrix} = \begin{bmatrix} \frac{1}{2}\rho C_D \int_T^0 D \dot{q} |\dot{q}| dz \\ 0 \\ 0 \\ 0 \\ -\frac{1}{2}\rho C_D \int_T^0 z D \dot{q} |\dot{q}| dz \\ 0 \end{bmatrix}. \quad (3.27)$$

$D$  is the effective platform diameter, plotted in Fig. 3-2 for the OC3-Hywind spar and OC4-DeepCwind semisubmersible platforms. The OC3-Hywind has a diameter of 6.5 m at the still water line, and a bottom diameter of 9.4 m. The OC4-DeepCwind semisubmersible has a main column with a diameter of 6.5 m, and 3 columns with diameters of 12 m at the still water line and bottom diameters of 24 m. The diameters of these 4 columns are summed to create the effective platform diameter plotted in Fig. 3-2.

We use the viscous drag coefficient,  $C_D = 0.6$  [66].

We define the total horizontal velocity of the water relative to the platform as

$$\begin{aligned} \dot{q} &= V_{\text{water}} - V_{\text{platform}} \\ &= \sum_j^n \Re e \left( \left\{ \frac{-a_j k_j g \cosh k_j(z+h)}{\omega_j \cosh k_j h} - i\omega_j X_{1j} - iz\omega_j X_{5j} \right\} e^{i(\omega_j t + \phi_j)} \right), \end{aligned} \quad (3.28)$$

where  $h$  is the water depth and  $\dot{q}$  is a function of the depth below the water,  $z$ . Future work could increase the accuracy of  $V_{\text{water}}$  by accounting for radiation and diffraction effects. We sum  $n$  ocean wave and platform response harmonics. For each ocean wave frequency harmonic,  $i$ ,  $\phi_j$  is a random variable with a uniform distribution for  $0 \leq \phi_j \leq 2\pi$ . The Central Limit Theorem guarantees that  $\dot{q}$  will be a Gaussian stochastic process for large  $n$ . As derived in Section 3.2, we may determine statistically equivalent linear damping

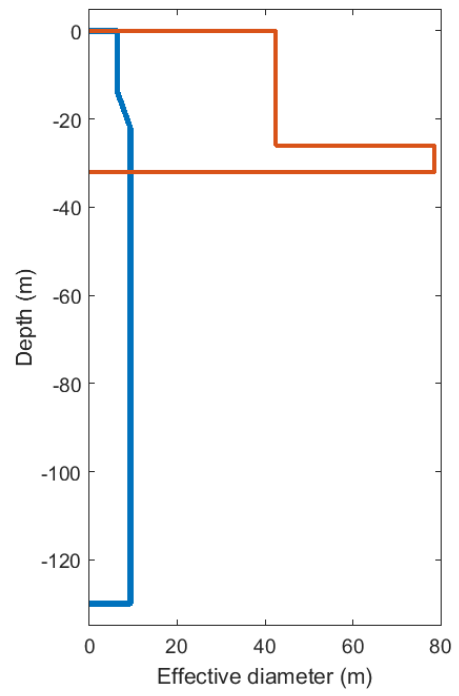


Figure 3-2: The effective platform diameter using for computing the viscous loads of the (Blue) OC3-Hywind spar and (Red) OC4-DeepCwind semisubmersible.



coefficients in the surge and pitch modes of the form

$$\mathbf{B}_{\text{Visc,eq}} = \begin{bmatrix} -E \left\{ \frac{\partial F_{V1}}{\partial \dot{x}_1} \right\} & 0 & -E \left\{ \frac{\partial F_{V1}}{\partial \dot{x}_5} \right\} & 0 & 0 & 0 \\ 0 & 0 & 0 & 0 & 0 & 0 \\ -E \left\{ \frac{\partial F_{V5}}{\partial \dot{x}_1} \right\} & 0 & -E \left\{ \frac{\partial F_{V5}}{\partial \dot{x}_5} \right\} & 0 & 0 & 0 \\ 0 & 0 & 0 & 0 & 0 & 0 \\ 0 & 0 & 0 & 0 & 0 & 0 \\ 0 & 0 & 0 & 0 & 0 & 0 \end{bmatrix}, \quad (3.29)$$

where  $E\{\}$  is the expectation of the Gaussian process. Substituting Eq.s 3.27 and 3.28 into Eq. 3.29, we obtain,

$$\mathbf{B}_{\text{Visc,eq}} = \begin{bmatrix} \rho C_D \int_T^0 D(z) E \{|\dot{q}(z)|\} dz & 0 & \rho C_D \int_T^0 z D(z) E \{|\dot{q}|\} dz & 0 & 0 & 0 \\ 0 & 0 & 0 & 0 & 0 & 0 \\ -\rho C_D \int_T^0 z D(z) E \{|\dot{q}|\} dz & 0 & -\rho C_D \int_T^0 z^2 D(z) E \{|\dot{q}|\} dz & 0 & 0 & 0 \\ 0 & 0 & 0 & 0 & 0 & 0 \\ 0 & 0 & 0 & 0 & 0 & 0 \\ 0 & 0 & 0 & 0 & 0 & 0 \end{bmatrix}. \quad (3.30)$$

We re-emphasize that this damping matrix, which affects the platform surge and pitch damping, is added to the platform damping matrix, Eq.s 2.8 as per Eq. 2.189. The platform damping matrix has nonzero damping terms for the platform degrees of freedom.

The Gaussian process  $\dot{q}$  has a probability density of the form,

$$f_{\dot{q}}(\dot{q}) = \frac{1}{\sqrt{2\pi}\sigma_{\dot{q}}} e^{-\frac{(\dot{q}-\bar{\dot{q}})^2}{2\sigma_{\dot{q}}^2}}, \quad (3.31)$$

where  $\sigma_{\dot{q}}$  is the random variable's standard deviation and  $\bar{\dot{q}} = 0$  is its mean. Then, the expected value of  $|\dot{q}|$  is

$$E \{|\dot{q}|\} = \int_{-\infty}^{\infty} |\dot{q}| f_{\dot{q}}(\dot{q}) d\dot{q} = \frac{\sqrt{2}\sigma_{\dot{q}}}{\sqrt{\pi}}. \quad (3.32)$$

$\mathbf{B}_{\text{Visc,eq}}$  on the left-hand-side of the equation of motion accounts for the external forcing of the incident water velocity on the platform.

In our frequency-domain method of calculating the floating wind turbine response, we iteratively solve for  $\mathbf{B}_{\text{Visc,eq}}$  and  $\vec{F}_{\text{Visc,eq}}$  until the system response,  $\sigma_{\vec{x}}$  converges to within 0.1%, which typically requires less than 7 iterations for the OC3 spar.

### 3.3.2 Rotor Aerodynamics and Control

Thrust forcing on the rotor is a more complex problem than the wave viscous forcing. We model it as function of the platform surge and pitch, and rotor speed and blade pitch angle.

We add two degrees of freedom to the FWT model; rotor speed in rad/s and collective blade pitch (all 3 blades pitch identically),

$$(I_{\text{Rotor}} + N_{\text{Gear}}^2 I_{\text{Gen}}) \dot{\Omega} = Q_{\text{Aero}} - N_{\text{Gear}} Q_{\text{Gen}}, \quad (3.33)$$

$$\theta = K_P N_{\text{Gear}} (\Omega - \Omega_{\text{Target}}) + N_{\text{Gear}} \int_0^t K_I (\Omega - \Omega_{\text{Target}}) dt, \quad (3.34)$$

where  $N_{\text{Gear}} = 97$  is the high-speed to low-speed gearbox ratio,  $I_{\text{Rotor}} = 867,637,000 \text{Kgm}^2$ , and  $I_{\text{Gen}} = 534 \text{Kgm}^2$ . The target speed for blade pitch control is,  $\Omega_{\text{Target}} = 122.9 \text{rad/s}$ .  $Q_{\text{Aero}}$  is the aerodynamic torque and  $Q_{\text{Gen}}$  is the generator torque. It is assumed that the drive shaft is sufficiently stiff that torsional deformation does not significantly affect the dynamics. These two equations of motion (rows) and degrees of freedom (columns) are added to the FWT-WEC matrix equation of motion in Eq. 2.186. Before statistical linearization, the only linear coefficients added to the EOM matrices for these two equations are  $(I_{\text{Rotor}} + N_{\text{Gear}}^2 I_{\text{Gen}})$  for the rotor inertia and 1 for the rotor blade pitch,  $\theta$ .

We use the control algorithm described by Jonkman in [68] to adjust  $Q_{\text{Gen}}$ . As described in [68], the National Renewable Energy Laboratory (NREL) reference 5-MW wind turbine

control law for the generator torque as a function of its speed is,

$$Q_{Gen}(\Omega) = \begin{cases} 0 \text{ Nm,} & \text{if } \Omega < 70.2 \text{ rad/s,} & \text{Region 1} \\ 922(\Omega - 70.2) \text{ Nm,} & \text{if } 70.2 < \Omega < 91.2 \text{ rad/s,} & \text{Region 1.5} \\ 2.332\Omega^2 \text{ Nm,} & \text{if } 91.2 < \Omega < 121.7 \text{ rad/s,} & \text{Region 2} \\ 3896(\Omega - 111) \text{ Nm,} & \text{if } 121.7 < \Omega < 122.9 \text{ rad/s,} & \text{Region 2.5} \\ 43,529 \text{ Nm,} & \Omega > 122.9 \text{ rad/s,} & \text{Region 3} \end{cases} \quad (3.35)$$

This control law is plotted in Fig. 3-3.

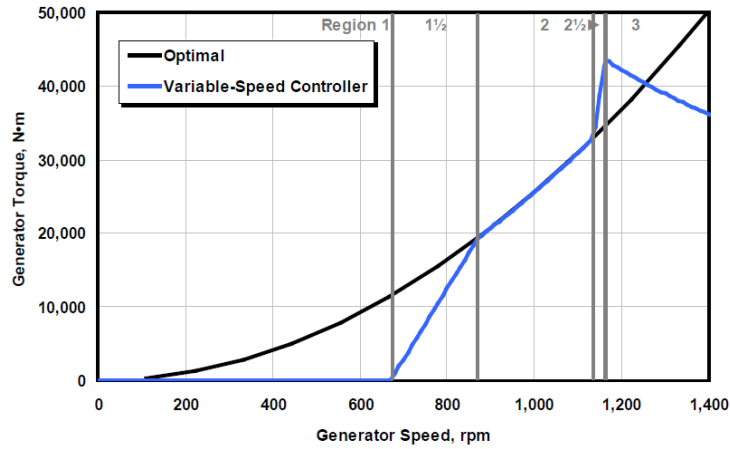


Figure 3-3: Torque versus speed response of the variable-speed rotor controller. Image from Jonkman, 2009 [68].

The NREL reference wind turbine uses blade pitch control in region 3 (when  $\Omega > 122$  rad/s) to try to maintain  $\Omega = 123$  rad/s. The control law for the blade pitch is the proportional-integral control in Eq. 3.34. Found by control optimization in [68], the control gains depend on the blade pitch according to,

$$K_P = \begin{cases} 0 & \text{if } \Omega < 122 \text{ rad/s,} & \text{Regions 1-2.5} \\ \frac{0.00628}{1 + \frac{\theta}{0.110}}, & \text{if } \Omega > 122 \text{ rad/s,} & \text{Region 3,} \end{cases} \quad (3.36)$$

$$K_I = \begin{cases} 0 & \text{if } \Omega < 122 \text{ rad/s, Regions 1-2.5} \\ \frac{0.0008965}{1 + \frac{\theta}{0.110}}, & \text{if } \Omega > 122 \text{ rad/s, Region 3,} \end{cases} \quad (3.37)$$

where  $\theta$  is in units of radians.

In Fig. 3-4, we reproduce the plots by Jonkman [68] that show the equilibrium values of  $\Omega$  and  $\beta$ .

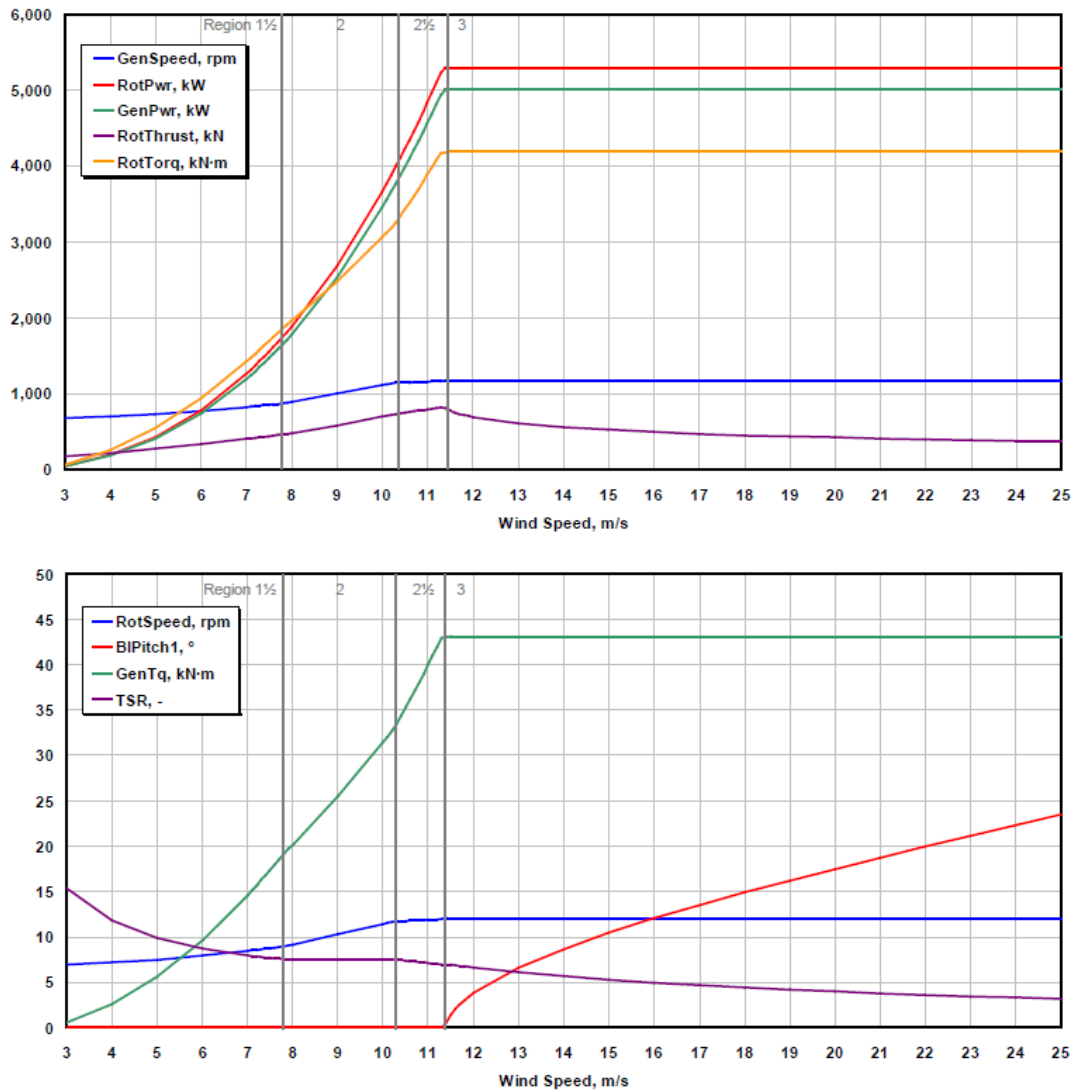


Figure 3-4: Equilibrium values of generator speed, generator torque, generator power, and blade pitch, among other variables. Image from Jonkman, 2009 [68].

In addition to the nonlinear control of the generator torque and blade pitch, the rotor

aerodynamics are nonlinear. The power coefficient, thrust coefficient, and torque coefficients are defined as,

- power coefficient,

$$C_P = \frac{P_{Rotor}}{\frac{1}{2}\rho_a S \dot{q}_W^3}, \quad (3.38)$$

- thrust coefficient,

$$C_T = \frac{F_{Thrust}}{\frac{1}{2}\rho_a S \dot{q}_W^2}, \quad (3.39)$$

- torque coefficient,

$$C_Q = \frac{Q_{Aero}}{\frac{1}{2}\rho_a S R \dot{q}_W^2}, \quad (3.40)$$

where  $\rho_a$  is the air density,  $R$  is the rotor radius,  $S$  is the rotor swept area, and  $\dot{q}_W$  is the wind velocity relative to the nacelle,

$$\dot{q}_W = U - \dot{x}_1 - L_{Nac}\dot{x}_5. \quad (3.41)$$

$U$  is the steady, uniform wind speed and  $L_{Nac}$  is the elevation of the nacelle above the still waterline.

Fig.s 3-5 to 3-7 show the power coefficient, thrust coefficient, and torque coefficient as functions of the blade pitch,  $\beta$ , and tip-speed ratio,

$$TSR = \frac{R_{Rotor}\Omega}{\dot{q}_W}. \quad (3.42)$$

The values in Fig.s 3-5 to 3-7 were computed using the NREL blade element momentum program AeroDyn [69].

### Statistically Equivalent Matrices

The 5 nonlinear forces related to the rotor as described in the previous section are,

1. Rotor aerodynamic thrust,  $F_{Thrust}$ , implicitly defined in Eq. 3.39 and plotted in Fig. 3-6. The thrust force multiplied by the nacelle height causes a pitch torque.
2. Aerodynamic torque,  $Q_{Aero}$ , implicitly defined in Eq. 3.40 and plotted in Fig. 3-7.

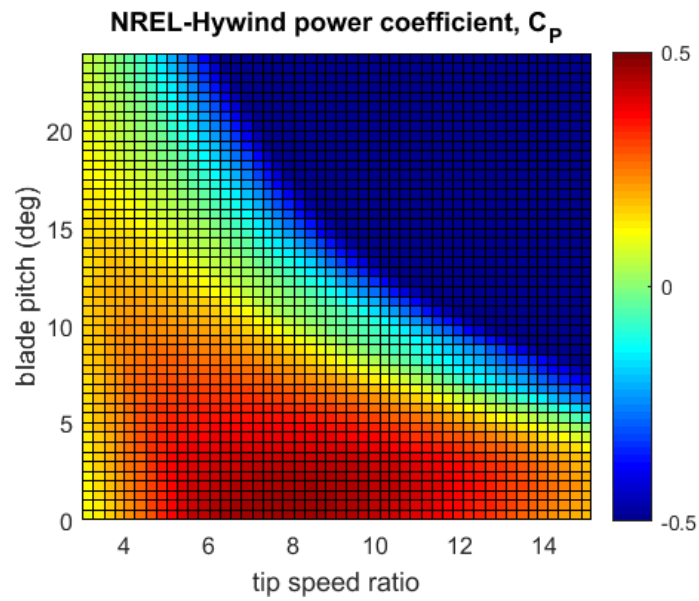


Figure 3-5: NREL-Hywind power coefficient.

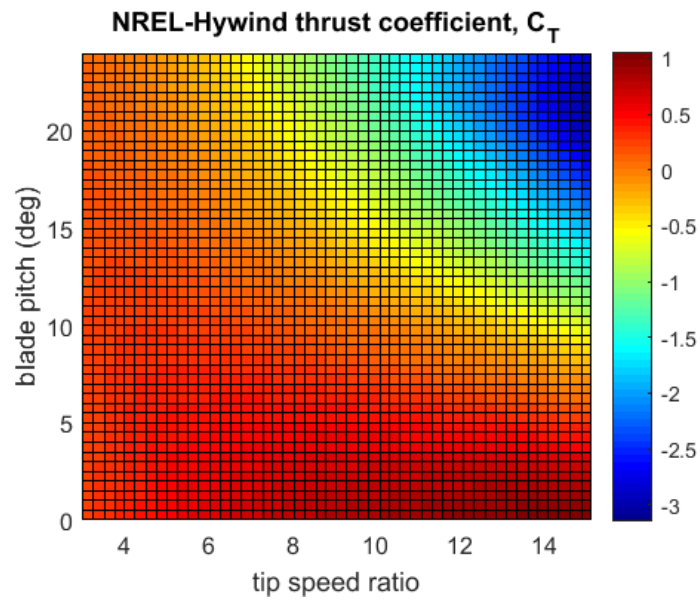


Figure 3-6: NREL-Hywind thrust coefficient.

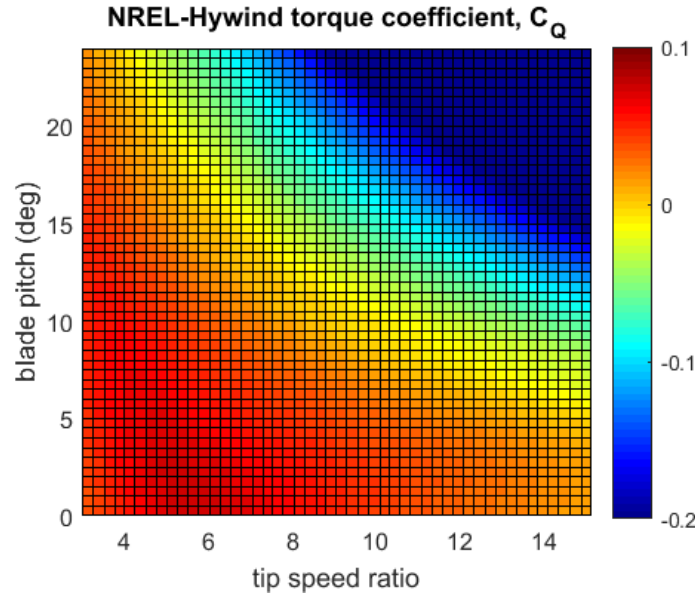


Figure 3-7: NREL-Hywind torque coefficient.

3. Generator torque,  $N_{Gear}Q_{Gen}$ , defined in Eq. 3.35 and plotted in Fig. 3-3.
4. Blade pitch proportional control,  $K_P N_{Gear}(\Omega - \Omega_{Target})$ , defined in Eq. 3.36,
5. Blade pitch integral control,  $N_{Gear} \int_0^t K_I(\Omega - \Omega_{Target})$ , defined in Eq. 3.37.

These nonlinear forces are functions of the 4 degrees of freedom,

$$\vec{x} = \begin{bmatrix} x_1 \\ x_5 \\ \Omega \\ \theta \end{bmatrix} = \begin{bmatrix} \text{platform surge} \\ \text{platform pitch about SWL} \\ \text{rotor angular velocity} \\ \text{rotor blade pitch} \end{bmatrix}, \quad (3.43)$$

The statistically equivalent linear matrices defined below are added to the full equation of motion matrices in Eq. 2.186 (when additional columns and rows are added for the two degrees of freedom,  $\Omega$  and  $\theta$ ).

As per Eq.s 3.22 and 3.23, we determine statistically equivalent damping and stiffness matrices by taking the expectations of the partial derivatives of the nonlinear forces with respect to each degree-of-freedom's velocity and displacement.

Each degree of freedom is directly affected by the nonlinear forces according to,

$$\begin{bmatrix} x_1 \\ x_5 \\ \Omega \\ \theta \end{bmatrix} = \begin{bmatrix} f(F_{Thrust}) \\ L_{Nac}f(F_{Thrust}) \\ f((Q_{Aero}, N_{Gear}Q_{Gen})) \\ f\left(K_P N_{Gear}(\Omega - \Omega_{Target}), N_{Gear} \int_0^t K_I(\Omega - \Omega_{Target})\right) \end{bmatrix}, \quad (3.44)$$

The 5 nonlinear forces are functions of each degree of freedom according to,

$$\begin{bmatrix} F_{Thrust} \\ Q_{Aero} \\ N_{Gear}Q_{Gen} \\ F_{P,Pitch} = -K_P N_{Gear}(\Omega - \Omega_{Target}) \\ F_{I,Pitch} = -N_{Gear} \int_0^t K_I(\Omega - \Omega_{Target}) \end{bmatrix} = \begin{bmatrix} f(\dot{x}_1, \dot{x}_5, \Omega, \theta) \\ f(\dot{x}_1, \dot{x}_5, \Omega, \theta) \\ f(\Omega) \\ f(\Omega, \theta) \\ f(\Omega, \theta) \end{bmatrix}, \quad (3.45)$$

where we define  $F_{P,Pitch}$  and  $F_{I,Pitch}$  to simplify Eq.s 3.49 and 3.50 below.

Accordingly, the statistically equivalent linear terms are

$$\mathbf{B}_{Rotor,eq} = \begin{bmatrix} -E\left\{\frac{\partial F_{Thrust}}{\partial \dot{x}_1}\right\} & -E\left\{\frac{\partial F_{Thrust}}{\partial \dot{x}_5}\right\} & 0 & 0 \\ -L_{Nac}E\left\{\frac{\partial F_{Thrust}}{\partial \dot{x}_1}\right\} & -L_{Nac}E\left\{\frac{\partial F_{Thrust}}{\partial \dot{x}_5}\right\} & 0 & 0 \\ -E\left\{\frac{\partial Q_{Aero}}{\partial \dot{x}_1}\right\} & -E\left\{\frac{\partial Q_{Aero}}{\partial \dot{x}_5}\right\} & 0 & 0 \\ 0 & 0 & 0 & 0 \end{bmatrix}. \quad (3.46)$$

$$\mathbf{K}_{Rotor,eq} = \begin{bmatrix} 0 & 0 & -E\left\{\frac{\partial F_{Thrust}}{\partial \Omega}\right\} & -E\left\{\frac{\partial F_{Thrust}}{\partial \theta}\right\} \\ 0 & 0 & -L_{Nac}E\left\{\frac{\partial F_{Thrust}}{\partial \Omega}\right\} & -L_{Nac}E\left\{\frac{\partial F_{Thrust}}{\partial \theta}\right\} \\ 0 & 0 & -E\left\{\frac{\partial(N_{Gear}Q_{Gen})}{\partial \Omega}\right\} - E\left\{\frac{\partial Q_{Aero}}{\partial \Omega}\right\} & -E\left\{\frac{\partial Q_{Aero}}{\partial \theta}\right\} \\ 0 & 0 & -E\left\{\frac{F_{P,Pitch}}{\partial \Omega}\right\} & -E\left\{\frac{F_{P,Pitch}}{\partial \theta}\right\} \end{bmatrix}. \quad (3.47)$$



$$\mathbf{L}_{\text{Rotor,eq}} = \begin{bmatrix} 0 & 0 & 0 & 0 \\ 0 & 0 & 0 & 0 \\ 0 & 0 & 0 & 0 \\ 0 & 0 & -E \left\{ \frac{F_{l,Pitch}}{\partial \Omega} \right\} & -E \left\{ \frac{F_{l,Pitch}}{\partial \theta} \right\} \end{bmatrix}. \quad (3.48)$$

$\mathbf{B}_{\text{Rotor,eq}}$ ,  $\mathbf{K}_{\text{Rotor,eq}}$ , and  $\mathbf{L}_{\text{Rotor,eq}}$  can be further expressed as,

$$\mathbf{B}_{\text{Rotor,eq}} = \begin{bmatrix} -\rho_a S E \{C_T \dot{q}_W\} & -L_{Nac} \rho_a S E \{C_T \dot{q}_W\} & 0 & 0 \\ -L_{Nac} \rho_a S E \{C_T \dot{q}_W\} & -L_{Nac}^2 \rho_a S E \{C_T \dot{q}_W\} & 0 & 0 \\ -\rho_a S R E \{C_Q \dot{q}_W\} & -L_{Nac} \rho_a S R E \{C_Q \dot{q}_W\} & 0 & 0 \\ 0 & 0 & 0 & 0 \end{bmatrix}. \quad (3.49)$$

$$\mathbf{K}_{\text{Rotor,eq}} = \begin{bmatrix} 0 & 0 & -\frac{1}{2} \rho_a S E \left\{ \dot{q}_W^2 \frac{\partial(C_T)}{\partial \Omega} \right\} & -\frac{1}{2} \rho_a S E \left\{ \dot{q}_W^2 \frac{\partial(C_T)}{\partial \theta} \right\} \\ 0 & 0 & -L_{Nac} \frac{1}{2} \rho_a S E \left\{ \dot{q}_W^2 \frac{\partial(C_T)}{\partial \Omega} \right\} & -L_{Nac} \frac{1}{2} \rho_a S E \left\{ \dot{q}_W^2 \frac{\partial(C_T)}{\partial \theta} \right\} \\ 0 & 0 & -E \left\{ \frac{\partial(N_{Gear} Q_{Gen})}{\partial \Omega} \right\} - \frac{1}{2} \rho_a S R E \left\{ \dot{q}_W^2 \frac{\partial(C_Q)}{\partial \Omega} \right\} & -\frac{1}{2} \rho_a S R E \left\{ \dot{q}_W^2 \frac{\partial(C_Q)}{\partial \theta} \right\} \\ 0 & 0 & N_{Gear} E \{K_p\} & N_{Gear} E \left\{ \frac{\partial K_p}{\partial \theta} (\Omega - \Omega_{Target}) \right\} \end{bmatrix}. \quad (3.50)$$

$$\mathbf{L}_{\text{Rotor,eq}} = \begin{bmatrix} 0 & 0 & 0 & 0 \\ 0 & 0 & 0 & 0 \\ 0 & 0 & 0 & 0 \\ 0 & 0 & N_{Gear} E \{K_I\} & N_{Gear} E \left\{ \frac{\partial K_I}{\partial \theta} (\Omega - \Omega_{Target}) \right\} \end{bmatrix}. \quad (3.51)$$

The statistically linearized damping, stiffness, and integral matrices described here are added to the linear FWT damping and stiffness matrices described in Section 2.8.

To determine the coefficients in Eq.s 3.49, 3.50, and 3.51, we numerically determine the Gaussian p.d.f.'s,  $f_{\vec{x}}$ , for grids of possible (*rotor velocity, blade pitch, wind speed relative to the rotor*) values using Matlab's built-in function *mvnpdf.m*. We correspond values of the nonlinear functions to the p.d.f. using Matlab's *interp3.m* function to numerically interpolate values over pre-computed grids of the nonlinear function. Then, we numerically

sum,

$$E\{h\} = \int_0^{\infty} f_{\vec{x}} h \delta \vec{x}, \quad (3.52)$$

for the nonlinear function,  $h$ . Statistically linearizing the wind thrust-rotor problem typically requires less than 8 iterations to converge.

Additionally, the steady-wind causes a mean force on the rotor,

$$\bar{F}_{Thrust} = \frac{1}{2} \rho_a C_T \left( \frac{R\bar{\Omega}}{U}, \bar{\theta} \right) S U^2. \quad (3.53)$$

As derived in Eq. 3.8 and shown Fig. 3-4, this force and wind speed results in a mean platform surge and pitch, tower deflection, rotor angular velocity, and blade pitch.

### 3.3.3 Mooring Lines

Our mooring lines model is simpler than the viscous wave forcing and rotor aerodynamics/control. As described in [58], modeling the mooring lines as quasi-static springs (rather than accounting for their viscous forces, damping, and inertia) is usually sufficient for determining their effect on platform motion. Except for at the extreme platform deflections, catenary mooring lines apply a negligible force on the platform and therefore have a negligible effect on the dynamics. Nevertheless, here we demonstrate how one could statistically linearize this nonlinear force.

We consider just the lateral fairleads force, which affects the platform surge and pitch. Accordingly, if the degrees of freedom considered are part of the vector,

$$\begin{bmatrix} x_1 \\ x_5 \end{bmatrix} = \begin{bmatrix} \text{platform surge} \\ \text{platform pitch} \end{bmatrix}, \quad (3.54)$$

then the mooring line force affects those degrees of freedom by

$$\mathbf{F}_{Mooring} = \begin{bmatrix} 1 & L_{FL} \\ L_{FL} & L_{FL}^2 \end{bmatrix} \begin{bmatrix} F_{Surge} \\ F_{Mooring} \end{bmatrix}, \quad (3.55)$$

where  $L_{FL} = -70$  m is the fairleads depth for the OC3 platform, and  $F_{Mooring}^{Surge}$  is the fairleads

force in the surge direction.

We numerically compute the fairleads force in the surge direction as a function of the fairleads horizontal displacement (which accounts for platform surge and pitch) using the NREL multi-segment quasi-static model, MAP++ [94]. Fig. 3-8 plots the results.

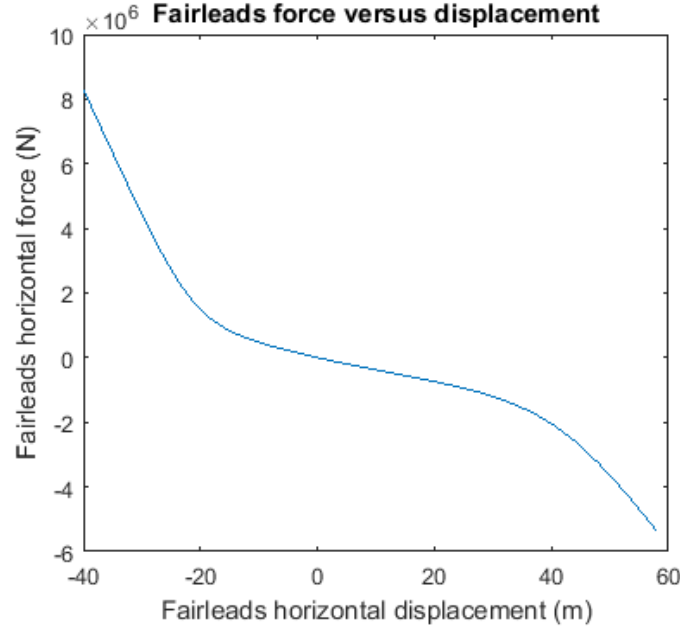


Figure 3-8: NREL-Hywind power coefficient.

As per Eq. 3.23, the statistically equivalent mooring line stiffness matrix is,

$$\mathbf{K}_{\text{Mooring,eq}} = - \begin{bmatrix} 1 & L_{FL} \\ L_{FL} & L_{FL}^2 \end{bmatrix} E \left\{ \begin{array}{c} \frac{\partial F_{\text{Surge}}}{\partial q_{FL}} \\ \frac{\partial F_{\text{Mooring}}}{\partial q_{FL}} \end{array} \right\}, \quad (3.56)$$

where  $q_{FL}$  is the platform horizontal deflection at the fairleads accounting for platform surge and pitch,

$$q_{FL} = x_1 + L_{FL}x_5. \quad (3.57)$$

In our Matlab code implementation of the FWT model, we compute the statistics (standard deviation) of  $q_{FL}$  by summing the transfer functions of the platform surge and pitch for each discretized wave frequency, and then multiplying by the wave power spectrum. This is computationally more efficient than adding an additional degree of freedom to the model

to track  $q_{FL}$ .

### 3.3.4 Taylor Series Linearization

The traditional frequency domain dynamics computation uses linearized terms and only 1 iteration of the Weiner-Khinchine equation, Eq. 2.193. In this procedure, one linearizes nonlinear terms using the first-order terms of Taylor series expansion,

$$f_{Non}(x_1, x_2, \dots) \approx f_{Non}(x_{1,Eq}, x_{2,Eq}, \dots) + \left. \frac{\partial f_{Non}}{\partial x_1} \right|_{\vec{x}_{Eq}} (x_1 - x_{1,Eq}) + \left. \frac{\partial f_{Non}}{\partial x_2} \right|_{\vec{x}_{Eq}} (x_2 - x_{2,Eq}) \dots \quad (3.58)$$

where  $(x_{1,Eq}, x_{2,Eq}, \dots)$  are the equilibrium d.o.f. values. Eq. 3.58 shows that a nonzero Taylor series linear term exists if the first derivative of the function is nonzero when evaluated at its equilibrium value.

#### Viscous wave forcing

Without a mean fluid flow (current), equilibrium values of the viscous force and its derivatives equal 0. That is, Taylor series linearization cannot account for the viscous forcing effects.

#### Rotor aerodynamics and control

We define the wind thrust force, based on the definition in Eq. 3.39 as,

$$F_{Thrust} = \frac{1}{2} \rho_a S C_T (U - \dot{x}_1 - L_{Nac} \dot{x}_5)^2, \quad (3.59)$$

which is a nonlinear function of the platform surge  $x_1$ , pitch  $x_5$ , rotor angular velocity  $\Omega$ , and collective blade pitch  $\theta$ . The mean wind speed corresponds to a mean set of,

$$\vec{x}_{Eq} = (x_{1Eq}, x_{5Eq}, \Omega_{Eq}, \theta_{Eq}), \quad (3.60)$$

as shown in Fig. 3-4. By definition of a equilibrium vibration, the mean platform velocities  $\dot{x}_{1Eq}$  and  $\dot{x}_{5Eq}$  are zero.

We linearize the wind thrust force as,

$$F_{\text{Thrust, Taylor}} \approx \left. \frac{\partial F_{\text{Thrust}}}{\partial \dot{x}_1} \right|_{\vec{x}_{Eq}} \dot{x}_1 + \left. \frac{\partial F_{\text{Thrust}}}{\partial \dot{x}_5} \right|_{\vec{x}_{Eq}} \dot{x}_5 + \left. \frac{\partial F_{\text{Thrust}}}{\partial \Omega} \right|_{\vec{x}_{Eq}} (\Omega - \Omega_{Eq}) + \left. \frac{\partial F_{\text{Thrust}}}{\partial \theta} \right|_{\vec{x}_{Eq}} (\theta - \theta_{Eq}), \quad (3.61)$$

which can be expressed as,

$$F_{\text{Thrust, Taylor}} \approx -\rho_a S C_T(U) \dot{x}_1 - \rho_a S C_T(U) L_{Nac} \dot{x}_5 + \frac{1}{2} \rho_a S U^2 \frac{\partial C_T(U)}{\partial \Omega} (\Omega - \Omega_{Eq}) + \frac{1}{2} \rho_a S U^2 \frac{\partial C_T(U)}{\partial \theta} (\theta - \theta_{Eq}). \quad (3.62)$$

For the degrees of freedom,

$$\vec{x} = \begin{bmatrix} x_1 \\ x_5 \\ \Omega - \Omega_{Eq} \\ \theta - \theta_{Eq} \end{bmatrix} = \begin{bmatrix} \text{platform surge} \\ \text{platform pitch about SWL} \\ \text{rotor angular velocity} \\ \text{rotor blade pitch} \end{bmatrix}, \quad (3.63)$$

the linearized wind thrust damping and stiffness matrices are,

$$\mathbf{B}_{\text{Rotor, Taylor}} = \rho_a S C_T(U) \begin{bmatrix} 1 & L_{Nac} & 0 & 0 \\ L_{Nac} & L_{Nac}^2 & 0 & 0 \\ 0 & 0 & 0 & 0 \\ 0 & 0 & 0 & 0 \end{bmatrix}. \quad (3.64)$$

$$\mathbf{K}_{\text{Rotor, Taylor}} = \frac{1}{2} \rho_a S U^2 \begin{bmatrix} 0 & 0 & 0 & 0 \\ 0 & 0 & 0 & 0 \\ 0 & 0 & 1 & 0 \\ 0 & 0 & 0 & 1 \end{bmatrix} \quad (3.65)$$

Eq.s 3.64 and 3.65 show that the Taylor linearized matrices neglect how dynamically changing rotor angular velocity and blade pitch affect the platform surge and pitch. They neglect other cross-coupling terms accounted for in the statistically linearized Eq.s 3.49 and 3.50, as well. Eq.s 3.64 and 3.65 do account for the negative platform damping effects

due to blade pitch [65]: as shown in Fig. 3-6,  $\partial C_T / \partial \theta$  may be negative. This agrees with the negatively-sloped equilibrium  $C_T$  versus wind speed in Fig. 3-4 at large wind speeds when blade pitch control is applied.

### Mooring Lines

The mooring lines can be linearized as constant stiffness coefficients for the platform surge and pitch degrees of freedom,

$$\begin{bmatrix} x_1 \\ x_5 \end{bmatrix} = \begin{bmatrix} \text{platform surge} \\ \text{platform pitch} \end{bmatrix}. \quad (3.66)$$

The corresponding Taylor series linearized mooring line force matrix is,

$$\mathbf{F}_{\text{Mooring, Taylor}} = \begin{bmatrix} 1 & L_{FL} \\ L_{FL} & L_{FL}^2 \end{bmatrix} \left. \frac{\partial F_{\text{Surge Mooring}}}{\partial q_{FL}} \right|_{\vec{x}_{Eq}}, \quad (3.67)$$

where  $F_{\text{Surge Mooring}}(q_{FL})$  is plotted in Fig. 3-8.

## 3.4 Results for the OC3-Hywind and OC4 semi-submersible Floating Wind Turbines

In this section, we compare the computed FWT response statistics for the 2 different platforms (OC3 Hywind spar and OC4 semisubmersible) using the 3 different computation approaches (Taylor series linearization in the frequency domain, statistical linearization in the frequency domain, and nonlinear time domain) in several different wind-sea states.

The goal of this study is to determine if the response statics found using statistical linearization in the frequency domain are more accurate than those found using Taylor series linearization in frequency domain. Response statistics computed from the nonlinear equations of motion in the time domain are considered the most accurate. If the computed platform motion, tower stress, or wind turbine power computed by the statistical linearization approach are significantly more accurate than the Taylor linearized frequency domain

approach, then statistical linearization is useful for FWT and WEC parameter optimization. Unfortunately, the time domain results presented here still need to be more rigorously debugged, so the results shown in this section are not be completely finalized.

While working on this thesis, we did compute some response statistics using the NREL code FAST [67], but we suspect that differences in the physical models used by FAST and this thesis resulted in different responses that can not be used to directly compare the computation methods.

Our time domain computations simulated the system for 1000 seconds using ode45 in Matlab with time steps of 0.1 seconds. We assumed uniform, steady wind and a wave spectrum with stochastic phases approximated using the Box-Muller method [64]. The statistics were computed based on the time series responses between 500-1,000 seconds. The frequency domain results were computed using 400 frequencies between 0.001-0.45 Hz. Relative velocity between the platform and incident waves was discretized into 10 elements between the still waterline and platform keel for both platforms.

We note that these time domain results required a 660 second computation time (11 minutes), the statistical linearization results required 9 seconds, and the Taylor series linearization required 3 seconds. At a computation time ratio of 76:1 with the time domain approach and possible 7-15% more accurate lifetime stress prediction than the Taylor series approach, statistical linearization may be a promising parameter optimization method for nonlinear FWT's and WEC's. We also note that a single sea state may have significant nonlinear effects, but averaged over the system lifetime, these nonlinear effects may be less significant. Therefore, a nonlinear computation method may be most useful for extreme sea states rather than lifetime performance prediction. Future work will continue to investigate this research question.

### 3.4.1 Response Amplitude Operators

Fig. 3-9 plots response amplitude operators (RAO's) of the platform surge, platform pitch, and tower bending stress in a wind-sea state that consists of a white-noise wave power spectrum with a significant wave height  $H_s = 0.01$  m and a wind speed  $U = 0$  m/s. With

small wave forcing and no wind, this RAO plots the linear responses computed by all 3 methods, serving as a baseline before adding nonlinearities. As expected, Taylor series linearization in the frequency domain and statistical linearization in the frequency domain agree perfectly for both the spar and semisubmersible in these conditions. Also as expected, the time series RAO's follow similar trends to the frequency domain RAO's but show significant noise. This noise could be reduced if the systems are simulated for longer times. With a lot of noise, it is difficult to make confident conclusions about the time domain and frequency domain agreement. In general, it seems that the spar time domain results agree closely with the frequency domain results, except for predicting a larger response between 0.01-0.03 Hz. The time- and frequency-domain results for the semisubmersible also seem to show general agreement except for at frequencies below 0.02 Hz.

Fig. 3-10 plots response amplitude operators (RAO's) of the platform surge, platform pitch, and tower bending stress in a wind-sea state that consists of a white-noise wave power spectrum with a significant wave height of  $H_s = 0.5$  m and a wind speed  $U = 8$  m/s. With large wave forcing and wind, we expect both nonlinear aerodynamic forcing and viscous wave forcing to be significant. For both platforms, all 3 methods show minimal change in surge between the  $U = 0, C_D = 0$  case (Fig. 3-9) and  $U = 8$  m/s,  $C_D = 0.6$  case (Fig. 3-10). Both the Taylor linearized and time domain results predict a larger surge response than statistical linearization at frequencies less than 0.02 Hz, which suggests that the statistical linearization code might have an error or the approach might not work in these conditions. In pitch, all 3 methods follow the same general trend: damping effects from the wind thrust and wave viscosity smooth out peaks in the RAO plot. The spar peaks are more significantly smoothed than the semisubmersible peaks. At frequencies greater than 0.16 Hz, the time domain approach significantly overestimates the pitch response compared to the frequency domain approaches. For tower stress, the time domain results generally show much larger responses than the frequency domain results, which may be due to a code error. There are significant differences between the statistically linearized and Taylor series linearized responses, which is likely a significant result. For both the spar and semisubmersible, the Taylor series computations underpredict stress compared to the statistical linearization computations at some frequencies.



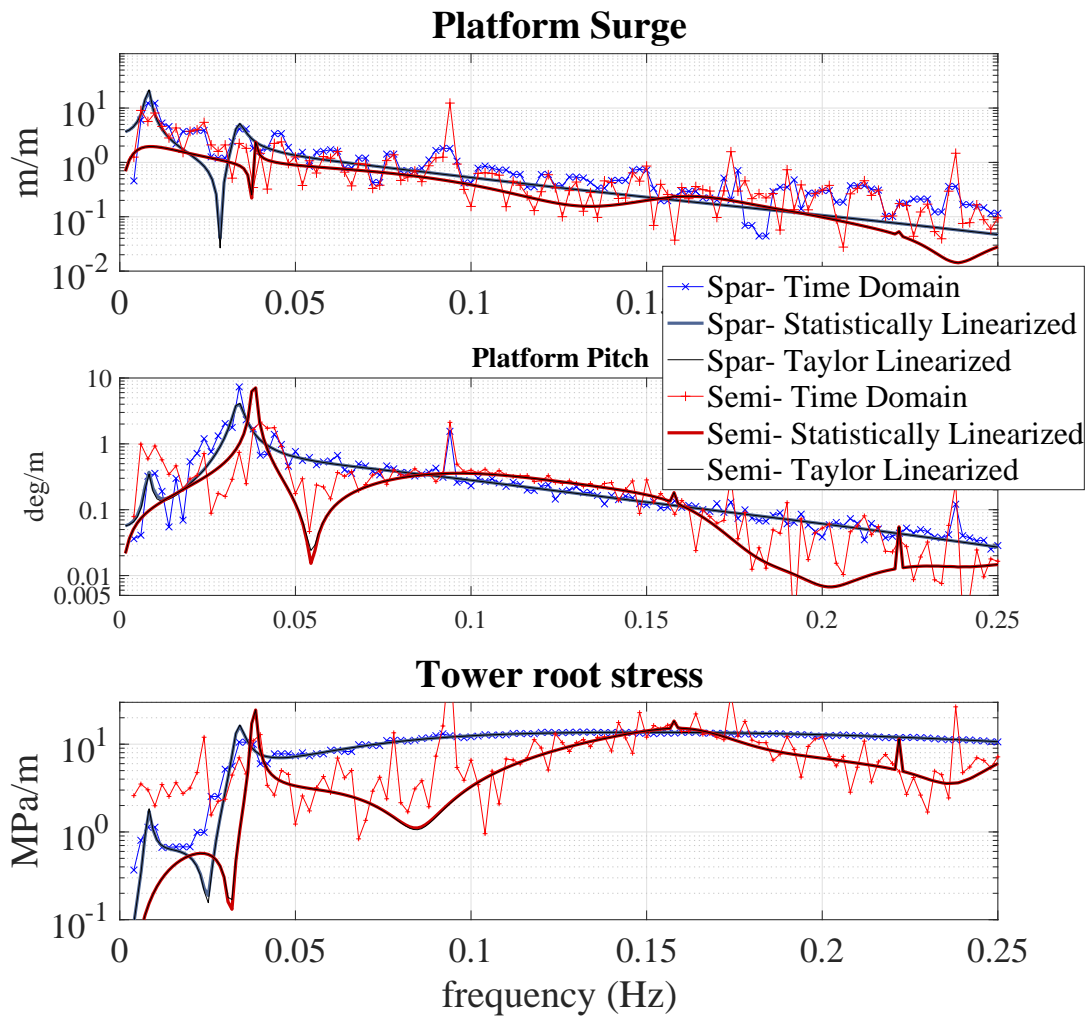


Figure 3-9: Response amplitude operators computed using Taylor series linearization and statistical linearization in the frequency domain for white noise wave excitation, with significant wave height  $H_s = 0.01$  m and wind speed  $U = 0$  m/s. Thick lines: statistically linearized. Thin lines: Taylor series linearized. Markers: time domain.

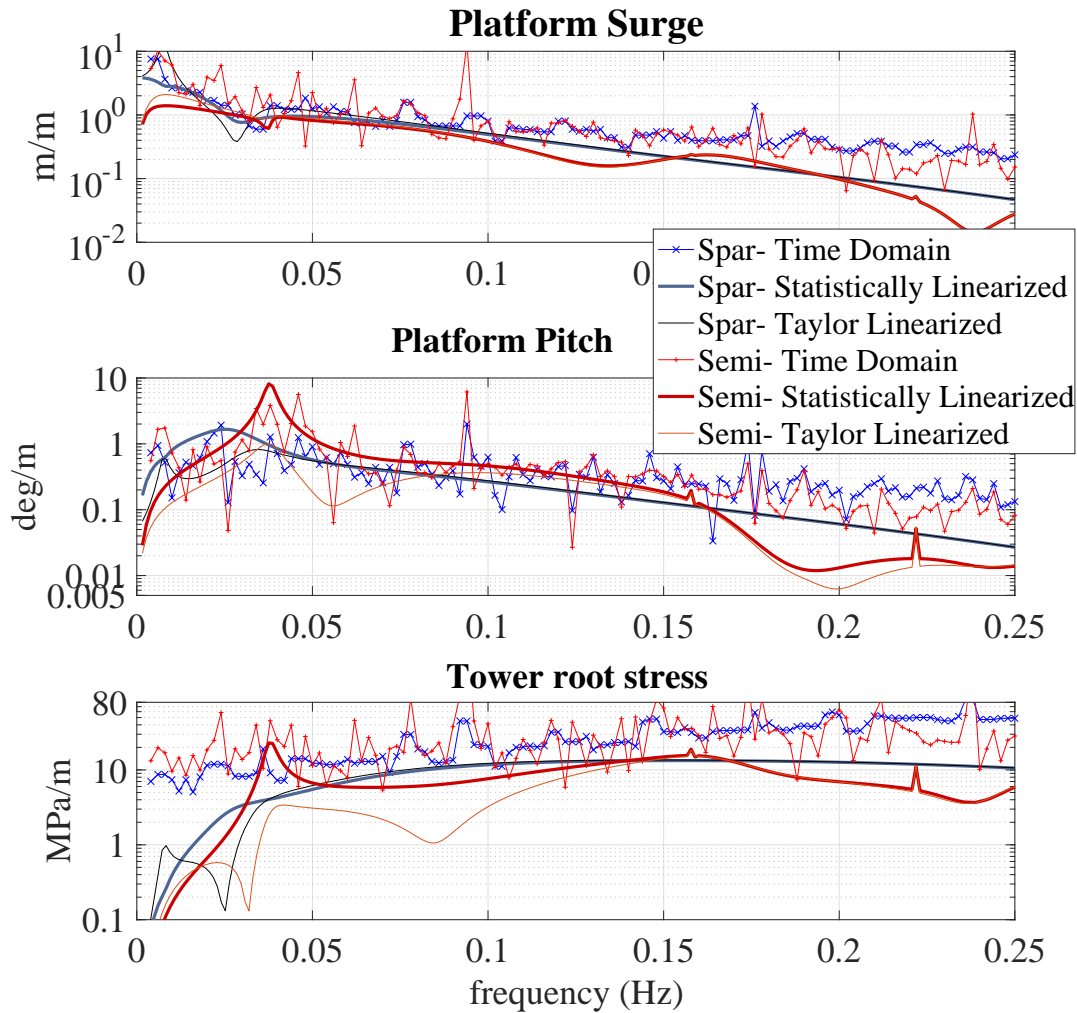


Figure 3-10: Response amplitude operators computed using Taylor series linearization and statistical linearization in the frequency domain for white noise wave excitation, with significant wave height  $H_s = 1$  m and wind speed  $U = 8$  m/s. Thick lines: statistically linearized. Thin lines: Taylor series linearized. Markers: time domain.

### 3.4.2 Computed Statistics

Fig. 3-11 plots the effective fatigue stress, root mean square platform surge, and root mean square platform pitch computed by the different methods for the two platforms in a Bretschneider wind/sea state that has  $H_s = 8$  m,  $T_p = 12.5$  s, and  $U = 0$  m/s. With  $U = 0$  m/s, this plot compares the effects of viscous damping. The spar frequency domain results agree closely, which is expected because a deep-draft platform is less sensitive to

viscous wave forcing near the still waterline (the spar is a more linear system than the semisubmersible). The spar time domain computation estimates a smaller response than the frequency domain computations. For the semisubmersible, the statistical linearization computation estimates a stress that is 15% higher than the Taylor linearized computation and within 1% of the time domain stress. This apparent close agreement is probably a result of statistical linearization computing a smaller platform pitch response and higher stress sensitivity to pitch than both frequency domain approaches.

Fig. 3-12 plots the effective fatigue stress, root mean platform surge, and root mean square platform pitch computed by the three different methods for the two platforms in a Bretschneider wind/sea state with  $H_s = 8$  m,  $T_p = 12.5$  s, and  $U = 8$  m/s. With nonlinear aerodynamics, the statistically linearized computations tend to overpredict responses compared to the time domain while the Taylor series linearized computations tend to underpredict the responses compared to the time domain (with the exception of surge). The wind power and tower stress are more sensitive to pitch than to surge.

In Fig. 13-3, we compute the system lifetime response statistics based on the 22 wind-sea states listed in Table 3.1 for both platforms using the two frequency domain approaches. There is little difference in the wind power computed by the two methods. For both platforms, the statistical linearization approach predicts a lifetime equivalent fatigue stress (EFS) that is 7% larger than the EFS predicted by the frequency domain. Fig. 13-3 shows that in a storm state that occurs during these FWT lifetimes, statistical linearization may predict a much larger surge and pitch response than the Taylor series linearization.

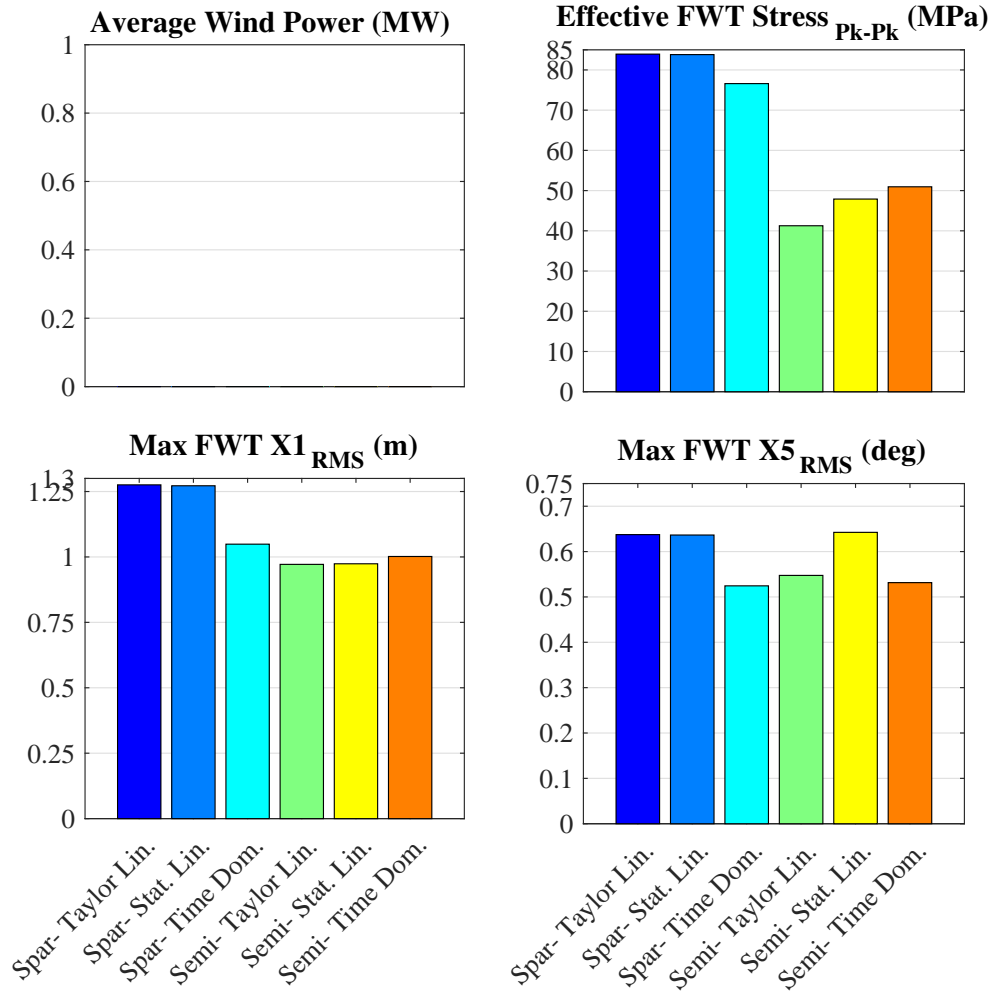


Figure 3-11: Response statistics for the OC3 spar and OC4 semisubmersible computed using Taylor series linearization in the frequency domain, statistical linearization in the frequency domain, and the nonlinear time domain, in a Bretschneider sea state with  $H_s = 8$  m,  $T_p = 12.5$  s,  $U = 0$  m/s.

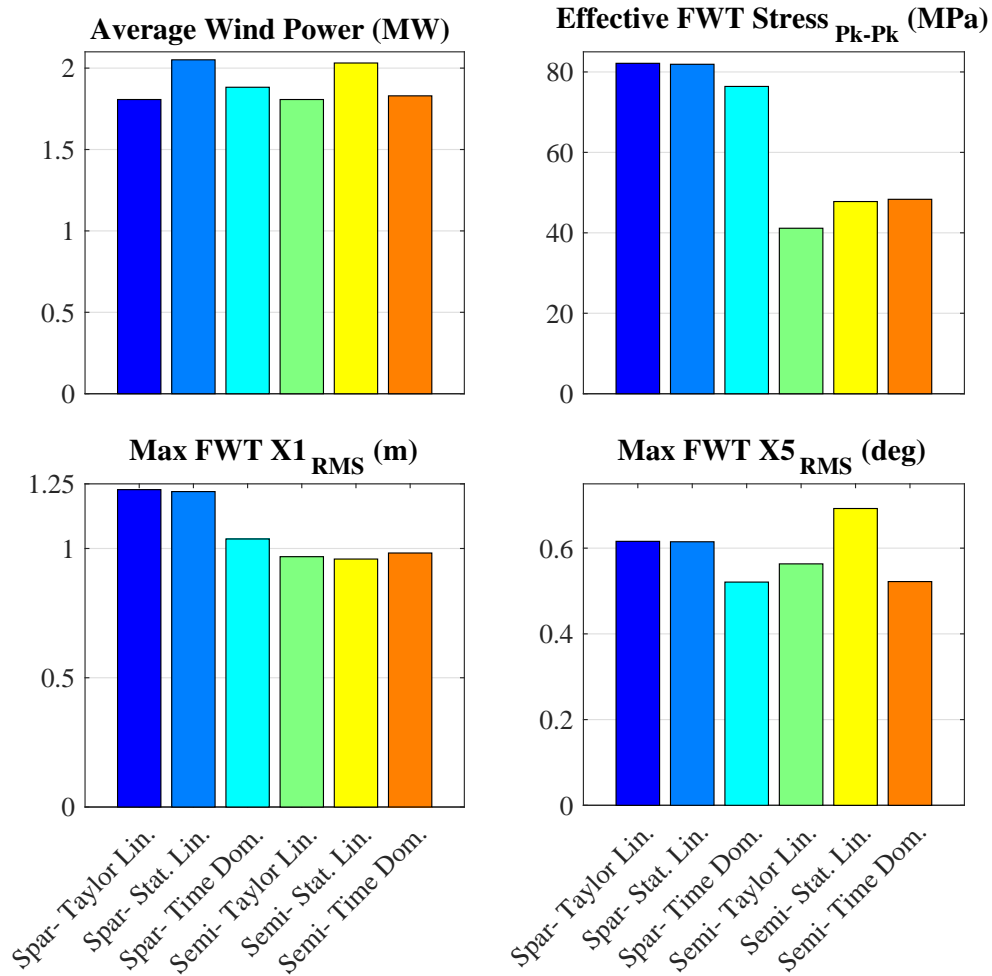


Figure 3-12: Response statistics for the OC3 spar and OC4 semisubmersible computed using Taylor series linearization in the frequency domain, statistical linearization in the frequency domain, and the nonlinear time domain, in a Bretschneider sea state with  $H_s = 8$  m,  $T_p = 12.5$  s,  $U = 8$  m/s.

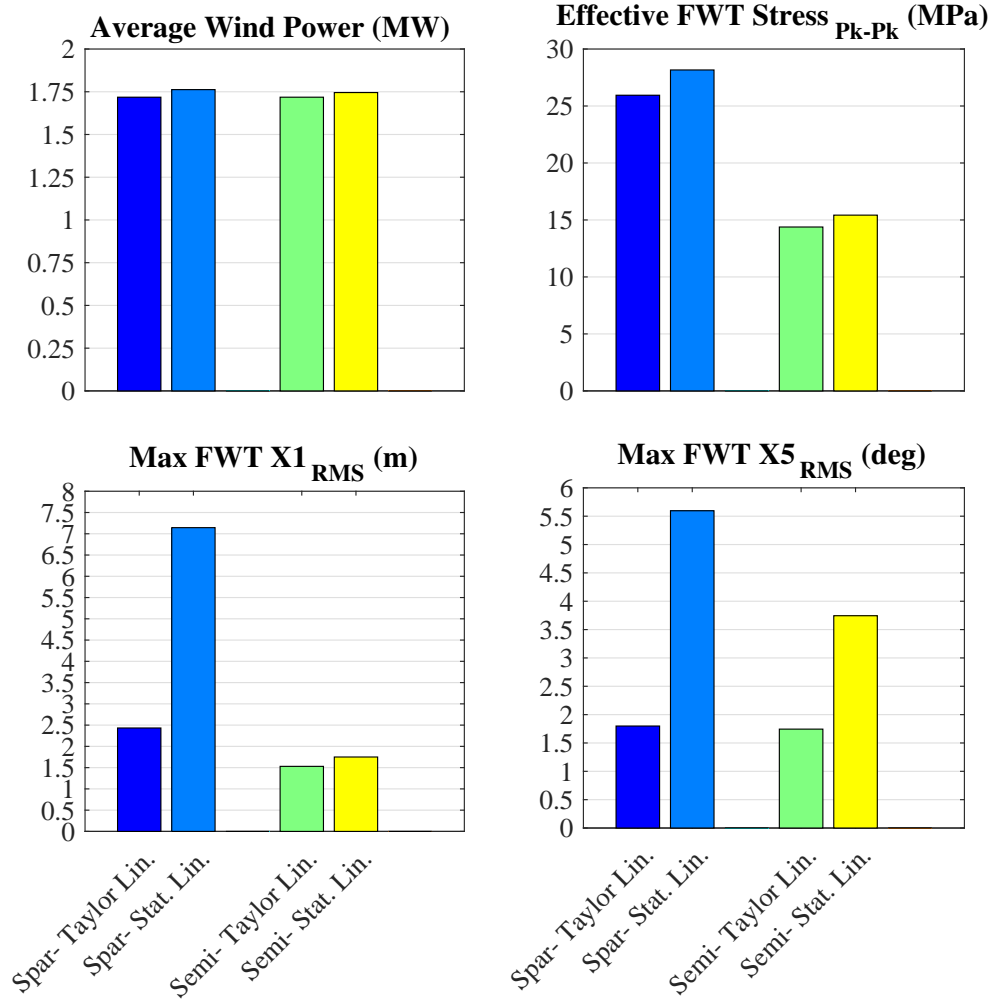


Figure 3-13: Response statistics computed for the OC3 spar and OC4 semisubmersible using Taylor series linearization and statistical linearization in the frequency domain over a 22 wind-sea state lifetime off the coast of Eureka, CA.

Table 3.1: Sea and wind states used in the statistical linearization study that has response statistics plotted in Fig. 3-13. These wind-sea states are based on data from a NOAA buoy 10 NM off the coast of Eureka, CA from 2005-2014.  $H_S$  is the significant wave height,  $T_P$  is the dominant wave period,  $U$  is the mean wind speed, and  $p$  is the state occurrence probability. We model the sea conditions by the Bretschneider spectrum.

State	$H_S$ (m)	$T_P$ (s)	$U$ (m/s)	$p$
1	0.5	31.4	2	$7.1 \times 10^{-3}$
2	0.5	15.7	2	$2.1 \times 10^{-2}$
3	0.5	10.5	2	$1.2 \times 10^{-2}$
4	0.5	7.85	2	$1.3 \times 10^{-2}$
5	1	31.4	4	$4.0 \times 10^{-2}$
6	1	15.7	4	$2.2 \times 10^{-1}$
7	1	10.5	4	$1.7 \times 10^{-1}$
8	1	7.85	4	$9.8 \times 10^{-2}$
9	2.5	31.4	10	$2.9 \times 10^{-2}$
10	2.5	15.7	10	$1.9 \times 10^{-1}$
11	2.5	10.5	10	$9.1 \times 10^{-2}$
12	2.5	7.85	10	$2.7 \times 10^{-2}$
13	4	31.4	16	$8.5 \times 10^{-3}$
14	4	15.7	16	$4.7 \times 10^{-2}$
15	4	10.5	16	$9.5 \times 10^{-3}$
16	4	7.85	16	$1.1 \times 10^{-3}$
17	5	31.4	20	$5.2 \times 10^{-3}$
18	5	15.7	20	$1.2 \times 10^{-2}$
19	5	10.5	20	$1.5 \times 10^{-3}$
20	5	7.85	20	$5.0 \times 10^{-5}$
21	6	31.4	24	$6.6 \times 10^{-5}$
22	6	15.7	24	$5.0 \times 10^{-5}$





# Chapter 4

## Dynamics of a Wave Energy Converter with Cubic Nonlinear Hydrostatic Stiffness

### 4.1 Introduction

In this chapter, we consider the design of a nonlinear heave-mode hydrostatic stiffness, that may increase the WEC's ability to absorb power when excited by different wave frequencies, resulting in more power generation in a given sea state and more power robustness over many sea states. While WEC parameter control will still be required in a real machine, this nonlinearity may reduce the required control and associated parasitic losses and complexities.

As described in the Introduction chapter of this thesis, one of the main challenges for WEC design is how to maintain good power performance in different sea states. Typical uncontrolled linear WEC motion and power both decay when the ocean wave dominant frequency differs from the WEC resonant frequency.

Many different approaches have been considered for increasing WEC power robustness in different sea states. In the WEC industry, these approaches include,

1. An inertial trapping, to adjust the oscillating mass (and corresponding natural fre-

- quency) in different sea states [52],
2. Rigidly connecting or disconnecting a light floating mass from a submerged heavier mass, allowing the WEC to have two distinct natural frequencies [45]
  3. Varying the distribution of mass and length in a pendulum [53],
  4. Varying the tension in a taut mooring line [51],
  5. Controlling the generator power takeoff to produce reactive power that acts a like a spring [112],
  6. Using latching to hold and release the oscillating mass so that the wave force and WEC velocity remain in-phase, the condition for maximum power extraction that occurs when a system resonates [12], [43], [42].

Another robustness mechanism that has been studied in other environmental vibration energy applications, but has not yet been extensively applied to wave energy harvesting, is using a nonlinear spring. Essentially nonlinear springs (that is nonlinear springs without linear stiffness components) do not have preferential linear frequencies. Therefore, they are more robust to variations in the external excitation and preserve their good performance level for a wide range of conditions, as described in Vakakis et al. [141], Gendelman et al. [48], Sapsis et al. [120], and Quinn et al. [110]. We investigated the improved robustness of a nonlinear human walking vibration energy harvester in [78, 80]. Fig. 4-1, reproduced from [111], illustrates how introducing a cubic nonlinearity into an oscillator can increase its response bandwidth.

A nonlinear spring may be physically realized in many different ways. One way to implement a nonlinear cubic spring is for linear springs to support a proof mass at various angles to its direction of travel, so that the springs have to increasingly stretch for increasing transverse displacements of the mass. MacFarland et al. [97] investigates this configuration using piano wire while Hajati et al. [56] investigates it with a doubly-clamped beam. Kantor and Afanas'eva [74] expand this principle to a clamped circular plate with variable thickness along its radius.

Another way to implement a nonlinear spring is for the flexure to effectively increase in thickness as the spring deflects. Freeman [46] does this by designing helical springs with thickening coil wires and changing overall spring diameters. In leaf springs of automobile suspensions, several layers of arc-shaped spring steel are clamped together. As the center of the upper arc deflects, it contacts the arc below it, and both springs further deflect in contact. As more and more arcs deflect, the spring effectively stiffens [46].

We have studied nonlinear springs implemented by beams that increasingly contact curved rigid surface as they deflect. This shortens the effective beam length and causes it to stiffen [81, 82, 83].

These structural implementations of a nonlinear spring may be useful for future WEC studies, when the WEC reacts against a second body.

In this chapter, we consider another type of cubic nonlinear spring that can be used for improved WEC power performance. We physically implement this spring by a varying WEC cross section, so that as the WEC displaces, its cross-section at the still waterline increases, and therefore its heave hydrostatic stiffness increases. We describe the dynamics model of this nonlinear WEC in Section 4.3. In Section 4.4, we describe how the non-linearity may be statistically linearized in WEC response computations. In Chapter 6, we optimize the nonlinear wave energy converter (WEC) parameters for power performance. Section 6.4.3 shows the optimization plots. Section 6.4.4 compares the nonlinear WEC performance statistics and response amplitude operators to optimized linear WEC's. Future work on this project will be to experimentally verify the computed performance.

## 4.2 Cubic Stiffness Design

Our cubic-stiffness heave-mode wave energy converter with a floating oscillating water column chamber is shown in Fig. 4-2. The nonlinear hydrostatic stiffness is physically implemented by an increasing radius,  $R_{Out}$ , in both the positive and negative  $z$  directions away from the equilibrium still water line location on the WEC.

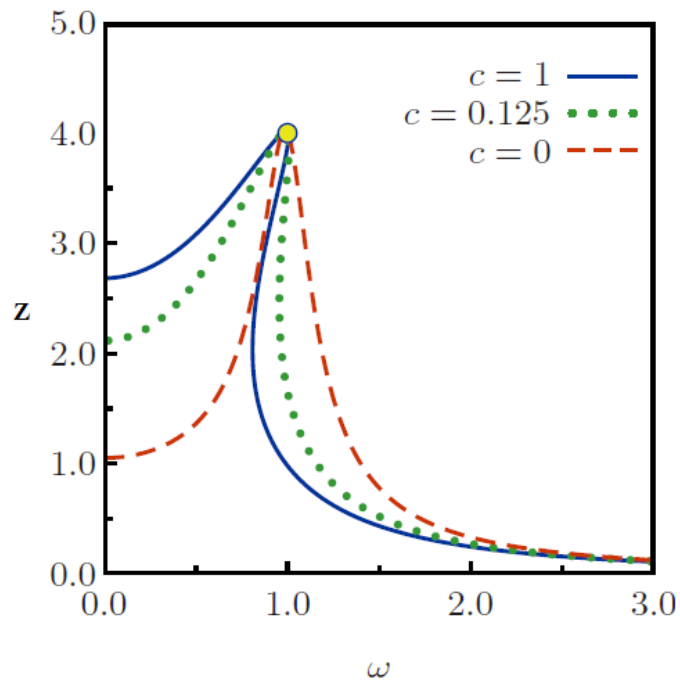


Figure 4-1: Steady state amplitude responses of a single degree of freedom oscillator with the governing equation,  $\ddot{z} + b\dot{z} + \alpha((1 - c)z + cz^3) = F\cos(\omega t)$ . The red curve is the linear system response, the blue curve is the essentially nonlinear system response, and the green curve is a weakly nonlinear system response. Image and analysis from Quinn et al., 2011 [111].

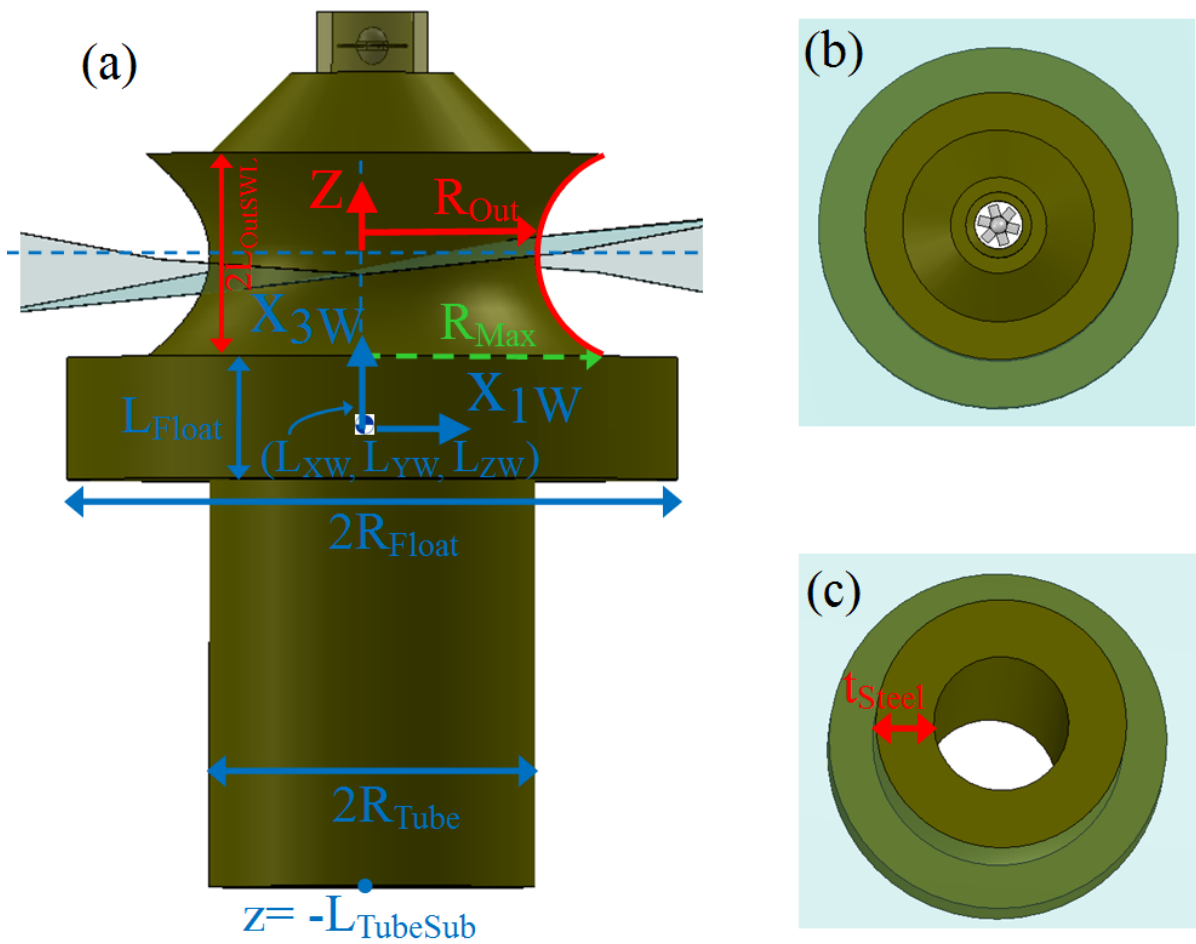


Figure 4-2: Diagram of a spar oscillating water column with a cubic nonlinear hydrostatic stiffness: (a) side view, (b) top view with air Wells turbine, (c) top view with hidden Wells turbine and air chamber top.

The net instantaneous heave-mode buoyancy force on the WEC is,

$$F_{Hydro,3Net} = \rho g V_{SubWEC} - m_W g. \quad (4.1)$$

At equilibrium, the buoyancy and gravity forces cancel out, leaving,

$$F_{Hydro,3Net} = \rho g \Delta V_{SubWEC}, \quad (4.2)$$

where  $\rho$  is the water density,  $g = 9.81 \text{ m/s}^2$  is gravitational acceleration,  $\Delta V_{SubWEC}$  is the additional submerged volume compared to equilibrium. When the WEC travels downwards (or upwards), the submerged volume increases and the hydrostatic force pushes upwards (or pulls downwards). The change in submerged volume is,

$$\Delta V_{SubWEC} = \int_0^{-\zeta_3} A(z) dz, \quad (4.3)$$

where  $z$  is the fixed coordinate along the WEC,  $\zeta_3$  is the WEC heave displacement upwards, and  $A(z)$  is the WEC cross-sectional area.

Instantaneous hydrostatic stiffness is defined as,

$$C_{33Inst} = \frac{-\partial F_{Hydro,3Net}}{\partial \zeta_3}. \quad (4.4)$$

Substituting Eq.s 4.2 and 4.3 into Eq. 4.4,

$$C_{33Inst} = \rho g A(z). \quad (4.5)$$

We decompose the cross-sectional areas and corresponding hydrostatic stiffnesses each into a linear and nonlinear component,

$$A(z) = A_{Tube} + A_{Additional}(z), \quad (4.6)$$

$$C_{33Inst} = C_{33Lin} + C_{33Non} z^2. \quad (4.7)$$

The tube cross-section at the still waterline generates the linear hydrostatic stiffness,

$$C_{33Lin} = \rho g A_{Tube} = 2\rho g \pi r_{Tube} t_{Steel}, \quad (4.8)$$

where  $r_{Tube}$  is the tube mean radius and  $t_{Steel}$  is the tube steel thickness.

For the additional cubic hydrostatic stiffness,  $C_{33Non}$ , the cross-sectional area needs to increase proportionally to  $z^2$ ,

$$A_{Additional}(z) = \frac{C_{33Non}}{\rho g} z^2. \quad (4.9)$$

Increasing the radius dimension beyond the linear tube radius contributes to an additional area,

$$A_{Additional} = \pi (R_{Out}(z))^2 - \pi r_{Tube}^2, \quad (4.10)$$

where  $R_{Out}$  is the an casing encircling the tube.

Equating Eq. 4.9 and 4.10,

$$\frac{C_{33Non}}{\rho g} z^2 = \pi R_{Out}^2 - \pi r_{Tube}^2. \quad (4.11)$$

Rearranging Eq. 4.11, the required  $R_{Out}$  is,

$$R_{Out} = \sqrt{\frac{C_{33Non}}{\rho g \pi} z^2 + r_{Tube}^2}. \quad (4.12)$$

That is, the cross-sectional area increases proportionally to  $z^2$ , and the radius increases approximately linearly with  $z$ .

Other nonlinearities besides a cubic stiffness can be implemented. By a similar derivation as above, a fourth order nonlinear spring stiffness of the form,

$$F_{non4} = C_{N4} z^4, \quad (4.13)$$

may be implemented by an outer radius that varies according to,

$$R_{Out4} = \sqrt{\frac{C_{N4}}{\rho g \pi} z^3 + r_{Tube}^2}. \quad (4.14)$$

### 4.3 Dynamics Model

The governing dynamics of this WEC are similar to those of a linear spar-shaped WEC with a constant cross-section and hydrostatic stiffness, as described in Section 2.4.3. The main difference between the two WECs' equations of motion is the cubic nonlinear spring stiffness in the heave-mode equation. Smaller differences arise in the surge and sway equations of motion due to the varied frontal area seen by waves.

We consider 5 degrees of freedom for the WEC,

$$\vec{x}_{WEC} = \begin{bmatrix} x_{WEC} \\ y_{WEC} \\ z_{WEC} \\ z_{Col} \\ p_C \end{bmatrix} = \begin{bmatrix} \text{WEC surge} \\ \text{WEC sway} \\ \text{WEC heave} \\ \text{Vertical water column heave relative to WEC} \\ \text{Vertical water column chamber pressure} \end{bmatrix}. \quad (4.15)$$

The coupled equations of motion are,

$$\begin{bmatrix} (m_W + A_{11,W}) \ddot{x}_{WEC} + B_{11,W} \dot{x}_{WEC} & = & F_{1,WEC} \\ (m_W + A_{22,W}) \ddot{y}_{WEC} + B_{22,W} \dot{y}_{WEC} & = & 0 \\ (m_W + A_{33,W}) \ddot{x}_{3,W} + B_{33,W} \dot{x}_{3,W} + C_{33n} x_{3,W}^3 & = & F_{3,WEC} + P_C A_{ColZ} \\ P_C + \frac{I_{ZCol}}{A_{ColZ}} (\ddot{z}_{WEC} + \ddot{z}_{Col}) + \frac{B_{33,Col}}{A_{ColZ}} (\dot{z}_{WEC} + \dot{z}_{Col}) + \rho g (z_{WEC} + z_{Col}) & = & \frac{F_{3,Wave,Col}}{A_{ColZ}} \\ p_C + \frac{k_{Wells} V_{Air}}{\gamma P_{Atm}} \dot{p}_C - k_{Wells} A_{Col} \dot{z}_{Col} & = & 0 \end{bmatrix}. \quad (4.16)$$

The equations of motion and parameter definitions are identical to those in Sections 2.4 and 2.4.3 except for the 3rd row, which is the governing equation of the WEC heave motion and is now nonlinear.



Other differences between to the spar parameters are that Eq. 2.60 becomes,

$$V_{SubSWL} = \int_{-L_{OutSWL}}^0 \pi (R_{Out}^2 - r_{Tube}^2) dz. \quad (4.17)$$

Eq. 2.69 becomes,

$$S_{ASWL} = \int_{-L_{OutSWL}}^{L_{OutSWL}} 2\pi R_{Out} dz + 2\pi r_{OutSWLMax}^2 - \pi r_{Tube}^2, \quad (4.18)$$

where the maximum radius of the SWL modification is,

$$r_{OutSWLMax} = \left( \sqrt{\frac{C_{33Non}}{\rho g \pi} z^2 + r_{Tube}^2} \right) \Big|_{z=L_{OutSWL}}, \quad (4.19)$$

which accounts for the outer side, top, and bottom.

## 4.4 Statistical Linearization of the Cubic Nonlinear Hydrostatic Stiffness

As derived in Roberts and Spanos,(1999) [116], the nonlinear spring force,

$$g(x) = -C_{33n} x_{3,W}^3, \quad (4.20)$$

results in the statistically equivalent stiffness,

$$C_{Eq,33n} = E \left\{ \frac{-\partial g(x)}{\partial x_{3,W}} \right\} = 3C_{33n} \sigma_{x_{3,W}}^2, \quad (4.21)$$

where  $\sigma_{x_{3,W}}$  is the standard deviation of the WEC heave displacement, found using the Weiner Khinchine theorem and statistical linearization procedures described in Sections 2.9 and 3.2 for a WEC excited by an ocean wave spectrum.

In Chapter 6, we use this statistical linearization procedure to optimize the nonlinear wave energy converter (WEC) parameters for power performance. Section 6.4.3 shows the optimization plots. Section 6.4.4 compares the nonlinear WEC performance statistics and

response amplitude operators to linear WEC's. Future work on this project will include experimentally verifying the computed performance.

# Chapter 5

## Cost Model

### 5.1 Introduction

As mentioned in the Introduction chapter, one of the main goals of this thesis is to reduce the wave energy converter's levelized cost of energy (WEC LCOE), or average dollars per kWh. The LCOE is a useful normalizer for comparing the costs of different electricity sources. The cost models in the Sandia National Laboratory report [102] are intentionally kept basic for the purpose of transparency. We follow that approach here because our goal is to identify significant energy cost effects correlated to the dynamics effects. We also emphasize that as basic as this cost model is, it shows relative cost improvements among the different WEC's considered in this thesis.

We calculate the WEC LCOE as [134],

$$LCOE_{WEC} = \frac{(ICC_{WEC})(FCR) + AOE_{WEC}}{AEP_{WEC}}. \quad (5.1)$$

The LCOE accounts for the average machine installed capital cost  $ICC$ , fixed charge rate  $FCR$ , annual operation expenses  $AOE$ , and annual energy production  $AEP$ .

In this thesis, we base the WEC capital cost on the cost models described in Sandia National Laboratory reports, which break down the capital cost into different project components [102, 143]. These project component costs correspond to a 100-unit array and are proportional to the machine power capacity. We eliminate costs associated with the moor-

ing lines and infrastructure (maintenance facilities and vessels). We modify the WEC steel cost to correspond to the amount of steel in each of our computed WEC designs. We assume a typical fixed charge rate. We determine uncertainties in some of the cost parameters, and compute high and low cost estimates for the *ICC* and *LCOE*.

## 5.2 Capital Cost

We base our installed capital cost (*ICC*) model on the Sandia National Laboratory and national Renewable Energy Laboratory (NREL) cost models of WEC's that are part of a 100-unit (36 MW) array [143, 102].

Fig. 5-1 shows the *ICC* for two reference WEC's analyzed by Sandia National Laboratory [15], [143], [102]. One reference WEC is a surge-mode flap with a power capacity of 360 kW, *ICC* = \$5.0M, and *LCOE* = \$0.69/kWh. The other reference WEC is a heave-mode point absorber that slides along an axis attached to a floating reaction plate, which has a power capacity of 286 kW, *ICC* = \$3.9M, and *LCOE* = \$0.76. The point absorber higher costs are due to a similar capital cost but lower power production.

As shown in Fig. 5-1, the average *ICC* breakdown for these WEC's (in order of decreasing contribution) is the structural components (46%), mooring lines (14%), installation cost (9%), power conversion chain (9%), contingency costs (8%), infrastructure (electric cables, and docks and ships for maintenance; 5.8%), subsystem integration and profit margin (5.4%), permitting and environmental compliance (1.5%), project design and management (1.3%), and site assessment (0.1%).

This thesis investigates changes to the WEC structural components, power conversion chain, mooring lines, and infrastructure, which comprise 74.8% of the standalone WEC cost. We assume that all of the other cost components remain the same, and use their average cost per kWh values from the reference flap and point absorber. That is, we assume the design and engineering costs, site assessment, permitting and environmental compliance, installation, subsystem integration, and contingency costs are \$3469/kW. We remove the costs of mooring lines and infrastructure from our WEC because our WEC does not have its own mooring lines, and it shares cables and maintenance ships/dockside facilities with the

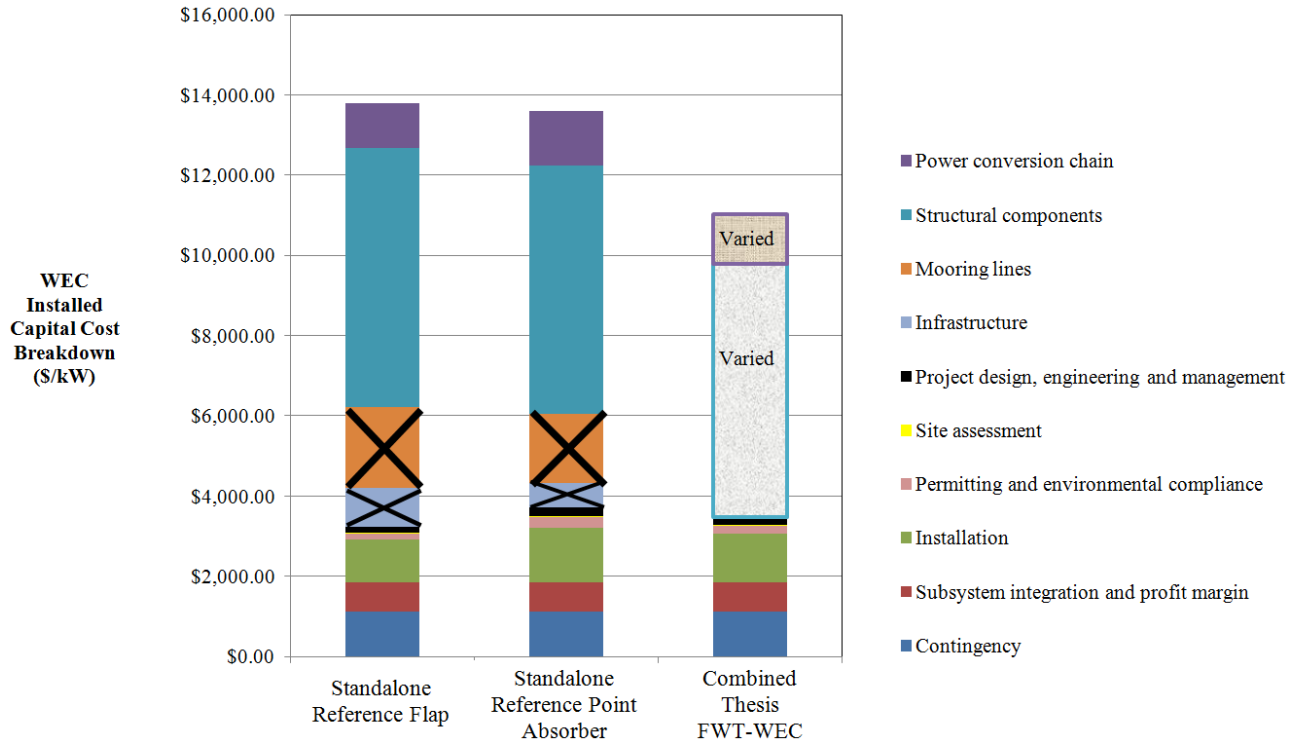


Figure 5-1: Installed Capital Cost Model based on Sandia National Laboratory flap and point absorber WEC references.

floating wind turbine (FWT). Significantly, this equates to an immediate *ICC* cost reduction of  $\$2688/kW$  (19%). Additional cost savings are achieved by eliminating a reaction frame structure, as long as added linkage steel is small.

We model the structure costs in Section 5.2.1, and we model the power conversion chain costs in Section 5.2.2.

### 5.2.1 Structure Costs

We consider the costs of steel and concrete in the WEC, links connecting the WEC and FWT, and a ballast used to stabilize the FWT. We base the WEC structural cost predictions on two different WEC's described in Sandia National Laboratory studies. One WEC is a 300 kW capacity, 2,025 ton backwards bent duct buoy (L-shaped) floating oscillating water column [15]. The other WEC is the 286 kW capacity, 208 ton point absorber float sliding along a 470 ton floating column track and reaction plate [102].

The reference WEC's use A36 steel plates with stiffener bars [15, 102]. The plate thickness, stiffener bar separation and size (along the vertical structure direction), and girder separation and size (along the horizontal structure direction) are chosen to satisfy a safety factor in stress during a predicted severe storm load. A severe storm load is conservatively modeled as the hydrostatic pressure from a 6 m high wave in addition to a 19 m submergence.

[15] and [26] ascertain that the backwards bent duct buoy requires a plate thickness of 1.6 cm, stiffeners of  $0.0048 \text{ m}^2$  cross-sectional area spaced 0.75 m apart, and girders of  $0.0032 \text{ m}^2$  cross-sectional area spaced 1.97 m apart. The assembly mass distribution is approximately equivalent to a steel sheet with 0.0344 m thickness. The system has an internal bulkhead wall in the middle of the 27 m wide chamber with an equivalent 0.047 m thickness.

By similar calculation, [102] suggests that a floating toroid with a 20 m outer diameter, 6 m inner diameter, and height of 5.2 m has an equivalent steel plate thickness of 0.0232 m. The float is filled with concrete ballast to satisfy buoyancy stabilization.

In this thesis, we assume a steel thickness of  $0.0288 \pm 0.0056$  m, which is the average effective thickness of the backwards bent duct buoy and and point absorber toroid. We assume that all additional required WEC mass is made up by concrete ballast, which has a cost of \$0.10/Kg, much lower than steel.

For the steel links connecting the FWT and WEC, we assume that the link must maintain a safety factor in stress,  $S.F. = 2$  when subject to the force at the still water level from an incident of amplitude  $a_{max} = 6$  m. This force magnitude is,

$$F_{1Max} = -(\rho V_{SubWEC} + A_{11WEC})a_{max}g, \quad (5.2)$$

where  $\rho$  is the water density,  $g$  is gravitational acceleration,  $V_{SubWEC}$  is the submerged volume,  $A_{11WEC}$  is the surge added mass, and  $k$  is the wave number. We compute  $V_{SubWEC}$  and  $A_{11WEC}$  using the model described in Chapter 2.

The axial stress along the link,  $\sigma$ , must satisfy,

$$\sigma = \frac{F_{1Max}}{A} \leq \frac{\sigma_Y}{S.F.} \longrightarrow A = \frac{(S.F.)F_{1Max}}{\sigma_Y}, \quad (5.3)$$

where we assume a steel yield stress of  $\sigma_Y = 250$  MPa and  $A$  is the link cross-sectional area. We use the minimum allowable  $A$  to minimize cost. The link length corresponds to the center-center distance from the FWT to the WEC.

For the link and WEC body steel, we assume that the steel material costs of  $\$1.32 \pm 0.47/\text{Kg}$  multiplied by a manufacturing factor of  $2 \pm 1$ , based on cost modeling assumptions in [100, 102].

We assume a concrete cost of  $\$0.10 \pm \$0.05/\text{Kg}$  [24]. Most academic studies on offshore wind turbines and wave energy converters neglect the cost of concrete ballast compared to steel [100, 143]. The NREL OC3-Hywind floating wind turbine platform uses 1700 tons of steel and 5700 tons of concrete, which results in an estimated steel cost of \$22.4 million and concrete cost of \$570 thousand [66, 100]. That is, the concrete costs approximately 2% of the steel cost. The concrete cost of  $\$0.10 \pm \$0.05/\text{Kg}$  is a negligible cost, especially considering the steel cost uncertainty of  $\$ \pm 0.47/\text{Kg}$ . It may or may not have a significant effect on the final FWT or WEC cost. A potential substitution of fly ash for concrete ballast may be a synergistic use of the coal waste product that reduces the \$570 thousand ballast cost of a 5 MW floating wind turbine platform.

## 5.2.2 Power Takeoff Costs

This thesis considers WEC's that use air Wells turbine power takeoffs, hydrokinetic Wells turbine power takeoffs, and hydraulic junction power takeoffs.

We estimate costs for an air Wells turbine using the model described in the Sandia report, [15]. Most of the cost for the power conversion chain is due to fabricated circular parts ( $\$1,100/\text{kW}$ ) followed by fabricated rectangular components ( $\$300/\text{kWh}$ ). For a 100-unit array, the total air Wells turbine power conversion chain has a cost of  $\$1550/\text{kW}$ .

The Sandia report [102] estimates that a tidal current power takeoff mechanism costs  $\$1400/\text{kW}$ , and a river current power takeoff mechanism costs  $\$1750/\text{kW}$ . The average cost

of these is \$1575.

The NREL report [143] describes the costs of a hydraulic power conversion chain. For a 100-unit array, a hydraulic power conversion chain has a cost of \$1500/kW, which is with 3% of the air Wells turbine cost. The main components that comprise this cost are 28% for the reservoir, 21% for the hydraulic cylinders, 16% for plumbing, and 15% for high pressure accumulators [143].

We use a cost of  $\$1550 \pm 150/kW$  for the air turbine, water turbine, and hydraulic power takeoff.

### 5.3 Fixed Charge Rate

We assume a fixed charge rate,

$$FCR = 0.117 \pm 0.02, \quad (5.4)$$

which accounts for the annual average cost of financing for the return on debt, return on equity, taxes, depreciation, and insurance, as a percent of the capital cost. This is the typical cost for offshore renewable energy projects [134].

### 5.4 Annual Energy Production

We calculate the WEC annual energy production from its power output in each sea state,  $\bar{P}_{wi}$ , the occurrence frequency of each sea state,  $p_i$ , and the number of hours in a year,

$$AEP_{WEC,kW} = \left( \sum_{\text{State } i} p_i \bar{P}_{wi} \right) 8766 \frac{\text{hours}}{\text{year}}. \quad (5.5)$$

### 5.5 Annual Operating Expenses

Operating costs during the project lifetime consist of environmental monitoring, insurance, consumables, replacement parts, shoreside operations, and marine operations. The Sandia



point absorber has  $AOE = \$211/kW$  while the flap surge converter has  $AOE = \$222/kW$ , both for a 100-unit array [102, 143]. We use the mean value,

$$AOE_{WEC} = \$215/kW. \quad (5.6)$$

## 5.6 Final Cost Equation and Uncertainty

Summarizing the above model, we estimate the WEC installed capital cost as,

$$ICC_{WEC, \$} = (3470 + 1550)P_{Cap, kW} + 1.32(C.F.)M_{Steel, Kg} + 0.10M_{Concrete, Kg}, \quad (5.7)$$

The parameters of this equation are listed in Table 5.1.

The Sandia reports give their LCOE models a  $\pm 30\%$  uncertainty range. This high uncertainty is due to many machines not being fully implemented before. [15] assigns high uncertainty to the cost of infrastructure (dock and vessel for maintenance), structural components, installation, and contingency. [15] assigns low uncertainty to the cost of the mooring and power conversion chain. We assign uncertainties to the different components based on [26, 15, 100, 102], and compute cost uncertainty during the parameter optimization. We emphasize that the level of uncertainty in the combined FWT-WEC cost is similar to the level of uncertainty in the Sandia cost models. Even though there may be high uncertainty in the exact cost, any significant reduction in the WEC mooring, infrastructure, and structure costs will certainly have a significant relative cost reduction compared to the standalone machines.

Table 5.1: WEC cost model parameters

<b>Parameter</b>	<b>Assumed value</b>	<b>Uncertainty considered</b>
Steel thickness	0.0288 m	±0.006 m
Link cross-sectional area	$(S.F.)F_{1Max}/250e6 m^2$	-
Link arm safety factor in stress, <i>S.F.</i>	2	+1
Steel density	7800Kg/m <sup>3</sup>	-
Raw steel material cost, 100-unit	\$1.32/Kg	±\$0.47
Concrete density	2400Kg/m <sup>3</sup>	-
Concrete cost	\$0.10/Kg	±\$0.05/Kg
manufacturing complexity factor, <i>C.F.</i>	2	±1
Air Wells turbine	\$1550/kW	±\$150/kW
Water Wells turbine	\$1550/kW	±\$150/kW
Junction hydraulic power takeoff	\$1550/kW	±\$150/kW
Fixed charge rate, <i>FCR</i>	0.117	±0.02
Annual operating expenses, <i>AOE</i>	\$215/kW	-

# Chapter 6

## System Optimization Under Stochastic Conditions

### 6.1 Introduction

As described in the Introduction of this thesis, the optimal design of a combined floating wind turbine- wave energy converter (FWT-WEC) will,

1. Decrease the nacelle motion. Nacelle motion reduces wind turbine efficiency.
2. Decrease tower root stress. Reducing the tower stress increases the factor of safety in stress.
3. Minimize the WEC levelized cost of energy. This is accomplished by minimizing the WEC cost (a function of the power takeoff capacity and material mass) while maximizing the WEC power efficiency.

Regarding items 1 and 2, if a FWT-WEC design reduces the OC3-Hywind nacelle motion and tower stress, then one could reduce the platform and tower material. This could reduce FWT cost while maintaining the same wind power efficiency and safety factor in stress as the original standalone FWT.

To investigate how well different FWT-WEC configurations accomplish these 3 design criteria, we vary the system parameters and compute the performance statistics over a 20-

year lifetime using the dynamics and cost models described in Chapters 2-5. We model the environment by the 3 wind-sea states listed in Table 6.1.

The various statistics we consider include the platform maximum root mean square surge  $X_{1RMS}$ , heave  $X_{3RMS}$ , and pitch  $X_{5,RMS}$  motions among the 3 sea states, and the tower equivalent lifetime stress. We also consider the WEC capital cost, average power, and levelized cost of energy.

We consider the following configurations:

1. Ideal hydrokinetic turbine and mass inertia elements, rigidly attached to the FWT in Section 6.2. We vary the damping and inertia magnitudes, and submergence depths. These results indicate what general effects WEC or ballast placement has on the FWT.
2. Ideal linear WEC's, including internal tuned mass dampers (TMD) and external spherically-shaped linear WEC's in Section 6.3. We constrain the WEC to have a mass of 500 tons (reducing the FWT ballast to maintain neutral buoyancy for the internal TMD). We vary the energy-harvesting mode (surge or heave), power take-off location (an ideal horizontal axis hydrokinetic Wells turbine in the WEC, ideal vertical axis hydrokinetic Wells turbine in the WEC, or ideal junction power takeoff mechanism). The only connection between the FWT and WEC is a junction spring in the WEC energy-harvesting direction that is tuned for maximized WEC motion in each sea state.
3. Linear heave-mode oscillating water column (OWC) that is rigidly attached to the FWT in Section 6.4.1. The water column is the only WEC degree of freedom that is not rigidly connected to the FWT.
4. Linear heave-mode floating oscillating water columns (FOWC's) attached by hinges to the FWT in Section 6.4.2.
5. Nonlinear heave-mode FOWC's attached by hinges to the FWT in Section 6.4.2. The nonlinearity is a nonlinear hydrostatic stiffness, implemented by a varied cross-section, as described in Chapter 4.

6. Multiple WEC’s attached to the FWT in Section 6.4.5. We consider arrays of the nonlinear FOWC with the best performance.

We compare the water column system performance in Section 6.4.4. Table 8.1 in the Conclusion chapter summarizes and compares the optimal performance of all the WEC types.

### 6.1.1 Common constraints for all computations

We compute the average system responses over a simplified 20-year lifetime that consists of 3 wind and sea states, listed in Table 6.1. We make this simplification to reduce the computation time on the standard laptop computer used for this thesis. WEC optimization is typically site-specific. An expansion of this work would include an optimization of the systems over many site-specific wind-sea states.

Table 6.1: Basic sea and wind state distribution loosely based on Eureka, CA NOAA buoy data.  $H_S$  is the significant wave height,  $T_P$  is the dominant wave period,  $U$  is the mean wind speed, and  $p$  is the state occurrence probability. We model the sea conditions by the Bretschneider spectrum.

State	$H_S$ (m)	$T_P$ (s)	$U$ (m/s)	$p$
1	3	8	8	0.33
2	3	11	16	0.33
3	3	16	20	0.33

We restrict the WEC masses to be less than or equal to approximately 500 tons, which is similar to the National Renewable Energy Laboratory reference WEC’s [102, 143]. The WEC’s are made neutrally buoyant by adding concrete ballast.

We constrain all of the WEC’s to have a capacity factor of at least 30% by reducing the power in stormy sea states to match the power in less stormy sea states. For an air Wells turbine, this could be accomplished by using a bypass relief valve [41].

We consider the National Renewable Energy Laboratory reference OC3-Hywind spar and wind turbine [66].

## 6.2 Ideal Hydrokinetic and Mass Inertia Elements Rigidly Attached to FWT

Fig. 6-1 shows the effects of attaching an external cylindrical ballast with varied outer radius and submergence to the FWT spar. In general, larger radii increase the platform surge, heave, and pitch response. Increasing the submergence depth beyond 20 m increases the platform surge and pitch- and aligns their phase so that tower stress is increased. A submergence depth of 20 m minimizes the FWT motion and stress. This submergence depth corresponds to the point where the difference, [platform lateral motion] – [wave lateral motion], is maximized, so that the cylinder has a larger damping effect than wave forcing effect.

Fig. 6-2 shows the effects of attaching a massless hydrokinetic Wells turbine with varied effective damping and submergence to the FWT spar. A Wells turbine with large damping generally increases the platform motion when it is submerged beyond 70 m and decreases platform motion when it is submerged less than 70 m. The platform metacenter and center of buoyancy is at  $z = -62$  m. The platform center of mass is at  $z = -78$  m. Placing the Wells turbine below the center of mass causes inverted-pendulum behavior and decreases platform stability.

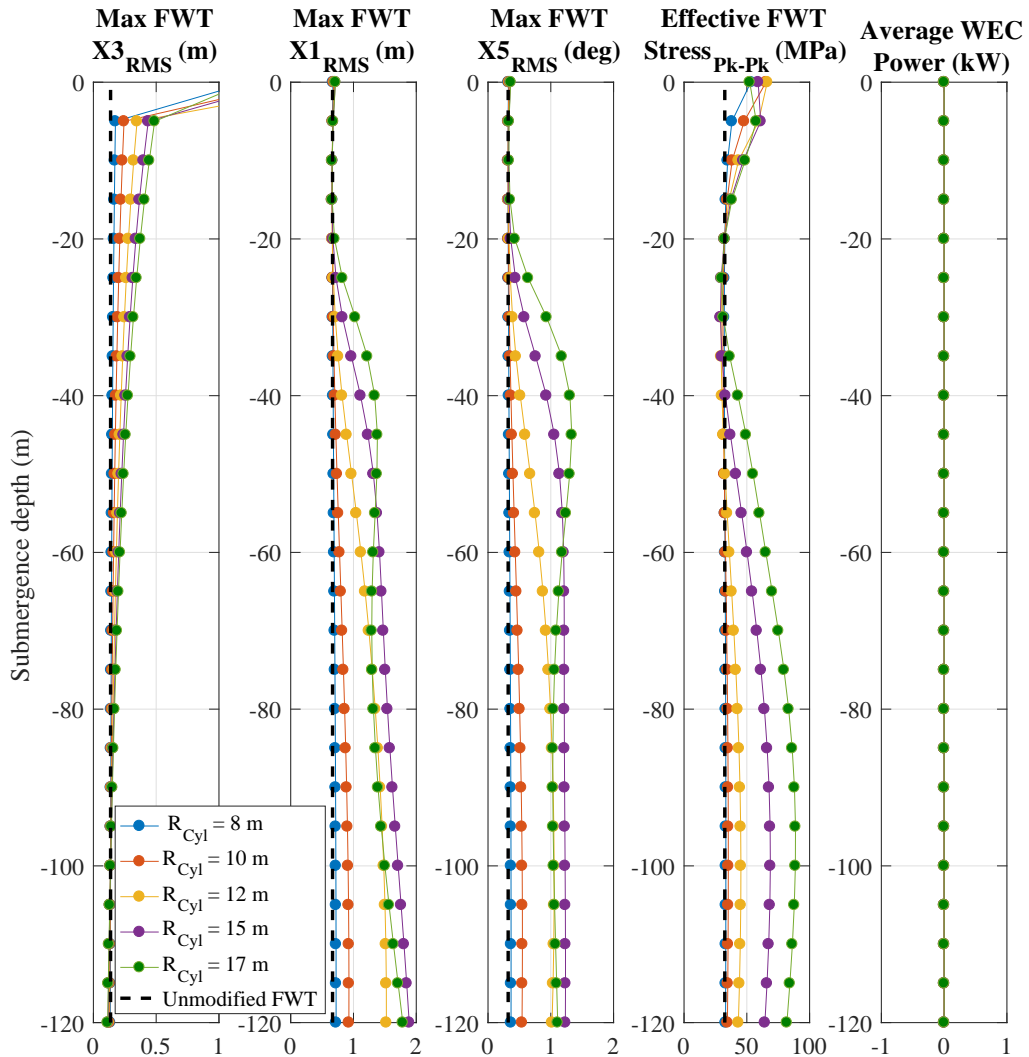


Figure 6-1: Response statistics for a neutrally buoyant external cylindrical ballast rigidly attached to the FWT at varied depth.

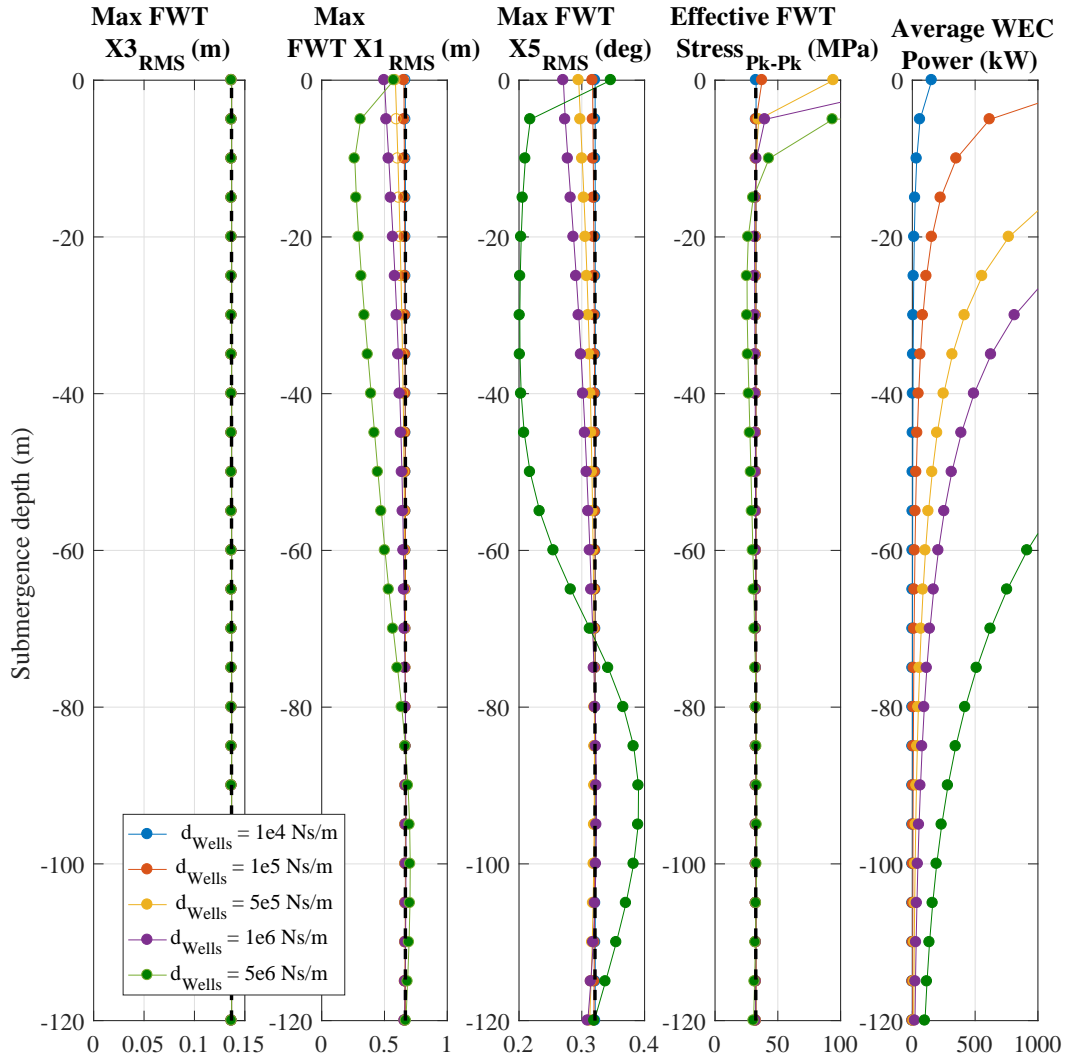


Figure 6-2: Response statistics for a massless damping element between the FWT and incident waves at varied depth. The dashed line represents the unmodified FWT.

### 6.3 Linear Spherical WEC's With Tuned Spring Coupling to the FWT

Now, we consider WEC's attached to the FWT platform by a spring tuned to maximize the WEC power. We restrict the WEC types to neutrally-buoyant spherically-shaped WEC's attached only to the FWT (rather than also attached to the seafloor by mooring lines, which



Table 6.2: Linear spherical WEC’s attached to FWT considered in this section

Linear WEC configuration number	Location relative to FWT	Power harvesting motion	Power take-off mechanism
1	Internal, in nacelle	Surge	Junction
2	Internal, at still waterline	Surge	Junction
3	Internal, at still waterline	Heave	Junction
4	External, submerged 10 m	Surge	Junction
5	External, submerged 10 m	Surge	Wells turbine
6	External, submerged 10 m	Heave	Junction
7	External, submerged 10 m	Heave	Wells turbine
8	External, at still waterline	Heave	Wells turbine

would increase cost). We consider WEC’s with a power takeoff (PTO) mechanism that uses the relative motion between the WEC and FWT, or a PTO that uses the relative motion between the WEC and ocean waves [32]. The first PTO may be implemented by a linear or rotary mechanism with a mechanical or hydraulic drive-train powering the generator [129]. The second PTO may be implemented by a Wells turbine [13]. Additionally, we consider tuned mass dampers inside the FWT [131]. The various systems are listed in Table 6.2 and illustrated in Fig. 6-3.

To simplify a parameter sweep optimization, we do a modal analysis on the model to determine the required parameter relationship for maximizing WEC power. We use these findings to investigate the power production, cost of energy, and effect on FWT motion of the various WEC configurations.

### 6.3.1 Modal Analysis

In a real ocean environment, the FWT-WEC is excited by a continuous spectrum of frequencies. For the modal analysis, we assume that the dominant behavior of the system can be represented by its behavior at the dominant ocean wave frequency (Joo and Sapsis, 2014; Trimble, 2011) [71, 140]. Table 6.1 lists typical sea states based on NOAA buoy data 10 nautical miles NW of Eureka, CA over a ten year period (NOAA, 2016) [1].

It is important that one or more WEC parameters are adjustable in order to tune the WEC resonant frequency to match the the sea state dominant frequency. Otherwise, the well-known mistuned power decay phenomenon occurs [71]. Placed in between the rela-

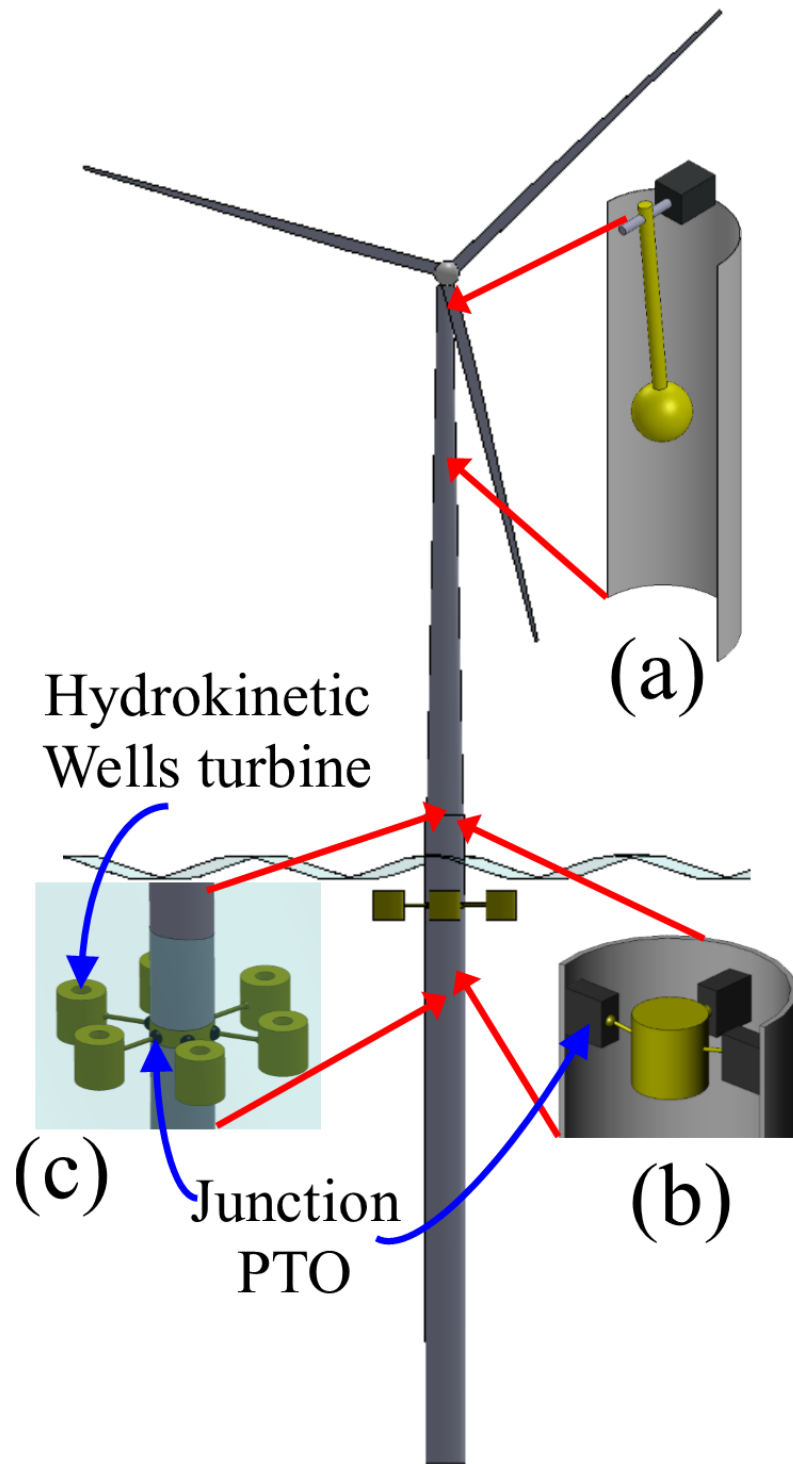


Figure 6-3: Sketches of combined FWT-WEC array concepts for the OC3-Hywind floating wind turbine: (a) surge-mode internal surge tuned mass damper, (b) heave-mode internal tuned mass damper, and (c) heave-mode external WEC.

Table 6.3: Relation of vibration analysis parameters to FWT-WEC parameters

Analysis parameter	Surge-mode WEC	Heave-mode WEC
$I_W$	$I_{11W}$	$I_{33W}$
$I_F$	$I_{11F}$	$I_{33F}$
$F_W$	$F_{1W}$	$F_{3W}$
$F_F$	$F_{1F}$	$F_{3F}$
$K_W$	0	$C_{3W}$
$K_J$	$K_{1J}$	$K_{3J}$
$K_F$	$C_{11F}$	$C_{33F}$

tively large FWT and WEC bodies, the junction spring  $K_J$  is likely the most easily tune-able system parameter, as opposed to adjusting the WEC inertia.  $K_J$  may be implemented by a mechanical or electromagnetic actuator [112].

Here, we develop an expression for the FWT-WEC junction spring,  $K_J$ , that maximizes harvested wave power as a function of the other parameters. We determine the optimal  $K_J$  value by analyzing the free body diagram shown in Fig. 6-4. This diagram represents the governing dynamics of the various FWT-WEC configurations considered in this paper.  $x_W$  and  $x_F$  represent the WEC and FWT, respectively. Table 6.3 lists the diagram's relationship to the FWT-WEC parameters.

To simplify the forced harmonic vibration analysis, we neglect the effects of damping. After adding in the damping effects, we expect optimal power performance to occur for the same  $K_J$  value and at the same corresponding WEC resonant mode as for the undamped system [114]. The WEC power is maximized when the undamped WEC amplitude is maximized (for a Wells turbine PTO system) or undamped relative amplitude between the WEC and FWT is maximized (for a junction PTO system). Therefore, we compute the steady-state WEC amplitude and WEC-FWT relative amplitude and determine the parameters that maximize both amplitudes.

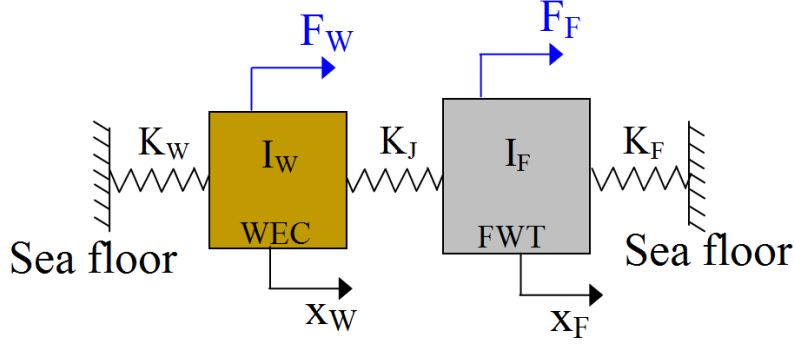


Figure 6-4: Idealized free body diagram for analyzing the mode shapes of the combined floating wind turbine-wave energy converter.

The free body diagram in Fig. 6-4 corresponds to the coupled equations of motion,

$$I_F \ddot{x}_F + K_F x_F - K_J (x_F - x_W) = F_F, \quad (6.1)$$

$$I_W \ddot{x}_W + K_W x_W + K_J x_{x_W - x_F} = F_W. \quad (6.2)$$

From Eq.s 6.1-6.2, the response amplitude operators for the FWT and WEC motion are,

$$X_F = \frac{(-I_W \omega^2 + K_W + K_J) F_F + K_J F_W}{I_F I_W \omega^4 - (I_F K_W + (I_W + I_F) K_J + I_W K_F) \omega^2 + K_J (K_W + K_F) + K_F K_W}, \quad (6.3)$$

$$X_W = \frac{K_J F_F + (-I_F \omega^2 + K_F + K_J) F_W}{I_F I_W \omega^4 - (I_F K_W + (I_W + I_F) K_J + I_W K_F) \omega^2 + K_J (K_W + K_F) + K_F K_W}, \quad (6.4)$$

The relative amplitude between the WEC and FWT is,

$$X_R = X_W - X_F. \quad (6.5)$$

From the response amplitude operators in Eq.s 6.3 - 6.5, the junction spring,  $K_J$ , maximizes the WEC absolute and relative amplitudes when it minimizes the denominator. This occurs when  $K_J$  satisfies,

$$K_J = \frac{-I_F I_W \omega^4 + (I_F K_W + I_W K_F) \omega^2 - K_F K_W}{-(I_F + I_W) \omega^2 + K_F + K_W}. \quad (6.6)$$

We use this value of  $K_J$  for each sea state and WEC type in our FWT-WEC dynamics

Table 6.4: Floating wind turbine - wave energy converter properties

Parameter	Value
FWT Platform mass	$7.4 \times 10^3$ Tons
FWT Platform base diameter	9.4 m
FWT platform concrete ballast mass	5950 Tons
FWT platform concrete ballast submergence	98 m
Nacelle-rotor-hub mass	350 Tons
Nacelle height above still water line	87.6 m
Ocean depth	320 m
WEC mass	540 Tons
External WEC diameter	10 m
Submerged WEC depth	10 m
External WEC steel thickness	5 cm
Steel density	$8500 \text{ Kg/m}^3$
Steel cost per ton	\$2.8k
PTO Cost per kW	\$2.5k
WEC fixed cost component	\$340k
Junction PTO efficiency, $\eta_J$	0.85
Wells turbine efficiency, $\eta_W$	0.6

computations. Using this  $K_J$  value, we parameter sweep the damping coefficient to identify if certain parameters allow significant WEC power generation and minimized FWT motion.

### 6.3.2 Results

We use the previously described dynamics and cost model to compute the response statistics for 8 different WEC-FWT configurations, listed in Table 6.2. We constrain all of the WEC's to have the same shared parameters listed in Table 6.4. For each WEC, we set certain elements of **I**, **K**, **D**, and **F** to zero or infinity, according to the WEC definition (for example, a submerged surge converter does not have a hydrostatic restoring coefficient,  $C_{3W} = 0$ ).

We assume that a WEC moves rigidly with the FWT in its non-power harvesting degree of freedom, so we set the corresponding junction spring value to  $K_J = 10^{12}$  N/m. We assume that the junction spring,  $K_J$ , for the WEC's flexible mode is adjusted by a control mechanism to an optimal constant value in each sea state given by Eq. 6.6. We reduce the FWT floating platform ballast mass for the internal WEC systems in order to maintain buoyancy. Among the 3 sea states for each WEC, we reduce the power harvested during

the most powerful sea states and replace it with the power harvested during the next less powerful sea state, until the WEC capacity factor is greater than 0.3. The results for several performance objectives are shown in Figs 6-5 and 6-6.

Fig. 6-5 shows that the external heave WEC with a Wells turbine power takeoff coefficient,  $d_w = 10^6 \text{ Ns/m}$ , generates the largest amount of electricity, 75 kW. This results in the lowest cost of energy, \$0.35/kWh. However, this large damping coefficient may not be physically feasible based on space considerations [13]. We also note that the heave WEC's have an unfavorable effect on the FWT, increasing the tower root stress by 17% compared to the standalone FWT.

The external heave WEC with a Wells turbine also produces significant power, 39 kW for a small damping coefficient of  $d_w = 10^4 \text{ Ns/m}$ . This small damping coefficient makes the system more practical, but the WEC has an impractically large amplitude of 2.7 m RMS.

We note that the external surge WEC with a Wells turbine PTO and effective damping coefficient of  $d_w = 10^6 \text{ Ns/m}$  generates 51 kW, slightly less power than the heave WEC with a Wells turbine.

The surge and heave external WEC's with junction power takeoffs each generate less power than their counterparts with Wells turbine power takeoffs. This is due to there being a smaller motion difference between the WEC and FWT than between the WEC and incident waves. The heave WEC with a junction PTO of  $d_w = 7 \times 10^4 \text{ Ns/m}$  can generate an average power of 46 kW, which may be an acceptable amount. As previously mentioned, a WEC with a junction PTO may be able to achieve a larger effective damping coefficient, be more efficient, and cost less than a WEC with both a controlled Wells turbine and controlled junction spring (Raffero et al., 2014).

The internal WECs (tuned mass dampers- TMD's) have the most favorable effects on the FWT motion and stress. The TMD in the nacelle can reduce the FWT tower stress from 32 MPa to as low as 23 MPa (28%). This is expected because the internal WEC only extracts power from the FWT whereas the external WECs also receive power from the ocean waves.

The external surge WEC with small junction damping,  $d_w = 7 \times 10^4 \text{ Ns/m}$  reduces the FWT stress by 3%. This is due to the dynamics phenomenon where for carefully tuned WEC motions, the force acting on the FWT due to the out-of-phase FWT-WEC mode shape noticeably counteracts the wave excitation force on the FWT. Unfortunately, this effect only occurs for careful tuning and light WEC damping, which does not produce significant WEC power.

Adding a heave hydrostatic stiffness between the WEC and ground by making the heave-mode WEC surface piercing can generate a maximum power of 52 kW when  $d_w = 9 \times 10^4 \text{ Ns/m}$ , which is the maximum power generated for  $d_w < 1 \times 10^5 \text{ Ns/m}$ . Therefore, we conclude that the hydrostatic stiffness helps tune the WEC performance.

A surge-mode WEC has a rigid heave-mode connection to the FWT, and thereby increases both the structure's heave inertia and heave forcing. For these WEC form factors, the WEC heave forcing exceeds the WEC resistance to forcing (inertia), which results in an increase in heave motion.

While one system alone does not generate significant WEC power and decrease the FWT motion, the results of this study suggest that two systems may be simultaneously added to the FWT to reach these design goals. For example, placing a tuned mass damper (that does not generate electricity) inside the FWT and adding an external WEC may allow the tuned mass damper to offset the added forcing on the FWT due to the external WEC. In such a system, the total cost of energy for the wave power may still remain less than for a standalone WEC.

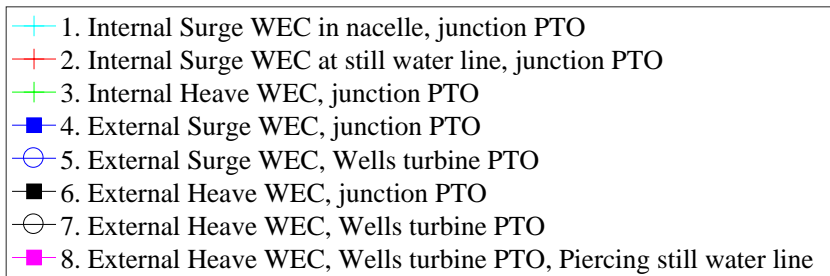
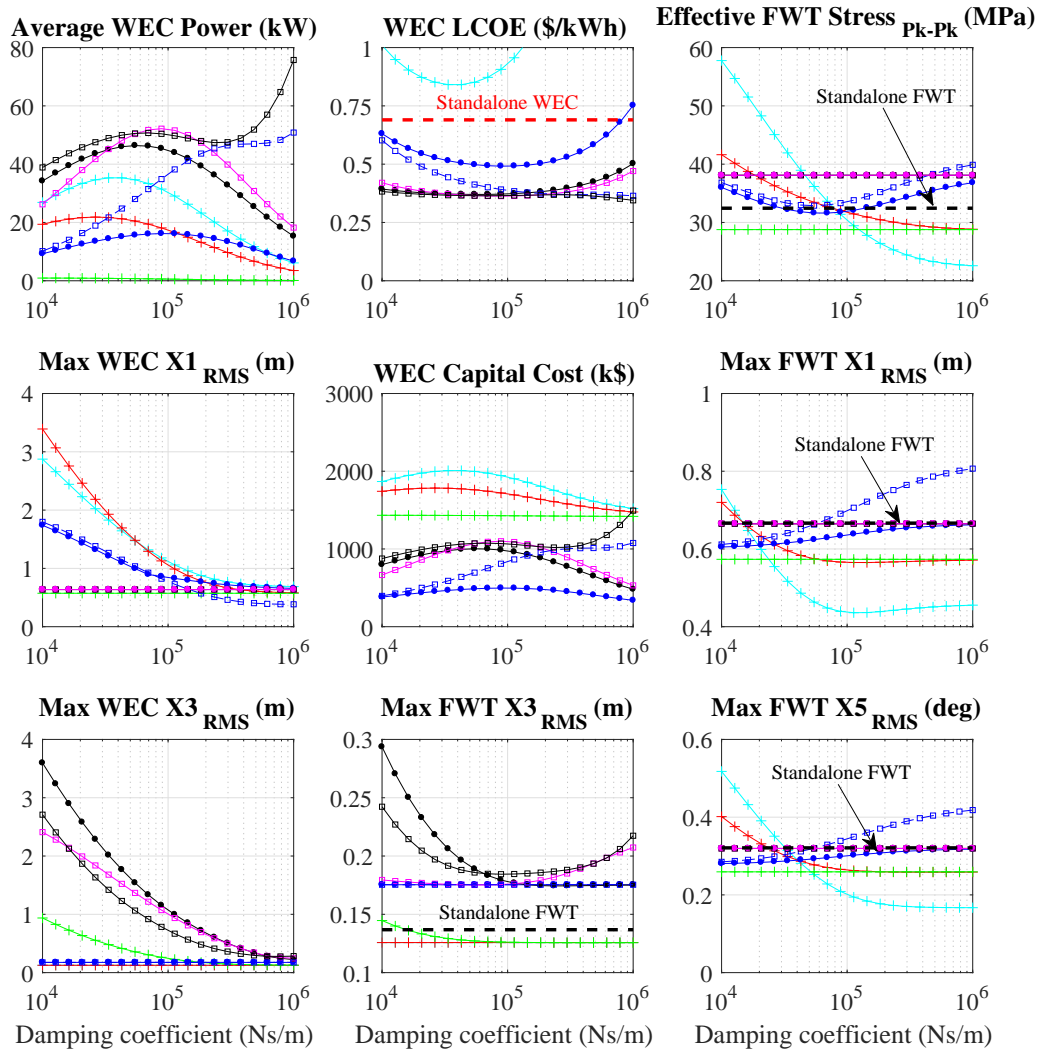
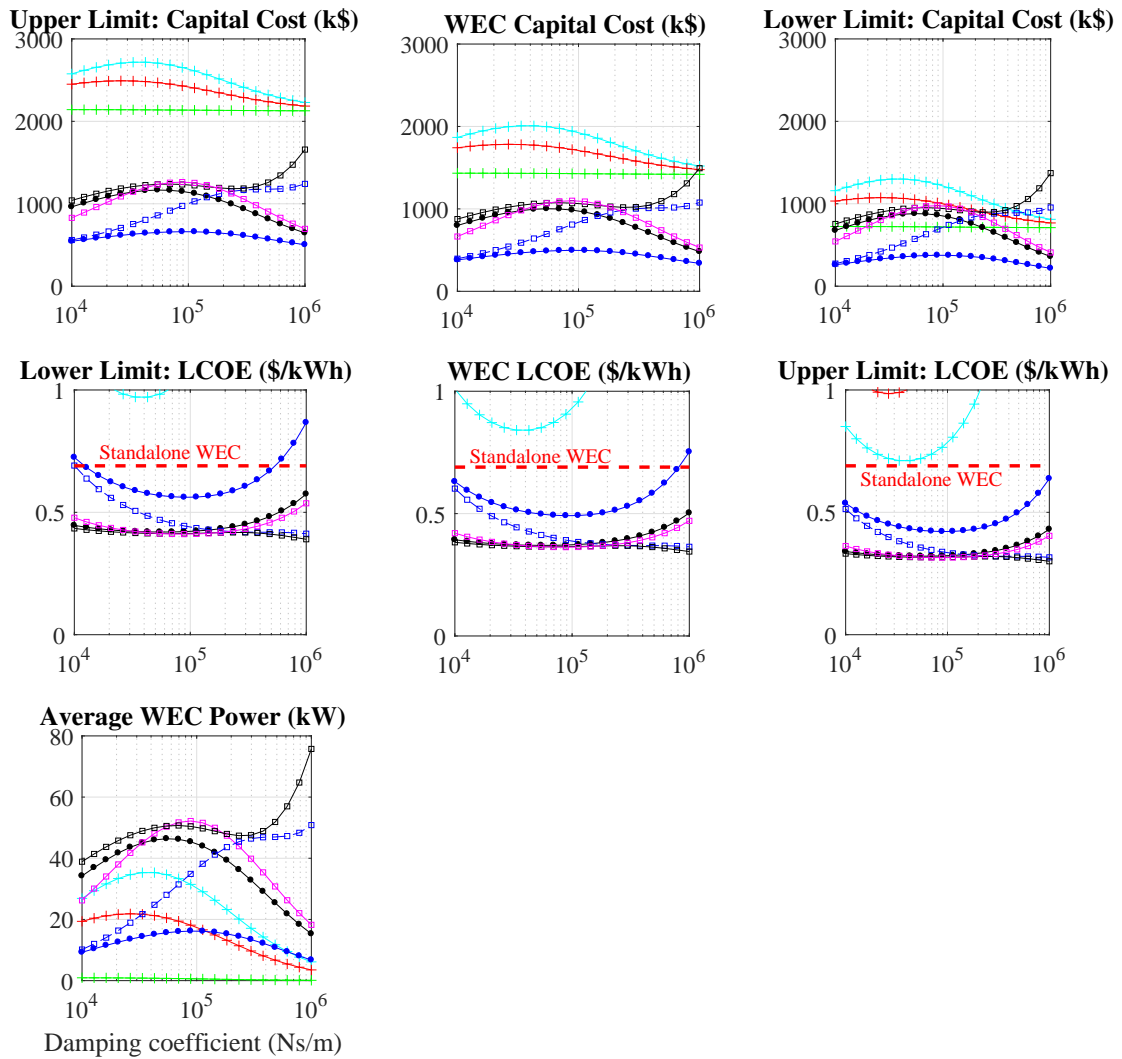


Figure 6-5: Annual response statistics for various FWT-WEC's attached by a spring  $K_j$  for 1 : -1 modal tuning.





- 1. Internal Surge WEC in nacelle, junction PTO
- 2. Internal Surge WEC at still water line, junction PTO
- 3. Internal Heave WEC, junction PTO
- 4. External Surge WEC, junction PTO
- 5. External Surge WEC, Wells turbine PTO
- 6. External Heave WEC, junction PTO
- 7. External Heave WEC, Wells turbine PTO
- 8. External Heave WEC, Wells turbine PTO, Piercing still water line

Figure 6-6: Cost uncertainty for various FWT-WEC's attached by a spring  $K_J$  for 1 : -1 modal tuning.

## **6.4 Heave-Mode Floating Oscillating Water Columns With Varied Coupling to the FWT**

In this section, we consider 3 types of oscillating water columns (OWC's): an OWC that is rigidly attached to the FWT in Subsection 6.4.1, a linear floating OWC that is coupled by a hinge to the FWT in Subsection 6.4.2, and a nonlinear floating OWC that is coupled by a hinge to the FWT in Subsection 6.4.3.

The parameters of each type of OWC are optimized separately, and then the optimum OWC of each type are compared in Section 6.4.4. Each optimization study considers a single OWC with a 4 meter radius attached to the FWT. For the rigidly-attached OWC, the submerged tube length is varied. For the hinged linear floating OWC, the OWC still water line area is varied. For the nonlinear hinged OWC, the nonlinear spring stiffness (severity of the float outer radius variation) is varied. These parameters affect the system resonant frequencies. Additionally, the Wells turbine coefficient is varied for all three systems. As these parameters are varied, the Matlab code calculates the WEC surface area and assumes a constant steel thickness over that area, to determine the WEC mass and steel cost. The code also adjusts the concrete ballast in a float (toroid encircling part of the tube length) to maintain neutral buoyancy. The fixed and optimum parameters for each OWC type are listed in Table 6.5.

Finally, this section considers the effects of an array of nonlinear floating OWC's in Subsection 6.4.5.

### 6.4.1 Rigidly Attached Oscillating Water Column

As mentioned in this thesis Introduction, previous studies have considered rigidly attaching arrays of oscillating water columns to the FWT platform [7, 77]. Those studies consider short-draft and large-radius OWC's. In this study, we hold the OWC radius fixed at 4 m, and vary the OWC tube draft and OWC Wells turbine coefficient.

Fig. 6-7 shows a CAD illustration of the system. Fig. 6-8 shows the heave-mode and surge-mode free body diagrams of the coupled WEC and FWT. This simplified FBD does not show the FWT platform coupling with other degrees of freedom, such as platform pitch and the rotor. Like the other OWC systems considered in this thesis, the OWC tube is rigidly attached to the FWT in surge and pitch. This WEC differs from the hinged WEC's by having a rigid spring connection between the WEC tube and FWT in the heave mode.

We compute the system response statistics as we vary the tube submergence length and Wells turbine coefficient. The tube has a hollow toroid encircling it with a 5-m outer radius and 5 m length. This volume is filled with air and varied amounts of concrete to maintain neutral buoyancy. Fig. 6-9 shows the response statistics for the varied submerged tube length and Wells turbine coefficient. Fig. 6-10 shows cost predictions and uncertainty.

Based on Fig. 6-9, increasing the submerged tube length increases the harvested power. the optimal system has a submerged tube length of 30 m and Wells turbine damping coefficient of  $400 \text{ Pas/m}^3$ . It generates 17 kW average, resulting in a levelized cost of energy of \$0.75/kWh, and increases the FWT tower fatigue stress by 12% and heave motion by 122% (more than doubles). Fig. 6-9 shows that further increasing the Wells turbine coefficient could increase the harvested power, but we set practical limits to the turbine coefficient, as discussed in Section 2.5.

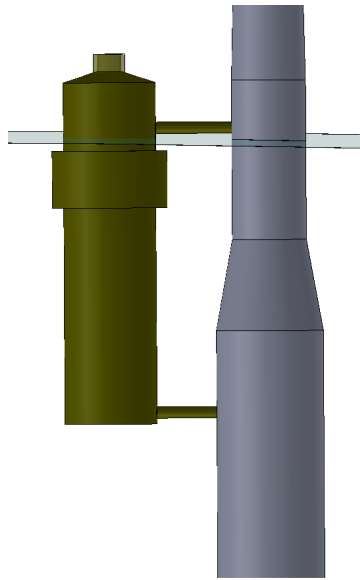


Figure 6-7: CAD illustration of the rigidly-attach oscillating water column

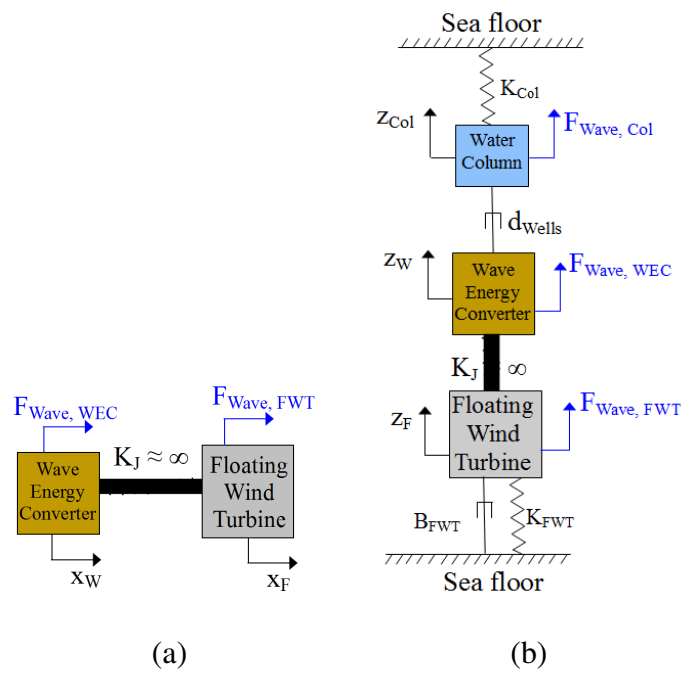


Figure 6-8: Representative free body diagrams of the rigidly attached oscillating water column FWT-WEC system in a) surge and b) heave

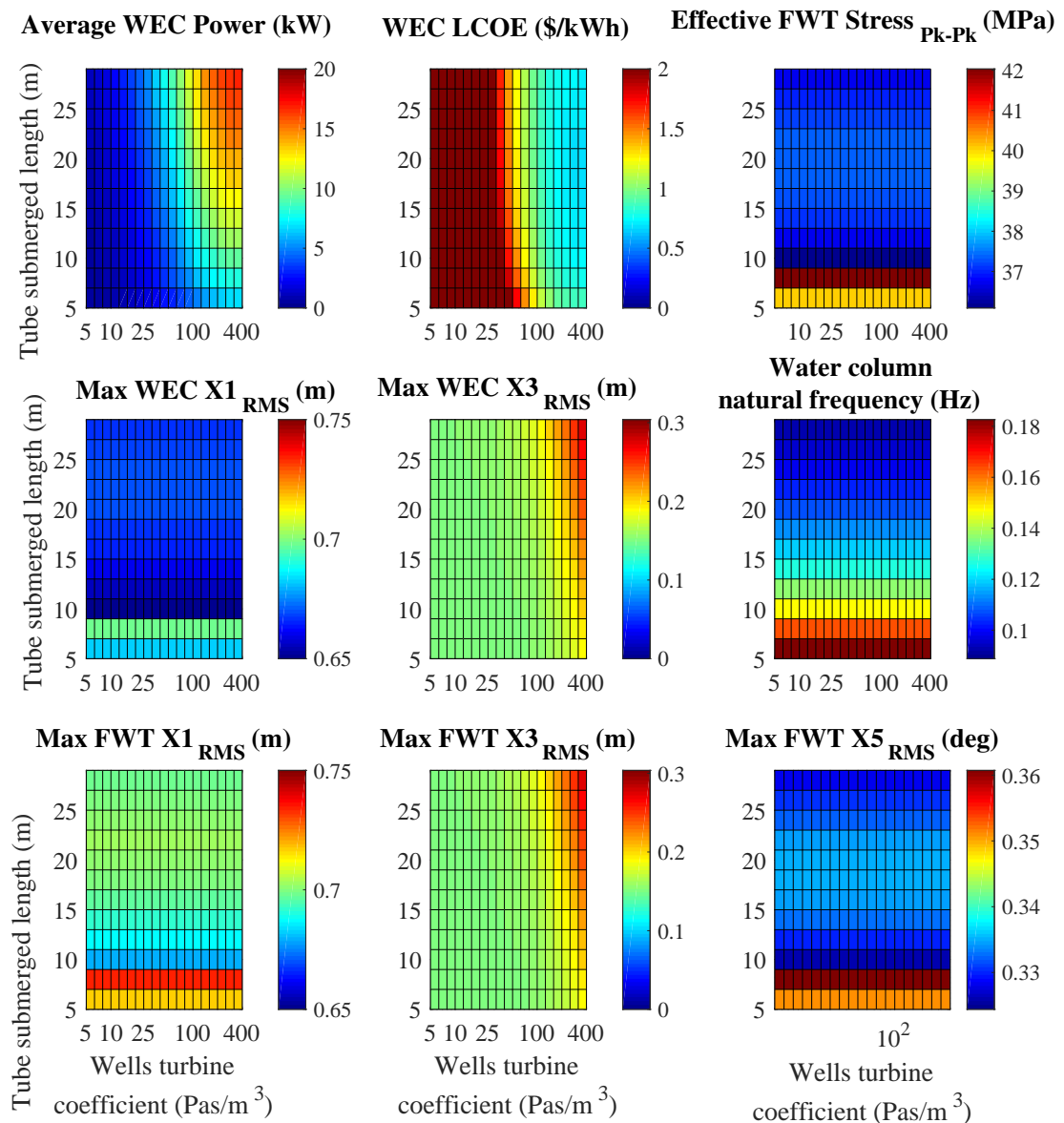


Figure 6-9: Response statistics of an oscillating water column rigidly attached to the FWT, for varied submerged tube length and Wells turbine coefficient, for the 3 wind-sea states representing a year in Eureka, CA

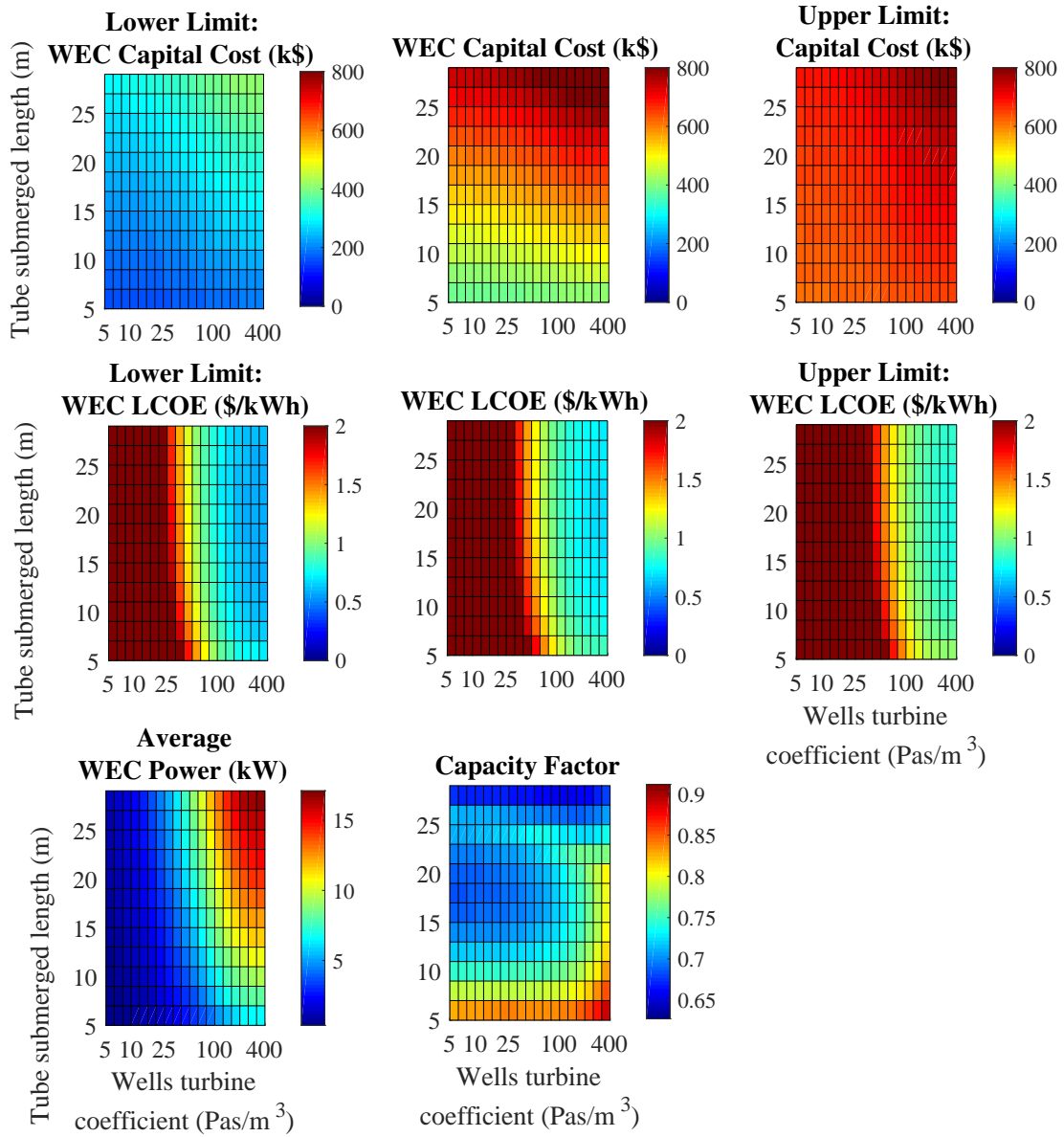


Figure 6-10: Cost uncertainty of an oscillating water column rigidly attached to the FWT, for varied submerged tube length and Wells turbine coefficient, for the 3 wind-sea states representing a year in Eureka, CA

## 6.4.2 Linear Oscillating Water Column Attached by Hinges

In this section, we consider an oscillating water column that is attached by a hinge rather than rigidly attached to the FWT, as in the previous section. In the previous section, we found that with the rigid tube connection, little power was generated even when the water column resonated in the tube, and the FWT heave motion was doubled. In this section, we investigate if the hinge attachment lessens these negative effects.

Fig. 6-11 shows a CAD illustration of the system. Fig. 6-12 shows the heave-mode and surge-mode free body diagrams of the coupled WEC and FWT. This simplified FBD does not show the FWT platform coupling with other degrees of freedom, such as platform pitch and the rotor. Like the other OWC systems considered in this thesis, the OWC tube is rigidly attached to the FWT in surge and pitch. Unlike the rigidly connected WEC, this WEC has a hinge that we assume causes negligible resistance in the heave direction for small WEC heave motions.

We compute the system response statistics as we vary the WEC still waterline area and Wells turbine coefficient. The still waterline area is adjusted by adjusting the radius of a hollow toroid that encircles the tube and extends  $\pm 3$  m from the still water line. The tube has an additional hollow toroid encircling it with a radius of 8.5 m and height of 1.5 m. This toroid has a large cross-sectional area for wave heave forcing. The toroid volume is filled with air and varied amounts of concrete to maintain neutral buoyancy. As in the previous section, we hold the OWC radius fixed at 4 m.

Fig. 6-13 shows the response statistics for the varied still water line area and Wells turbine coefficient. Fig. 6-14 shows cost predictions and uncertainty.

Based on Fig. 6-13, the maximum power is harvested for a still waterline area of  $23 \text{ m}^2$ , which corresponds to a toroid outer radius of 4.8 m encircling the tube, and a Wells turbine coefficient of  $34 \text{ Pas/m}^3$ . This optimal system generates 51 kW average, resulting in a levelized cost of energy of  $\$0.27/\text{kWh}$ . It has a negligible effect on the FWT stress and heave motion (neither an increase or decrease compared to the standalone FWT). The WEC decreases the FWT surge by 10%.

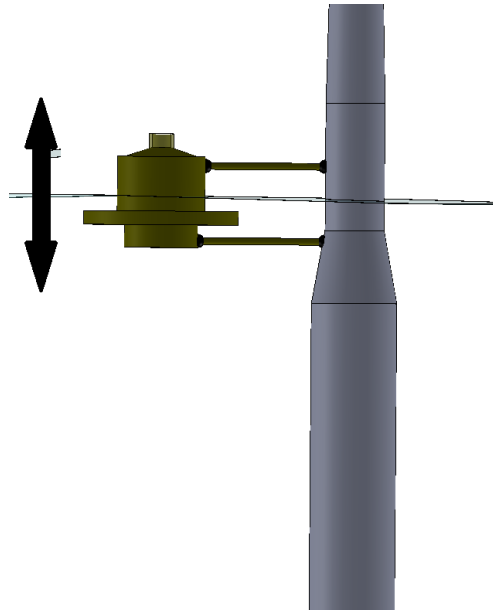


Figure 6-11: CAD illustration of the linear oscillating water column attached by a hinge to the FWT

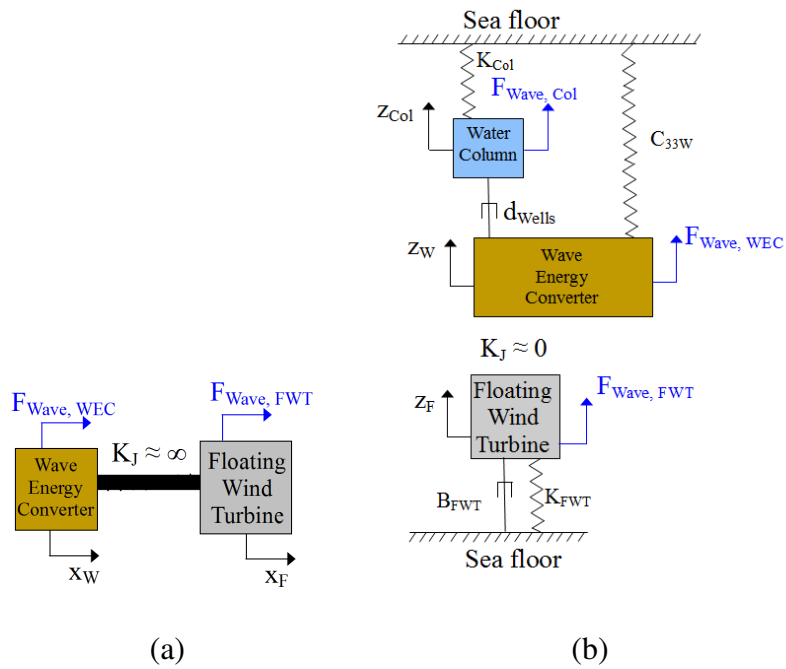


Figure 6-12: Representative free body diagrams of the hinged linear oscillating water column FWT-WEC system in a) surge and b) heave



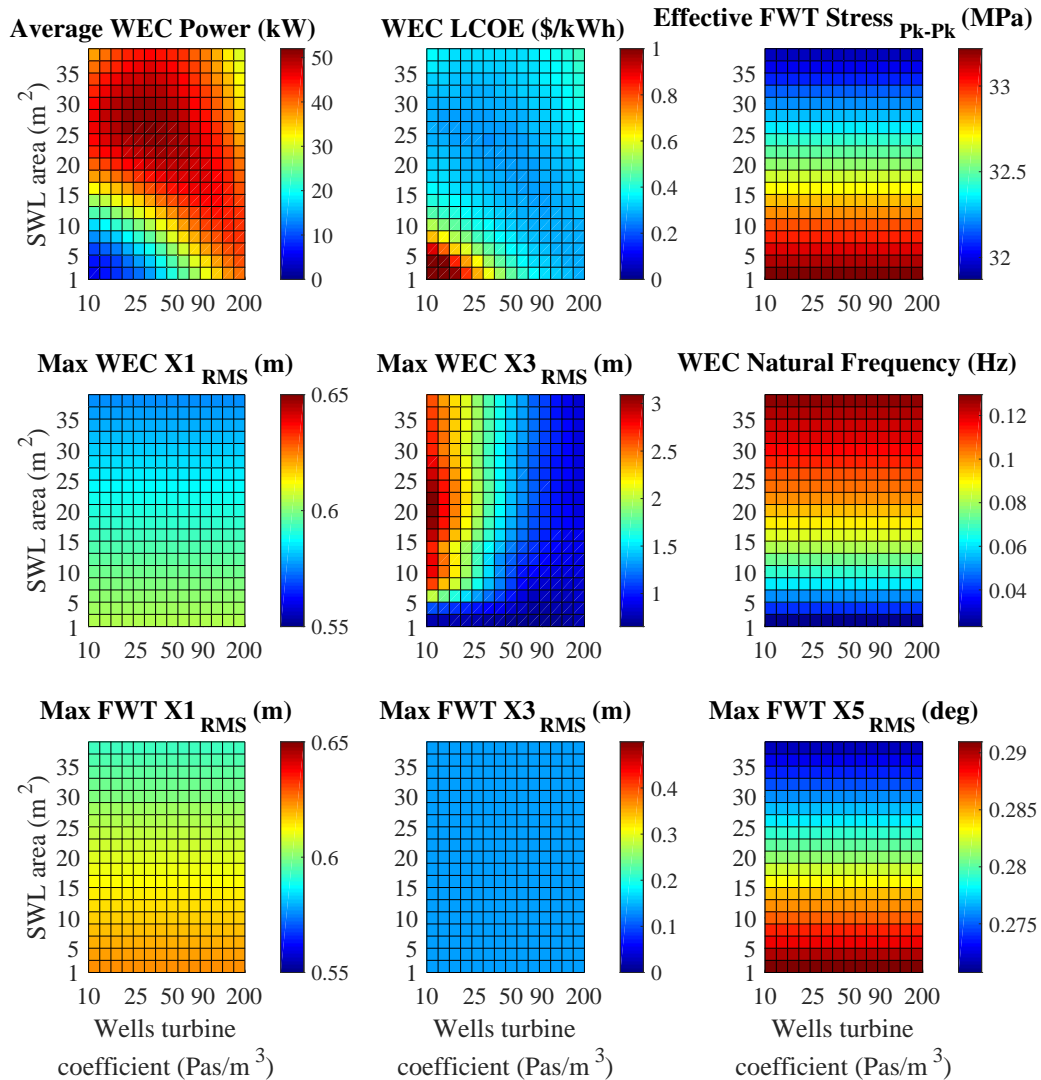


Figure 6-13: Response statistics of a linear oscillating water column attached by hinges to the FWT, for varied still waterline area and Wells turbine coefficient, for the 3 wind-sea states representing a year in Eureka, CA

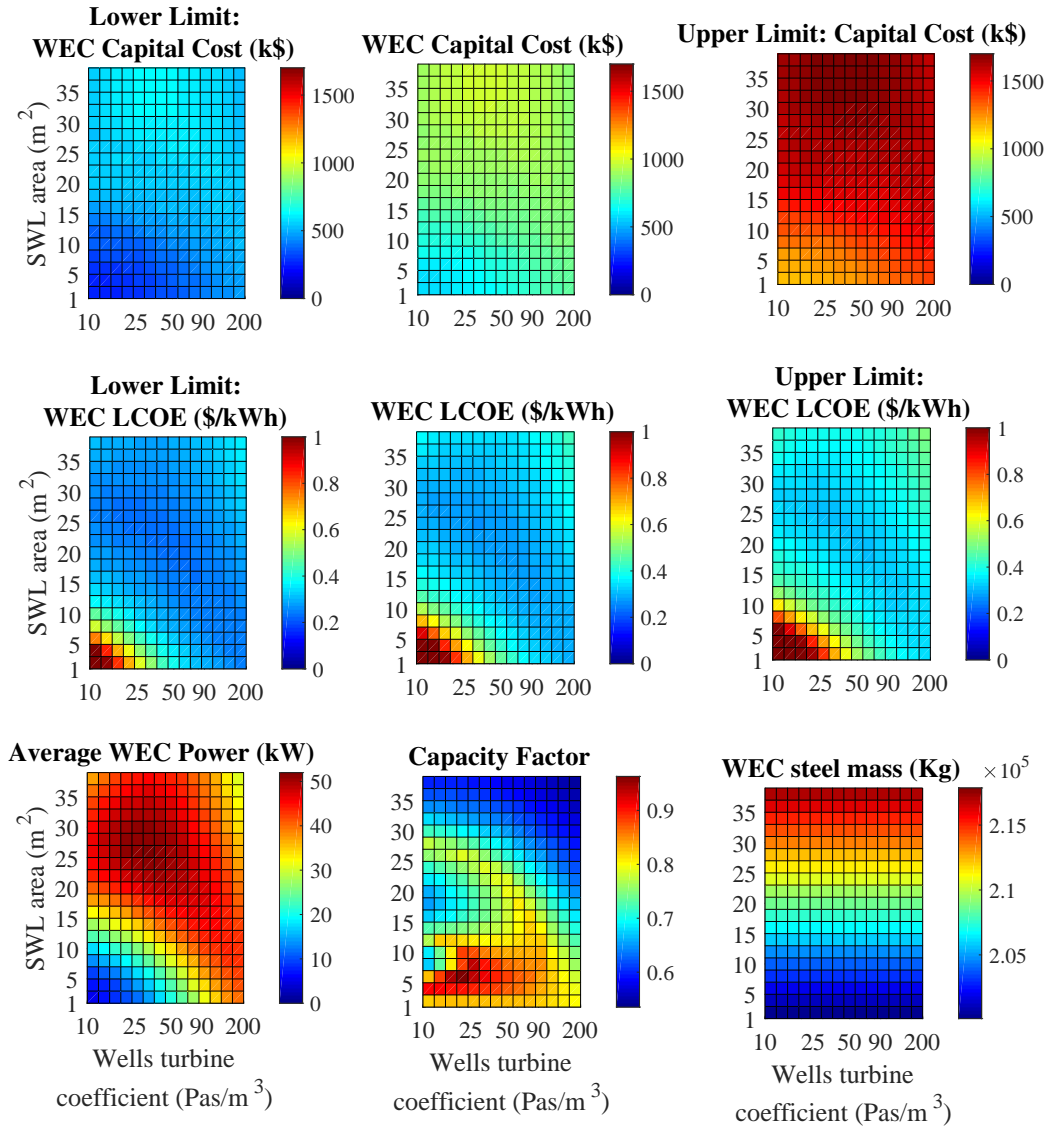


Figure 6-14: FWT-WEC cost uncertainty for a floating oscillating water column with varied still waterline area and Wells turbine coefficient.

### 6.4.3 Nonlinear Oscillating Water Columns Attached by Hinges

In this section, we consider an oscillating water column that is attached by a hinge to the FWT and has a nonlinear hydrostatic stiffness rather than the linear hydrostatic stiffness that was considered in the previous section. The nonlinearity is implemented by an outer radius that linearly increases along the WEC vertical axis away from the still water line, as described in Chapter 4. A linearly increasing radius results in a quadratically increasing

cross-sectional area, which in turn, results in a cubically increasing stiffness. We investigate if the nonlinearity improves the power performance.

Fig. 6-15 shows a CAD illustration of the system. Fig. 6-16 illustrates the physical implementation of an increasing nonlinearity. Fig. 6-17 shows the heave-mode and surge-mode free body diagrams of the coupled WEC and FWT. This simplified FBD does not show the FWT platform coupling with other degrees of freedom, such as platform pitch and the rotor. Like the other OWC systems considered in this thesis, the OWC tube is rigidly attached to the FWT in surge and pitch. Unlike the rigidly connected WEC, this WEC has a hinge that causes negligible resistance in the heave direction for small WEC heave motions. In addition to the linear hydrostatic stiffness, this WEC also has a nonlinear hydrostatic stiffness due to the increasing cross-sectional area.

We compute the system response statistics as we vary the nonlinear stiffness and Wells turbine coefficient. The nonlinear surface encloses a volume that is filled with air and varied amounts of concrete to maintain neutral buoyancy. As in the previous sections, we hold the OWC radius fixed at 4 m.

Fig. 6-18 shows the response statistics for the varied nonlinearity and Wells turbine coefficient. Fig. 6-19 shows cost predictions and uncertainty.

Based on Fig. 6-18, the maximum power is harvested for a nonlinear stiffness of  $3.25e5$   $N/m^3$ . This corresponds to a nonlinear volume outer radius of 4 m at the still waterline (matching the tube radius) and a linearly increased outer radius of 10.4 m at  $z = \pm 3$  m above and below the still waterline. This optimal system generates 87 kW average, resulting in a levelized cost of energy of \$0.26/kWh. It decreases the FWT stress by 5.2%, has a negligible effect on the FWT heave, and decreases the FWT surge by 16%, compared to the standalone FWT.

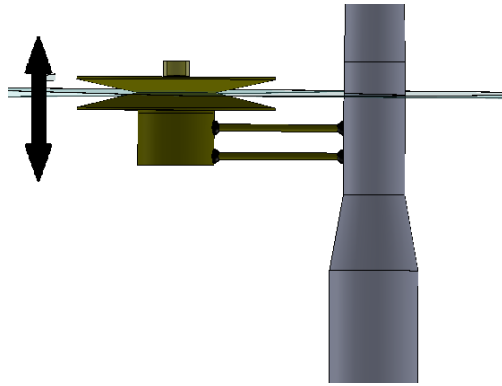


Figure 6-15: CAD illustration of the nonlinear oscillating water column attached by a hinge to the FWT.

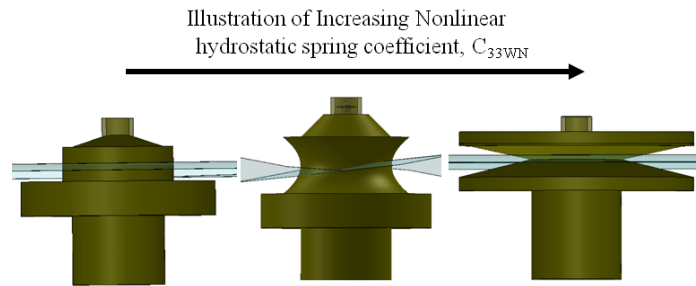


Figure 6-16: CAD illustration of increasing hydrostatic stiffness nonlinearity.

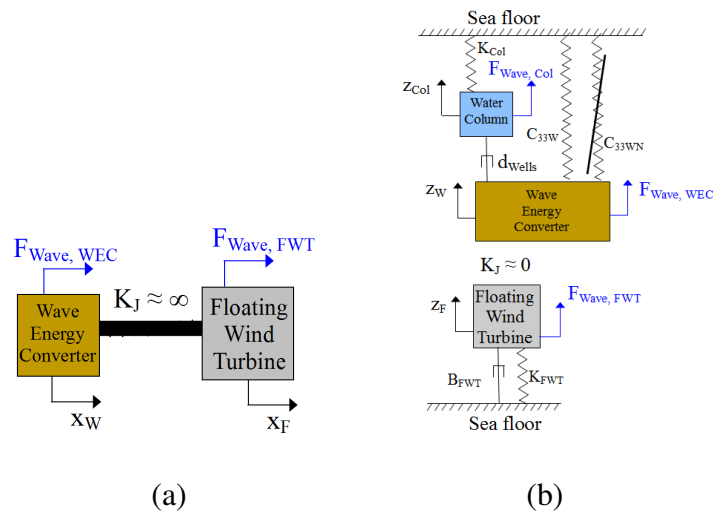


Figure 6-17: Representative free body diagrams of the hinged nonlinear oscillating water column FWT-WEC system in a) surge and b) heave.

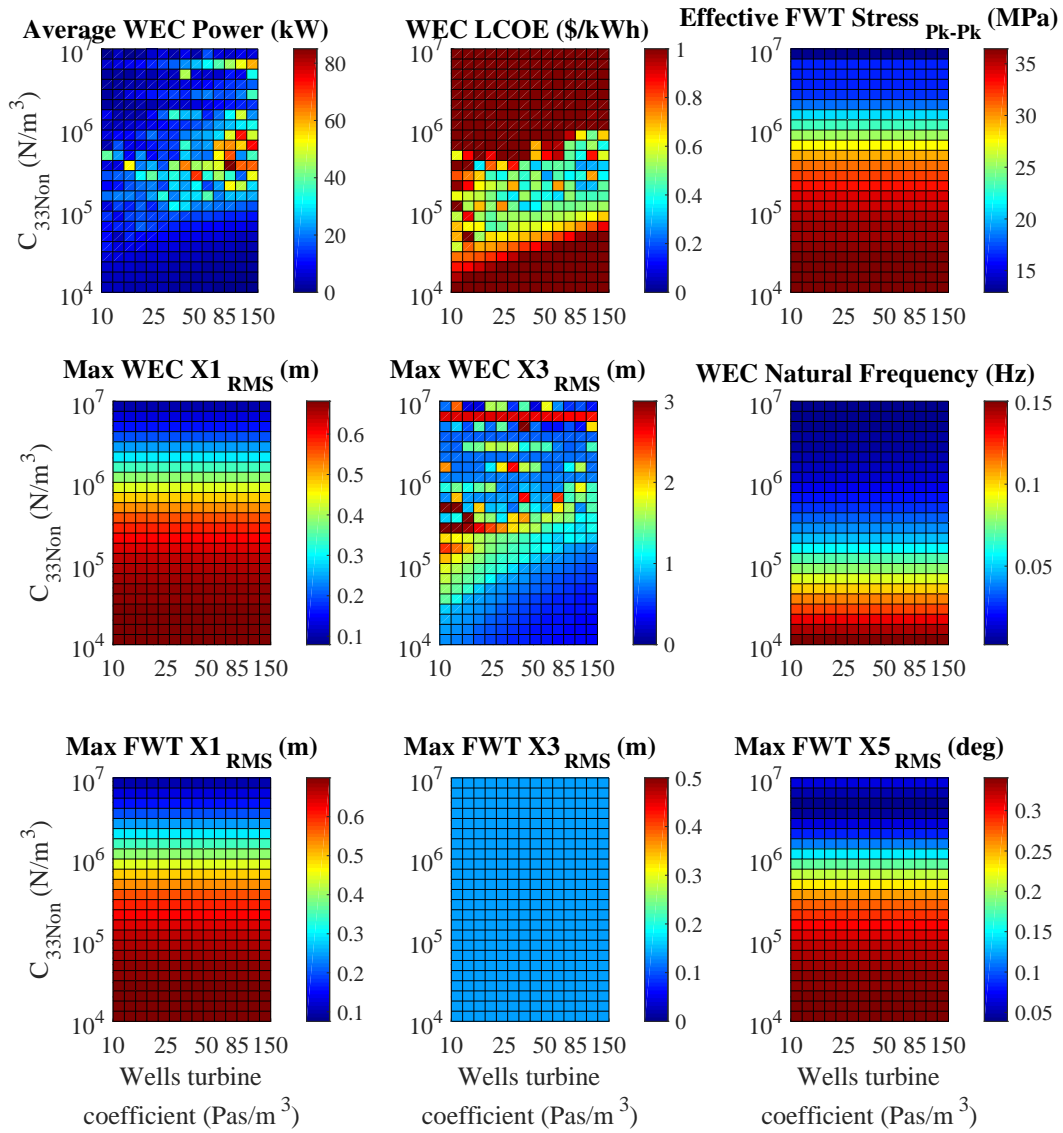


Figure 6-18: Response statistics of a nonlinear oscillating water column attached by hinges to the FWT, for varied nonlinear spring coefficient and Wells turbine coefficient, for the 3 wind-sea states representing a year in Eureka, CA.

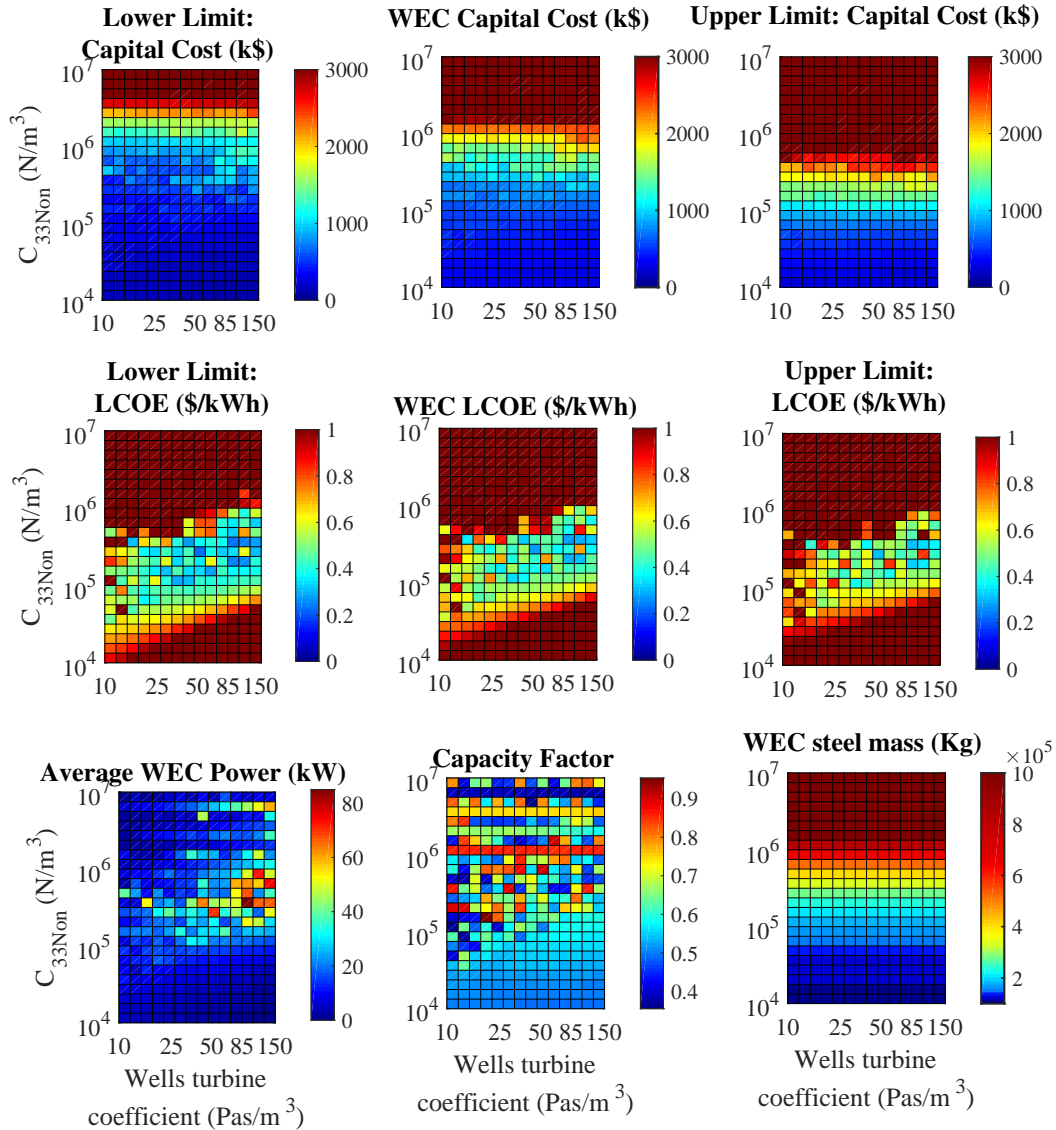


Figure 6-19: FWT-WEC cost uncertainty for varied nonlinear spring coefficient and Wells turbine coefficient.

#### 6.4.4 Oscillating Water Column Comparison

In Table 6.5, we list the optimized parameters of each type of OWC; the rigidly attached OWC tube, the linear floating OWC tube attached by a hinge, and the nonlinear floating OWC tube attached by a hinge. Fig. 6-20 compares the performance statistics of the 3 optimal systems and standalone systems (linear floating oscillating water column and the baseline OC3-Hywind FWT). Fig. 6-21 lists the 4 systems' cost uncertainty. Table 8.1 in

the Conclusion chapter summarizes and compares the optimal performance of all the WEC types.

From Fig.s 6-20 and 6-21, we see that the nonlinear system has the most favorable statistics: the largest power production, lowest levelized cost of energy (LCOE), and greatest reduction in FWT tower root stress compared to the standalone system. The nonlinear WEC requires 57% more steel than the linear WEC but produces 72% more power on average. This combination results in a slightly more favorable LCOE for the nonlinear WEC, the larger amount of steel more significantly decreases the FWT motion and tower root stress.

It is likely that one could further increase the linear WEC parameters for better performance: increasing the linear WEC mass and still waterline area, would maintain the same WEC natural frequencies, and result in a larger ratio of total WEC mass:steel mass.

For a better understanding of the performance statistics, we plot the response amplitude operators of the FWT platform and WEC's in Fig.s 6-22 and 6-23, respectively. Fig. 6-22 shows that the rigidly attached WEC increases the platform surge resonant response at 0.04 Hz, and generally increases the platform heave and pitch response over all frequencies, which agrees with the statistics findings. The linear and nonlinear floating oscillating water columns slightly decrease the platform surge resonant response at 0.04 Hz, have negligible effect on the platform heave, and generally decrease the platform pitch response over all frequencies.

Fig. 6-23 illustrates how the nonlinear floating oscillating water column (nonFOWC) peak frequency response adapts to the sea state. In sea state 1, the most energetic sea state, which has a wave peak frequency of  $f_p = 0.125$  Hz, the nonFOWC peak response matches the peak frequency. In the lower energy sea states 2 and 3, which have peak wave frequencies of  $f_p = 0.091$  Hz and  $f_p = 0.0625$  Hz, respectively, the nonFOWC peak response decreases to 0.05 Hz. The peak frequency of the nonFOWC depends on the energy level in the response: larger amplitude responses of the nonFOWC correspond to an effectively stiffer system. At low frequencies the nonFOWC frequency remains close to the linearized WEC frequency, and the WEC adaptability is limited.

Future studies could further investigate the adaptability advantage of the nonFOWC

over a larger number of sea states. The choice of how to limit the WEC capacity factor has a significant effect on the WEC capital cost and levelized cost of energy. We chose to set the WEC power in the most powerful sea state equal to the WEC power in the second most powerful sea state if the original capacity factor was less than 0.3. This choice gave the WEC's extra high capacity factors at the expense of lower average power production. Future studies could further optimize the capacity factor choice.



Table 6.5: Final Parameters of Heave-Mode Oscillating Water Columns

Parameter	Rigidly attached	Hinge- attached Linear	Hinge- attached Nonlinear
Mass, $m_W$ (Kg)	$1.7e5$	$3.5e5$	$6.6e5$
Steel mass, $m_{Steel}$ (Kg)	$3.0e5$	$2.1e5$	$3.3e5$
Tube radius, $r_{Tube}$ (m)	4	4	4
Toroid radius at still water line, $r_{OutSWL}$ (m)	0	4.8	0
Height of toroid at still water line, $h_{OutSWL}$ (m)	0	3	0
Still water line area, $A_{SWL}$ (m <sup>2</sup> )	0.73	23	5
WEC radius at $z = 3$ m (m)	4	4	10.4
Tube total length, $L_{Tube}$ (m)	33	9	9
Tube submerged length, $L_{TubeSub}$ (m)	30	6	6
Float radius, $r_{Float}$ (m)	5	8.5	0
Float height, $L_{Float}$ (Kg)	5	1.5	0
Wave forcing center, $z_{Force}$ (m)	-5.5	-3.75	-3
Surge added mass, $A_{11W}$ (Kg)	$1.7e6$	$6.6e5$	$6.5e5$
Heave added mass, $A_{33W}$ (Kg)	$2.1e3$	$2.0e5$	$5.6e5$
Heave linear hydrostatic stiffness, $C_{33W}$ (N/m)	$7.3e3$	$2.3e5$	$5.0e4$
Heave nonlinear hydrostatic stiffness, $C_{33Wn}$ (N/m <sup>3</sup> )	0	0	$3.2e5$
Wells turbine coefficient, $k_{Wells}$ (Pa/m <sup>3</sup> )	400	34	84
OWC air chamber volume, $V_{Chamber}$ (m <sup>3</sup> )	151	151	151
Water column inertia, $I_{Col}$ (Kg)	$1.7e6$	$4.4e5$	$4.3e5$
Water column hydrostatic stiffness, $C_{33Col}$ (N/m)	$5.1e5$	$5.1e5$	$5.1e5$
Water column area, $A_{Col}$ (m <sup>2</sup> )	50	50	50
WEC x-coordinate, $L_{xW}$ (m)	-13.5	-13.5	-13.5
WEC pitch mass inertia, $I_{55W}$ (Kgm <sup>2</sup> )	$4.0e7$	$1.6e6$	$7.6e5$
WEC pitch added mass inertia, $A_{55W}$ (Kgm <sup>2</sup> )	$4.8e8$	$8.0e6$	$5.7e6$
WEC pitch hydrostatic stiffness, $C_{55W}$ (Nm/rad)	$1.0e7$	$1.8e6$	$7.0e6$

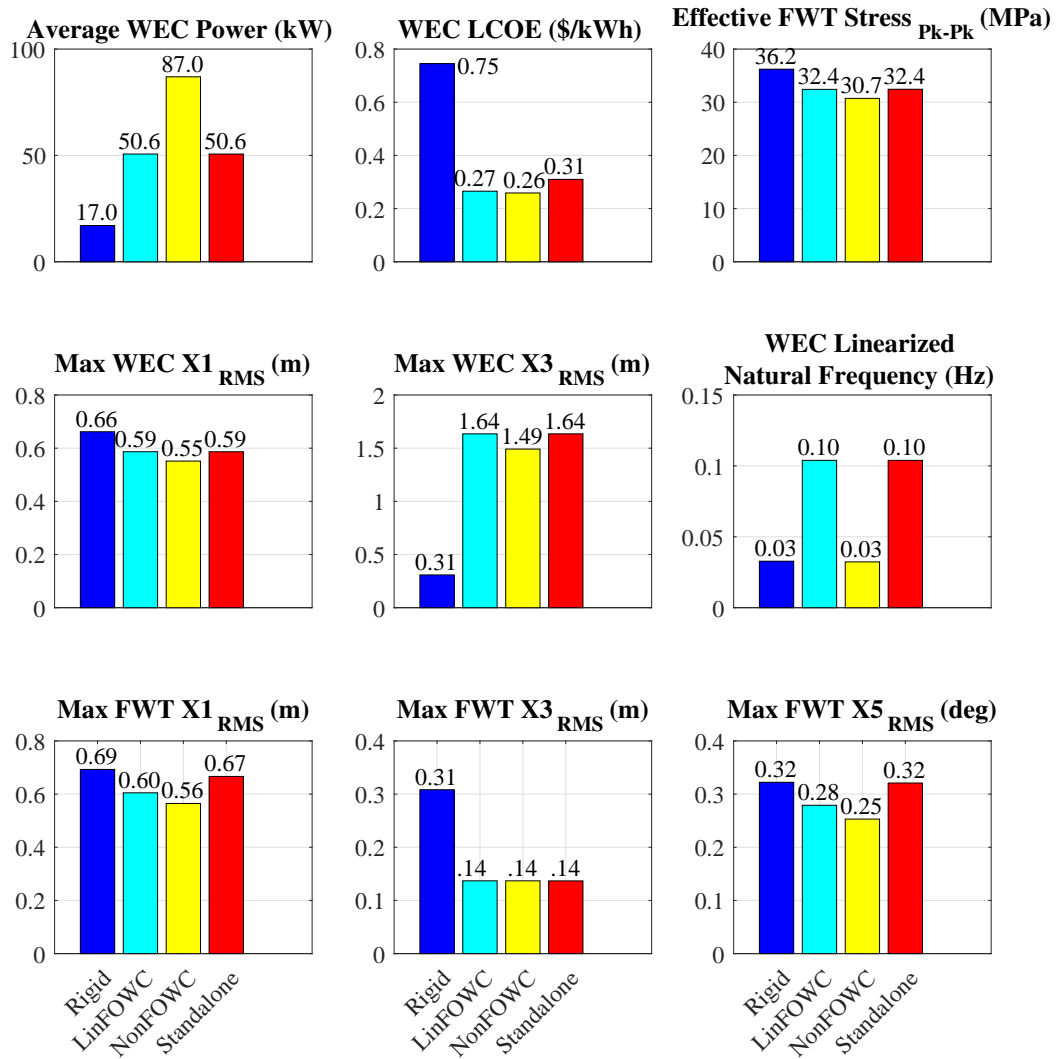


Figure 6-20: Performance comparison for linear and nonlinear floating oscillating water columns, attached to the FWT in different ways.

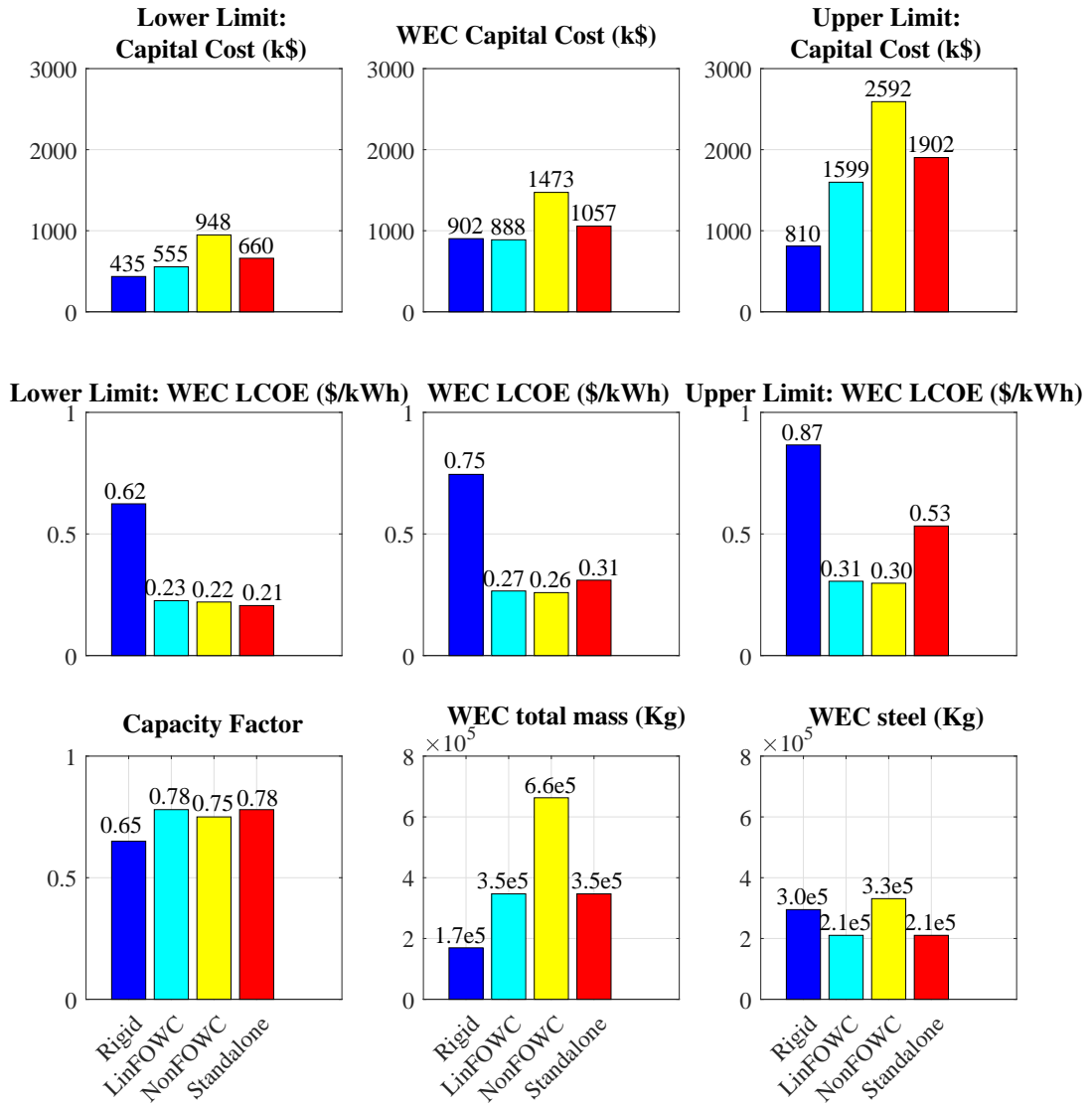


Figure 6-21: Cost comparison for linear and nonlinear floating oscillating water columns, attached to the FWT in different ways.

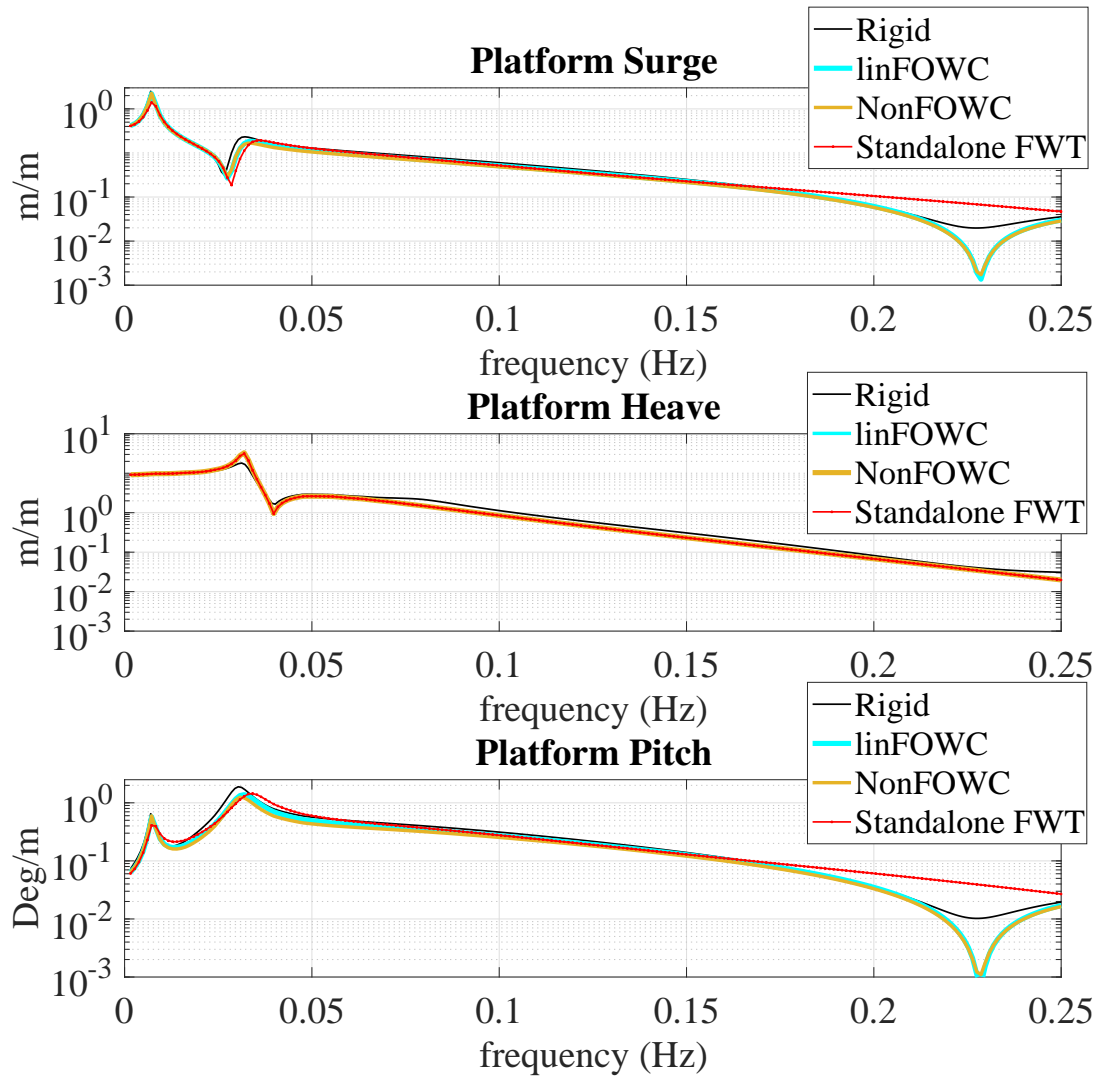


Figure 6-22: Comparison of the response amplitude operators for linear and nonlinear floating oscillating water columns, attached to the FWT in different ways. These RAO's are independent of the sea state.

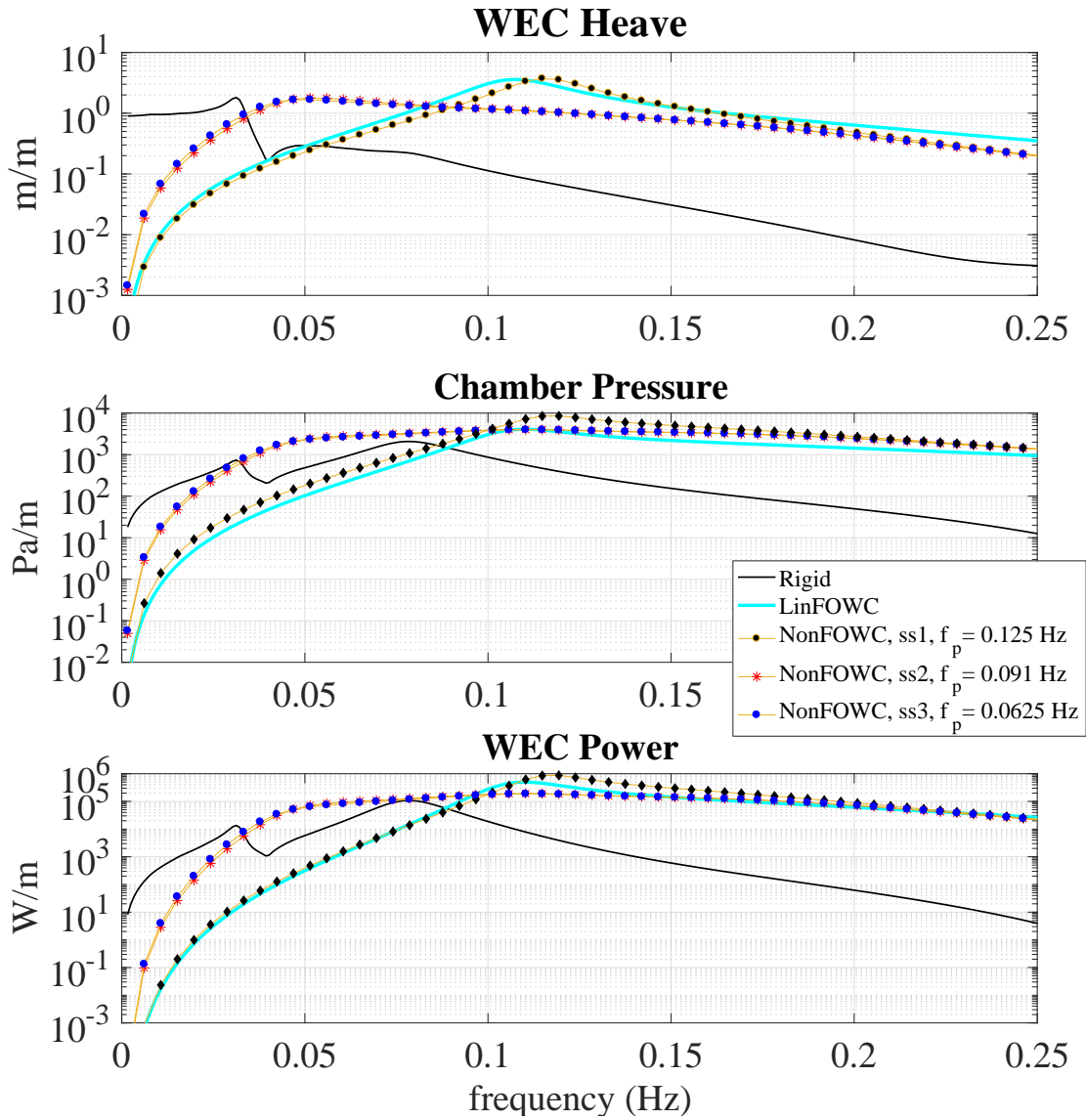


Figure 6-23: Comparison of the heave and pressure response amplitude operators for linear and nonlinear floating oscillating water columns, attached to the FWT in different ways. The rigid and LinFOWC RAO's remain the same in different sea states. The NonFOWC response changes for the different sea states. The 3 sea states considered are listed in Table 6.1.

## 6.4.5 Array of Nonlinear Heave-Mode Floating Oscillating Water Columns

In this section, we investigate the FWT-WEC performance when multiple WEC's are attached to the FWT instead of just a single WEC, which was the case in all previous sections of this chapter. Fig. 6-24 illustrates a 6-WEC circular array comprised of nonlinear floating oscillating water columns, with the parameters listed in Table 6.5.

Fig. 6-25 shows the system performance statistics for an increasing number of WEC's in an array encircling the FWT. For each array, we placed the WEC's in equal angular spacing around the 360° circle around the FWT, with the first WEC placed in front of the FWT as incident waves approached the structure. We considered only head-on waves.

Fig. 6-27 provides more details on these statistics by plotting the platform response amplitude operators for an increased number of WEC's. Fig. 6-27 shows that the platform surge and pitch motions significantly decrease over the region of important frequencies for the ocean, 0.04-0.1 Hz.

With our model, which does not consider hydrodynamic coupling, the average array power increases linearly and the levelized cost of energy remains unchanged. As an increasing number of WEC's are added to the array, the FWT surge and pitch motion significantly decreases. This is a result of the WEC contributing a larger inertia-stabilizing effect than wave-forcing effect on the system. With 6 WEC's, the array may produce an average of 400 kW (18% of a 5 MW wind turbine's average power), and stress on the FWT tower may be reduced by up to 72%. These are promising results that could be further refined by a more detailed model.

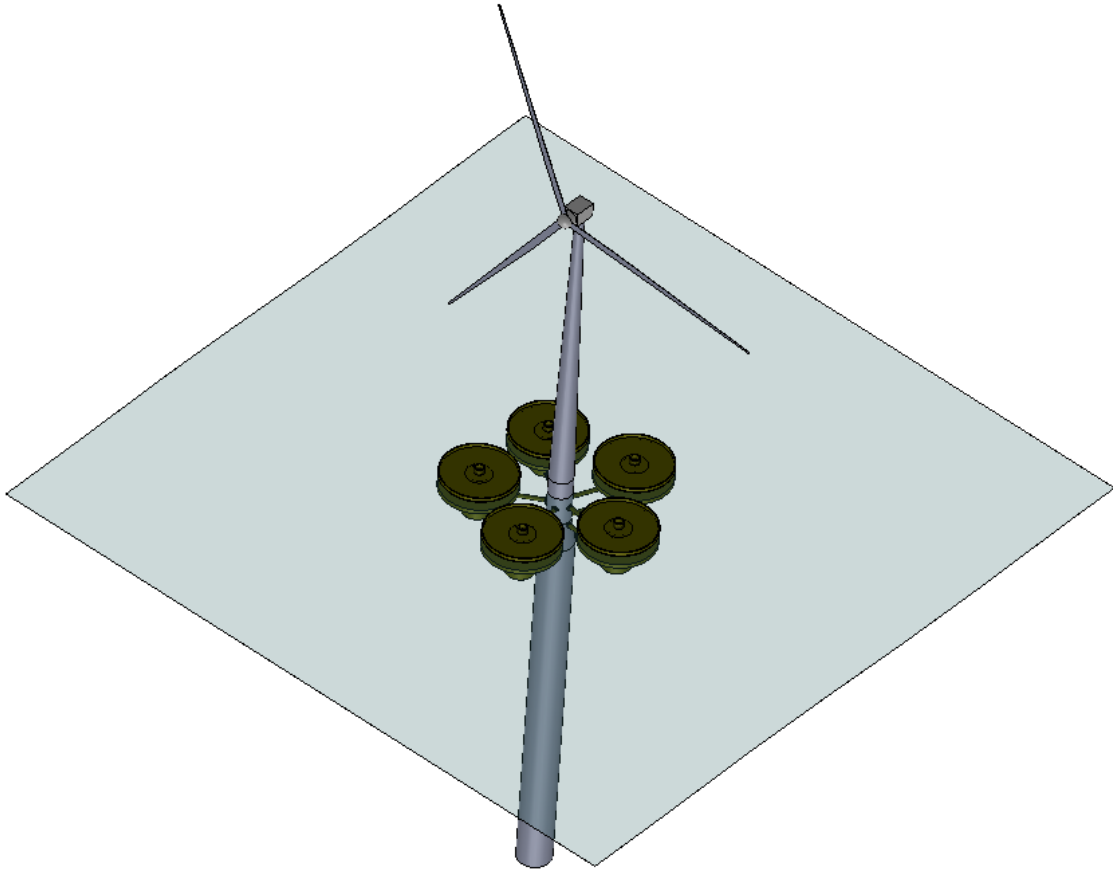


Figure 6-24: CAD illustration of a nonlinear WEC array with 6 WEC's

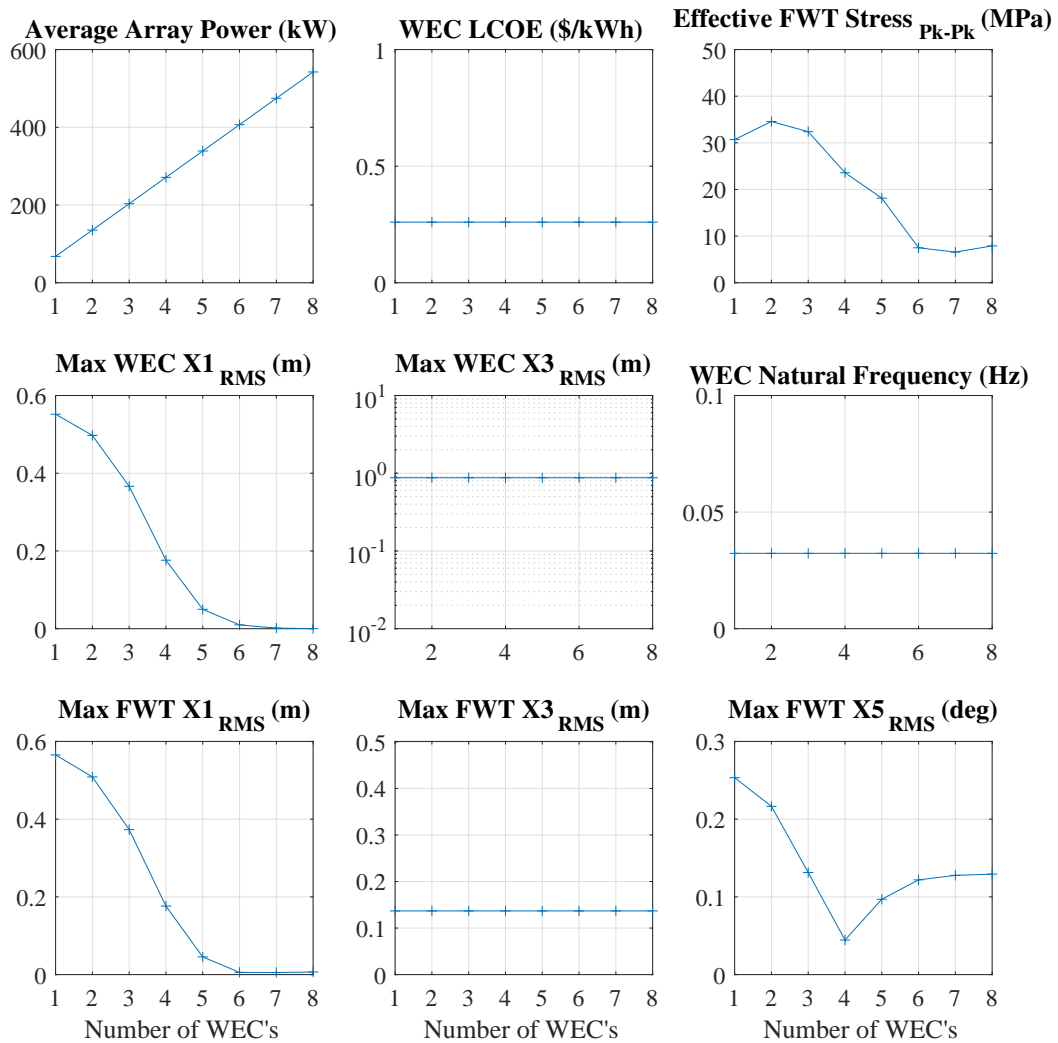


Figure 6-25: Response statistics for an array of nonlinear oscillating water columns attached by hinges to the FWT, for an increased number of WEC's in the array. The WEC uses the optimal nonlinear spring coefficient and Wells turbine coefficient for the 3 wind-sea states representing a year in Eureka, CA.



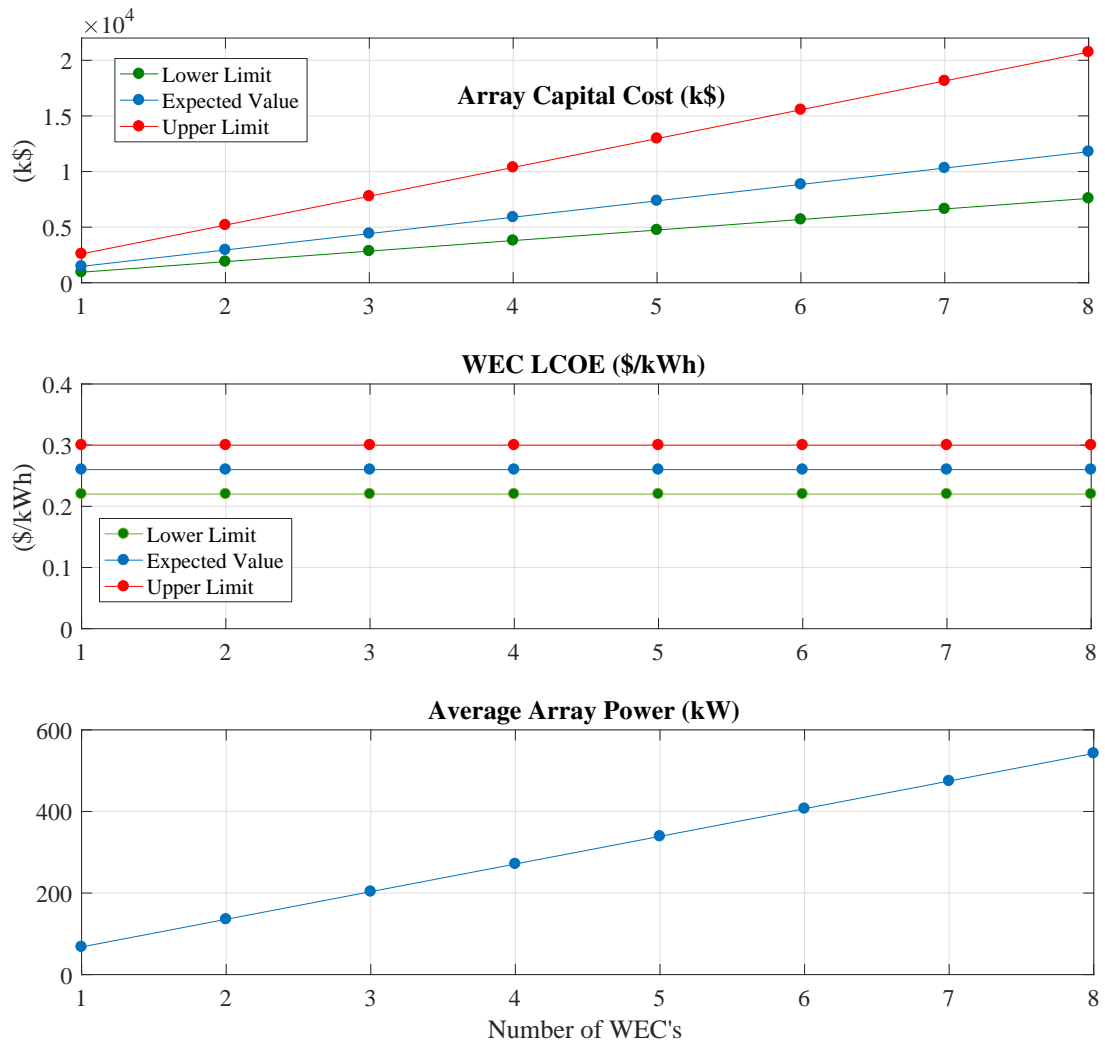


Figure 6-26: FWT-WEC cost uncertainty for an array of nonlinear oscillating water columns attached by hinges to the FWT, for an increased number of WEC's in the array. The WEC uses the optimal nonlinear spring coefficient and Wells turbine coefficient for the 3 wind-sea states representing a year in Eureka, CA.

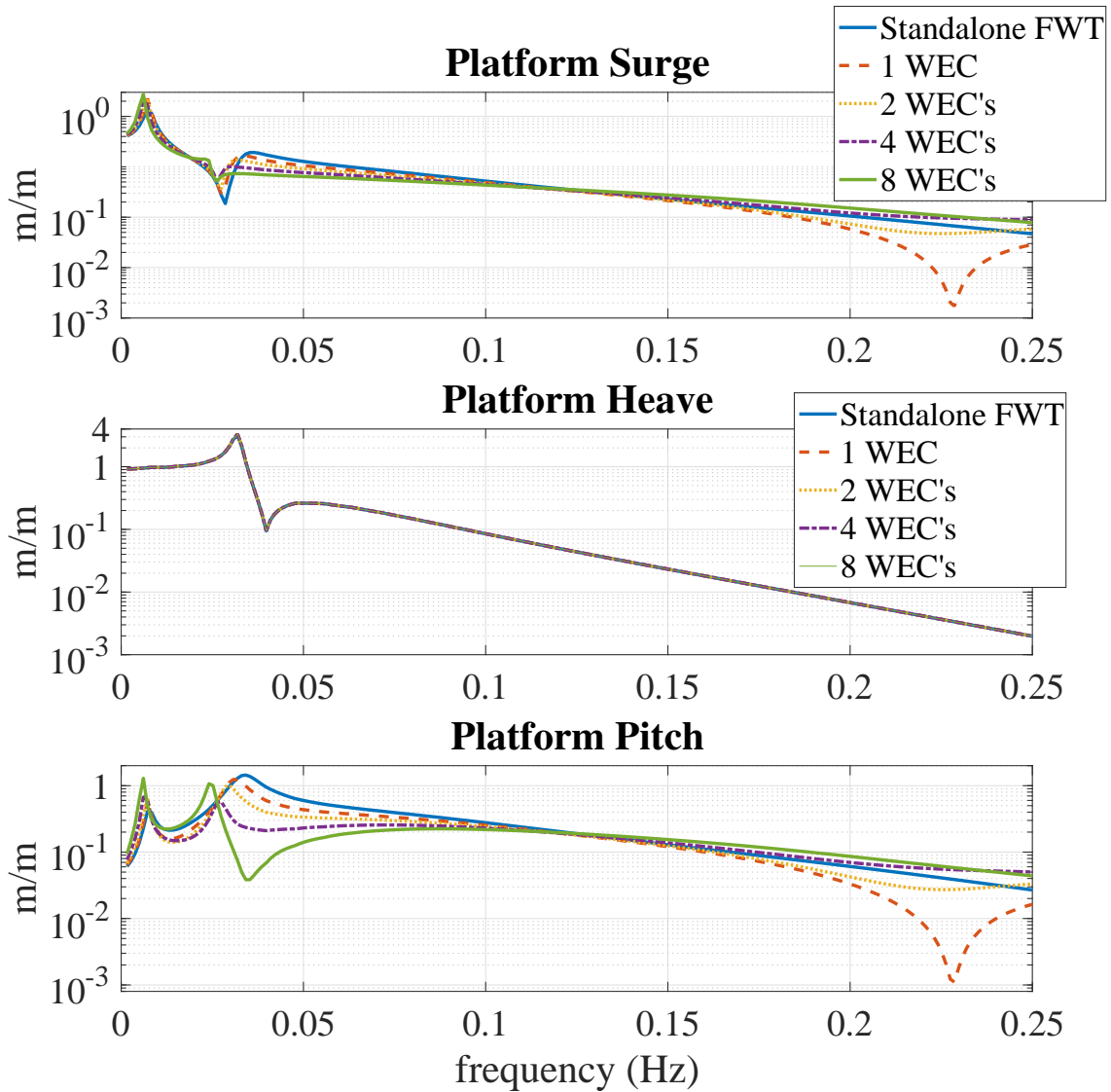


Figure 6-27: Comparison of the platform response amplitude operators for an increasing number of nonlinear WEC's in an array encircling the FWT. The WEC uses the optimal nonlinear spring coefficient and Wells turbine coefficient for the 3 wind-sea states representing a year in Eureka, CA

# Chapter 7

## Wave Tank Experiments

### 7.1 Introduction

The goal of these experiments is to verify the computed results, especially the effects of different WEC configurations on the FWT platform motion. In Section 7.2, we Froude scale the FWT and WEC's by a factor of 150, and use a plate orifice to approximate the scaled Wells turbine dynamics. In Section 7.3, we describe the 4 different WEC's tested: two rigidly-attached oscillating water columns, and two flexibly-attached oscillating water columns. Section 7.4 plots and discusses the experimental results. Trends in the experimental dynamics agree with the computed dynamics.

### 7.2 Model Scaling

#### 7.2.1 Froude scaling

We Froude scale the floating wind turbine and wave energy converters to maintain similar dynamics between the model and full scale systems. The Froude number measures the ratio of fluid inertial force to fluid weight,

$$Fr = \frac{u_0}{\sqrt{gl_0}}, \quad (7.1)$$

Table 7.1: Froude scaling

Parameter, $X$	Unit	Power, $n$
Length	$m$	1
Area	$m^2$	2
Volume	$m^3$	3
Mass	$Kg$	3
Moment of Inertia	$Kgm^2$	5
Density	$Kg/m^3$	1
Time	$s$	0.5
Frequency	$1/s$	-0.5
Force	$Kgm/s^2$	3

where  $u_0$  is the fluid velocity,  $g$  is gravitational acceleration, and  $l_0$  is a characteristic length. Maintaining the same  $Fr$  number when scaling  $l_0$  up by a factor  $\lambda$  requires increasing the velocity,  $u_0$  by  $\sqrt{\lambda}$ , or equivalently decreasing the characteristic time by  $\sqrt{\lambda}$ . We scale by the Froude number,

$$\lambda = 150, \quad (7.2)$$

so that the FWT spar keel remains approximate 30 cm above the wave tank floor. The other parameters are scaled according to,

$$X_{F.S.} = \lambda^n X_{M.S.}, \quad (7.3)$$

where  $F.S.$  is for full scale and  $M.S.$  for model scale. The value of  $n$  depends on the variable being considered, so that the model scale Froude number equals the full scale Froude number, as listed in Table 7.1.

## 7.2.2 Orifice model for a Wells Turbine

We approximate a Wells turbine effective damping coefficient by an orifice in the top of the air chamber. An orifice has the governing equation [142],

$$Q = \alpha A_{Orifice} \sqrt{\frac{2p_c}{\rho}}, \quad (7.4)$$

where

$$\alpha = f(\beta, Re_D) = \frac{C_d}{(1 - \beta^4)^{1/2}}, \quad (7.5)$$

$$\beta = \frac{D_{Orifice}}{D_{Chamber}}, \quad (7.6)$$

$$C_d \approx 0.6. \quad (7.7)$$

$q$  is the volumetric flow rate through the orifice,  $p_c$  is the gauge pressure in the chamber,  $\rho$  is the fluid density,  $C_d$  is the empirical drag coefficient,  $D_{Orifice}$  is the orifice diameter, and  $D_{Chamber}$  is the chamber cross-sectional diameter. In these experiments, we approximate the flow by a linear relationship from  $p_c = 0$  to  $p_c = p_{cMax}$ , where  $p_{cMax}$  is measured during the experimental trials,

$$Q \approx \alpha A_{Orifice} \sqrt{\frac{2p_{cMax}}{\rho} \frac{p_c}{p_{cMax}}}, \quad (7.8)$$

leading to an approximated effective Wells turbine coefficient,

$$k_{Wells} = \frac{p_c}{Q} \approx \frac{p_{cMax}}{\alpha A_{Orifice}} \sqrt{\frac{\rho}{2p_{cMax}}}. \quad (7.9)$$

### 7.3 Systems Tested

We tested a 1:150 Froude-scaled OC3-Hywind floating wind turbine with 4 different attached WEC's, shown in Figs 7-4 to 7-7. Throughout this chapter, we refer to these systems as,

- System 1: 3-OWC array, shown in Fig. 7-4,
- System 2: Large-OWC chamber, shown in Fig. 7-5,
- System 3: Linear floating oscillating water column (linFOWC), shown in Fig. 7-6,
- System 4: Nonlinear floating oscillating water column (NonFOWC), shown in Fig. 7-7.

For each system, we tested two configurations at up to 7 different monochromatic frequencies: a freely floating configuration to determine the response amplitude operators,

and a configuration where three load cells held the FWT fixed in the surge, heave, and pitch directions to determine the forcing on the platform due to the incident waves and WEC's (the flexible WEC's remained free to move). The experimental set-up is shown in Figs 7-1 to 7-3. Wave probes measured wave elevation. A Sparkfun 9DOF accelerometer was placed in the platform at the still waterline. For the tests with the flexibly-attached WEC's, the accelerometers malfunctioned, so videos of the experiments were used to track the FWT and WEC motions.

For the 3-OWC-rigid array, an Omega 5 psig silicon pressure transducer measured the pressure in the OWC air chamber. As shown in Fig. 7-4, a challenge of this approach was that the Omega pressure gauges each weigh 153 grams, so mounting the pressure gages on the WEC's sunk the structure. The solution used for the 3-OWC-rigid array tests was to mount the Omega gages on a cart next to the WEC's, and measure the air pressure using 1/4-in diameter tubes. A challenge with doing that is that the tubes may affect the dynamics. As shown in Figs 7-8 and 7-9, it fortunately seems that the FWT motion with and without the tubes is very similar. For the other 3 systems tested, we used Honeywell MPX5010 silicon pressure sensors with a 10 kPa gauge range and 10 gram mass.

For the wave force tests, load cells were mounted on a stationary cart above the wave tank and were each connected to the FWT via stinger rods: 0.086-in diameter, 5-in length rods that transmitted loads only along their axes. Two horizontal-axis load cells, placed 8.5 inches apart, connected to the FWT tower and held the FWT fixed in surge and pitch. One vertical-axis load cell connected to the top of the tower and held the FWT fixed in heave.

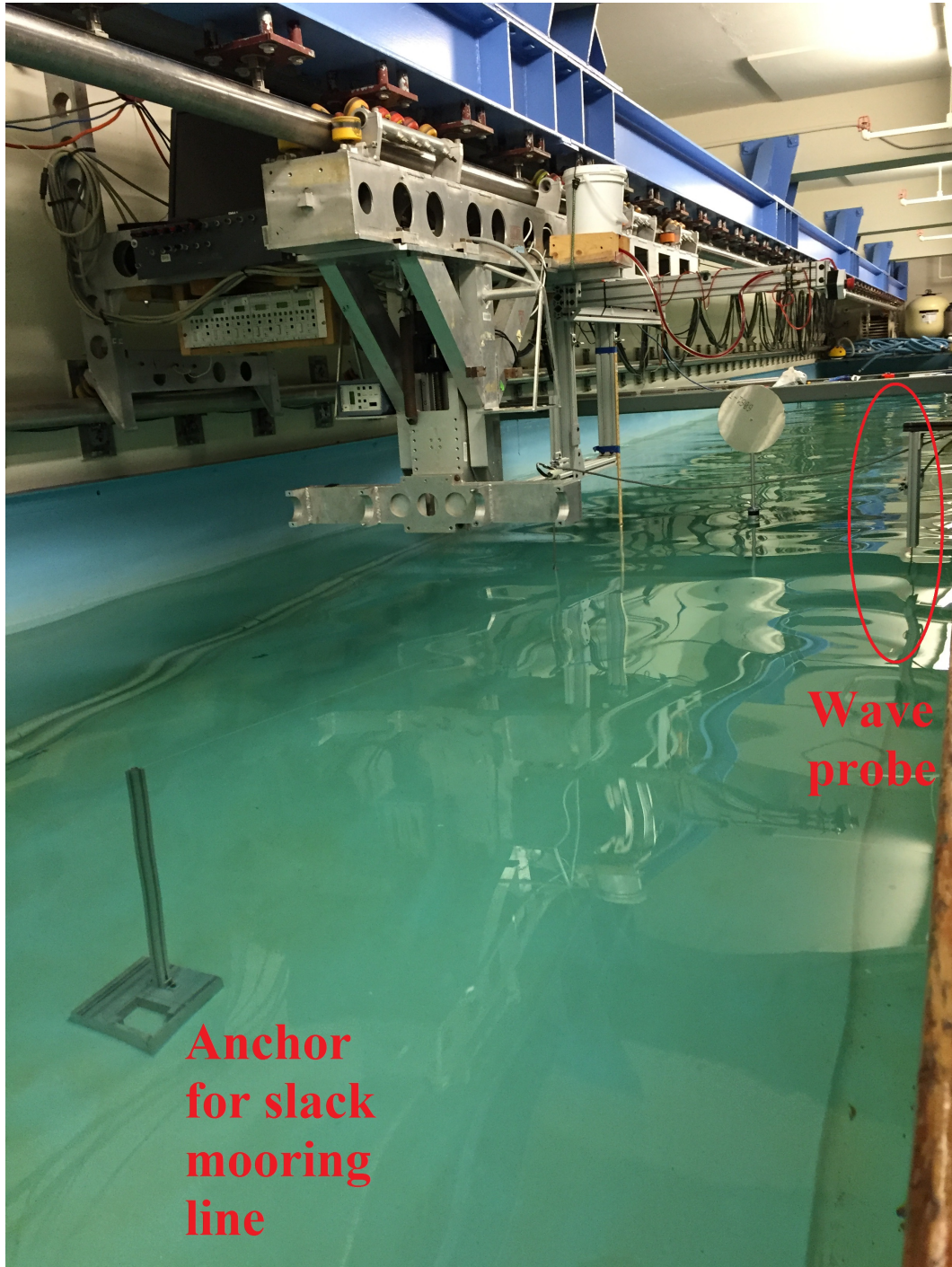


Figure 7-1: Experiment set-up in the MIT Tow Tank.



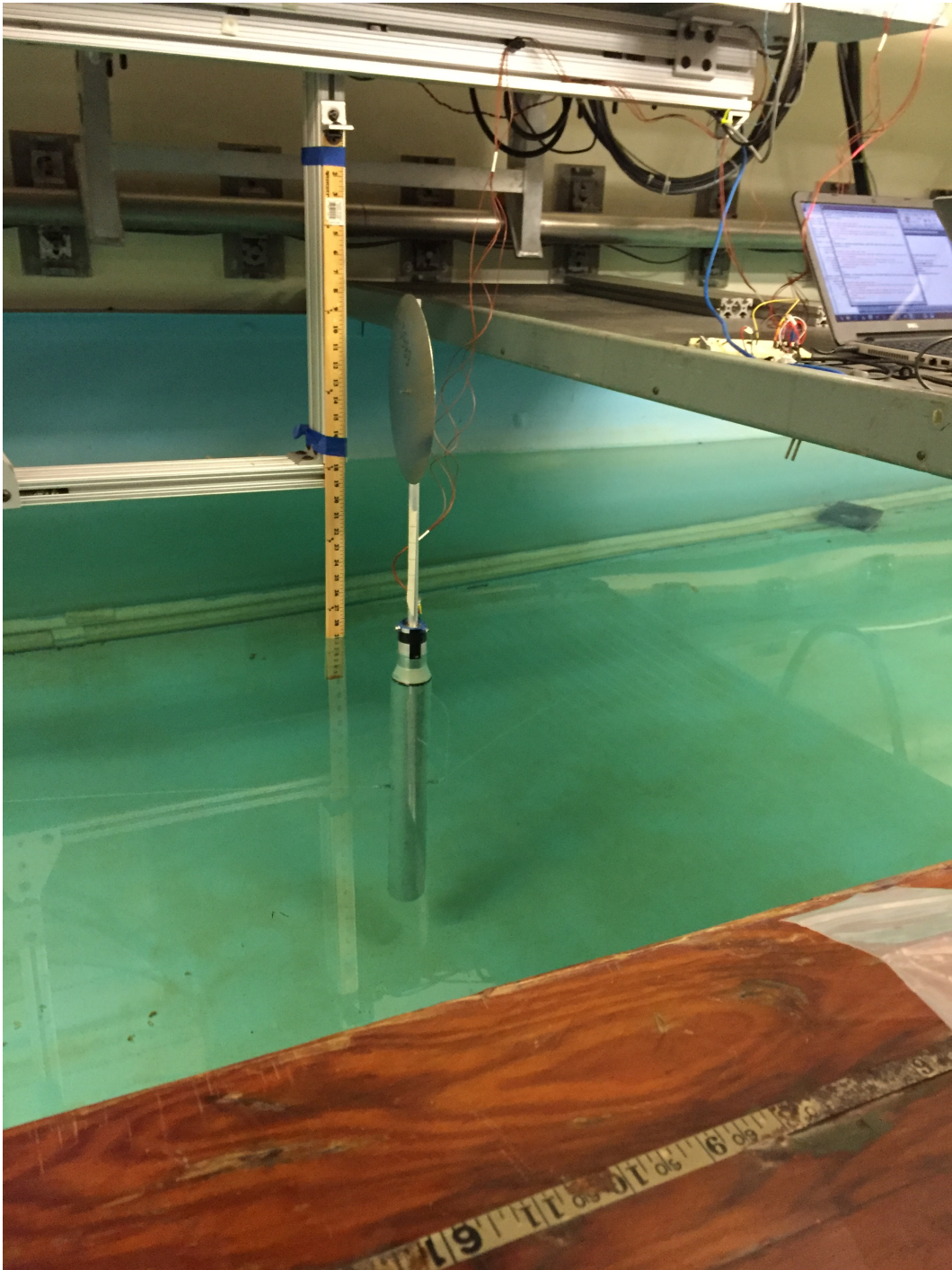


Figure 7-2: Freely floating experiment set-up.



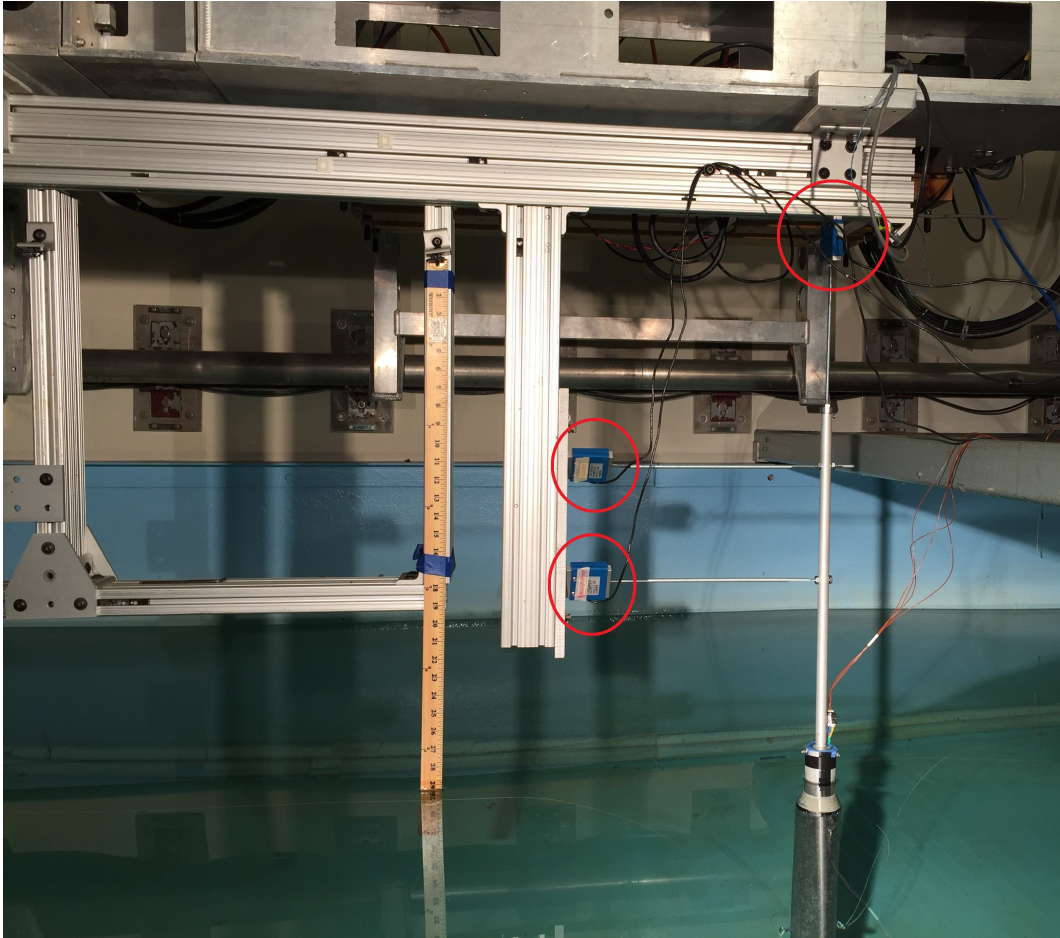


Figure 7-3: Fixed load cell experiment set-up.

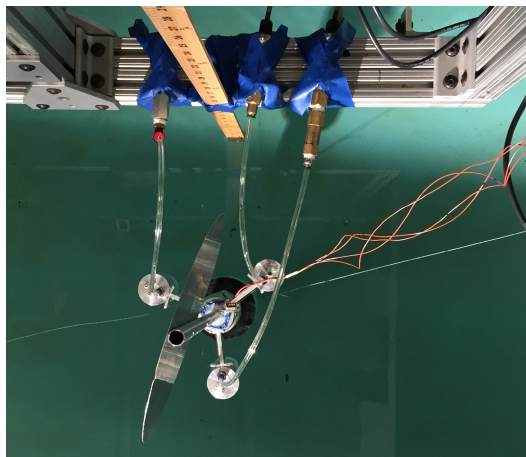
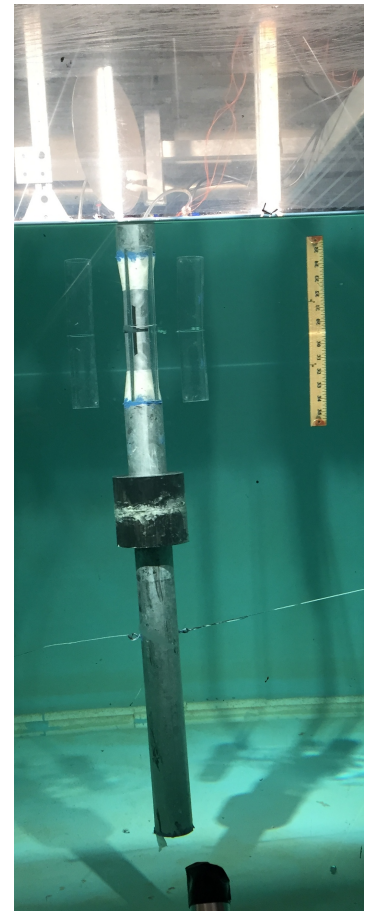
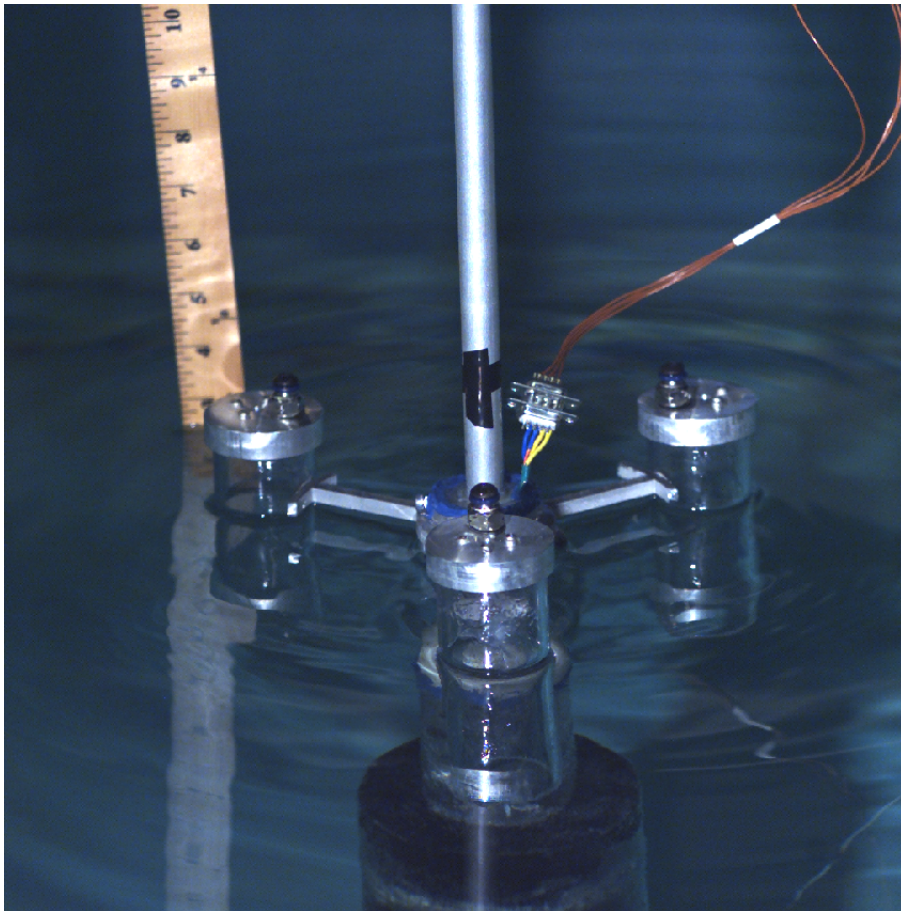


Figure 7-4: Experiment set-up for rigidly attached 3-OWC array.

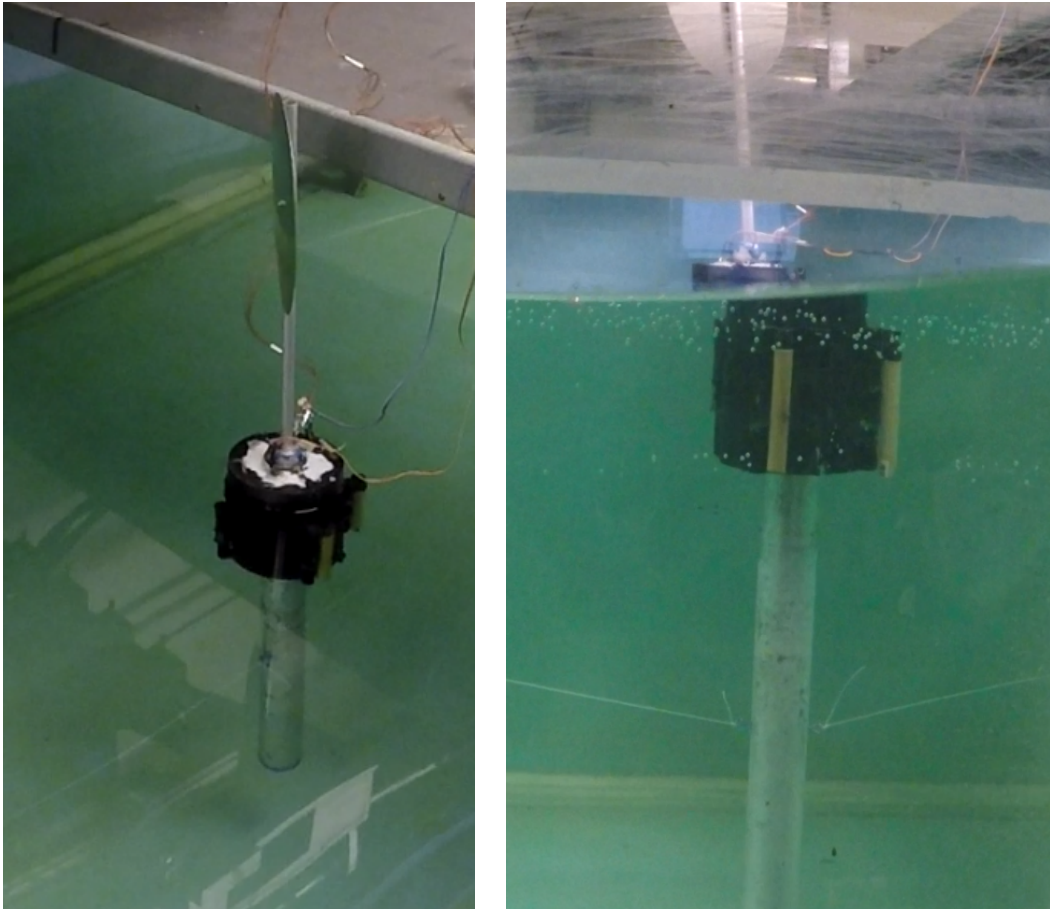
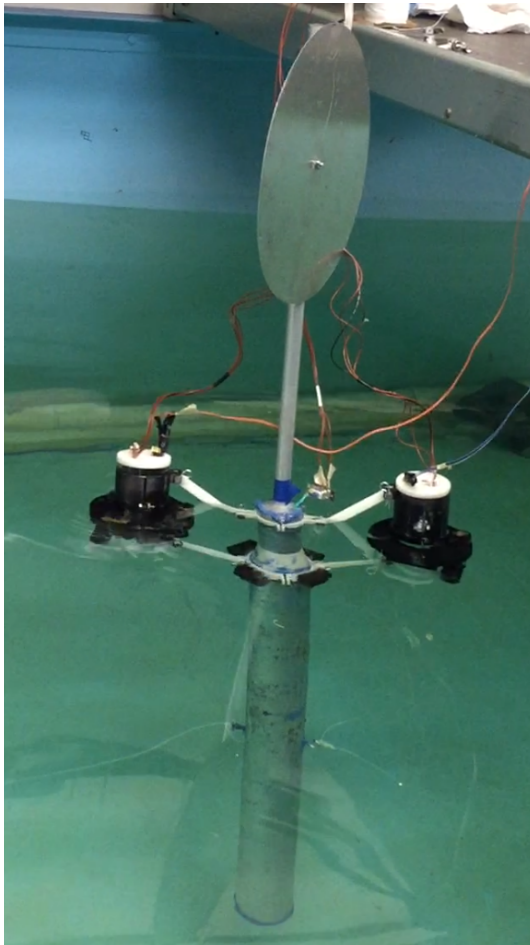
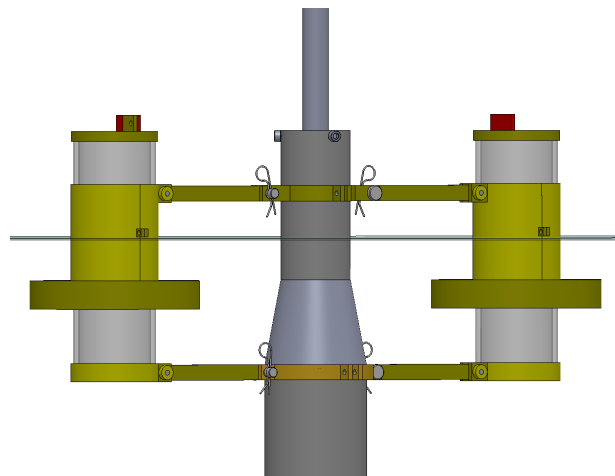


Figure 7-5: Experiment set-up for rigidly attached, large OWC chamber.



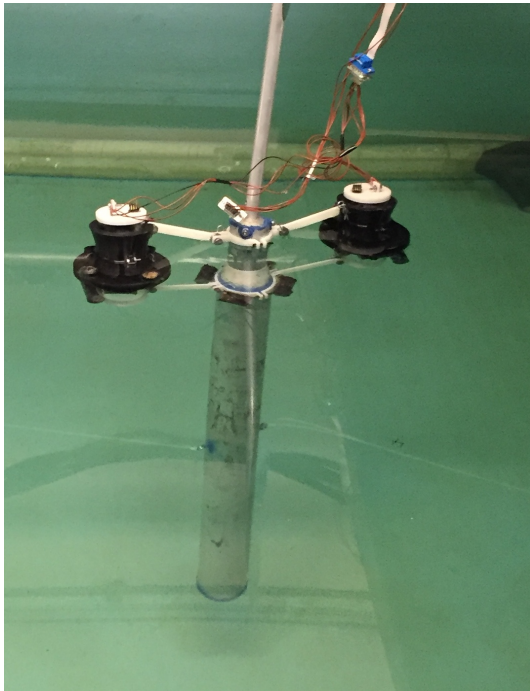


(a)

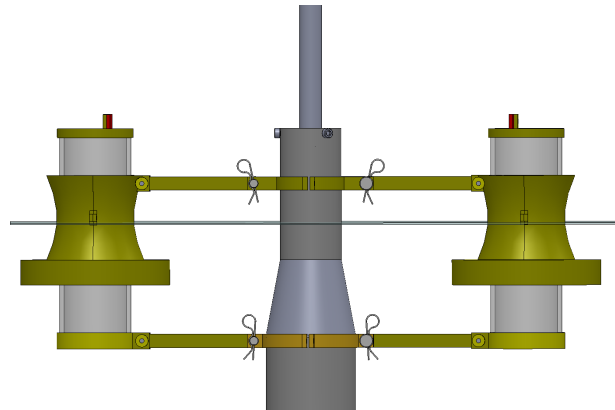


(b)

Figure 7-6: Flexibly attached linear floating OWC's: (a) experiment set-up, (b) CAD rendering with more details.



(a)



(b)

Figure 7-7: Flexibly attached nonlinear floating OWC's: (a) experiment set-up, (b) CAD rendering with more details.

Table 7.2: Parameters of the experimental rigidly-connected WEC systems

Parameter	3-OWC array		Large OWC chamber	
	Full scale	Model scale	Full scale	Model scale
OWC chamber outer radius, $r_{TubeOuter}$	3.4 m	2.3 cm	11.9 m	7.9 cm
OWC chamber wall thickness, $t_{Tube}$	0.48 m	3 mm	0.48 m	3 mm
OWC chamber total length, $L_{Tube}$	32.4 m	0.22 m	32.4 m	21.6 cm
OWC chamber submerged length, $L_{TubeSub}$	25.5 m	0.17 m	25.7 m	17.1 cm
Polycarbonate tube density, $\rho_{Polycarbonate}$	1245 Kg/m <sup>3</sup>	1245 Kg/m <sup>3</sup>	1245 Kg/m <sup>3</sup>	1245 Kg/m <sup>3</sup>
Aluminum density, $\rho_{Aluminum}$	2650 Kg/m <sup>3</sup>	2650 Kg/m <sup>3</sup>	N/A	N/A
3D printed material density, $\rho_{3Dprinted}$	N/A	N/A	403 Kg/m <sup>3</sup>	403 Kg/m <sup>3</sup>
WEC mass not counting frame, $m_W$	3.6e5 Kg	107 g	5.9e5 Kg	175 g
WEC center of mass, $\bar{z}_m$	-1.6 m	-1 cm	-11.4 m	-7.6 cm
Submerged volume used for pitch, $V_{Sub,Rotation}$	145 m <sup>3</sup>	43 cm <sup>3</sup>	9,346 m <sup>3</sup>	2,729 cm <sup>3</sup>
WEC center of buoyancy, $\bar{z}_{Buoy}$	-7.8 m	-5.2 cm	-12.8 m	8.5 cm
WEC still water line area, $A_{SWL}$	17.9 m <sup>2</sup>	7.95 cm <sup>2</sup>	34.0 m <sup>2</sup>	15.1 cm <sup>2</sup>
Water column cross-sectional area, $A_{Col}$	34.9 m <sup>2</sup>	1.56e-3 m <sup>2</sup>	34.9 m <sup>2</sup>	1.56e-3 m <sup>2</sup>
Orifice diameter, $D_{orifice}$	0.45 m	3.0 mm	0.3 m	2 mm
Wells turbine coefficient, $k_{Wells}$	2500 Pa/m <sup>3</sup>	5.6e7 Pa/m <sup>3</sup>	2500 Pa/m <sup>3</sup>	5.6e7 Pa/m <sup>3</sup>
Array arm $L$	17.2 m	0.115 cm	0	0
Array WEC angle spacing in $x - y$ plane	120°	120°	N/A	N/A
Cylinder ballast depth	-46 m	0.31 m	N/A	N/A
Cylinder ballast outer radius	9.0 m	6 cm	N/A	N/A
Cylinder ballast length	16 m	10.6 m	N/A	N/A
Cylinder ballast density	403 Kg/m <sup>3</sup>	403 Kg/m <sup>3</sup>	N/A	N/A

Table 7.3: Parameters of the experimental flexibly-connected WEC systems

Parameter	Linear Floating OWC's		Nonlinear Floating OWC's	
	Full scale	Model scale	Full scale	Model scale
Float radius, $r_{Float}$	7.95	0.053 m	7.95	0.053 m
Float height, $H_{Float}$	2.7	0.01778 m	2.7	0.01778 m
Effective $H_{Float}$	3.75	.025 m	3.75	.025 m
Float submergence, $L_{Z,Float}$	-5.36 m	-0.0357 m	-5.36 m	-0.0357 m
OWC chamber outer radius, $r_{TubeOuter}$	3.81	0.0254 m	3.81	0.0254 m
OWC chamber wall thickness, $t_{Tube}$	0.477 m	3.17 mm	0.477 m	3.17 mm
Tube encasing radius at SWL, $r_{outSWLMod,SWL}$	<b>4.10 m</b>	<b>0.027335 m</b>	<b>4.10 m</b>	<b>0.027335 m</b>
Tube encasing maximum radius, $r_{outSWLMod,Max}$	<b>4.10 m</b>	<b>0.027335 m</b>	<b>5.211 m</b>	<b>.03474 m</b>
Linear heave hydrostatic stiffness, $C_{33Lin}$	1.80e5 N/m	12.3 N/m	1.80e5 N/m	12.3 N/m
Nonlinear heave hydrostatic stiffness, $C_{33non}$	<b>0</b>	<b>0</b>	<b>1.60e4 N/m<sup>3</sup></b>	<b>1.60e4 N/m<sup>3</sup></b>
Tube encasing submerged length, $L_{SWLMod,Sub}$	4.5 m	0.03 m	4.5 m	0.03 m
OWC chamber total length, $L_{Tube}$	22.5	0.15 m	22.5	0.15 m
OWC chamber submerged length, $L_{TubeSub}$	13.4	0.089 m	13.4	0.089 m
Polycarbonate tube density, $\rho_{Polycarbonate}$	1245 Kg/m <sup>3</sup>	1245 Kg/m <sup>3</sup>	1245 Kg/m <sup>3</sup>	1245 Kg/m <sup>3</sup>
3D printed material density, $\rho_{3Dprinted}$	403 Kg/m <sup>3</sup>	403 Kg/m <sup>3</sup>	403 Kg/m <sup>3</sup>	403 Kg/m <sup>3</sup>
WEC mass, $m_W$	$5.2 \times 10^5$ Kg	153.8 g	$5.2 \times 10^5$ Kg	153.8 g
WEC center of mass, $\bar{z}_m$	-3 m	-0.02 m	-3 m	-0.02 m
Submerged volume used for pitch, $V_{Sub}$	$3.37 \times 10^2$ m <sup>3</sup>	$1.54 \times 10^{-4}$ m <sup>3</sup>	$3.37 \times 10^2$ m <sup>3</sup>	$1.54 \times 10^{-4}$ m <sup>3</sup>
WEC center of buoyancy, $\bar{z}_{Buoy}$	-6.75 m	-0.045 m	-6.75 m	-0.045 m
WEC still water line area, $A_{SWL}$	17.9 m <sup>2</sup>	$7.956 \times 10^{-4}$ m <sup>2</sup>	17.9 m <sup>2</sup>	$7.956 \times 10^{-4}$ m <sup>2</sup>
Front WEC x-coordinate, $L_{xW1}$	-13.5 m	-0.09 m	-13.5 m	-0.09 m
Rear WEC x-coordinate, $L_{xW2}$	13.5 m	0.09 m	13.5 m	0.09 m
Water column cross-sectional area, $A_{Col}$	34.9 m <sup>2</sup>	1.56e-3 m <sup>2</sup>	34.9 m <sup>2</sup>	1.56e-3 m <sup>2</sup>
Orifice diameter, $D_{orifice}$	0.45 m	3 mm	0.45 m	3 mm
Wells turbine coefficient, $k_{Wells}$	2500 Pa/m <sup>3</sup>	5.6e7 Pa/m <sup>3</sup>	2500 Pa/m <sup>3</sup>	5.6e7 Pa/m <sup>3</sup>

The full-scale mass rotational inertia about  $(0, 0, \bar{z}_m)$  for the large OWC chamber is,

$$I_{Full, Large OWC} = \begin{bmatrix} 4.7e3 & 0 & 0 \\ 0 & 4.7e3 & 0 \\ 0 & 0 & 3.1e3 \end{bmatrix}, \quad (7.10)$$

with units of  $Kgm^2$ .

The full-scale mass rotational inertia about  $(L_{xW}, 0, 0)$  for the 3-OWC array, including

the aluminum frame and all 3 aluminum tube caps and polycarbonate tubes is,

$$I_{\text{Full, 3-OWC}} = \begin{bmatrix} 4.9e12 & -3.2e12 & 9.8e10 \\ -3.2e12 & 2.1e12 & -1.5e11 \\ 9.8e10 & -1.5e11 & 7.0e12 \end{bmatrix}, \quad (7.11)$$

with units of  $Kgm^2$ .

The flexibly-connected WEC's each have full scale mass rotational inertia about  $(L_{xW1}, 0, \bar{z}_m)$ ,

$$I_{\text{Model}} = \begin{bmatrix} 2.6e7 & 1.2e5 & 4.0e4 \\ 1.2e5 & 2.3e7 & 4.9e4 \\ 4.0e4 & 4.9e4 & 1.1e7 \end{bmatrix}, \quad (7.12)$$

with units of  $Kgm^2$ .

The added mass  $\mathbf{A}$ , hydrodynamic damping  $\mathbf{B}$ , and wave forcing  $\vec{F}$ , are frequency-dependent and computed using the Haskind and G.I. Taylor long wavelength approximations, described in Chapter 2.

## 7.4 Results and Discussion

Figs 7-8 to 7-13 compare the experimental and theoretical responses of the different systems.

Figs 7-8 and 7-9 shows the surge, heave, pitch, and pressure response amplitude operators for the two WEC systems that are rigidly attached to the FWT. Fig. 7-10 shows the surge, heave, and pitch wave forces for the two WEC systems that are rigidly attached to the FWT.

The theoretical and experimental trends agree at most frequencies: Both the large OWC chamber and 3-OWC array decrease the surge and pitch resonant peak at 0.033 Hz. In heave, the OWC chamber shifts the FWT heave resonant peak to a higher frequency: the theoretical undamped natural frequency is 0.043 Hz. Both theoretically and experimentally, large Wells turbine damping expands the resonant response peak width. The theory



does not capture the increased heave responses of both the 3-OWC and large OWC system between 0.033 and 0.06 Hz. At larger frequencies, the 3-OWC array decreases the surge, heave, and pitch response while the large OWC chamber increases all three response amplitudes. We note that the 3-OWC system is a lot heavier than the large OWC system and has a submerged ballast- both of which contribute to a smaller response amplitude and larger cost.

The large OWC system pressure measurements agree closely with the theory. The 3-OWC pressure measurements are off- possibly because of inaccuracies of the Omega sensor set-up or because the large orifice diameter invalidates the theory used to estimate the orifice damping coefficient.

The 3-OWC array and large OWC chamber both increase the surge force by nearly identical amounts at frequencies below 0.08 Hz. At higher frequencies, the 3-OWC array theoretically has less surge forcing than the large OWC chamber system. At large frequencies, the theory underestimates the surge force on the large OWC and overestimates the surge force on the 3-OWC array system, compared to the experiments. The experiment and theoretical trends in pitch torque agree for the large OWC system, but the theory underestimates the magnitude. Pitch torque was not measured for the 3-OWC system due to a loosening of the epoxyed tower base during those trials. The theoretical and experimental trends agree for heave forcing of both the 3-OWC and large OWC systems, but the theory generally underestimates the 3-OWC forcing magnitude and overestimates the peak frequency of the large OWC forcing.

Figs 7-11 and 7-12 show the surge, heave, and pitch response amplitude operators for the two WEC systems that are flexibly attached to the FWT. Fig. 7-13 shows the surge, heave, and pitch wave forces for the two WEC systems that are flexibly attached to the FWT.

Some experimental and theoretical trends agree: the FWT surge resonant response at 0.033 Hz is reduced, and the surge response converges to match the FWT alone at larger frequencies. In heave, the resonant response is shifted to a higher frequency and reduced in magnitude. Rear nonlinear FOWC pressure measurements agree closely with the theory while front nonlinear FOWC pressure measurements exceed the theory- possibly related to

wave reflection and shielding by the FWT. The front linear FOWC pressure measurements generally agree with the front nonlinear FOWC, while large over and under-performance is shown for the linear WEC.

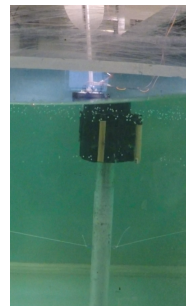
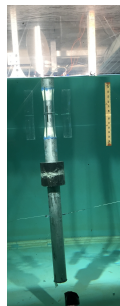
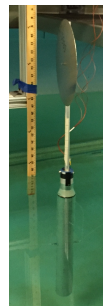
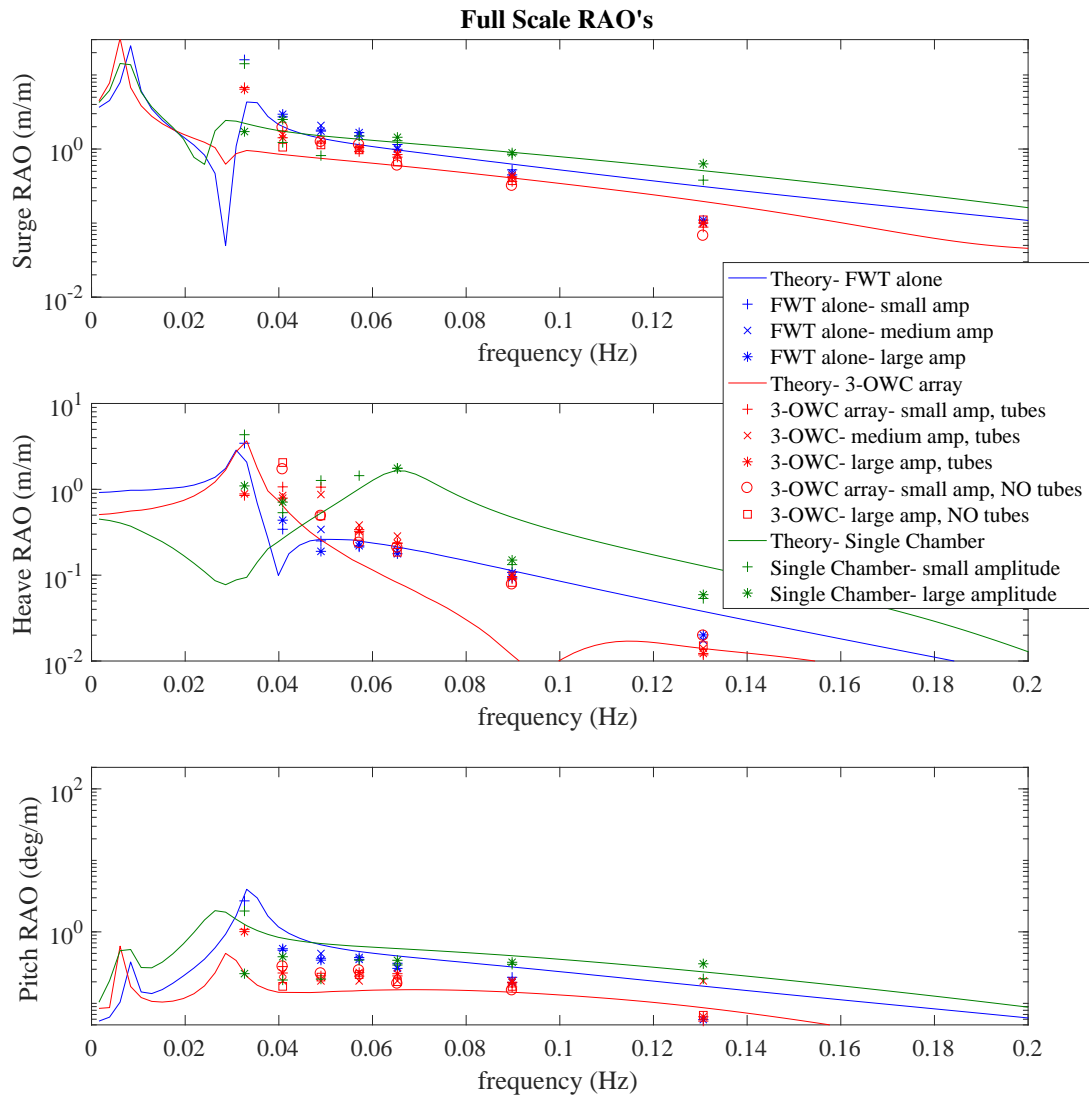
This experiment had several errors that should be avoided in future work: because of buoyancy issues, the equilibrium angle of the links was not at 0, coupling between the FWT and WEC heave modes was significant (the theory uses small angle assumptions and assumes the heave coupling is negligible). Heave coupling may also have been due to resistance at the pivot points. These issues contribute to the FWT and WEC's having similar responses rather than different responses, which is the goal of the joint coupling.

Another error was that the nonlinear FOWC did not have a sufficiently extreme increase in the radius along its  $z$  axis. This error was due to an error in the computation and rapid prototyping. The error causes the nonlinear FOWC to respond almost identically to the linear FOWC.

Finally, a third error was that the accelerometers in the FWT and WEC malfunctioned, so they did not record data. Fortunately, videos of the FWT-WEC's served as back-up data, but they did not have the same resolution as the accelerometers.

In terms of which FWT-WEC system shows the best results: we can conclude that rigidly attaching a heavy WEC to the platform, with a submerged ballast significantly reduces the FWT motion, but we expect that this is not cost-effective, so it is not a good option. Rigidly attaching a large OWC chamber to the platform is also not a good option because it increases the FWT platform motion. We experimentally verified that flexibly attaching WEC's with a small frontal area that is aligned with the FWT frontal area decreases the surge motion. We expect that the WEC's similarly decrease the pitch motion, although we did not collect this data due to the accelerometer malfunction. While the experiments show that the flexibly-attached WEC's significantly increased the FWT heave motion, the experiments also provide evidence that this occurred due to experimental set-up errors: 1. the hinges were not at an equilibrium horizontal position, which we expect would decrease the FWT-WEC heave coupling; 2. the FWT and WEC's have almost identical heave motion, which suggests that the hinges did not work properly; and 3. the FWT heave forcing data (Fig. 7-13 shows that the nonlinear WEC had only a small increase in

the heave forcing. The heave forcing test may have had better adjusted WEC buoyancy (and hinge equilibrium angle) than the heave motion test. For these reasons, we conclude that a flexibly attached WEC that causes a minimal surge frontal area increase to the FWT structure may decrease the FWT surge and pitch motion while having a minimal effect on the FWT heave motion.



FWT alone

3-OWC

Single Large OWC

Figure 7-8: Comparison of experimental motion results for the FWT alone and two rigidly connected WEC arrays.

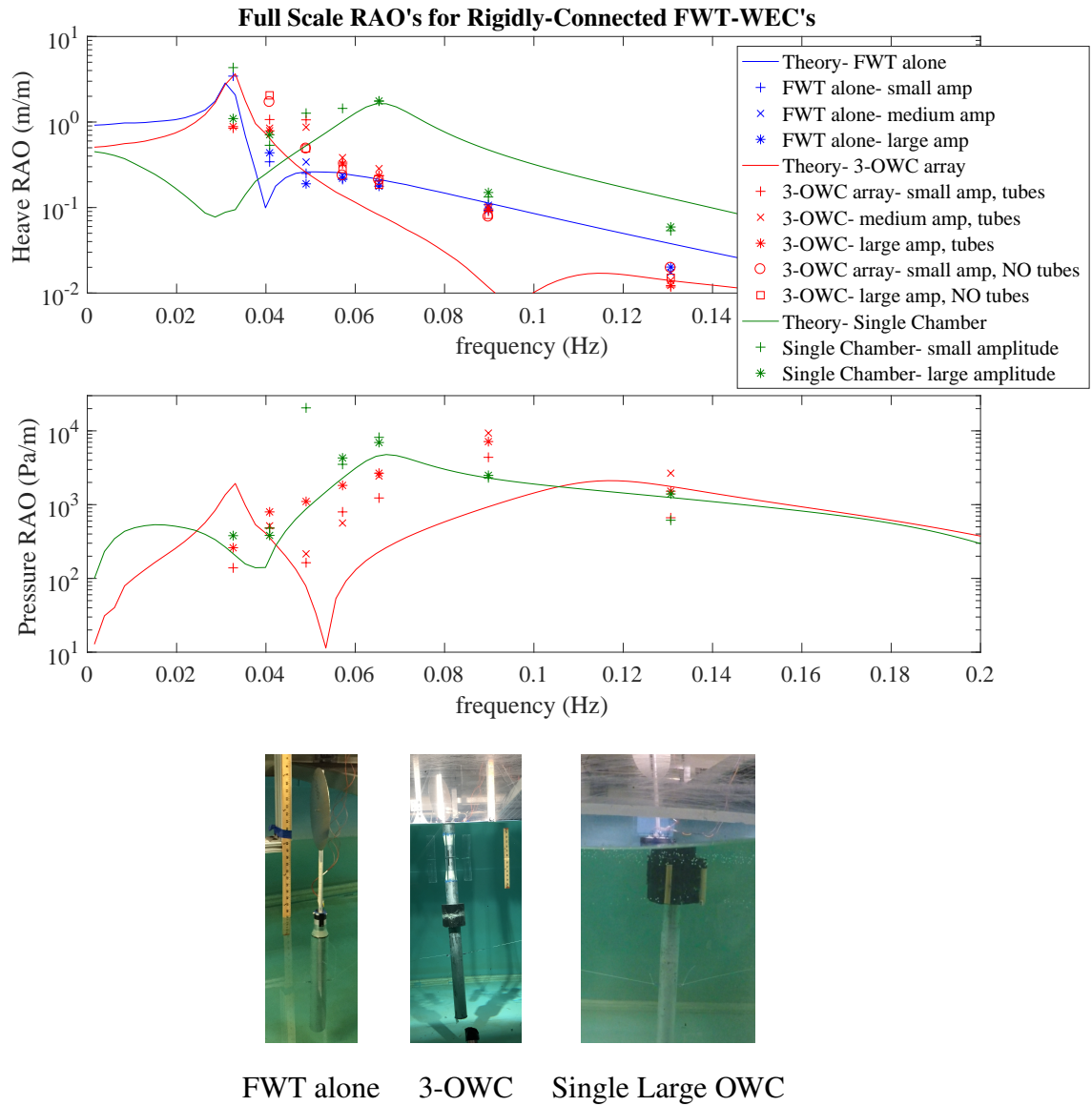
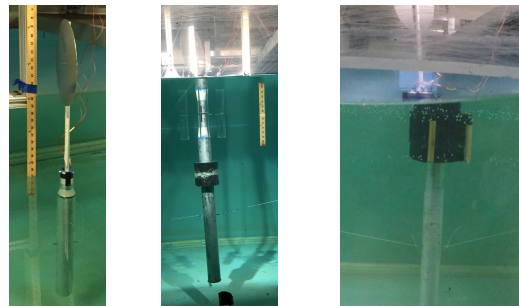
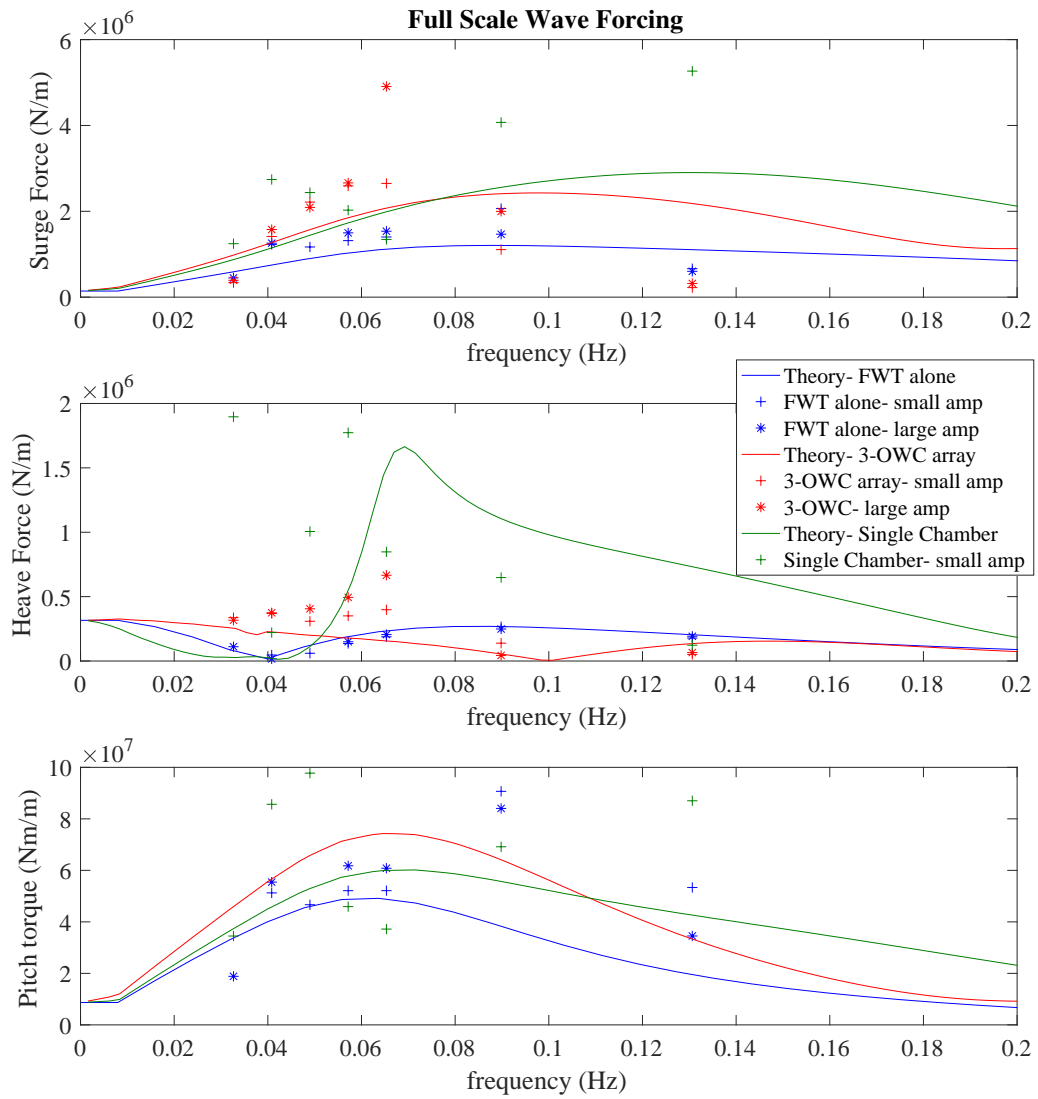


Figure 7-9: Comparison of heave motion and chamber pressure experimental results for the FWT alone and two rigidly connected WEC arrays.



FWT alone    3-OWC    Single Large OWC

Figure 7-10: Comparison of experimental forcing results for the FWT alone and two rigidly connected WEC arrays.

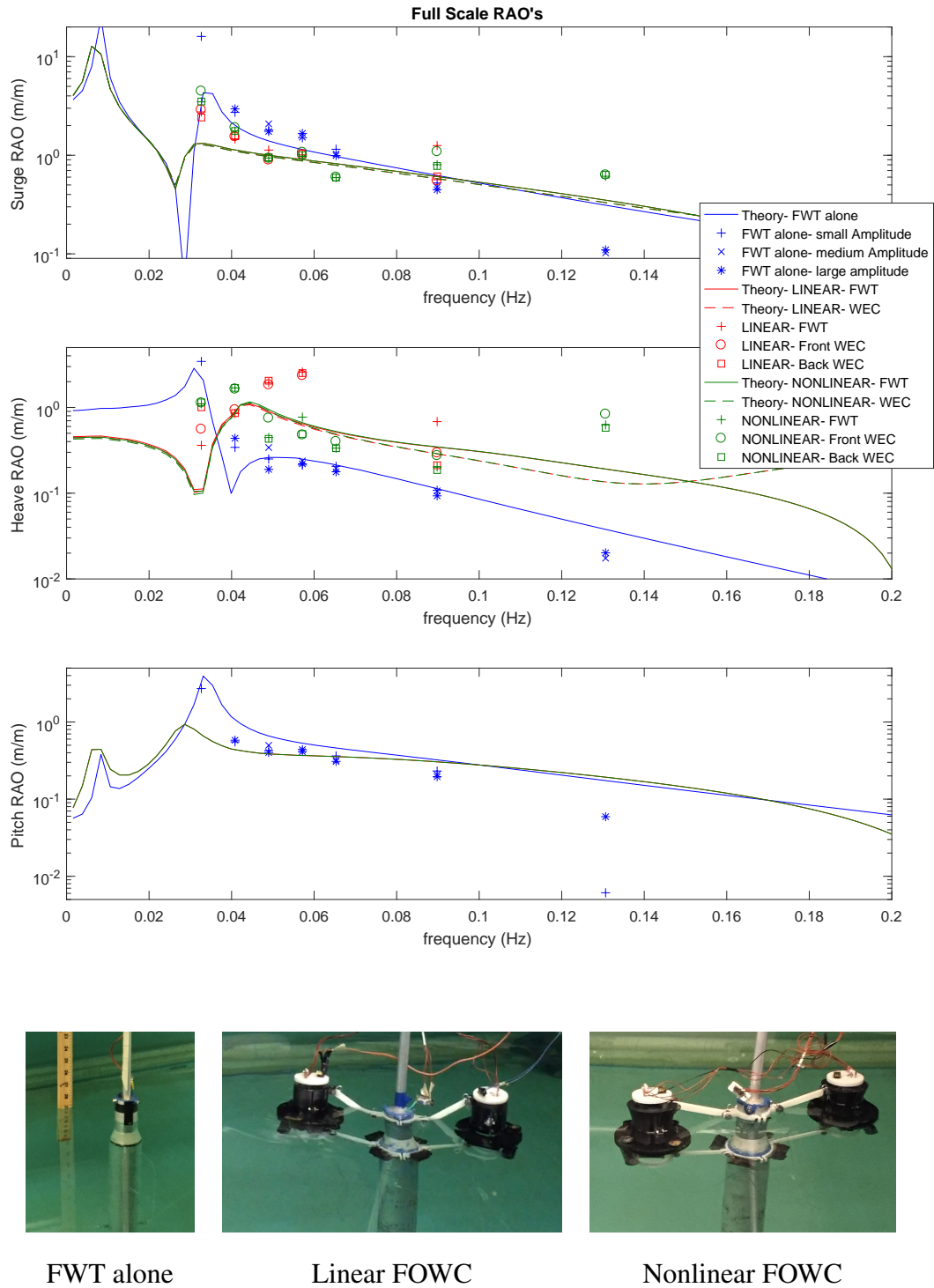
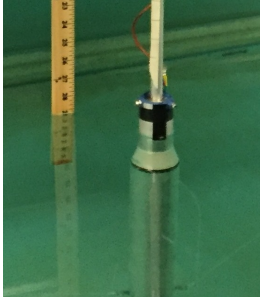
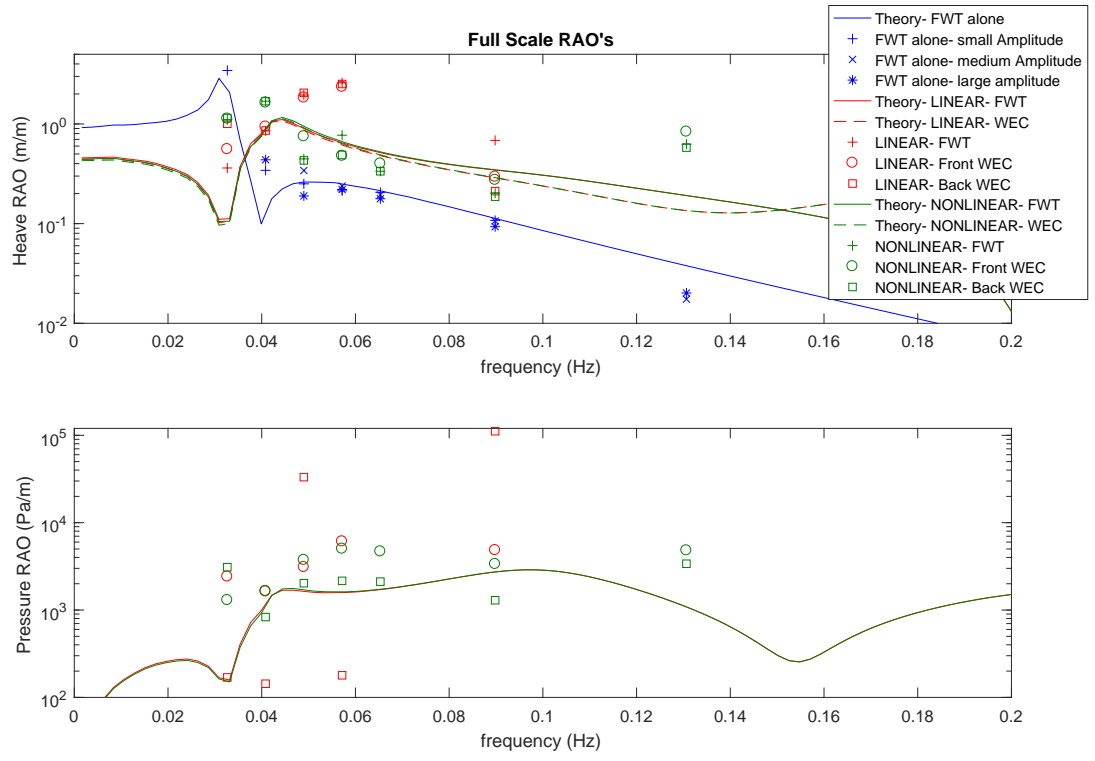


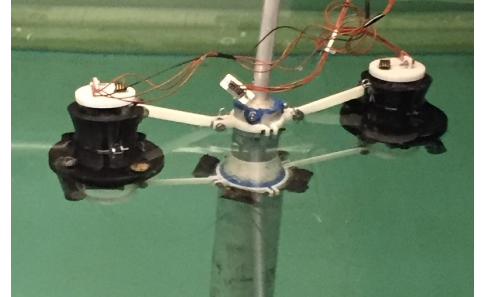
Figure 7-11: Comparison of experimental motion results for the FWT alone and two flexibly connected WEC arrays.



FWT alone



Linear FOWC



Nonlinear FOWC

Figure 7-12: Comparison of heave motion and chamber pressure experimental results for the FWT alone and two flexibly connected WEC arrays.



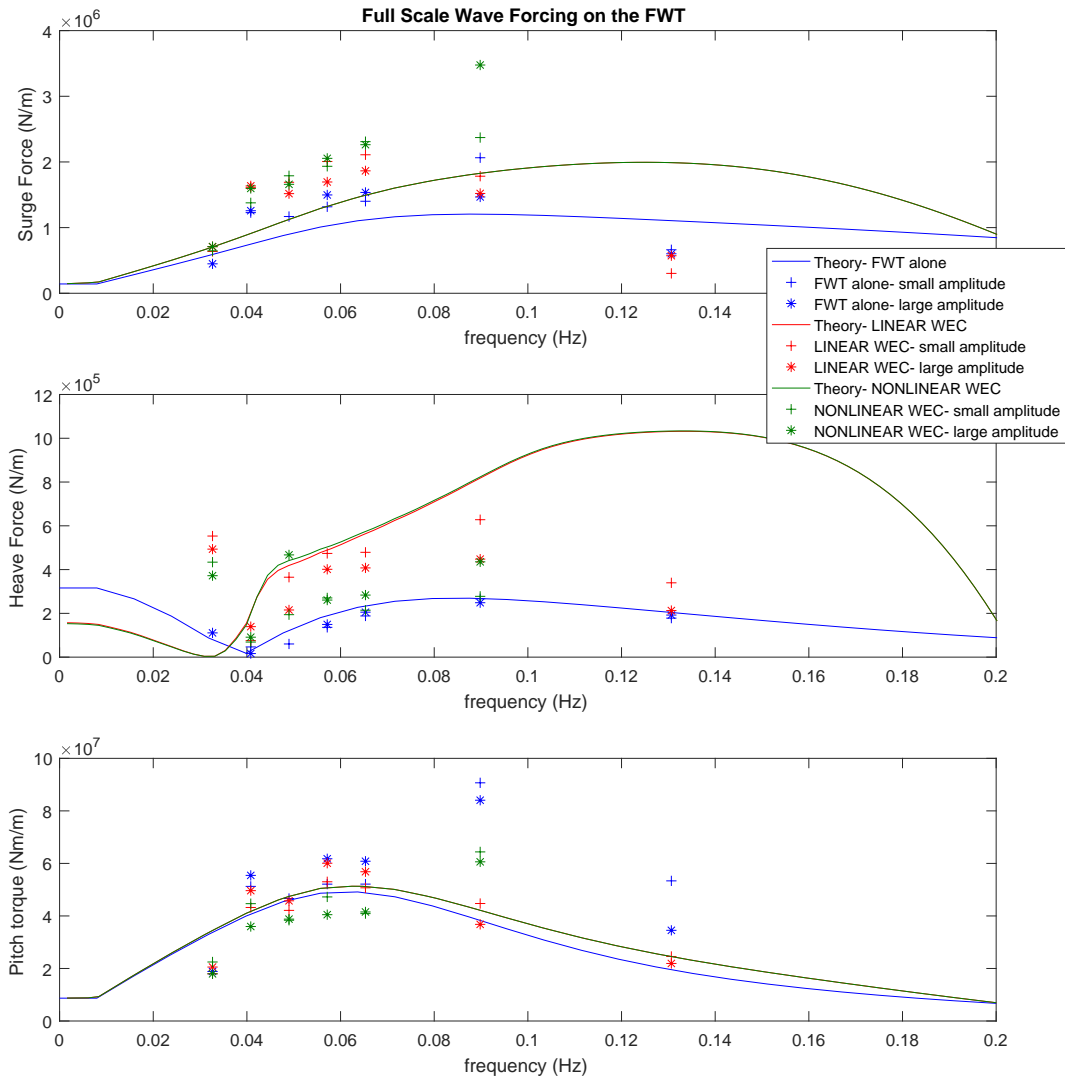


Figure 7-13: Comparison of experimental forcing results for the FWT alone and two flexibly connected WEC arrays.



# Chapter 8

## Conclusions and Future Work

This Ph.D. investigated optimizing the mechanical structure of a WEC attached to a FWT with the goal of WEC power maximization and FWT motion minimization. Fig. 8-1 shows the design flow chart used for determining the optimal WEC. Table 8.1 summarizes the WEC's considered and their performance results. Main findings of this Ph.D. include:

1. We developed a statistical linearization method for computing the FWT and WEC response statistics with high computational efficiency (76 times better than time domain simulations) while accounting for nonlinearities (traditional Taylor series linearization may underpredict tower fatigue stress by 15% in some sea states).
2. Using a long wavelength hydrodynamics model, we computed the dynamics statistics of structurally coupled FWT-WEC's. We found that the best structural coupling for a heave-mode WEC is weak coupling in heave and rigid coupling in surge and pitch. This is because the WEC can add inertial resistance to the FWT lateral motion, but structural coupling in the heave direction adds more forcing than inertial resistance to the FWT and increases the FWT's resonant frequency.
3. We developed a simple WEC cost model and power takeoff constraints. Combining the WEC to the FWT removes approximately 19% of the standalone WEC capital cost associated with mooring lines and infrastructure (electric lines and maintenance vessels).

4. We found that linking a single linear floating oscillating water column (OWC) to the FWT by a horizontal hinge had the positive effects of reducing the WEC levelized cost of energy by 13%, reducing the FWT surge motion by 12%, reducing the FWT maximum pitch motion by 13%, and having a negligible effect on the FWT tower stress. This WEC has a water column radius of 4 m and submerged float radius of 8.5 m, and can generate 51 kW average power.
5. Adding a nonlinear hydrostatic stiffness of  $C_{33Wn} = 3.2e5 \text{ N/m}^3$  to the floating OWC tube increased the WEC power performance to 87 kW (70% increase compared to the optimized linear WEC). This added nonlinearity increased the heave forcing cross-sectional area radius to 10.4 m, and increased the WEC steel from 210 tons to 330 tons (57%). This FWT-nonlinear-WEC design had a reduced levelized cost of energy (16%), reduced FWT surge motion (16%), reduced FWT pitch motion (21%), and reduced FWT tower equivalent fatigue stress (6%) compared to the baseline standalone FWT and standalone linear WEC.
6. Attaching multiple WEC's to the FWT in an array continues the trends in WEC power production and FWT platform motion found by attaching a single WEC.
7. We experimentally validated the FWT-WEC dynamics model in wave tank experiments, for which different WEC configurations had different stabilizing or destabilizing effects on the FWT platform motion.

Future work on this project could include:

- Applying the method of statistical linearization to improve FWT rotor control.
- Considering a WEC with a more optimized levelized cost of energy, such as a surge converter, or the other WEC's listed in Fig. 1-6.
- Considering a more detailed hydrodynamics model that incorporates FWT and WEC hydrodynamic coupling.
- Experimentally testing a more mechanically robust and more strongly nonlinear WEC model in the wave tank.

- Considering other nonlinearities such as latching and Coulomb damping for improved WEC power performance.
- Reducing the FWT platform steel of a combined FWT-WEC to achieve cost savings.
- Continuing to explore the parameter options for improved performance.
- Investigating the cost effects of a nonlinear structure versus electronic control. As shown in Chapter 6, a WEC with a nonlinear hydrostatic stiffness can have an improved levelized cost of energy compared to a linear WEC due to how its effective linear stiffness adapts to different sea states. Using controls to adjust effective linear stiffness in place of the nonlinearity to achieve adaptability may be more or less cost effective.
- Considering the dynamics and cost effects of using fly ash as FWT platform ballast instead of concrete. This could be a synergistic role for coal waste product to reduce the FWT ballast cost and landfill.

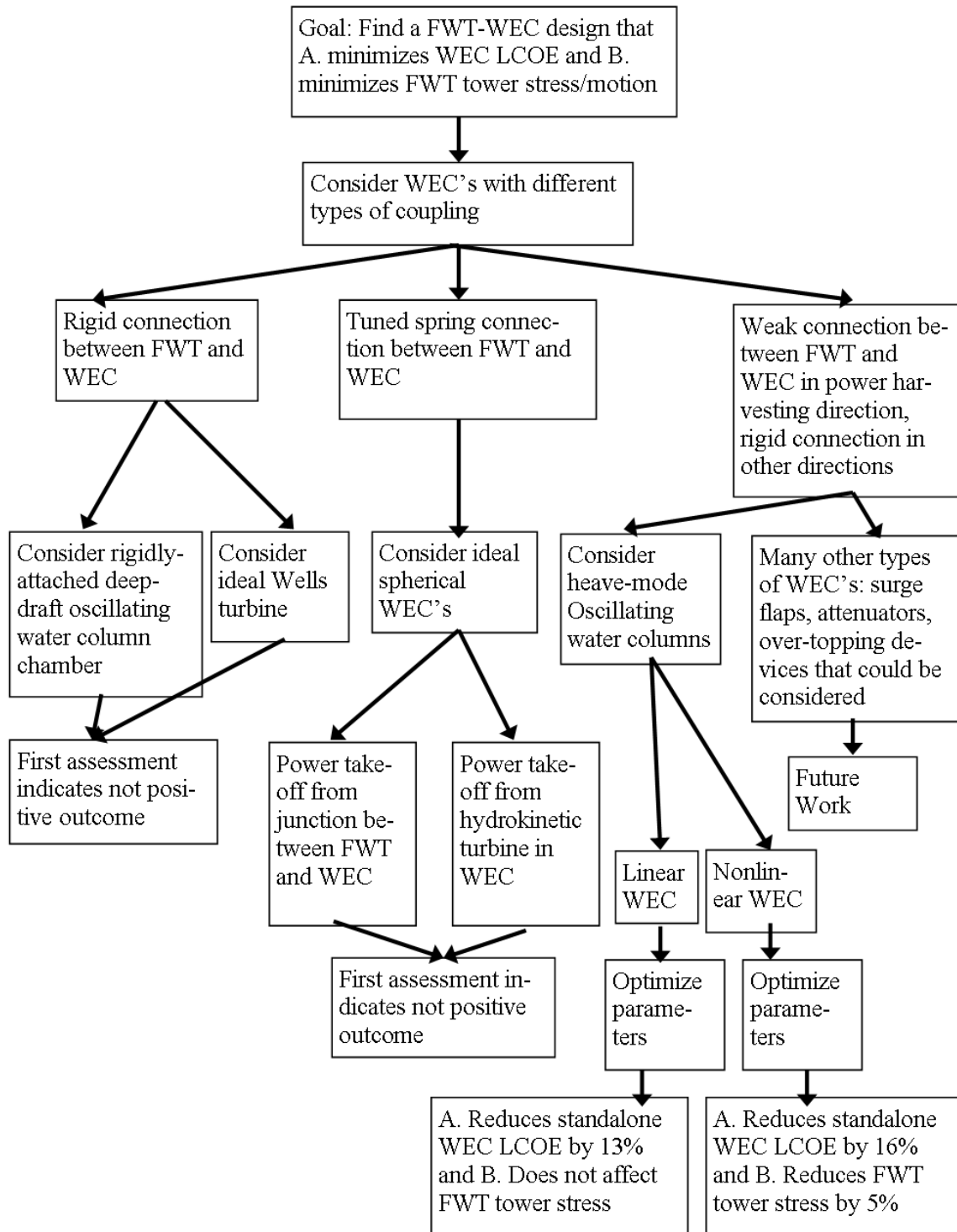
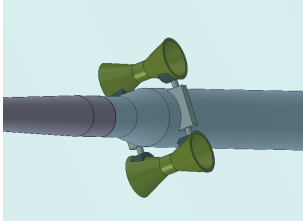
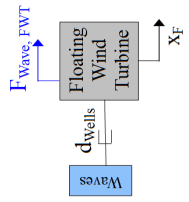
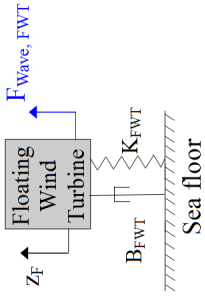
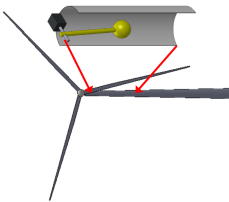
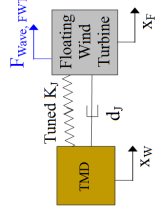
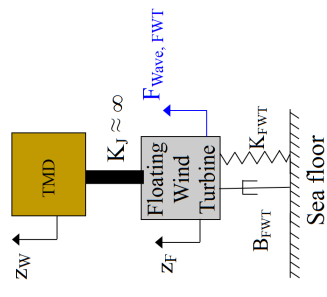


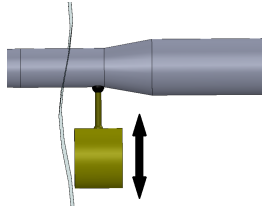
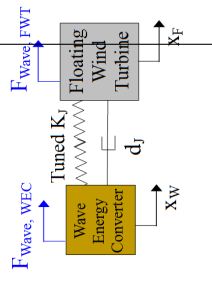
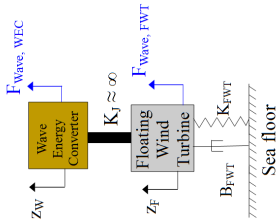
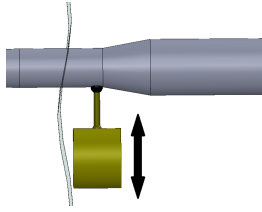
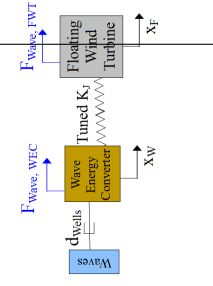
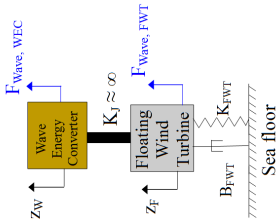
Figure 8-1: Thesis design flow chart.

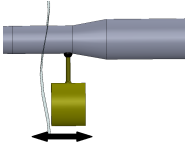
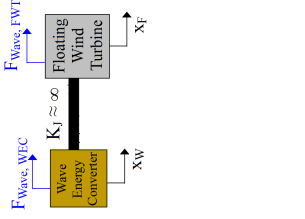
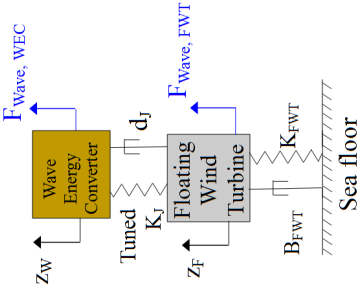
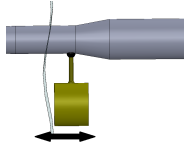
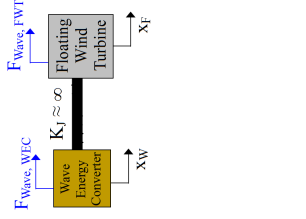
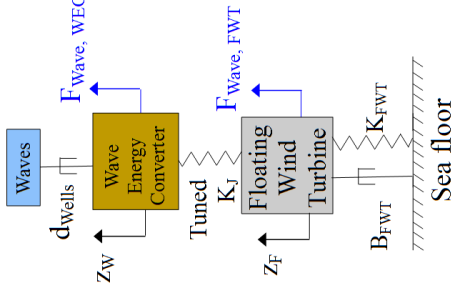
Table 8.1: Summary of performance for FWT-WEC's considered in this thesis.

Configuration	Illustration	Surge free body diagram	Heave free body diagram	Average WEC power (kW)	Levelized Cost of Energy (\$/kWh)	FWT tower stress (MPa)	Max FWT heave
0. Standalone FWT and linear WEC				50.6	0.27	32.4	0.14
1. Rigidly attached cylinder, $r_{Cyl} = 10$ m, $z_{Cyl} = -35$ m				N/A	N/A	31	0.19

Configuration	Illustration	Surge free body diagram	Heave free body diagram	Average WEC power (kW)	Levelized Cost of Energy	FWT tower stress	Max FWT heave
<p>2. Rigidly attached Wells turbine,  <math>d_{wells} = 5e5</math>Ns/m,  <math>z_{wells} = -20</math> m</p>				770	N/A	N/A	0.14
<p>3. Internal mass tuned damper in nacelle,  <math>d_J = 4.8e5</math> Ns/m</p>				12	1.91	23	0.14



Configuration	Illustration	Surge free body diagram	Heave free body diagram	Average WEC power (kW)	Levelized Cost of Energy	FWT tower stress	Max FWT heave
4. Surge-mode spherical WEC with modal-tuned spring and junction power takeoff, $d_J = 1.1e5$ N s/m				16	0.49	32	0.17
5. Surge-mode spherical WEC with modal-tuned spring and Wells turbine power takeoff, $d_J = 1.1e5$ N s/m				46	0.37	37	0.17

Configuration	Illustration	Surge free body diagram	Heave free body diagram	Average WEC power (kW)	Levelized Cost of Energy	FWT tower stress	Max FWT heave
<p>6. Heave-mode spherical WEC with modal-tuned spring and junction power takeoff, <math>d_J = 5.5e4</math> N s/m</p>				46	0.36	38	0.19
<p>7. Heave-mode spherical WEC with modal-tuned spring and Wells turbine power takeoff, <math>d_{Wells} = 1e6</math> N s/m</p>				75	0.34	38	0.21

Configuration	Illustration	Surge free body diagram	Heave free body diagram	Average WEC power (kW)	Levelized Cost of Energy	FWT tower stress	Max FWT heave
8. Rigidly attached oscillating water column				17	0.75	36	0.31
9. Hinged linear oscillating water column				51	0.27	32.4	0.14

Configuration	Illustration	Surge free body diagram	Heave free body diagram	Average WEC power (kW)	Levelized Cost of Energy	FWT tower stress	Max FWT heave
10. Hinged Nonlinear oscillating water column				87	0.26	30.7	0.14

# Appendix A

## Floating Wind Turbine Parameters

This thesis uses floating wind turbine parameters for the OC3-Hywind spar described by Jonkman et al. in National Renewable Energy Laboratory (NREL) reports, [66], [68], [64]. This thesis also considers the OC4-DeepCwind Semisubmersible in the statistical linearization study of Chapter 3. Robertson et al. describe the OC4-DeepCwind semisubmersible parameters in detail in the NREL report, [118]. These hydrodynamic parameters were computed using the WAMIT panel method [88].

For dissertation completeness, those parameters are duplicated here.

For both platforms, the rigid platform degrees of freedom are,

$$\vec{x}_{platform} = \begin{bmatrix} x_1 \\ x_2 \\ x_3 \\ x_4 \\ x_5 \\ x_6 \end{bmatrix} = \begin{bmatrix} surge \\ sway \\ heave \\ roll \\ pitch \\ yaw \end{bmatrix}. \quad (\text{A.1})$$

## A.1 OC3-Hywind spar

For these 6 degrees of freedom, the platform inertia matrix about the still water line is,

$$\mathbf{M}_{Platform} = \begin{bmatrix} 7466330 & 0 & 0 & 0 & -671338795 & 0 \\ 0 & 7466330 & 0 & 671338795 & 0 & 0 \\ 0 & 0 & 7466330 & 0 & 0 & 0 \\ 0 & 671338795 & 0 & 64592993432 & 0 & 0 \\ -671338795 & 0 & 0 & 0 & 64592993432 & 0 \\ 0 & 0 & 0 & 0 & 0 & 164230000 \end{bmatrix}, \quad (\text{A.2})$$

where the elements have standard International System (SI) Units of  $Kg$ ,  $Kgm$ , and  $m$ .

The frequency-dependent potential flow added mass and hydrodynamic damping are shown in Fig. A-1. The frequency-dependent wave forces normalized by wave amplitude are shown in Fig. A-2. These figures are reproduced from [66].

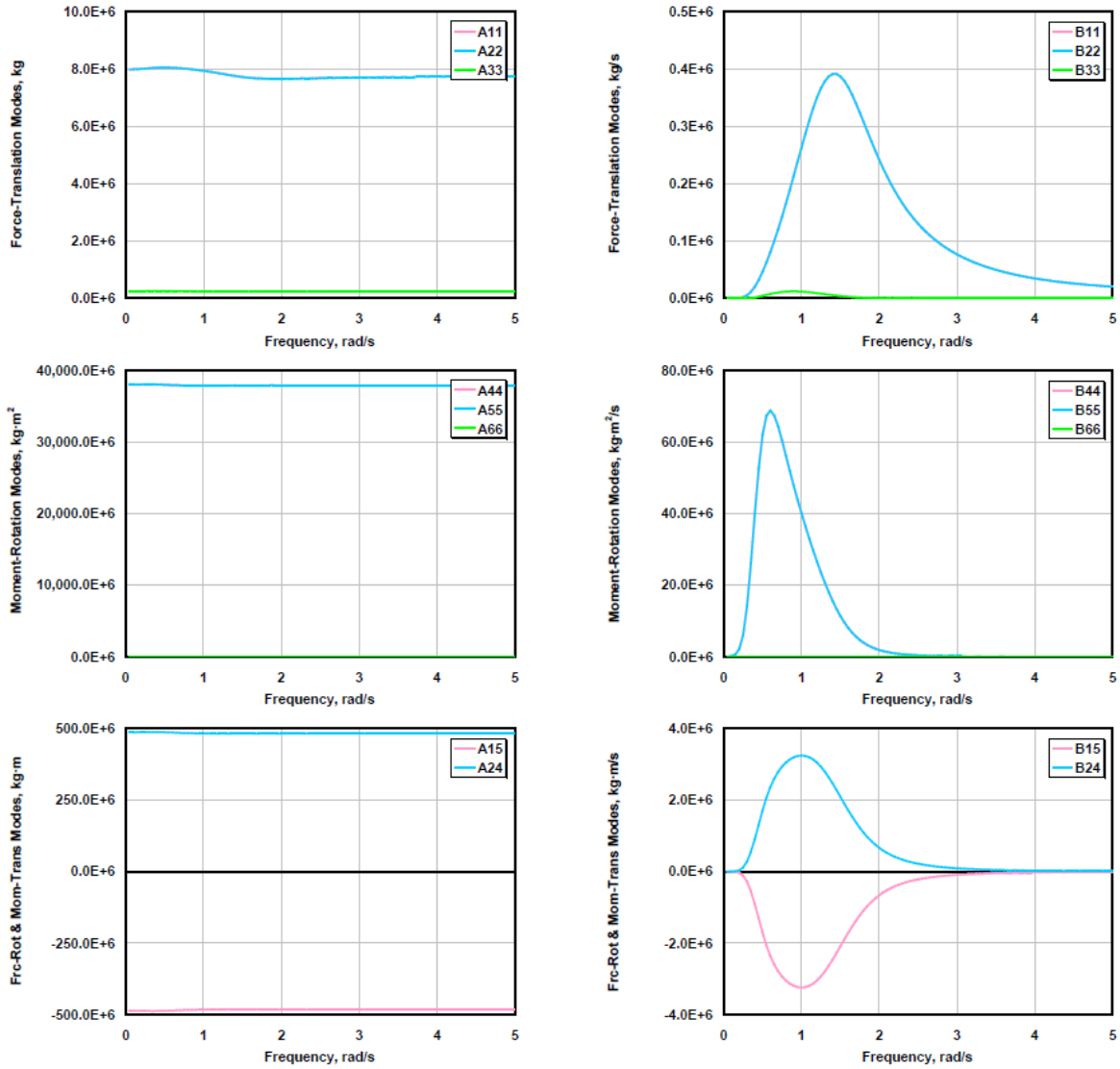


Figure A-1: OC3-Hywind frequency-dependent hydrodynamic added mass and damping from [66].

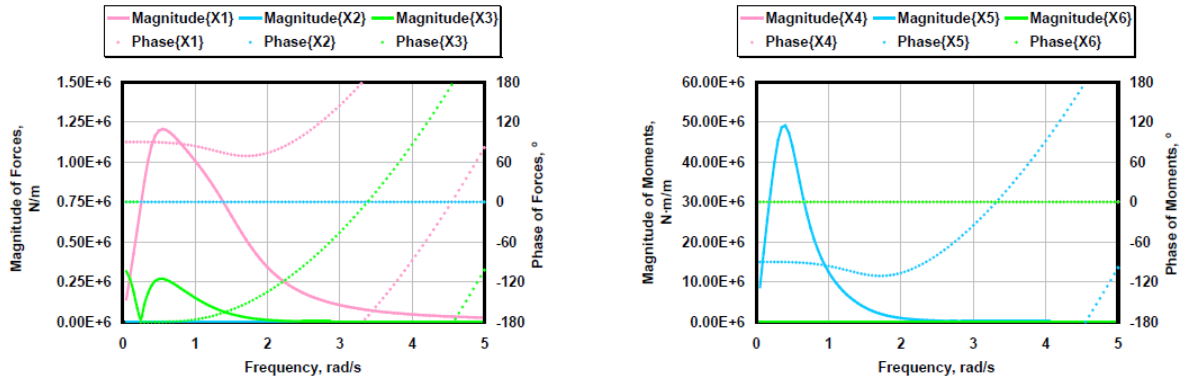


Figure A-2: OC3-Hywind frequency-dependent wave force normalized by wave amplitude from [66].

The OC3-Hywind has hydrostatic stiffness,

$$\mathbf{C}_{Platform} = \begin{bmatrix} 0 & 0 & 0 & 0 & 0 & 0 \\ 0 & 0 & 0 & 0 & 0 & 0 \\ 0 & 0 & 3.33e5 & 0 & 0 & 0 \\ 0 & 0 & 0 & 1.28e9 & 0 & 0 \\ 0 & 0 & 0 & 0 & 1.28e9 & 0 \\ 0 & 0 & 0 & 0 & 0 & 0 \end{bmatrix}, \quad (\text{A.3})$$

where the elements have standard International System (SI) Units of  $N/m$ ,  $Nm/rad$ .

The mooring lines are attached to platform fairleads at a submerged depth of 70 m. The mooring lines have a linearized stiffness about the platform 0-deflection point,

$$\mathbf{K}_{Mooring} = \begin{bmatrix} 41180 & 0 & 0 & 0 & -2882600 & 0 \\ 0 & 41180 & 0 & 2882600 & 0 & 0 \\ 0 & 0 & 11940 & 0 & 0 & 0 \\ 0 & 2882600 & 0 & 201782000 & 0 & 0 \\ -2882600 & 0 & 0 & 0 & 201782000 & 0 \\ 0 & 0 & 0 & 0 & 0 & 109900000 \end{bmatrix}, \quad (\text{A.4})$$

where the elements have standard International System (SI) Units of  $N/m$ ,  $Nm/rad$ .



## A.2 OC4-DeepCwind Semisubmersible

For these 6 degrees of freedom, the platform inertia matrix about the still waterline is,

$$\mathbf{M}_{Platform} = \begin{bmatrix} 13473000 & 0 & 0 & 0 & -181346580 & 0 \\ 0 & 13473000 & 0 & 181346580 & 0 & 0 \\ 0 & 0 & 13473000 & 0 & 0 & 0 \\ 0 & 181346580 & 0 & 9267924967 & 0 & 0 \\ -181346580 & 0 & 0 & 0 & 9267924967 & 0 \\ 0 & 0 & 0 & 0 & 0 & 12260000000 \end{bmatrix}, \quad (\text{A.5})$$

where the elements have standard International System (SI) Units of  $Kg$ ,  $Kgm$ , and  $m$ .

The frequency-dependent potential flow added mass and hydrodynamic damping are shown in Fig. A-3. The frequency-dependent wave force normalized by the wave amplitude is shown in Fig. A-4. These figures are reproduced from [118].

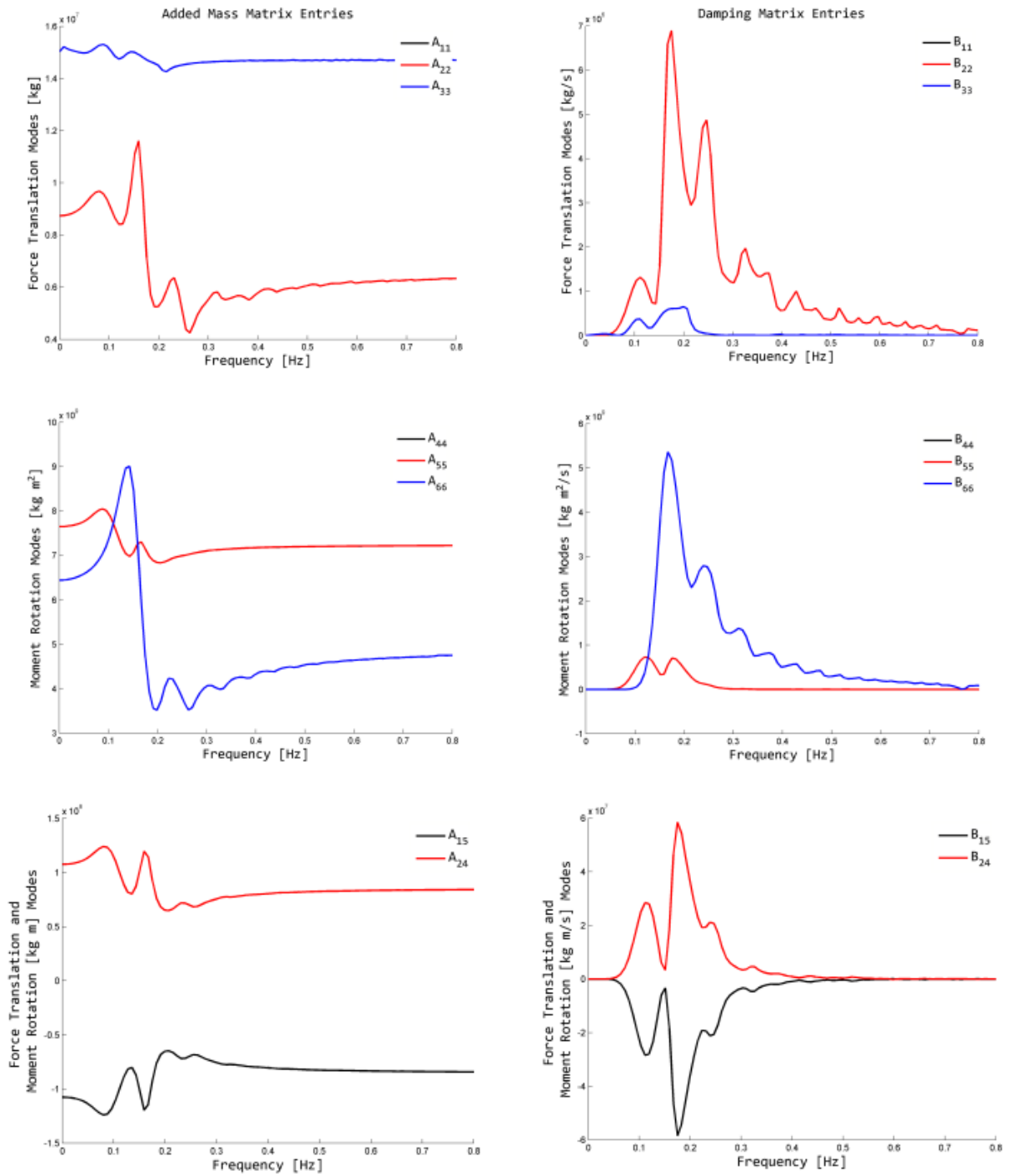


Figure A-3: OC4-DeepCwind semisubmersible frequency-dependent hydrodynamic added mass and damping from [118].

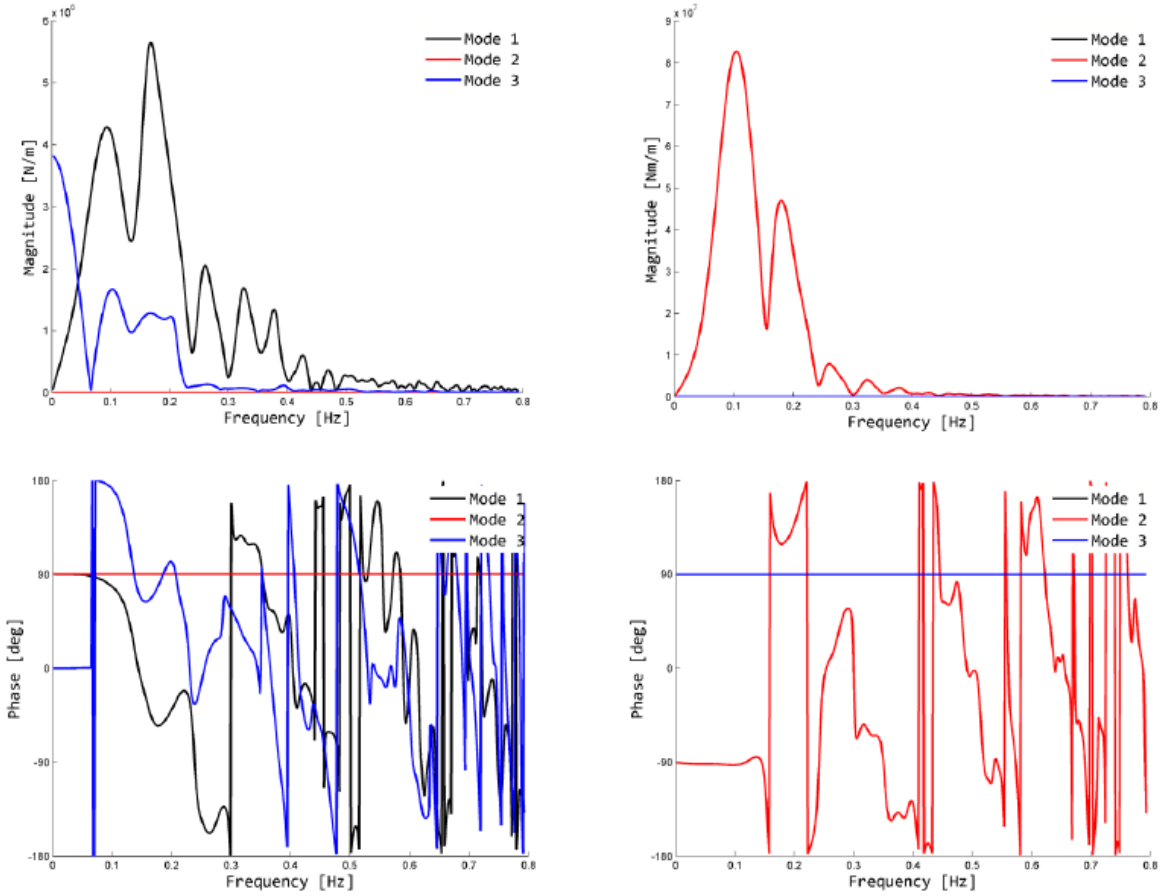


Figure A-4: OC4-DeepCwind semisubmersible frequency-dependent wave force normalized by wave amplitude from [118].

The OC4-DeepCwind semisubmersible has hydrostatic stiffness,

$$\mathbf{C}_{Platform} = \begin{bmatrix} 0 & 0 & 0 & 0 & 0 & 0 \\ 0 & 0 & 0 & 0 & 0 & 0 \\ 0 & 0 & 3860000 & 0 & 0 & 0 \\ 0 & 0 & 0 & 101250000 & 0 & 0 \\ 0 & 0 & 0 & 0 & 101250000 & 0 \\ 0 & 0 & 0 & 0 & 0 & 0 \end{bmatrix}, \quad (\text{A.6})$$

where the elements have standard International System (SI) Units of  $N/m$ ,  $Nm/rad$ .

The mooring lines are attached to platform fairleads at a submerged depth of 14 m. The

mooring lines have a linearized stiffness about the platform 0-deflection point,

$$\mathbf{K}_{Mooring} = \begin{bmatrix} 7.08e4 & 0 & 0 & 0 & -1.08e5 & 0 \\ 0 & 7.08e4 & 0 & 1.08e5 & 0 & 0 \\ 0 & 0 & 1.91e4 & 0 & 0 & 0 \\ 0 & 1.07e5 & 0 & 8.73e7 & 0 & 0 \\ -2882600 & 0 & 0 & 0 & 8.73e7 & 0 \\ 0 & 0 & 0 & 0 & 0 & 1.17e8 \end{bmatrix}, \quad (\text{A.7})$$

where the elements have standard International System (SI) Units of  $N/m$ ,  $Nm/rad$ .

# Bibliography

- [1] National oceanic and atmospheric administration national data buoy center. Accessed online April 14, 2015. <http://www.ndbc.noaa.gov/>.
- [2] Past projects: Mk3, 2010. Accessed Online April 14, 2015. <http://www.oceanlinx.com/projects/past-projects/mk3-2010>.
- [3] *Simscape Multibody: Getting Started Guide*, 2017.
- [4] U. Alibrandi and G. Ricciardi. *Nondeterministic mechanics*, chapter Stochastic methods in nonlinear structural dynamics. Springer, 2012.
- [5] A. Smith and T. Stehly and W. Musial. 2014-2015 offshore wind technologies market. Technical Report NREL/TP-5000-64283, National Renewable Energy Laboratory, 2015.
- [6] Harry Asada. *Introduction to Robotics*. Massachusetts Institute of Technology, 2005. [ocw.mit.edu/courses/mechanical-engineering/2-12-introduction-to-robotics-fall-2005/lecture-notes/](http://ocw.mit.edu/courses/mechanical-engineering/2-12-introduction-to-robotics-fall-2005/lecture-notes/).
- [7] A. Aubault, M. Alves, A. Sarmiento, D. Roddier, and A. Peiffer. Modeling of an oscillating water column on the floating foundation windfloat. In *Proceedings of the ASME 2011 30th International Conference on Ocean, Offshore and Arctic Engineering*, Rotterdam, The Netherlands, 2011.
- [8] Oscar Barambones. A robust control for maximizing the power output from a wave power generation plants. In *Conference Proceedings of AEDIE*.
- [9] I. Baring-Gould. Offshore wind energy market overview. Presentation, 2013. National Renewable Energy Laboratory.
- [10] G. Bir. *User's guide to BModes*. National Renewable Energy Laboratory, Golden, CO, 2007.
- [11] R. Booton. The analysis of nonlinear central systems with random inputs. *IRE Transactions on Circuit Theory*, 1:32–34, 1954.
- [12] T.K.A. Brekken, A. von Jouanne, and H.Y. Han. Ocean wave energy overview and research at oregon state university. In *Power Electronics and Machines in Wind Applications*, 2009. IEEE.

- [13] A. Brito-Melo, L.M.C. Gato, and A.J.N.A. Sarmiento. Analysis of wells turbine design parameters by numerical simulation of the owc performance. *Ocean Engineering*, 29, 2002.
- [14] D. Bull and E. Johnson. Optimal resistive control strategy for a floating owc device. Technical report, Sandia National Labs, 2013.
- [15] Diana Bull, Chris Smith, D.S. Jenne, Paul Jacob, Andrea Copping, Steve Willits, Arnold Fontaine, Dorian Brefort, Guild Copeland, Margaret Gordon, and Rich Jepsen. Reference model 6 (rm6): Oscillating wave energy converter. Technical Report SAND2014-18311, Sandia National Laboratories, 2014.
- [16] S. Butterfield, W. Musial, and J. Jonkman. Engineering challenges for floating offshore wind turbines. In *Proceedings of the Copenhagen Offshore Wind Conference*, Copenhagen, 2005.
- [17] CADDET. The mighty whale. Technical report, CADDET Renewable energy Newsletter, March 1999.
- [18] T. Caughey. Equivalent linearization techniques. *Journal of the Acoustical Society of America*, 1963.
- [19] S. Ceballos, J. Rea, I. Lopez, J. Pou, E. Robles, and D.L. O’Sullivan. Efficiency optimization in low inertia wells turbine-oscillating water column devices. *IEEE Transactions on energy conversion*, 28, 2013.
- [20] S. Christiansen, T. Bak, and T. Knudsen. Damping wind and wave load on a floating wind turbine. *energies*, 6:4097–4116, 2013.
- [21] C. Chu. *Random vibration of nonlinear building-foundation systems (Damage, Reliability)*. University of Illinois at Urbana-Champaign, 1985.
- [22] The European Commission. European wave energy pilot plant on the island of pico, azores, portugal. phase 2: Equipment. Technical report, The European Commission, 1998.
- [23] The European Commission. Islay limpet wave power plant. Technical report, The Queen’s University of Belfast, 2002.
- [24] ConcreteNetwork. Concrete price considerations. Online. <http://www.concretenetwork.com/concrete-prices.html>.
- [25] M. Constantinou and I. Tadjbakhsh. Response of a sliding structure to filtered random excitation. *Journal of Structural Mechanics*, pages 401–418, 1984.
- [26] G. Copeland, D. Bull, R. Jepsen, and M. Gordon. Oscillating water column structural model. Technical Report SAND2014-18082, Sandia national Laboratories, 2014.

- [27] A. Cordle and J. Jonkman. State of the art in floating wind turbine design tools. In *Proceedings of the 21st International Offshore and Polar engineering Conference*, Maui, Hawaii, 2011.
- [28] A. Cornett. A global wave energy resource assessment. In *Proceedings of ISOPE*, Vancouver, 2008.
- [29] Georgia Tech Research Corporation. Assessment of energy production potential from ocean currents along the united states coastline. Technical report, Georgia Tech, 2013.
- [30] J. Cruz. *Ocean Wave Energy: Current status and future perspectives*. Springer, 2008.
- [31] G.J. Dalton, R. Alcorn, and T. Lewis. Case study feasibility analysis of the pelamis wave energy converter in ireland, portugal and north america. *Renewable Energy*, 35:443–455, 2010.
- [32] B. Drew, A.R. Plummer, and M.N. Sahinkaya. A review of wave energy converter technology. *J. Power and Energy*, 2009.
- [33] EERE. Marine and hydrokinetic resource assesment and characterization. Technical report, Office of Energy Efficiency.
- [34] B. Epps, J. Ketcham, and C. Chryssostomos. Propeller blade stress estimates using lifting line theory. In *Grand challenges in modeling and simulation: Proceedings of the Summer Simulation Multiconference*, Ottawa, ON, Canada, 2010.
- [35] A. Arapogianni et al. Deep water: the next step for offshore wind energy. Technical report, European Wind Energy Association, 2013.
- [36] B. Hamilton et al. U.s.offshore wind market and economic analysis. Technical report, Navigant, 2014.
- [37] D.V. Evans and R. Porter. Efficient calculation of hydrodynamic properties of owc-type devices. *J. Offshore Mechanics and Arctic Engineering*, 119, 1997.
- [38] A. Falcao. Modelling and control of oscillating-body wave energy converters with hydraulic power take-off and gas accumulator. *Ocean Engineering*, 34:2021–2032, 2007.
- [39] A. Falcao. Wave energy utilization: A review of the technologies. *Renewable and Sustainable energy Reviews*, 14:899–918, 2010.
- [40] A. Falcao, J. Henriques, and J. Candido. Dynamics and optimization of the owc spar buoy wave energy converter. *Renewable energy*, 48:369–381, 2012.
- [41] A. Falcao and P. Justino. Owc wave energy devices with air flow control. *Ocean engineering*, 26, 1999.

- [42] J. Falnes and K. Budal. Wave-power conversion by power absorbers. *Norweg Mar Res*, 6, 1978.
- [43] J. Falnes and J. Hals. Heaving buoys, point absorbers, and arrays. *Philosophical transactions of the royal society*, 370:246–277, 2012.
- [44] O.M. Faltinsen. *Sea loads on ships and offshore structures*. Cambridge University Press, 1990.
- [45] V. Ferdinande and M. Vantorre. The concept of a bipartite point absorber. In *Hydrodynamics of Ocean Wave-Energy Utilization*, Lisbon, 1985. International Union of Theoretical and Applied Mechanics.
- [46] D.C. Freeman. *Nonlinear springs with applications to flow regulation valves and mechanisms*. PhD thesis, Massachusetts Institute of Technology, 2008.
- [47] A. Gareev. *Analysis of variable pitch air turbines for oscillating water column wave energy converters*. PhD thesis, University of Wollongong, 2011.
- [48] O.V. Gendelman, T. Sapsis, A.F. Vakakis, and L.A. Bergman. Enhanced passive targeted energy transfer in strongly nonlinear mechanical oscillators. *J. Sound and Vibration*, 330:1–8, 2011.
- [49] P. Georgilakis. Technical challenges associated with the integration of wind power into power systems. *Renewable and Sustainable Energy Reviews*, 12:852–863, 2008.
- [50] G.D. Gkikas, N.I. Xiros, G.A. Athanassoulis, and K.A. Belibassakis. A nonlinear model for oscillating water column analysis, design and control. In *Proceedings of the Sixteenth (2006) International Offshore and Polar Engineering Conference*, 2006.
- [51] B. Gregory. Wave energy converter, 2009. U.S. Patent 20090309366.
- [52] B. Gregory. Dynamically tuned wave energy converter, 2011. U.S. Patent 20110089689A1.
- [53] B. Gregory. Dynamically tuned wave energy converter, 2011. U.S. Patent 20110089689.
- [54] M. Grigoriu, M. ASCE, and B. Alibe. Response of offshore structures to random waves. *Journal of Engineering Mechanics*, 1986.
- [55] O. Gumestad and J. Connor. Linearization methods and the influence of current on the nonlinear hydrodynamic drag force. *Applied Ocean Research*, 5, 1983.
- [56] A. Hajati, S.P. Bathurst, H.J. Lee, and S.G. Kim. Design and fabrication of a nonlinear resonator for ultra wide-bandwidth energy harvesting applications. In *Proceedings of the IEEE International Conference on Micro Electro Mechanical Systems (MEMS)*, pages 1301–1304, April 2011.



- [57] M. Hall. Moordyn user's guide. Technical report, University of Maine, 2015.
- [58] M. Hall and A. Goupee. Validation of a lumped-mass mooring line model with deep-wind semisubmersible model test data. *Ocean Engineering*, 104:590–603, 2015.
- [59] R. Harrison and J. Hammond. Approximate, time-domain, non-stationary analysis of stochastically excited, non-linear systems with particular motion of vehicles on rough ground. *Journal of Sounds and Vibration*, 1986.
- [60] S. Hauptmann, M. Bulk, L. Schon, S. Erbsloh, K. Boorsma, F. Grasso, M. Kuhn, and P. Cheng. Comparison of the lifting-line free vortex wake method and the blade element momentum theory regarding the simulated loads of multi-mw wind turbines. In *The science of making torque from wind*. IOP Publishing, 2014.
- [61] G. Hayman. *Mlife Theory Manual for Version 1.00*. National Renewable Energy Laboratory, 2012.
- [62] T.V. Heath. A review of oscillating water columns. *Philosophical Transactions of the Royal Society*, 370:235–245, 2012.
- [63] R. James and M. Ros. Floating offshore wind: Market and technology review. Technical report, The Carbon Trust, 2015.
- [64] J. Jonkman. *Dynamics modeling and loads analysis of an offshore floating wind turbine*. PhD thesis, University of Colorado Boulder, 2007.
- [65] J. Jonkman. Influence of control on the pitch damping of a floating wind turbine. In *ASME Wind Energy Symposium*, Reno, Nevada, 2008.
- [66] J. Jonkman. Definition of the floating system for phase iv of oc3. Technical Report NREL/TP-500-47535, National Renewable Energy Laboratory, 2010.
- [67] J. Jonkman and M. Buhl. Fast user's guide. Technical report, national Renewable Energy Laboratory, 2005.
- [68] J. Jonkman, S. Butterfield, W. Musial, and G. Scott. Definition of a 5-mw reference wind turbine for offshore system development. Technical report, National Renewable Energy Laboratory, 2009.
- [69] J. Jonkman, G. Hayman, B. Jonkman, and R. Damiani. *AeroDyn v15 User's Guide and Theory Manual*, 2016.
- [70] J. Jonkman, T. Larsen, A. Hansen, T. Nygaard, K. Maus, M. Karimirad, Z. Gao, T. Moan, I. Fylling, J. Nichols, M. Kohlmeier, J.P. Vergara, D. Merino, W. Shi, and H. Park. Offshore code comparison collaboration within IEA Wind Task 23: Phase iv results regarding floating wind turbine modeling. In *Proc. European Wind Energy Conference*, Warsaw, Poland, 2010.
- [71] Han Kyul Joo. Single-degree-of-freedom energy harvesters by stochastic excitation. Master's thesis, Massachusetts Institute of Technology, 2014.

- [72] H.K. Joo. *Probabilistic optimization of vibrational systems under stochastic excitation containing extreme forcing events*. PhD thesis, Massachusetts Institute of Technology, 2017.
- [73] H.K. Joo and T.P. Sapsis. Performance measures for single-degree-of-freedom energy harvesters under stochastic excitation. *J. Sound and Vibration*, 333:4695–4710, 2014.
- [74] B. Kantor and L. Afanas'eva. Nonlinear flexure of a circular plate of variable thickness. *Prikladnaya Mekhanika*, 4(7):71–74, 1968.
- [75] M. Karimirad. Modeling aspects of a floating wind turbine for coupled wave-wind-induced dynamic analyses. *Renewable Energy*, 53:299–305, 2013.
- [76] M. Karimirad. *Offshore Energy Structures*. Springer, 2014.
- [77] Thomas Kelly, Thomas Dooley, John Campbell, and John V. Ringwood. Comparison of the experimental and numerical results of modelling a 32-oscillating water column (owc), v-shaped floating wave energy converter. *energies*, 6:4045–4077, 2013.
- [78] J. Kluger. Nonlinear beam-based vibration energy harvesters and load cells. Master's thesis, Massachusetts Institute of Technology, February 2014.
- [79] J. Kluger, T. Sapsis, and A. Slocum. A reduced-order, statistical linearization approach for estimating nonlinear floating wind turbine response statistics. In *Proceedings of the Twenty-sixth International Ocean and Polar Engineering Conference*, pages 545–552, Rhodes, Greece.
- [80] J. Kluger, T. Sapsis, and A. Slocum. Robust energy harvesting from walking vibrations by means of nonlinear cantilever beams. *Journal of Sound and Vibration*, 341:174–194, 2015.
- [81] J. Kluger, T. Sapsis, and A. Slocum. Beam-based nonlinear spring. U.S. Patent US 9382960, 2016.
- [82] J. Kluger, T. Sapsis, and A. Slocum. A high-resolution and large force-range load cell by means of nonlinear cantilever beams. *Precision Engineering*, 43:241–256, 2016.
- [83] J. Kluger, A. Slocum, and T. Sapsis. Ring-based stiffening flexure applied as a load cell with high resolution and large force range. *ASME Journal of Design*, Accepted 2017.
- [84] J.P. Kofoed, P. Frigaard, E. Friis-Madsen, and H.C. Sorensen. Prototype testing of the wave energy converter wave dragon. *Renewable Energy*, 31:181–189, 2006.
- [85] National Renewable Energy Laboratory. 2015 renewable energy data book.
- [86] T. Larsen and A. Hansen. *How 2 HAWC2*, 2007.

- [87] M. Lawson, Y. Yu, A. Nelessen, K. Ruehl, and C. Michelen. Implementing nonlinear buoyancy and excitation forces in wec-sim wave energy converter modeling tool. In *Proceedings of OMAE*, San Francisco, 2014.
- [88] C. Lee and J. Newman. *WAMIT user Manual 7.0*. WAMIT, Inc. and MIT, 2010.
- [89] B. Leira. Multidimensional stochastic linearisation of drag forces. *Applied Ocean Research*, pages 150–162, 1987.
- [90] A. Lewis, S. Estefen, J. Huckerby, W. Musial, T. Pontes, and J. Torres-Martinez. *IPCC Special Report on Renewable Energy Sources and Climate Change Mitigation*, chapter Ocean Energy. Cambridge University Press, 2011.
- [91] A. Lopez, B. Roberts, D. Heimiller, N. Blair, and G. Porro. U.s. renewable energy technical potentials: a gis-based analysis. Technical report, National Renewable Energy Laboratory, 2012.
- [92] I. Lopez, J. Andreu, S. Ceballos, and I. Alegria. Review of wave energy technologies and necessary power equipment. *Renewable and Sustainable Energy Reviews*, 27:413–434, 2013.
- [93] R. Lumpkin and G. Johnson. Global ocean surface velocities from drifters: mean, variance, el nino- southern oscillation response, and seasonal cycle. *Journal of Geophysical research: Oceans*, 118:2992–3006, 2013.
- [94] M. Masciola. *Mooring Analysis Program*. National Renewable Energy Laboratory, 2016.
- [95] Y. Masuda, T. Yamazaki, Y. Outa, and M. McCormick. Study of backward bent duct buoy. *IEEE*, 384, 1987.
- [96] D. Matha. Model development and loads analysis of an offshore wind turbine on a tension leg platform, with a comparison to other floating turbine concepts. Master’s thesis, University of Colorado, Boulder, CO, 2009.
- [97] D.M. McFarland, L.A. Bergman, and A.F. Vakakis. Experimental study of nonlinear energy pumping occurring at a single fast frequency. *International Journal of Non-Linear Mechanics*, 40:891–899, 2005.
- [98] C. Mei and D. Paul. Nonlinear multi-mode response of clamped rectangular plates to acoustic loading. *Journal of American Institute of Aeronautics and Astronautics*, pages 634–648, 1986.
- [99] M.J. Muliawan, M. Karimirad, Z. Gao, and T. Moan. Extreme responses of a combined spar-type floating wind turbine and floating wave energy converter(stc)system with survival modes. *Ocean Engineering*, 65:71–82, 2013.
- [100] A. Myhr, C. Bjerkseter, A. Agotnes, and T. Nygaard. Levelized cost of energy for offshore floating wind turbines in a life cycle perspective. *Renewable Energy*, 66:714–728, 2014.

- [101] A. Naess and T. Moan. *Stochastic dynamics of marine structures*. Cambridge University Press, Cambridge, UK, 2013.
- [102] V. Neary, M. Previsic, R. Jepsen, M. Lawson, Y. Yu, A. Copping, A. Fontaine, K. Hallett, and D. Murray. Methodology for design and economic analysis of marine energy conversion (mec) technologies. Technical Report SAND2014-9040, Sandia National Laboratories, 2014.
- [103] J. Newman. *Marine Hydrodynamics*. MIT Press, Cambridge, MA, 1977.
- [104] J. Newman and P. Sclavounos. The computation of wave loads on large offshore structures. In *Proceedings of BOSS*, 2006.
- [105] NREL. Dynamic maps, gis data, and analysis tools. Online, 2016.
- [106] NREL and Sandia. *Wave Energy Converter SIMulator*, 2015. <https://wec-sim.github.io/WEC-Sim/index.html>.
- [107] Hiroyuki Osawa, Yukihiwa Washio, Teruhisa Ogata, Yasusi Tsuritani, and Yoshinori Nagata. The offshore floating type wave power device 'mighty whale' open sea tests-performance of the prototype. In *Proceedings of The Twelfth (2002) International Offshore and Polar Engineering Conference*.
- [108] D.L. O'Sullivan and A.W. Lewis. Generator selection and comparative performance in offshore oscillating water column ocean wave energy converters. *IEEE Transactions on energy conversion*, 26, 2011.
- [109] I. Pineda and P. Tardieu. The european offshore wind industry. Technical report.
- [110] D. Quinn, O. Gendelman, G. Kerschen, T. Sapsis, L. Bergman, and A. Vakakis. Efficiency of targeted energy transfers in coupled nonlinear oscillators associated with 1:1 resonance captures: Part i. *Journal of Sound and Vibration*, pages 1228–1248, 2008.
- [111] D. Quinn, A. Triplett, L. Bergman, and A. Vakakis. Comparing linear and essentially nonlinear vibration-based energy harvesting. *Journal of Vibration and Acoustics*, 133:011001, 2011.
- [112] M. Raffero, M. Martini, B. Passione, G. Mattiazzo, E. Bicelli, and G. Bracco. Stochastic control of inertial sea wave energy converter. *The Scientific World Journal*, pages 1–14, 2014.
- [113] G.K.V. Ramachandran, A. Robertson, J.M. Jonkman, and M.D. Masciola. Investigation of response amplitude operators for floating offshore wind turbines. In *Proc. ISOPE*, Anchorage, Alaska, 2013. International Society of Offshore and Polar Engineers (ISOPE).
- [114] R. Rand. Vibrations mae 4770. Technical report, Cornell University, 2012.

- [115] J. Roberts and P. Spanos. Stochastic averaging: an approximate method of solving random vibration problems. *Nonlinear Mechanics*, 21:111–134, 1986.
- [116] J. Roberts and P. Spanos. *Random vibration and statistical linearization*. Dover, 2003.
- [117] A. Robertson and J. Jonkman. Loads analysis of several offshore floating wind turbine concepts. In *Proceedings of the International Society of Offshore and Polar Engineers*, Maui, Hawaii, 2011.
- [118] A. Robertson, J. Jonkman, M. Masciola, H. Song, A. Goupee, A. Coulling, and C. Luan. Definition of the semisubmersible floating system for phase ii of oc3. Technical Report NREL/TP-5000-60601, National Renewable Energy laboratory, 2014.
- [119] M. Sakata, K. Kimura, and M. Utsumi. Nonstationary response of nonlinear liquid motion in a cylindrical tank subjected to random base excitation. *Journal of Sounds and Vibration*, 1984.
- [120] T. Sapsis, A. Vakakis, O. Gendelman, L. Bergman, G. Kerschen, and D. Quinn. Efficiency of targeted energy transfers in coupled nonlinear oscillators associated with 1:1 resonance captures: Part ii, analytical study. *Journal of Sound and Vibration*, pages 297–320, 2008.
- [121] D. Schlipf, F. Sandner, S. Raach, D. Matha, and P. Cheng. Nonlinear model predictive control of floating wind turbines. In *Proceedings of the International Offshore and Polar Engineering*, Anchorage, Alaska. ISOPE.
- [122] P. Sclavounos. Intersections between marine hydrodynamics and optimal control theory. In *21st International Workshop on Water Waves and Floating Bodies*, Loughborough, England, 2006.
- [123] P. Sclavounos. 2.24: Ocean waves and energy systems course notes, 2015.
- [124] T. Sebastian and M. Lackner. Characterization of the unsteady aerodynamics of offshore floating wind turbines. *Wind Energy*, 16:339–352, 2013.
- [125] Y. Shao, J. You, and E. Glomnes. Stochastic linearization and its application in motion analysis of cylindrical floating structure with bilge boxes. In *Proceedings of ASME Conference on Ocean, Offshore, and Arctic Engineering*.
- [126] A.H. Slocum. *FUNdaMENTALS of Design*. MIT, 2008.
- [127] A.H. Slocum. Symbiotic offshore energy harvesting and storage systems. In *Proceedings of 2014 Offshore Energy and Storage Symposium*, Windsor, Ontario, Canada, July 2014. UWCAES Society.
- [128] A. Smith, T. Stehly, and W. Musial. 2014-2015 offshore wind technologies market report. Technical Report NREL/TP-500-64283, National Renewable Energy Laboratory, 2015.

- [129] R. So, S. Casey, S. Kanner, A. Simmons, and T. Brekken. Pto-sim: development of a power take off modeling tool for ocean wave energy conversion. In *Power and Energy Society General Meeting*. IEEE, 2015.
- [130] P. Spanos and V. Agarwal. Response of a simple tension leg platform model to wave forces calculated at displaced position. *ASME Journal of Energy Resources Technology*, 106:437–443, 1984.
- [131] G. Stewart and M. Lackner. Offshore wind turbine load reduction employing optimal passive tuned mass damping systems. *IEEE Transactions on Control Systems Technology*, 21, 2013.
- [132] X. Tang and L. Zuo. Enhanced vibration energy harvesting using dual-mass systems. *J. Sound and Vibration*, 330:5199–5209, 2011.
- [133] A.H. Techet. 13.42 design principles for ocean vehicles. MIT course lecture notes, 2005.
- [134] S. Tegen, E. Lantz, M. Hand, B. Maples, A. Smith, and P. Schwabe. 2011 cost of wind energy review. Technical report, NREL, 2013.
- [135] Tethys. Oceanlinx mk3. Accessed Online April 14, 2015. <http://tethys.pnnl.gov/annex-iv-sites/oceanlinx-mk3>.
- [136] R. Tidball, J. Bluestein, N. Rodriguez, and S. Knoke. Cost and performance assumptions for modeling electricity generation technologies. Technical report, NREL, 2010.
- [137] R. Tiron, C. Pinck, E. Reynaud, and F. Dias. Is biofouling a critical issue for wave energy converters? In *Proceedings of the twenty-second international offshore polar engineering conference*, Rhodes, Greece, 2012.
- [138] T. Tran and D. Kim. The platform pitching motion of floating offshore wind turbine: a preliminary unsteady aerodynamic analysis. *Journal of Wind Engineering and Industrial Aerodynamics*, 142:65–81, 2015.
- [139] T. Tran, D. Kim, and J. Song. Computational fluid dynamic analysis of a floating offshore wind turbine experiencing platform pitching motion. *energies*, 7:5011–5026, 2014.
- [140] A.Z. Trimble. *Energy harvesting of random wide-band vibrations with applications to an electromagnetic rotational energy harvester*. PhD thesis, Massachusetts Institute of Technology, 2011.
- [141] A.F. Vakakis, O.V. Gendelman, L.A. Bergman, D.M. McFarland, G. Kerschen, and Y. S. Lee. *Nonlinear Targeted Energy Transfer in Mechanical and Structural Systems*. Springer, 2009.
- [142] F. White. *Fluid Mechanics*. McGraw Hill, 2011.

- [143] Y. Yu, D. Jenne, R. Thresher, A. Copping, S. Geerlofs, and L. Hanna. Reference model 5 (rm5): Oscillating surge wave energy converter. Technical Report NREL/TP-5000-62861, National Renewable Energy Laboratory, 20015.
- [144] W. Zhao and D. Wan. Numerical study of interactions between phase ii of oc4 wind turbine and its semi-submersible floating support system. *Journal of Ocean and Wind Energy*, 2(1):45–53, 2015.